Unraveling the molecular and cellular complexities of the kidney in health and disease

A dissertation presented

by

Eriene-Heidi Sidhom

to

The Division of Medical Sciences

in partial fulfillment of the requirements

for the degree of

Doctor of Philosophy

in the subject of

Biological and Biomedical Sciences

Harvard University

Cambridge, Massachusetts

May 2019

Dissertation Advisor: Anna Greka Eriene-Heidi Sidhom

Unraveling the molecular and cellular complexities of the kidney in health and disease

Abstract

Chronic kidney disease (CKD) affects over 500 million people worldwide, and despite this significant disease burden, therapeutic innovation in nephrology has lagged. This trend is partly attributed both to an incomplete understanding of the molecular mechanisms of kidney dysfunction and a lack of appropriate *in vitro* and *in vivo* models, a reflection of the multifactorial nature CKD and the complex cellular complexity of the kidney.

Genetically defined rare diseases can provide insight into disease pathogenesis. We thus, sought to understand the mechanism underlying a rare Coenzyme Q (CoQ)-deficiency-associated podocytopathy. Podocytes are a terminally differentiated, post-mitotic cell type, essential for kidney filter function. An *in vitro* podocyte model of CoQ deficiency revealed a susceptibility to ROS-mediated injury and a perturbation in polyunsaturated fatty acid metabolism. Single nucleus sequencing from the kidneys of CoQ-deficient mice validated podocyte-specific transcriptomic changes consistent with *in vitro* findings and revealed a novel, disease-specific parietal epithelial cell population. Our analysis further revealed the BRAF-targeting GDC-0879 as a putative therapeutic strategy.

Kidney organoids derived from human induced pluripotent stem cells (iPSCs) are an emerging technology with the potential to both recapitulate the cellular diversity of the kidney and to further our understanding of disease. However, this progress is dependent on understanding the reproducibility and quality of organoids derived from multiple patients-donors. Thus, we generated a 412,358 single cell census of 47 organoid and iPSC samples derived from four cell lines across four time points of differentiation. All cell lines contained representative segments of the developing nephron, but varied in their proportions of cell types and in the presence of off-

target populations. Comparison to single cell fetal kidney data revealed that the organoids were most similar to first trimester fetal kidney. While long-term *in vitro* culture did not affect organoid composition, *in vivo* transplantation of organoids resulted in reduced off-target populations.

Table of Contents

List of Figures

Chapter 1

Chapter 2

Chapter 3

Appendix 1

Appendix 2

List of Tables

Chapter 1

Appendix 1

Appendix 2

Glossary

AD:	Autosomal dominant
AR:	Autosomal recessive
4-HB:	4-hydroxybenzoate
AA:	Arachidonic acid
ACAN:	Aggrecan
Actb:	Actin: beta
Actg1:	Actin: gamma: cytoplasmic 1
ADCK4:	AARF domain-containing kinase 4
ADPKD:	Autosomal dominant polycystic kidney disease
ANGPT:	Angiopoietin
APOE:	Apolipoprotein E
AQP2:	Aquaporin 2
AS:	iPSC line: Alstem
atRA:	all-trans retinoic acid
BMP:	Bone morphogenic protein
CAKUT:	Congenital anomalies of the kidney and urinary tract
CD:	Collecting duct
CD31:	Platelet and endothelial cell adhesion molecule 1
Cd74:	Invariant polypeptide of MHC class II antigen-associated
CDC42:	Cell division cycle 42
CDH1:	E-cadherin
CHD1L:	Chromodomain helicase DNA binding protein 1 like
CHG:	Chromogranin
CKD:	Chronic kidney disease
CLDN/Cldn:	Claudin
CM:	Cap mesenchyme
CoA:	Coenzyme A
COL:	Collagen
CoQ:	Coenzyme Q
CTNNB1:	Catenin beta 1
Cxcl1:	C-X-C motif chemokine ligand 1
D0:	Day 0 (iPSC state)
D15:	Day 15
D29:	Day 29
D32:	Day 32
D7:	Day 7
DA:	Differentially abundant (metabolites)
Dcdc2a:	Doublecortin domain containing 2a
DCN:	Decorin
DCT:	Distal convoluted tubule
DE:	Differentially expressed (genes)
Dgat2:	Diacylglycerol O-acyltransferase 2
DHODH:	Dihydroorotate dehydrogenase
DKD:	Diabetic kidney disease
DKK1:	Dickkopf WNT signaling pathway inhibitor 1
Dock10:	Dedicator Of cytokinesis 10
$\Delta\Psi_m$:	Mitochondrial membrane potential
EPYC:	Epiphycan

ESC:	Embryonic stem cell
ESRD:	End stage renal disease
ETC:	Electron transport chain
FGF:	Fibroblast growth factor
FISH:	Fluorescence *in situ* hybridization
Flt:	Fms related tyrosine kinase
FOXC2:	Forkhead box C2
FOXP2:	Forkhead box P2
FPE:	Foot process effacement
FPs:	Foot processes
FSGS:	Focal and segmental glomerulosclerosis
FXR:	Farsenoid X receptor
GAL:	Galanin and GMAP prepropeptide
GAS2:	Growth arrest specific 2
GATA3:	GATA binding protein 3
Gb3:	Globotriasylceramide
GBM:	Glomerular basement membane
GGdP:	Geranyl-geranyl pyrophosphate
GSEA:	Gene set enrichment analysis
GWAS:	Genome-wide association studies
HAND1:	Heart and neural crest derivatives expressed 1
HCR:	*in situ* Hybridization chain reaction
HDL:	High density lipoprotein
HES1:	Hes family bHLH transcription factor 1
hiPSC:	Human induced pluripotent cell
HIVAN:	HIV associated nephropathy
HMDB:	Human metabolome database
HOX:	Homeobox
hPSC:	Human pluripotent stem cell
HPSE2:	Heparanase 2
HRC:	Hereditary renal cystic
IC: I	ntercalated cell
ID3:	Inhibitor of DNA binding 3: HLH protein
IGF:	Insulin-life growth factor
Ikbkb:	Inhibitor of kappaB kinase beta
IM:	Intermediate mesoderm
IRX3:	Iroquois homeobox 3
JSD:	Jenson-Shannon Divergence
Kdr:	Kinase insert domain receptor
KLF6:	Kruppel like factor 6
LECT1:	Chondromodulinprovided
LHX1:	LIM homeobox 1
LOH:	Loop of Henle
LPC:	Lysophosphatidylcholine
Lrp2:	Megalin
LTL:	Lotus tetragonolobus lectin
MAL:	Mal: T cell differentiation protein
Mapk:	Mitogen activated kinase-like protein
MATN4:	Matrilin 4
MGP:	Matrix Gla protein

mitoTEMPO: (2-(2: 2: 6: 6-Tetramethylpiperidin-1-oxyl-4-ylamino)-2-oxoethyl)triphenylphosphonium chloride
MM: Metanephric mesenchyme
MPTP: Mitochondrial permeability transition pore
MUC1: Mucin 1
MYOG: Myogenin
N1/2: iPSC line: Normal 1: 2 (healthy human donor)
Nfkb1: Nuclear factor of kappa light polypeptide gene enhancer in B cells 1
Nfkbia: Nuclear factor of kappa light polypeptide gene enhancer in B cells inhibitor: alpha
NPCs: Nephron progenitor cells
NPHS1: Nephrin
NPHS2: Podocin
NR2F1: Nuclear receptor subfamily 2 group F member 1
NS: Nephrotic syndrome
NTRK2: Neurotrophic receptor tyrosine kinase 2
OCR: Oxygen consumption rate
OXPHOS: Oxidative phosphorylation
PAX: Paired box
PC: Phosphatidyl choline
PC: Principal cell
Pdss/PDSS: Decaprenyl diphosphate synthase subunit
Pdss2$^{kd/kd}$ (KDKD): Pdss2 kidney disease model: homozygous mutant
PEC: Parietal epithelial cell
PHB: Para-hydroxy benzoate
PKD1/2: Polycystin 1/2
PL: Phospholipid
Pla2g12a: Phospholipase A2 group 12A
Plvap: Pasmalemma vesicle associated protein
PMEL: Premelanosome protein
POU3F3: POU class 3 homeobox 3
PRDX2: Peroxiredoxin 2
PS: Primitive streak
PT: Proximal tubule
PTA: Pretubular aggregate
Ptprc: Protein tyrosine phosphatase: receptor type: C
PTPRS: Protein tyrosine phosphatase receptor type S
PU: Polyunsaturated
PUFA: Polyunsaturated fatty acid
RA: Retinoic acid
Rar: Retinoic acid receptor
RET: Ret proto-oncogene
Rhoa: Ras homolog family member A
RNA-seq: RNA sequencing
Rock2: Rho-associated coiled-coil containing protein kinase
ROS: Reactive oxygen species
RV: Renal vesicle
scRNA-seq: Single cell RNA sequencing
SD: Slit diaphragm
SLC12A1: Na-K-C cotransporter
SLC12A3: Na-Cl symporter

sNuc-seq:	Single nuclei RNA sequencing
SOST:	Sclerostin
SOX:	SRY-box
SPARC:	Secreted protein acidic and cysteine rich
SPP:	Osteopontin
SRNS:	Steroid resistant nephrotic syndrome
SSNS:	Steroid sensitive nephrotic syndrome
STMN1:	Stathmin 1
Synpo:	Synaptopodin
TAL:	Thick ascending limb
TF:	Transcription factor
TG:	Triglyceride
ThF:	iPSC line: Thermo Fisher
Tie1:	Tyrosine kinase with immunoglobulin-like and EGF-like domains 1
UB:	Ureteric bud
UUO:	Unilateral ureteral obstruction
Vcam1:	Vascular cell adhesion molecule 1
VEGF:	Vascular endothelial growth factor
WFDC2:	WAP four-disulfide core domain 2
WT1:	Wilms Tumor 1
ZEB2:	Zinc finger E-box binding homeobox 2

Acknowledgements

This dissertation would not have been possible without the help and support of so many people to whom I am sincerely grateful.

First, I would like to thank Anna Greka for being a wonderful advisor, role model, and mentor over the past four years. I have learned so much from her scientifically, professionally, and personally. First, Anna has taught me how to be rigorous in my science while being thoughtful of the larger question. I learn most from Anna simply by observing her: whether it be the way in which she manages and leads the lab or in her interactions with patients; I have been privileged to see how it is possible to combine intelligence, integrity, and honesty with compassion and empathy. In my first meeting with Anna, she noted how valuable her relationship with her PhD mentor has continued to be, and that she personally values being a mentor to others; I look forward to continuing to learn from Anna has I progress through my training and career.

Second, I would also like to thank other members of the Greka lab. To Moran, Yiming, and Nico, for being wonderful mentors since my first days in the lab. I feel so fortunate to have joined nearly simultaneously with three people who I admire so much as scientists and individuals. Second, to Abbe: even though I joined the lab not knowing I would have a fellow graduate student to go through the PhD with, being able to follow in your footsteps, in particular, in these past few months as we both prepare to graduate has made this process infinitely easier – thank you. Thank you to everyone in the lab who has made waking up and coming to lab every day for the past four years exciting and intellectually and personally rewarding. I have learned so much from each of you and feel so grateful to work with people who are so generous with their time and mentorship.

To all the faculty who have served on my dissertation advisory committee: Marcia Haigis, Vadim Gladyshev, Wolfram Goessling, Jagesh Shah, and David Clapham. My DAC committee meetings

have been some of my favorite parts of this process and their advice was critical in shaping my the trajectory of thesis work.

To all the wonderful administrators and mentors who are only an email away: Rick Mitchell, Patty Cunningham, Loren Walensky, Matthew Frosch, Amy Cohen, Yi Shen, thank you for your dedication and striving to help us all succeed personally and professionally. Thank you my HST and MD-PhD classmates: each of you inspires me, and I feel so fortunate to have matriculated with such a multi-talented class of peers.

Additionally, I would like to thank all the people who make up my support system in Boston and beyond. My running buddies, Colin, Katherine, and Ally: thank you for all the hours of listening and support along our favorite paths (and plank walks) by the Charles. It's been so cool accomplishing new goals with such amazing friends. Thank you to my college and childhood friends who have been understanding of my schedule for the past 10+ years and provide the perfect balance of both support and keeping me grounded: Katie, Alexis, Nicole, Griselle, Alanna, Jennifer, Miriam, Marina, Jillian and Ankita. Finally, to 123 Kent Street and honorary members, Emily, Jessica, Sarah, Sar, Josué, thank you for always believing in me and being ready to listen and give advice. To all of you, I could not ask for or imagine better friends.

And most importantly, thank you to my family. To my siblings, Mary and John: thank you for both being so inspiring to me in the passion and dedication that you bring to everything you do. To Leo, for being most willing to snuggle and keep me company while I analyze data. Finally, to my mom and dad, who have instilled in all of us the value of education and hard work, and to settle for nothing short of your best. Even more important, thank you for teaching us that beyond any sort of material or intellectual accomplishment, what is most valuable is who you are as individual and how you treat others. Thank you, mom and dad, for traveling to see me when I couldn't come home, believing in me, and providing unconditional love and support. I would not be where I am today without you.

Chapter 1:

Introduction

Podocyte biology and disease

The kidney plays many roles in physiologic homeostasis including water and electrolyte balance; excretion of toxic metabolites; and hormone secretion. The main functional unit of the kidney is the nephron which is comprised of the renal corpuscle followed by a segmented tubular compartment. The renal corpuscle, or glomerulus, consists of a capillary loop surrounded by Bowman's capsule (Greka and Mundel, 2012). Bowman's capsule is continuous with the tubular epithelium where secretion and reabsorption of electrolytes, organic small molecules, and water are critical for maintenance of fluid and electrolyte balance. The initial step of urine production, plasma filtration, occurs in the glomerulus.

Podocyte function

The glomerulus contains four resident cell types: glomerular endothelial cells, visceral epithelial cells (podocytes), parietal epithelial cells (PECs) of Bowman's capsule, and mesangial cells. The endothelial cells and podocytes share a common glomerular basement membrane (GBM) which together allow for selective plasma filtration based on size and charge. Water and small solutes (e.g. urea, glucose, amino acids, and ions) are freely filtered, while circulating cells and high molecular weight proteins (e.g. albumin) are retained in the vasculature (Scott and Quaggin, 2015).

The podocyte is a post-mitotic, terminally differentiated cell critical for selective filtration. Podocytes have a complex cellular organization consisting of a cell body which projects microtubule-rich major processes. These major processes further elaborate into actin-rich foot processes (FPs) that wrap around the capillary loop (Ichimura et al., 2007). FPs of adjacent podocytes interdigitate and are connected by a modified adherens junction structure known as the slit diaphragm (SD) (Reiser et al., 2000). The SD is the final barrier of filtration and confers selective permeability (Scott and Quaggin, 2015).

Podocyte dysfunction is characterized by the loss of the FP structure, a phenomenon known as foot process effacement (FPE) (Kerjaschki, 2001). Loss of filtration selectivity leading to protein in the urine, proteinuria, is a hallmark of podocyte injury. Clinically, patients with podocyte dysfunction present with nephrotic syndrome (NS). Nephrotic syndrome (NS) leads to large loss of protein in the urine (>3g/day compared to normal of 150mg/day), which manifests clinically as proteinuria, hypoalbuminemia, and edema (Robins and Takano, 2014). NS is a rare disease with an incidence of approximately 3 new cases per 100,000 adults each year and over 1-7 new pediatric cases per 100,000 children annually (Davin and Rutjes, 2011; Hull and Goldsmith, 2008). Currently, there are no targeted therapies to treat NS. NS is generally classified as steroid sensitive (SSNS) or steroid resistant (SRNS), based on initial response to corticosteroid treatment.

Genetic podocytopathies

There have been nearly 50 identified monogenic causes of hereditary glomerular disease (**Fig.1.1**) (Vivante and Hildebrandt, 2016). These monogenic rare diseases have provided important insight into the molecular pathways involved in podocyte function: SD function (*NPHS1*, *NPHS2*, *CRB2*) and cytoskeletal regulation (*CD2AP*, *ACTN4*, *MYO1E, INF2*, *ARHGDIA*, *TRPC6*). However, in addition to these mutations, there are additional mutations in mitochondrial and lipid metabolism pathways, for which the exact mechanism of podocyte dysfunction remains less clear.

Genetic diseases affecting the affecting SD function

Mutations in nephrin (*NPHS1*) and podocin (*NPHS2*) were among the first identified genetic defects leading to NS (Boute et al., 2000; Kestilä et al., 1998). Both proteins are critical protein components to the podocyte SD. Greater than 140 mutations in *NPHS1* have been identified including FIN_{major} (p.L41fs) and FIN_{minor} (p.R1109X) which together comprised 94% of congenital NS in the Finnish population (Beltcheva et al., 2001; Kestilä et al., 1998). Greater than 100 pathogenic mutations have been identified in *NPHS2*; recessive mutations in *NPHS2* are the

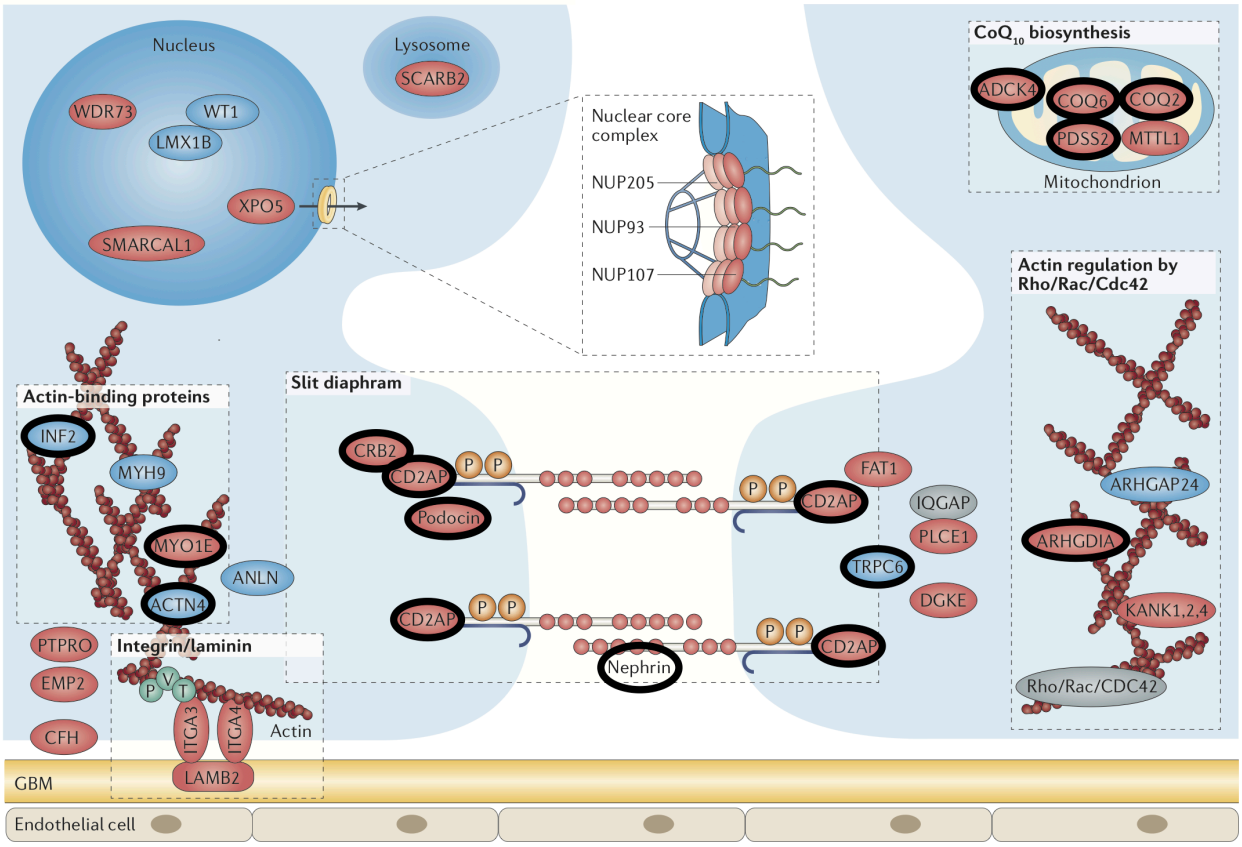

Figure 1.1. Monogenic causes of nephrotic syndrome. Genetically defined rare diseases leading to nephrotic syndrome have provided insight into important molecular pathways for podocyte function. Proteins discussed are outlined in bold. Proteins that when mutated lead to autosomal recessive NS are colored red; those that lead to autosomal dominant NS when mutated are colored blue. Modified from (Vivante and Hildebrandt, 2016)

most common identified genetic defect in early-onset NS in patients of Central European descent (Boute et al., 2000; Hinkes et al., 2007; Karle et al., 2002).

NPHS1 is a transmembrane protein with large extracellular domain that is critical for the formation of the multiprotein complex between adjacent foot processes (Akchurin and Reidy, 2015). SH2 domains of the cytoplasmic domain interact with Src tyrosine kinases and can modulate actin polymerization through NPHS1 phosphorylation and recruitment of downstream effectors, NCK1/2 and CFL1 (Garg et al., 2010; Jones et al., 2006; Verma et al., 2006). NPHS2 localizes to lipid rafts, where SD assembly occurs, and is important for recruitment of NPHS1 and TRPC6 (Huber, 2003; Huber et al., 2001; Kim et al., 2013; Roselli et al., 2002).

Additionally, NPHS1 is known to interact with cell polarity proteins, including PAR3, PAR6, and aPKCλ/ι (Hartleben et al., 2008). The SD forms the boundary between apical and basolateral domains on the podocyte FP (Scott and Quaggin, 2015). During glomerular development, apical tight junctions migrate towards the basolateral surface and develop into SDs (Akchurin and Reidy, 2015; Greka and Mundel, 2012). PAR3-PAR6-aPKCλ/ι complex is important for apical sorting, and aPKCλ/ι loss interferes with surface localization of NPHS1 and NPHS2 (Satoh et al., 2014). Further, human mutations in *CRB2*, also important for apical sorting, lead to proteinuric kidney disease (Ebarasi et al., 2009, 2015; Slavotinek et al., 2015). By contrast, loss of *SCRIB*, which directs basolateral trafficking, does not disrupt proper SD formation, suggesting that apical sorting is more important for SD assembly (Hartleben et al., 2012).

Genetic diseases affecting the regulation of podocyte cytoskeleton

Among cytoskeletal proteins, mutations in *CD2AP* (Gigante et al., 2009; Kim, 2003; Lowik et al., 2008; Löwik et al., 2007), *ACTN4*, and *MYO1E* (Mele et al., 2011) have been identified leading to proteinuric kidney disease. Four percent of familial cases of familial focal and segmental glomerulosclerosis (FSGS, a form of NS) are caused by mutations in *ACTN4* (Weins

et al., 2005). RHO GTPases (RHOA, RAC1, CDC42) regulate the actin cytoskeleton (Warner et al., 2019). Mutations in *INF2*, which regulates RHOA activity, lead to 9-17% of familial forms of autosomal dominant (AD) familial FSGS (Barua et al., 2013; Boyer et al., 2011; Brown et al., 2010; Gbadegesin et al., 2012). Activating mutations in *TRPC6*, a calcium channel that activates RHOA, also lead to AD familial FSGS (Gigante et al., 2011; Jiang et al., 2011; Reiser et al., 2005; Winn et al., 2005), and mutations in *ARHGDIA*, which regulates CDC42 and RAC1 activity, lead to early-onset SRNS (Gee et al., 2013).

Mitochondrial mutations leading to podocytopathies

Mitochondrial cytopathies are a diverse set of diseases that affect oxidative phosphorylation (OXPHOS) though electron transport chain (ETC) failure and result in ATP deficiency and reactive oxygen species (ROS) production (El-Hattab and Scaglia, 2016). Genetic defects that cause mitochondrial cytopathies can either be within the mitochondrial DNA (mtDNA) or nuclear DNA (nDNA). About 1,500 proteins are involved in maintaining mitochondrial structure and function, the vast majority being encoded in the nDNA.

Cells produce most of their required energy through the ETC. The ETC is comprised of five protein complexes and two electron carriers, coenzyme Q (CoQ) and cytochrome C. While mitochondria are involved in many cellular processes its central function is ATP generation, and pathomechanism of mitochondrial cytopathies is understood to be due to an inability to meet the energy demands of the cell. Consistently, mitochondrial cytopathies affect tissues with high energy demands, such as the central nervous system, skeletal muscle, heart, liver, endocrine system, and kidneys (El-Hattab and Scaglia, 2016; Emma and Salviati, 2017). Within the kidney, due to the high energy demand required for active secretion and reabsorption processes, mitochondrial cytopathies typically manifest with tubular dysfunction (Au et al., 2007; Lee et al., 2001; Morris et al., 1995; O'Toole, 2014; Pitchon et al., 2007; Tzoufi et al., 2013). However, there are both mtDNA and nDNA genetic defects which cause podocyte dysfunction manifesting as NS.

Among mitochondrial cytopathies causing podocyte dysfunction, all nDNA genetic defects lie within the CoQ biosynthesis pathway (**Table 1.1**) (Emma et al., 2016; Vivante and Hildebrandt, 2016). Mutations in five enzymes have been identified, leading to CoQ deficiency and podocyte dysfunction: *PDSS1* (Vasta et al., 2012), *PDSS2* (López et al., 2006; Scalais et al., 2013), *COQ2* (Diomedi-Camassei et al., 2007; Mollet et al., 2007), *COQ6* (Heeringa et al., 2011), *COQ8B*/*ACDK4* (Ashraf et al., 2013). With the exception of *ADCK4*, patients present with congenital or early-onset NS (Vivante and Hildebrandt, 2016): eleven patients have been identified with *COQ2* mutations with glomerular involvement; four patients have been identified with mutations in *PDSS2*, and one patient with *PDSS1*; eleven patients have been identified with mutations in *COQ6*. Thirty-eight patients have been described with *ADCK4* mutations (Ashraf et al., 2013; Vivante and Hildebrandt, 2016). Patients with *ADCK4* mutations typically have later-onset and isolated renal disease. Separate from these, mutations in *COQ9* (Danhauser et al., 2016; Duncan et al., 2009; Smith et al., 2018) and *COQ7* (Kwong et al., 2019) are associated with a tubulopathy, rather than a podocytopathy; COQ9 is known to be important for COQ7 stabilization and thus may not be surprising that they have a similar clinical presentation (Lohman et al., 2014).

In conclusion, rare genetic podocytopathies have provided insight into important pathways for podocyte function: elucidating the proteins involved in SD function and cytoskeletal regulation, including proteins involved directly in cytoskeleton binding, cell polarity, and calcium homeostasis. However, there is still much to be learned from additional gene defects affecting the podocyte. The unique podocyte dysfunction associated with CoQ deficiency is one such disease pathology that has remained poorly understood.

Table 1.1. Nuclear gene defects that affect mitochondrial electron transport chain. Modified from (Emma et al., 2016).

	Gene	Renal Phenotype	Reference
CoQ Biosynthesis	PDSS1	SRNS	(Vasta et al., 2012)
	PDSS2	SRNS	(López et al., 2006)
	COQ2	SRNS	(Diomedi-Camassei et al., 2007)
	COQ6	SRNS	(Heeringa et al., 2011)
	ADCK4	SRNS	(Ashraf et al., 2013)
	COQ7	Tubulopathy	(Kwong et al., 2019)
	COQ9	Tubulopathy	(Duncan et al., 2009)
Assembly Factors	COX10	Tubulopathy	(Valnot et al., 2000)
	SURF1	Tubulopathy	(Tay et al., 2005)
	BCS1L	Tubulopathy	(de Lonlay et al., 2001)
	UQCC2	Tubulopathy	(Tucker et al., 2013)
	TMEM70	Tubulopathy	(Magner et al., 2015)
mtDNA translation	MRPS22	Tubulopathy	(Saada et al., 2007)
	YARS2	Tubulopathy	(Nakajima et al., 2014)
	SARS2	Tubulopathy	(Belostotsky et al., 2011)
mtDNA maintenance	RRM2B	Tubulopathy	(Bourdon et al., 2007)
	TWINKLE	Tubulopathy	(Prasad et al., 2013)
	MPV17	Tubulopathy	(El-Hattab and Scaglia, 2013)
	SUCLA2	Tubulopathy	(Carrozzo et al., 2007)
	DGUOK	Tubulopathy	(Dimmock et al., 2008)

.

Lipid biology of the podocyte

Diabetic kidney disease (DKD) shows the strongest correlation with mortality in patients with diabetes, and half of all patients with end stage renal disease (ESRD) can be attributed to DKD (Barkoudah et al., 2012; Stadler et al., 2015). Furthermore, podocyte loss is an independent predictor of DKD progression (Meyer et al., 1999; Pagtalunan et al., 1997). Lipid accumulation in the kidney is a well described sequelae of diabetes and obesity in animal models and patients (Herman-Edelstein et al., 2014; Jiang et al., 2005; Proctor et al., 2006; de Vries et al., 2014; Wang et al., 2005). Additionally, drugs which reduce this accumulation, such as liver X receptor (LXR) agonists, farsenoid X receptor (FXR) agonists, and cyclodextrin protect against kidney injury (Kiss et al., 2013; Merscher-Gomez et al., 2013; Tachibana et al., 2012; Wang et al., 2010). In addition to acquired podocyte injury through diabetes-associated dyslipidemia and obesity, several genetic mutations in enzymes involved in lipid metabolism have also been described to lead to podocyte injury. For example, Fabry disease, which leads to podocyte-specific accumulation of globotriasylceramide (Gb3) is associated with podocyte injury (Najafian et al., 2011) and expression of SMPDL3B, which converts sphingomyelin to ceramide, is inversely correlated with recurrence of proteinuria in FSGS patients post-transplant (Fornoni et al., 2011).

Additionally, individuals of African American heritages have increased risk of chronic glomerular diseases; genome-wide association studies (GWAS) identified sequence variants in *APOL1* which confer increased risk of FSGS, HIV associated nephropathy (HIVAN), and hypertension-associated kidney disease (Genovese et al., 2010; Kao et al., 2008; Kopp et al., 2008; Lipkowitz et al., 2013; Parsa et al., 2013; Tzur et al., 2010). Two risk alleles were identified: a two amino acid substitution (p.S342G, p.I384M) and a two base pair deletion (p.N388-Y389del), which confer risk in an autosomal recessive (AR) pattern. APOL1, apolipoprotein L1, colocalizes with APOA1 in circulating high density lipoproteins (HDL) particles (Duchateau et al., 1997). However, it is thought that it is kidney expression of APOL1, and not circulating APOL1, which is

injurious to podocytes. In support of this hypothesis, glomerular staining of APOL1 is decreased in cases of FSGS and HIVAN (Madhavan et al., 2011), and transplanted kidneys from individuals with two *APOL1* risk alleles experience higher rates of early failure (Reeves-Daniel et al., 2011). Recently, podocyte-specific overexpression of APOL1 risk alleles, but not wildtype protein, led to kidney failure (Beckerman et al., 2017). *In vitro* studies in human podocytes with overexpression of mutant versus wildtype APOL1 have suggested protein accumulation in ER and subsequent ER stress to mediate mutant APOL1 injury (Chun et al., 2019; Wen et al., 2018).

In conclusion, the podocyte is affected both by acquired and genetic diseases which lead to intracellular dyslipidemia. However, much is yet to be understood about why and how this dyslipidemia is injurious to podocytes.

Emerging experimental tools in the kidney space

Kidney organoids as appropriate models for kidney development and cellular complexity

The adult kidney consists of greater than twenty unique cell types all which contribute to its many roles in physiologic homeostasis and can be differentially perturbed in the setting of disease (Little et al., 2019). While mouse models mimic the cellular complexity of the human kidney, they are limited in their ability to mimic to human disease. Conversely, human cell lines lack the three-dimensional (3D) architecture and cell-to-cell interactions of *in vivo* models. Thus, kidney organoids derived from human induced pluripotent cells (hiPSCs) provide a valuable *in vitro* human model of kidney biology, which mimics the 3D organization and cellular complexity of the organ *in vivo*.

Organoids have been developed for many organs in the body, including the gastrointestinal system (Cao et al., 2011; McCracken et al., 2014; Spence et al., 2011; Watson et al., 2014), the lung (Dye et al., 2015), and the brain (Lancaster et al., 2013; Ozone et al., 2016). Organoids can be generated from either resident stem cells in primary tissue (Barker et al., 2010; Boj et al., 2015; Chua et al., 2014; Gao et al., 2014; Greggio et al., 2013; Hisha et al., 2013; Li et

al., 2014a; Mondrinos et al., 2014; Nanduri et al., 2014; Sato et al., 2009; Schumacher et al., 2015; Yui et al., 2012) or through the directed differentiation of human pluripotent stem cells (hPSCs). To date, resident stem cells in the adult kidney have not been found (Kramann et al., 2015; Kusaba et al., 2014), and thus the generation of kidney organoids has been dependent on an understanding of mammalian kidney development in order to develop tissue culture protocols that mimic this process.

Kidney embryogenesis

During mammalian embryogenesis, three pairs of excretory organs develop from the intermediate mesoderm (IM): the pronephros, mesonephros, and metanephros (Little et al., 2019; Morizane and Bonventre, 2017a). The IM lies between the paraxial and lateral plate mesoderm and gives rise to the kidneys, gonads, and ureter. It develops from migrating cells from the primitive streak (PS), an elongating groove at the caudal end of the developing embryo. Of the three embryonic excretory organs, the mature adult kidney develops from the metanephros, which is derived from a WT1+/OSR1+/PAX2-/LHX1- region of the posterior IM (Taguchi et al., 2014).

The three embryonic excretory organs arise in a rostral to caudal pattern initiated by the formation of the nephric (Wolffian) duct, derived from the anterior IM. While little is known about the pronephros, the rostral tubules of the mesonephros contribute the efferent seminiferous tubules of the testes (Vazquez et al., 1998). Formation of the metanephric kidney (metanephric mesenchyme, MM) is initiated by the ureteric bud (UB), an outgrowth of the nephric duct. Reciprocal signals between the MM and UB lead to the development of both structures (Little and McMahon, 2012). Glial cell line-derived neurotrophic factor (GDNF) secretion by the MM leads to UB growth towards MM. Mesenchymal signals further lead to ureteric tip proliferation and ureteric tree branching, which eventually develops into the collecting duct (CD) system of the mature kidney. The ureteric tip and surrounding stroma also secrete signals which allow for both the maintenance of a self-renewing progenitor pool and a commitment to nephron formation.

Mesenchymal cells immediately surrounding the UB tips become a Sine Oculis Homeobox Homolog 2+ (SIX2+) self-renewing progenitor population known as the cap mesenchyme (CM) (Kobayashi et al., 2008). Lineage tracing experiments have determined that CM cells are the nephron progenitor cells (NPCs) which give rise to all epithelial cells in developing nephrons (Boyle et al., 2008; Kobayashi et al., 2008). Thus, any *in vitro* differentiation of kidney tissue must first generate NPCs.

Nephron initiation occurs below the uretic tip, at a *WNT4*+/*SIX2*- population, known as the pretubular aggregate (PTA) (Georgas et al., 2009; Little and McMahon, 2012; Little et al., 2007). The PTA undergoes mesenchymal-to-epithelial (MET) transition to form renal vesicles (RV, stage 1 nephron). The RV is polarized with the proximal RV developing into glomerular epithelial cells (visceral (podocytes) and parietal epithelial cells (PECs)) and the distal RV invading the ureteric tip, resulting in the tubular system from the proximal to connecting tubules. Elongation and segmentation of the RV results in progressively more mature structures: comma- and S-shaped bodies (stage 2 nephron). The final adult kidney possesses about one million nephron structures (Hughson et al., 2003) with nephron formation complete before birth in humans (Ryan et al., 2018), and within the first days following birth in mice (Rumballe et al., 2011).

Using principles of embryogenesis to build a kidney

Initial studies attempting to derive kidney tissue from hPSCs focused on the identification of growth factors that were potent inducers of kidney lineage cells. These include including activin, bone morphogenic proteins (BMP4, BMP7), retinoic acid, hepatocyte growth factor (HGF), and insulin-like growth factors (IGFs) (Bruce et al., 2007; Kim and Dressler, 2005; Kobayashi et al., 2005; Mae et al., 2010; Morizane et al., 2009, 2013; Nishikawa et al., 2012; Vigneau et al., 2007; Yamamoto et al., 2006). Subsequently, more complex differentiation protocols have been developed, generally divided in to two steps: (a) directed differentiation into the IM and NPCs; and (b) differentiation of NPCs into nephron structures.

First, to robustly generate NPCs, a precise understanding of the embryological origin of the metanephros was required. Mouse lineage tracing experiments found that MM is derived from the posterior IM in a Wt1+/Osr1+ and Pax2-/Lim1- (LHX1 in humans) negative region (Taguchi et al., 2014). These cells are derived from the center of the PS; the PS is patterned by a WNT3A/BMP4 gradient (Morizane and Bonventre, 2017a). In addition to topological signals, there is additional temporal patterning with cells migrating from the PS at earlier time points developing into more anterior signals. For example, T+ (Brachyury+) PS cells at E7.5 went on to develop the anterior nephric duct structures, whereas T+ PS cells at E8.5 developed into MM (Taguchi et al., 2014). Thus, the generation of NPCs requires the induction of cells located at the center of the late-stage PS. As there are no specific markers for this cell type, the successful generation of this population could only be determined by its subsequent differentiation into WT1+/HOXD11+ posterior IM cells. Consistent with late-stage PS development, longer treatment (4 days versus 1-2 days) with WNT activator, CHIR99021 (Lam et al., 2014; Takasato et al., 2014), followed by induction with activin A, was more likely to induce HOXD11 expression (Morizane et al., 2015).

The molecular signals required for the differentiation of the posterior PS into NPCs and subsequent nephron formation are better understood. Fibroblast growth factors (FGF9 and FGF20) are required for the maintenance of SIX2+ NPCs (Barak et al., 2012). FGF9 is produced by the UB and thus must be supplemented in the absence of UB structures (Morizane et al., 2015). From NPCs, nephron formation can be induced with a strong canonical WNT signal (e.g. spinal cord) or small molecule activators (e.g. CHIR99201) (Little et al., 2019; Morizane and Bonventre, 2017a). Of note, protocols which generate specifically NPCs followed by nephron induction, should specifically generate nephron derivatives of the MM, which comprise of epithelial structures from the glomerulus to the connecting tubules, without any CD structures.

Three groups have developed protocols to generated 3D kidney organoids. Of these, the protocol developed by Taguchi and Nishinakamura contains both UB- and MM-derived structures

(Taguchi and Nishinakamura, 2017). To generate 3D kidney organoids with both UB and MM-derived compartments, the authors generated each compartment separately followed by co-culture. A novel and complex protocol was required to derive the anterior mesoderm: (a) induction of the PS (activin A and BMP4 followed by BMP4 and CHIR99021); and (b) treatment with retinoic acid (RA), FGF9, SB431542 (TGF inhibitor), and LDN193189 (BMP inhibitor) to generate anterior IM. From the anterior IM, the Wolffian duct was generated by treatment with RA, CHIR99021, FGF9, and LDN193189 followed by sorting for CXCR4+/KIT+ cells. Finally, UB was generated by treatment with Rho-associated kinase inhibitor (Y27632), RA, CHIR99021, FGF9, FGF1, LDN193189, and GDNF. For the MM, the posterior IM was induced through treatment with (a) Activin A; (b) CHIR99021; (c) combined treatment with CHIR99021, Activin A, BMP4, and RA. Subsequently, MM was induced with FGF9 and low CHIR99021. These two separately generated lineages were subsequently co-cultured resulting in organized nephron structures, including a branched CD system. However, the complexity of this protocol makes it less amenable to generation of organoids for high throughput studies.

The protocol developed by Morizane *et al.* explicitly generates NPCs (**Fig. 1.2**) (Morizane et al., 2015). They induce the PS by treatment with high CHIR99021, followed by treatment with Activin A to induce the posterior IM, and finally treatment with low FGF9 to allow for differentiation of SIX2+ NPCs. Dissociation of cells and transfer into low-adherent 96-well plates with transient CHIR99021 followed by FGF9 treatment leads to self-organization of nephron structures from podocytes to late distal tubule. The specific differentiation into NPCs prior to self-organization, results in the absence of CD structures.

Finally, the protocol developed by Takasato *et al.* simultaneously differentiates both anterior and posterior IM rather than NPCs in an effort to generate epithelial derivatives of both the MM and UB (**Fig. 1.2**) (Takasato et al., 2015). They found high CHIR99021 to be sufficient for the generation of PS followed by high FGF9 treatment to induce differentiation of the IM.

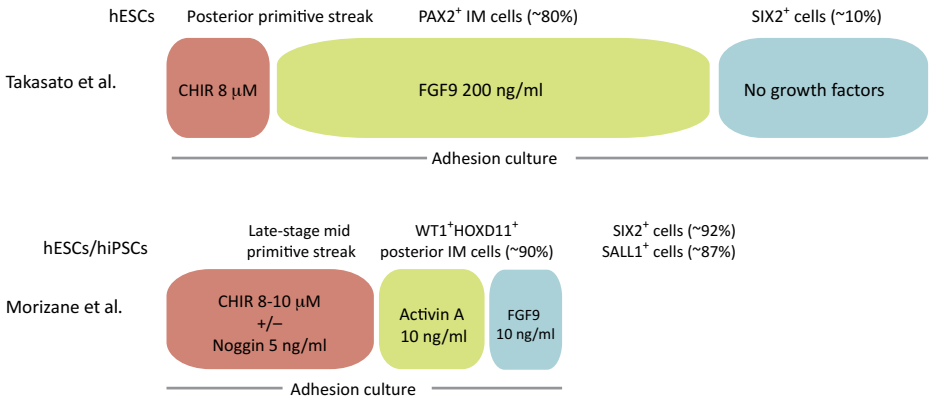

Figure 1.2. Comparison of nephron progenitor cell differentiation protocols. Comparison of two NPC differentiation protocols compared in Chapter 3 (Morizane et al., 2015; Takasato et al., 2015). Modified from (Morizane and Bonventre, 2017a).

Similar to *in vivo* temporal dynamics, they found that varying the time of CHIR99021 treatment could shift the balance between anterior and posterior IM structures. Following simultaneous differentiation of GATA3+ anterior mesoderm and HOXD11+ posterior mesoderm, 3D organoid culture with extended FGF9 treatment also led to self-organization of nephron structures from WT1+ podocytes to ECAD+/GATA3+ primitive CD structures. Additionally, they saw the simultaneous differentiation of endothelial cells and bulk RNA-seq on these organoids found them to be most similar to first trimester fetal kidney.

In conclusion, three groups have published protocols generating 3D kidney organoids with organized nephron structures. However, important questions still remain: how do these protocols compare with respect to maturity, reproducibility, and faithfulness to nephron differentiation? All these factors will impact the utility of kidney organoids in disease modeling based on their expression of relevant pathways and the reproducibility of organoids across various cell lines for modeling of disease from patient-derived iPSCs.

Single cell genomics in the kidney

Single cell RNA sequencing (scRNA-seq) is an emerging technology designed to characterize heterogeneity in large cell populations through the sequencing of individual cell transcriptomes. The kidney nephron is a segmented tubule with at least 15 different epithelial cell types (Lee et al., 2015) and thus scRNA-seq has the potential to provide unprecedent resolution into understanding normal function, development, and disease pathogenesis.

Using single cell genomics to understand the adult kidney

The first published comprehensive mouse single cell study by Park *et al.* generated 57,979 single cell transcriptomes from mouse kidney (Park et al., 2018). The authors demonstrated that disease-relevant genes are expressed predominantly in a single cell type in the adult mouse kidney, suggesting cell-specific etiology of disease pathology. Additionally, trajectory analysis of

CD cells identified a transitional cell between principal cells (PCs) and intercalated cells (ICs), which they postulated to be mediated by Notch signaling and to be perturbed in the setting of disease. This finding is consistent with prior single cell analysis of the collecting duct by Chen *et al.* which also found hybrid cell types expressing markers of both PCs and ICs (Chen et al., 2017).

Due to the large cell heterogeneity in the kidney and bias in cell dissociation protocols, not all cell types of the kidneys are well represented in scRNA-seq. Thus, compartment-specific scRNA-seq by prior enrichment can allow for further characterization of different kidney populations. To this end, Karaiskos *et al.* generated an atlas of nearly 13,000 single cell transcriptomes from mouse glomeruli allowing them to identify novel podocyte (*Wsb2*) and mesangial (*Pde3a*) markers as well as glomerular endothelial and podocyte subpopulations (Karaiskos et al., 2018).

In addition to bias introduced by the dissociation protocol, an additional limitation of scRNA-seq is the stress induced by enzymatic digestion of tissue to allow for single cell isolation prior to sequencing (Adam et al., 2017). A potential method to mitigate this stress is through single nuclei RNA sequencing (sNuc-seq) in which nuclei, rather than cells, are isolated, a procedure which takes place entirely on ice (Lake et al., 2017). Wu *et al.* compared scRNA-seq and sNuc-seq and demonstrated that while sNuc-seq enriches for a smaller proportion of different genes, these were mostly found to be mitochondrial genes and artifactual stress response genes (Wu et al., 2019). Both methods were equally able to determine cell identities and furthermore, sNuc-seq was able to enrich 20-fold for podocytes, which were absent in their scRNA-seq analysis.

Single cell genomics and the human embryonic kidney

Kidney development is a highly complex process which is not fully understood. Similarly, scRNA-seq technologies have led to novel biological insights and allowed for comparisons between mouse and human development. Magella *et al.* performed scRNAseq on E14.5 mouse

fetal kidneys and were able to identify 16 cells states from progenitor cell types to differentiated cells (Magella et al., 2018). Additionally, receptor-ligand analysis revealed *Gdnf* expression by stromal cells in the nephrogenic zone; *Gdnf*, required for UB branching morphogenesis, was thought to previously only be expressed by the CM (Little and McMahon, 2012) .

Menon *et al.* compared 17 week human fetal kidneys with mouse fetal kidneys (Menon et al., 2018). They generated 6,515 single cell transcriptomes from five human embryonic kidneys. They characterized differences in expression of genes (*IRX2*, *IRX3*, *HNF4A*) in distal tubular segments (*POU3F3*+) compared to mouse embryonic kidneys, and identified novel markers for CD (*AGR2*, *ADHIC*, *BCAT1*), immature podocytes (*OLFM3*, *SLC16A1*, *PCDH9*, *C19orf58*), and mature podocytes (*NTNG1*). Recent work by Hochane *et al.* generated nearly 18,000 single cell transcriptomes across five time points of human development (week 9, 11, 13, 16, 18), and also validated *OLFM3* as a marker of immature podocytes compared to *MAFB*+ mature podocytes (Hochane et al., 2019). Finally, Lindström and colleagues in two papers performed single cell analysis on 17 week human fetal kidney, generating 3,367 single cell transcriptomes (Lindström et al., 2018a, 2018b). They propose a time-dependent cell fate acquisition model by which proximal-distal patterning occurs by successive recruitment of NPCs resulting varying exposure to UB-secreted *Wnt9b*/*WNT9B* (Lindström et al., 2018b). The authors hypothesize that cells recruited earlier and have prolonged exposure to *WNT9b* have a distal phenotype with *JAG1* downregulation and *SOX9* upregulation. Comparison between human and mouse single cell transcriptomic profiles highlighted differences in progenitor cell populations: while mice had distinct nephron (NPCs) and interstitial (IPCs) progenitor populations, in human embryonic kidney NPCs and IPCs shared significant transcriptomic overlap (Lindström et al., 2018a).

Single cell genomics to improve kidney organoids

Recently Wu *et al.* published the first single cell comparison of kidney organoids by generating 83,130 single cell transcriptomes from 65 organoids (Wu et al., 2018). They compared

the prior published protocols of Morizane *et al.* and Takasato *et al.*, comparing iPSC- and embryonic stem cell- (ESC-) derived organoids. They describe similar populations of nephron cell types with both, including significant non-renal cell types (off-target populations, 10-20%) and absent UB-derived structures. Their work supports the early maturation state of these organoids, as demonstrated by low expression of trait-relevant genes defied by GWAS compared to adult kidney. They found that maturation was not improved by long-term culture and thus used receptor-ligand analysis to help improve organoid quality. Their analysis suggested that *BDBF-NTRK2* interactions were important for the neuronal cell population and that chemical inhibition of this axis lead to decreased neuronal off-targets.

Combes *et al.* subsequently provided a combined bulk and single cell analyses (8,323 single cells) of the Takasato *et al.* protocol focusing on comparisons within and between batches (Combes et al., 2019). They found equal variation between iPSC lines and between batches of the same iPSC lines. They found this variation to be determined by genes related to organoid maturation, nephron segmentation, and off-target populations. While their protocol was designed to generate both UB- and MM-derived structures, they were similarly unable to resolve UB *GATA3*+ structures in their single cell analysis. Subsequent comparison to human fetal kidney showed conserved gene expression between organoid and fetal kidney within endothelial, stromal, and nephron lineages (Harder et al., 2019).

In conclusion, the advent of single cell technology in the kidney space has allowed for insight into adult and developmental kidney pathways as well as a deeper understanding of the current status of kidney organoids and ways forward for their improvement.

Overview of Dissertation

Chronic kidney disease (CKD) affects over 500 million individuals worldwide and yet therapeutic development in the kidney space has lagged (Inrig et al., 2014; Jha et al., 2013). Innovation in the space is likely multifactorial, hindered both by the complex nature of the CKD

pathophysiology leading to an incomplete understanding the underlying molecular pathomechanism, and insufficient *in vitro* and *in vivo* models to study disease and test therapeutic strategies. This dissertation approaches these challenges both through investigating the pathomechanism of a rare kidney disease to better understand kidney biology and through characterization and improvement of kidney organoids, a human *in vitro* model for the study of kidney biology. Further, deployment of single cell transcriptomic technology is particularly appropriate for the study of kidney biology due to the organ's cellular complexity. We demonstrate how this technology can be used to understand cell-type specific pathology in disease and to further understand and develop kidney organoids.

Chapter 2:
Disruption of lipid metabolism in CoQ deficiency kidney disease

This chapter represents a manuscript being prepared for submission:

E.-H. Sidhom, M. Alimova, J. Avila-Pacheco, K. Vernon, J. Marshall, C. Kim, G. Kleiner, E. Reyes-Bricio, E. Grinkevich, A. Weins, F. Chen, C. M. Quinzii, C. Clish, A. Greka. Disruption of lipid metabolism in CoQ deficiency kidney disease.

Abstract

Mitochondrial cytopathies are a group of diverse genetic diseases which remain poorly understood. Among them, mutations affecting mitochondrial coenzyme Q (CoQ) biosynthesis lead to a rare syndrome associated with kidney failure, but mechanistic details and effective therapies remain elusive. Here we demonstrate that kidney podocyte-specific CoQ deficiency leads to susceptibility to ROS-induced cell death. A combination of transcriptomics and metabolomics experiments revealed that retinoic acid-mediated perturbations in polyunsaturated fatty acid (PUFA) metabolism contribute to ROS. *S*ingle nucleus RNA sequencing (sNuc-Seq) from dissociated kidneys of a mouse model of CoQ-deficiency revealed a unique, disease-specific parietal epithelial cell sub-population and a PUFA- and Braf/Mapk-mediated disease circuit in podocytes. Finally, we demonstrate that GDC-0879, a BRAF-targeting compound, rescues podocytes from CoQ-deficiency-mediated cell injury. Our studies provide insight into the mechanism of a mitochondrial cytopathy and show the power of using single cell genomics to identify targets and novel therapeutic strategies.

Introduction

Oxidative phosphorylation (OXPHOS) defects are a diverse group of mitochondrial cytopathies , leading to both ATP deficiency and increased production of reactive oxygen species (ROS) (El-Hattab and Scaglia, 2016). The mitochondria's primary function is ATP production by OXPHOS through the electron transport chain (ETC), which is comprised of five enzymatic complexes and two electron carriers, coenzyme Q (CoQ) and cytochrome c. CoQ, or ubiquinone (Ub), is a ubiquitous lipid present in all biological membranes, but particularly enriched in mitochondrial membranes where it has a well-established role in the electron transport chain (ETC) (Acosta et al., 2016; Turunen et al., 2004). In addition to its role in the ETC, CoQ has numerous other cellular functions including serving as an antioxidant, especially of lipid peroxidation (Frei et al., 1990; Shi et al., 1999), as an essential co-factor for numerous enzymes, and as a modulator of the mitochondrial permeability transition pore (MPTP) (Acosta et al., 2016; Belliere et al., 2012; Papucci et al., 2003; Turunen et al., 2004; Walter et al., 2000).

The synthesis of CoQ is divided in two parts: (i) synthesis of the isoprenoid tail; and (ii) modification of the benzoquinone head. Synthesis of the isoprenoid tail is downstream of the mevalonate pathway (which synthesizes farnesyl pyrophosphate from acetyl CoA (Kawamukai, 2016; Turunen et al., 2004)). The first committed step to CoQ biosynthesis is catalyzed by a heterotetramer (Pdss1/Pdss2 in *M. musculus*, PDSS1/PDSS2 in *H. sapiens*). PHB-polyprenyl diphosphate transferase (Coq2 in *M. musculus*, COQ2 in *H. sapiens*) mediates the prenylation of 4-hydroxybenzoate (4-HB) followed by seven additional reactions to complete the synthesis of CoQ.

Deep mechanistic understanding of genetically-defined diseases can provide insight into fundamental biology and potential therapeutic targets for the treatment of rare as well as more prevalent diseases. Nephrotic syndrome (NS) is a rare kidney disease with few therapeutic options limited to non-specific immunosuppressive regimens with significant toxicities (Downie et

al., 2017; Königshausen and Sellin, 2017). The cause of the disease centers on the podocyte, a specialized post-mitotic cell of the kidney's glomerular filtration barrier. Numerous mutations have been found which lead to hereditary autosomal recessive (AR) NS (Akchurin and Reidy, 2015). Among these, all mutations in mitochondrial proteins associated with AR NS cluster within the CoQ biosynthesis pathway, specifically in four enzymes (PDSS1, PDSS2, COQ2, COQ6, COQ8B/ADCK4) (Akchurin and Reidy, 2015; Emma and Salviati, 2017; Emma et al., 2012; Ozaltin, 2014). Patients with CoQ deficiency often have early onset neurologic abnormalities in addition to kidney dysfunction that become apparent in the first few years of life (Diomedi-Camassei et al., 2007; Heeringa et al., 2011; López et al., 2006; Mollet et al., 2007; Quinzii et al., 2006; Scalais et al., 2013; Vasta et al., 2012), although, patients with ADCK4 mutations typically manifest with late onset isolated kidney disease (Ashraf et al., 2013). Diagnosis of CoQ deficiency mitochondrial-cytopathies is critical, as it is partially responsive to oral CoQ supplementation (Heeringa et al., 2011; Montini et al., 2008; Quinzii et al., 2006; Rötig et al., 2000; Salviati et al., 2005). Although analogs of the CoQ intermediate, 4-HB, have shown some efficacy *in vitro* and *in vivo*, their mechanism of action is not clear, because their therapeutic effects are not due to increased levels of CoQ (Herebian et al., 2017; Hidalgo-Gutiérrez et al., 2019; Ozeir et al., 2011; Pierrel, 2017; Widmeier et al., 2019). Additionally, the lack of mechanistic insight into how COQ mutations specifically cause nephrotic syndrome has prevented the development of a targeted therapy.

The kidney, after the heart, has the second highest mitochondrial content and oxygen consumption in the body (Bhargava and Schnellmann, 2017; O'Connor, 2006). Due to the kidney's high ATP requirement, patients with mitochondrial-cytopathies frequently have kidney dysfunction (Emma and Salviati, 2017), affecting primarily proximal tubular epithelial cells. These cells reabsorb 80% of the kidney filtrate by active transport, and therefore they are the most frequently affected cell in mitochondrial-cytopathies (the most extreme form is Fanconi syndrome

(Au et al., 2007; Lee et al., 2001; Morris et al., 1995; O'Toole, 2014; Pitchon et al., 2007; Tzoufi et al., 2013)). Therefore, it is intriguing that CoQ biosynthesis enzyme mutations do not generally affect proximal tubular cells, but instead appear to cause podocyte damage and death, suggesting that CoQ deficiency is uniquely injurious to podocytes by an unknown mechanism that may not involve ATP production.

In support of this notion, work in patient fibroblasts has been inconclusive, despite efforts to investigate deficiencies in ATP production, increased oxidative stress, and decreased mitochondrial membrane potential ($\Delta\Psi_m$) in disease pathogenesis (Heeringa et al., 2011; Quinzii et al., 2008, 2010). Of interest, the *kd/kd* (kidney disease) mouse model is the result of a spontaneous missense mutation in Pdss2 (V117M, *Pdss2*$^{kd/kd}$) in a CBA/CaH colony resulting in nephrotic syndrome (Lyon and Hulse, 1971; Peng et al., 2004). ROS generation in this model has been shown to be specific to the kidney (Quinzii et al., 2013). A conditional knockout of Pdss2 specifically in podocytes, in contrast to a conditional knockout in tubular epithelial cells, developed kidney failure, in further support of the idea that podocyte dysfunction is central to CoQ deficiency kidney disease (Peng et al., 2008). Given the clinical presentation of nephrotic syndrome in patients (nephrotic syndrome is a clear podocytopathy) and these data from mouse models, we hypothesized that mechanistic insights into disease pathogenesis will only be possible through a detailed understanding of CoQ biology specifically in podocytes.

Here we show that CoQ-deficient podocytes have a specific susceptibility to ROS-mediated injury and broader metabolic effects due to the accumulation of CoQ precursor metabolites. Metabolomics and transcriptomics revealed a retinoic-acid-mediated perturbation of polyunsaturated fatty acids (PUFAs) and associated enzymes (Pla2g12a and Dgat2). sNuc-Seq from kidneys of *Pdss2*$^{kd/kd}$ mice confirmed *in vivo* that enzymes critical for PUFA metabolism were upregulated specifically in podocytes. Downstream of PUFA dysregulation, we also identified podocyte-specific changes in a Braf-Mapk disease circuit associated with podocyte injury. Finally,

we demonstrate that GDC-0879, a BRAF-targeting compound with podocyte-protective effects (Sieber et al., 2018), could rescue podocytes from PUFA-mediated cell death.

Results

CoQ-deficient podocytes are susceptible to oxidative stress-mediated cell death

To investigate the effects of CoQ deficiency in podocytes, we generated an *in vitro* model of podocyte CoQ deficiency using two different shRNAs to target Pdss2 in immortalized mouse podocytes. We validated successful protein depletion (**Fig. S1.1A**) and functional deficiency as indicated by decreased abundance of the end pathway metabolites, CoQ9 and CoQ10 (**Fig. S1.1B**). We also found increased apoptosis in CoQ-deficient podocytes (**Fig. 2.1A**) that was rescued by mitoQ, a mitochondrial-targeted analog of CoQ (**Fig. 2.1A**).

To understand CoQ deficiency-related mechanisms, we first evaluated four known functions of CoQ in podocytes. We assessed electron transport chain (ETC) function by a mitochondrial stress test using the Seahorse Flux Analyzer, but saw no decrease in oxygen consumption rates (OCR) either in standard or glucose-free media in CoQ-deficient podocytes relative to scrambled control (**Fig. S1.2A,B**). Uridine levels, a readout of pyrimidine nucleotide biosynthesis, were unchanged (**Fig. S1.2C**). Mitochondrial permeability transition pore (MPTP) opening and cellular ROS generation, assessed by high content imaging, were not meaningfully altered between CoQ-deficient podocytes compared to scrambled control (**Fig. S1.2D,E**).

We hypothesized that an additional stressor may unveil a susceptibility to injury *in vitro*. We therefore targeted each CoQ function with specific drugs: oligomycin, to inhibit the ETC; teriflunomide, an inhibitor of dihydroorotate dehydrogenase (DHODH) (Davis et al., 1996); C_2-cermide, which induces apoptosis and cell death through MPTP opening (Novgorodov et al., 2005; Siskind et al., 2006); and paraquat, which generates superoxide anions (Bus and Gibson, 1984). Oligomycin had no effect on cell viability in either CoQ-deficient podocytes or scrambled controls (**Fig. S1.3A**), despite a persistently elevated mitochondrial membrane potential ($\Delta\Psi_m$) indicating ETC inhibition (**Fig. S1.3B**). Similarly, teriflunomide also did not affect cell viability (**Fig. S1.3C**). C_2-ceramide was toxic to podocytes (**Fig. S1.3D**) and showed decreased $\Delta\Psi_m$, indicating

Figure 2.1. CoQ-deficient podocytes are susceptible to ROS-mediated injury and have increased levels of ROS-producing PUFAs in their media. **A.** Quantification of caspase-positive podocytes expressing either scrambled or Pdss2-targeted shRNAs, and rescue of apoptosis with mitoQ, n=6, two-way ANOVA, Tukey multiple comparison test. **B.** Quantification of cell death after paraquat treatment, n=4, one-way ANOVA, Sidak multiple comparison test. **C.** Rescue of paraquat treatment with mitoQ, n=4, two-way ANOVA, Sidak multiple comparison test. **D.** Live cell fluorescence imaging of mitochondrial membrane potential ($\Delta\Psi_m$, blue) and cell death (red) in cells treated with paraquat (1 mM) +/- mitoQ (1 μM) for 20 hours; scale bars, 100 μm. **E.** Heatmap of statistically significant metabolites (FDR <10%, Benjamini-Hochberg correction on a student's t-test) from conditioned media of CoQ-deficient podocytes compared to scrambled controls, n=4. **F.** Log2 fold changes of sum of abundances of polyunsaturated triglycerides (PU TG) and polyunsaturated phospholipids (PU PL) in CoQ-deficient podocytes compared to scrambled controls, n=4, two-way ANOVA, Tukey multiple comparison test; PU lipids limited to lipids with 4-8 double bonds. **G.** Quantification of cellular ROS production after arachidonic acid (AA) treatment for 12 hours, n=4, two-way ANOVA, Tukey multiple comparison test. **H.** Quantification of cell viability after arachidonic acid (AA) treatment for 84 hours, n=4, two-way ANOVA with Tukey multiple comparison test. **I.** Live cell fluorescence imaging of cellular ROS (blue) and cell death (red) in cells treated with AA (1 mM) for 84 hours; scale bars, 100 μm.

Figure 2.1 (Continued).

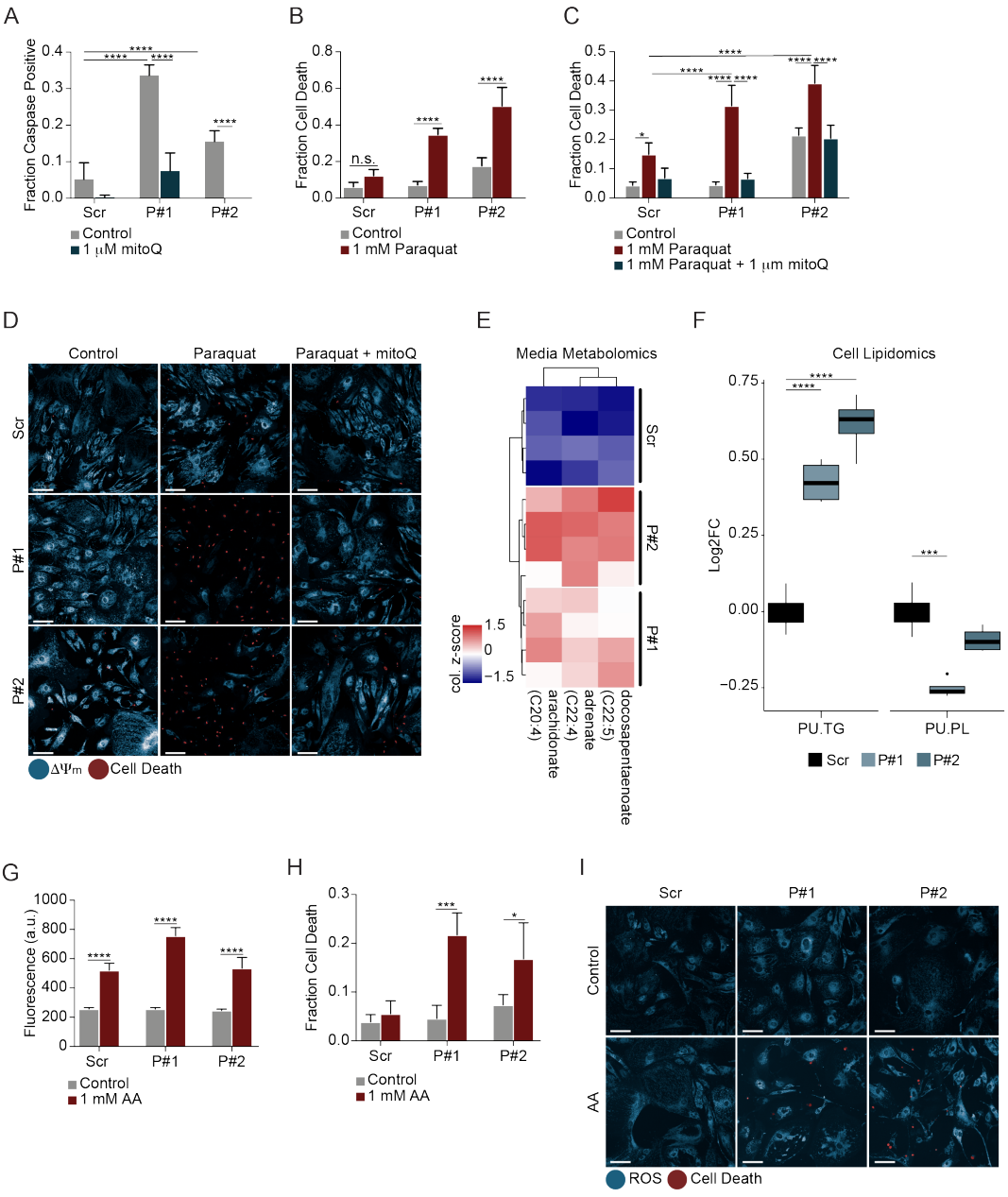

MPTP opening (**Fig. S1.3E**). However, it was equally toxic to both CoQ-deficient podocytes and scrambled controls (**Fig. S1.3D,F**). Finally, we found that CoQ-deficient podocytes were more susceptible to cell death following treatment with paraquat (**Fig. 2.1B**), which resulted in elevated cell death (and at earlier time points) compared to scrambled control (**Fig. S3G**). Cell death was rescued by both mitoQ and a mitochondrial-targeted radical scavenger, mitoTEMPO (**Fig. 2.1C,D, S1.3H**). Thus, among the functions of CoQ, we found that the loss of CoQ's antioxidant function was most injurious in podocytes.

Metabolomics reveals altered lipid profiles in CoQ-deficient podocytes

Since an additional stressor in the form of paraquat was required for CoQ-deficient podocyte death, we hypothesized that podocyte injury in the setting of CoQ deficiency may not only be due to depletion of CoQ but also due to broader perturbations in metabolic pathways. To assess these alterations, we performed mass spectrometry-based metabolite profiling (metabolomic) studies on CoQ-deficient podocytes compared to scrambled controls, on cell extracts and conditioned media. There were three metabolites differentially abundant (DA) in the conditioned media of CoQ-deficient podocytes, all of which were polyunsaturated fatty acids (PUFAs), specifically, arachidonic acid (AA, C20:4), adrenic acid (C22:4), and docosapentaenoic acid (C22:5) (**Fig. 2.1E, Table S1.1**). The majority of DA metabolites in cell lysates were also lipid species: we found increased abundance of triglycerides (TGs) and decreased abundance of phospholipids (PLs) (**Fig. S4, Table S1.2**). Looking at lipid species by class revealed a shift in polyunsaturated species with increased polyunsaturated triglycerides (PU TGs) and decreased polyunsaturated phospholipids (PU PLs) in CoQ-deficient podocytes (**Fig. 2.1F**).

PUFAs have been previously reported to increase ROS generation(Tanaka et al., 2017) and thus we hypothesized they may contribute to podocyte injury in CoQ deficiency. CoQ-deficient yeast are susceptible to cell death following treatment with PUFAs, which is mediated through ROS injury (Do et al., 1996; Poon et al., 1997), and analysis of blood cells following

dietary supplementation of CoQ in humans shows the reverse phenotype with increased incorporation of AA into PLs (Turunen et al., 2002). To evaluate the effect of PUFA generation in podocytes, we treated CoQ-deficient podocytes with AA and assessed ROS and cell viability. We found that AA increased ROS across all podocytes (**Fig. 2.1G**), but caused selective cell death only in CoQ-deficient podocytes (**Fig. 2.1H,I**). Thus, we concluded that elevation of PUFAs in CoQ-deficient podocytes could contribute to podocyte injury.

Transcriptomics identifies alterations in retinoic-acid-receptor-dependent lipid-metabolism enzymes and elevation in retinoic acid-related genes

Having established a perturbation in the lipid profile of CoQ-deficient podocytes, we sought to better understand the enzymes and upstream pathways regulating this perturbation. We performed bulk RNA sequencing (RNA-Seq) on CoQ-deficient podocytes compared to scrambled controls. We used the Human Metabolome Database (HMDB) to associate differentially expressed (DE) genes with DA metabolites (see methods). Of 1,447 DE genes, 423 were annotated within the HMDB, and among 116 DA metabolites, 91 were annotated with representative HMDB IDs. Of these, 31 DE genes mapped to 61 DA metabolites (**Fig. 2.2A**, **Table S1.3**). Among these, several DE genes were annotated to associate with DA PLs; for example, Pla2g12a, a secreted phospholipase A2 (Pla2) which cleaves AA from PLs (Dennis et al., 2011), and could be contributory to elevated PUFAs within the conditioned media. Of DE genes associated with DA TGs, Dgat2 catalyzes the formation of TGs from diglycerides and acyl-CoA. We confirmed the transcriptional up-regulation of these enzymes by RT-qPCR in CoQ-deficient podocytes (**Fig. S1.2B**).

To better understand the upstream regulation of these perturbations, we performed gene set enrichment analysis (GSEA) on the RNA-Seq data (**Table S1.4**), and discovered a single significant positively-enriched pathway in CoQ-deficient podocytes, retinol metabolism

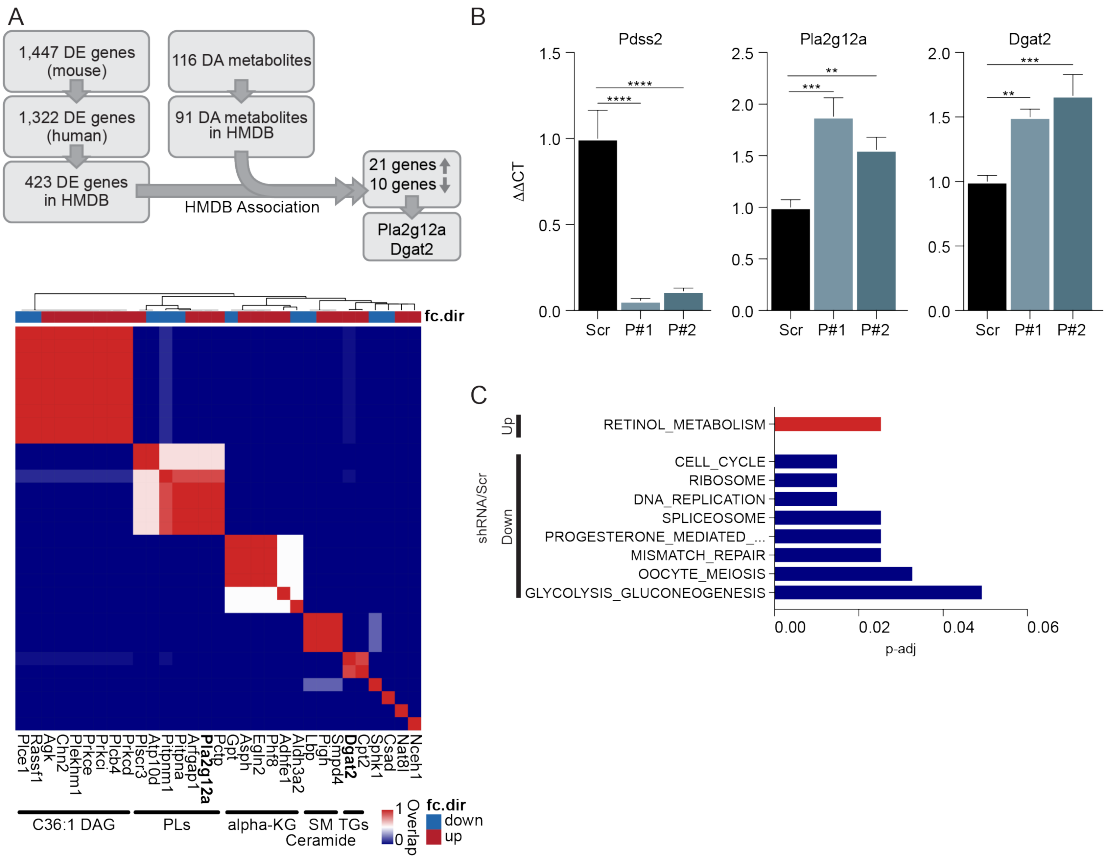

Figure 2.2. Integration of metabolomic and transcriptomic profiling reveals perturbation in lipid metabolism enzymes and retinoid pathway. A. (top) Schematic of metabolomics and transcriptomics data integration using the Human Metabolome Database (HMDB). (bottom) Heatmap showing correlation between DE genes from HMDB analysis based on overlap of associated DA metabolites; overlapping metabolites indicated on bottom and direction of gene expression change indicated by fc.dir color bar. Diacylglycerol (DAG), PLs (phospholipids), alpha-KG (alpha-ketoglutarate), SM (sphingomyelin), TGs (triglycerides). **B.** RT-qPCR validation of upregulation of Pla2g12a and Dgat2 gene expression in CoQ-deficient cells, n=3, two-way ANOVA, Tukey multiple comparison test. **C.** Significantly enriched KEGG pathways following gene set enrichment analysis (GSEA) on bulk RNAseq data from CoQ-deficient podocytes compared to scrambled controls, n=3

(**Fig. 2.2C**). Of interest, retinoic acid (RA) is associated with cell cycle arrest and cell differentiation in podocytes (Noy, 2010; Vaughan et al., 2005), and thus we hypothesized that the positive- and negative-enriched pathways (cell cycle regulation, **Fig. 2.2C**) may be a signature of increased RA receptor (Rar)-mediated transcriptional regulation. All-trans RA (atRA) has been associated with increased Pla2 activity (Antony et al., 2003; Farooqui et al., 2004), increased AA release (Levine, 2001), and increased incorporation of AA in TGs (Moon et al., 1986; Petroni et al., 1996), all consistent with the metabolomic changes observed in CoQ-deficient podocytes. Furthermore, the carboxylic acid form of geranyl-geranyl pyrophosphate (GGdP), Pdss2's substrate, can increase Rar-mediated transcription (Araki et al., 1995). We also searched the upstream promoter regions of Pla2g12a and Dgat2 for Rar-binding sites, as evidence of transcriptional regulation by RA: Rar binding sites were identified for both gene loci (**Table S1.5**). Synthesizing these data, we hypothesized that the loss of Pdss2 resulted in the accumulation of its substrate, GGdP, which elevated Rar-mediated transcription of metabolic enzymes, resulting in the observed lipid perturbations and the release of ROS-generating PUFAs, which in turn became selectively harmful to CoQ-deficient podocytes (**Fig 2.3A**).

Retinoic acid exacerbates injury in CoQ-deficient podocytes through associated lipid metabolism changes

Having proposed a RA-mediated disease pathway, we sought to validate that (a) GGdP can increase Rar-mediated transcription; (b) CoQ-deficient podocytes have elevated levels of Rar-mediated transcription; (c) further stress through this pathway is harmful; (d) phenotypically, atRA treatment resembles the lipidomic changes observed in CoQ-deficient podocytes.

To measure Rar-mediated transcription, we used a luciferase reporter assay (Hoffman et al., 2006). Treatment with GGdP phenocopied atRA treatment by increasing luciferase expression (**Fig. 2.3B, S1.5**), and upon stimulation with either GGdP or atRA, CoQ-deficient podocytes had

Figure 2.3. CoQ deficient podocytes have elevated retinoid signaling leading to metabolic perturbations. A. Schematic of proposed podocyte injury pathway in CoQ-deficient podocytes as a two-hit mechanism, by which the loss of CoQ leads to a susceptibility to ROS-mediated injury, and the buildup of Pdss2 substrate, geranyl-geranyl pyrophosphate (GGdP) leads to the release of ROS-generating PUFAs via retinoid signaling. **B.** Luminescence readout from a Retinoic Acid Receptor Element (RARE)-luciferase reporter assay following 24 hours of treatment with 100 nM all-trans retinoic acid (atRA) or 48 hours of treatment with 10 μM GGdP. Both increase Rar-mediated transcription, n=3, two-way ANOVA, Tukey multiple comparison test. **C.** Luminescence readout from a RARE-luciferase reporter assay, showing Rar-mediated transcription from CoQ-deficient podocytes compared to scrambled controls at baseline and after stimulation with either 10 μM GGdP or 100 nM atRA, n=3, two-way ANOVA, Tukey multiple comparison test. **D.** Live cell fluorescence imaging of cellular ROS (blue) and cell death (red) in cells treated with atRA (1 μM) for 84 hours; scale bars, 100 μm. **e.** Quantification of cell death after atRA treatment for 4 days, n=4, two-way ANOVA, Sidak multiple comparison test. **F.** Heatmap of statistically significant metabolites (FDR <10%, Benjamini-Hochberg correction on a student's t-test) from conditioned media podocytes treated with 1 μM atRA versus DMSO control, n=3. **G.** Log2 fold change of PUFA levels in conditioned media podocytes treated with 1 μM atRA versus DMSO control, n=3.

Figure 2.3 (Continued).

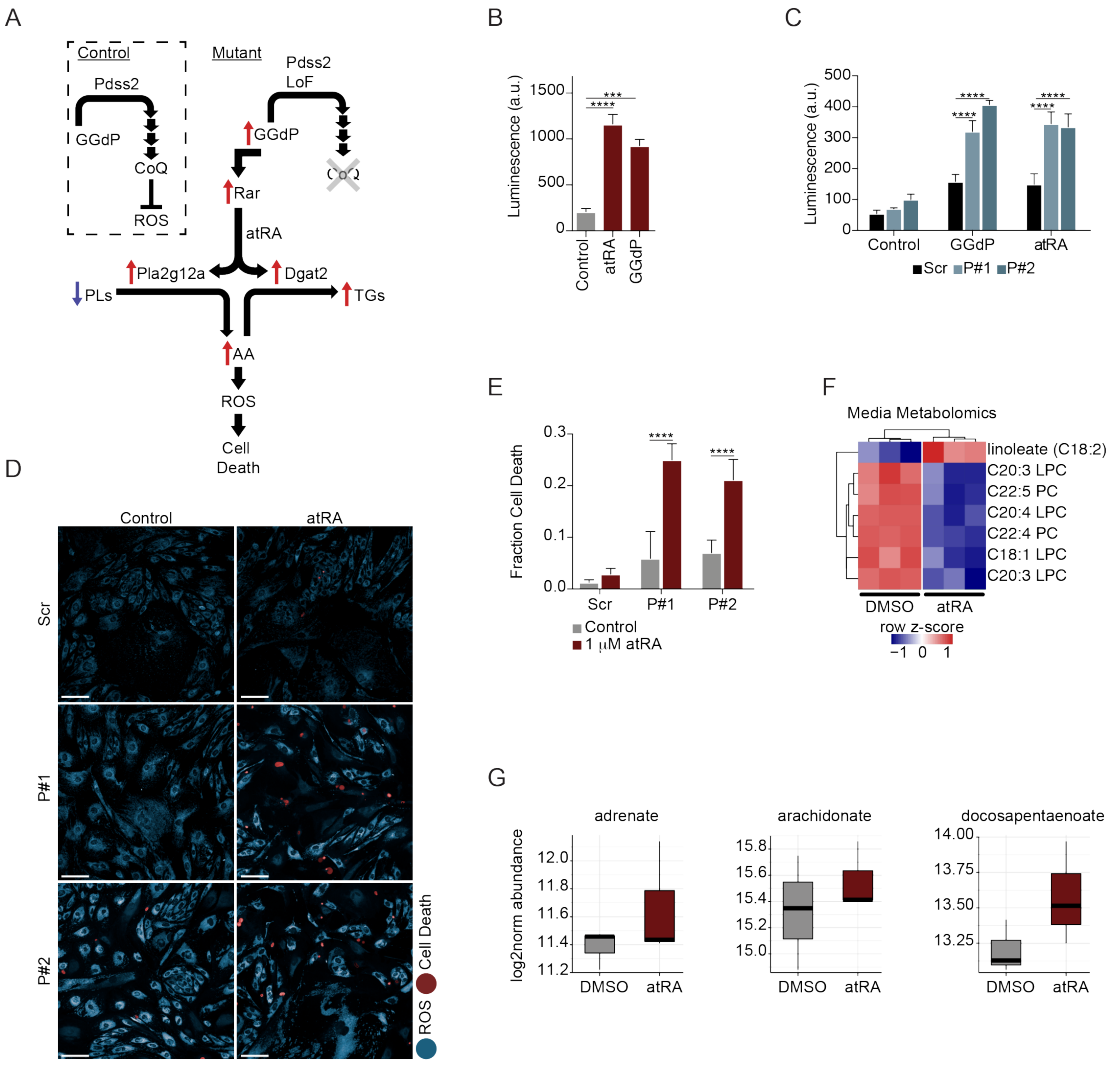

significantly elevated luciferase expression over controls (**Fig. 2.3C**). We hypothesized that if atRA is an upstream mediator of podocyte injury, then CoQ-deficient podocytes should be more susceptible to injury with atRA treatment. Consistently, CoQ-deficient podocytes had increased cell death following atRA treatment (**Fig. 2.3D,E**). Finally, we performed lipidomics of conditioned media from atRA treated podocytes, and, similar to CoQ-deficient podocytes, we found that linoleic acid, a PUFA, was significantly more abundant after atRA treatment (C18:2, **Fig. 2.3F**, **Table S1.6**). Additionally, there were a number of PU PLs that were significantly decreased in the media (**Fig. 2.3F**). Further, consistent with the elevated PUFAs in CoQ-deficient podocytes, both adrenic acid and docosapentaenoic acid were increased following atRA treatment (**Fig. 2.3G**). Thus, we concluded that Rar-mediated transcription was increased in CoQ-deficient podocytes, it was harmful to cells, and likely contributed to the observed lipid perturbations (**Fig. 2.3A**).

Single nucleus sequencing from kidneys of *Pdss2*$^{kd/kd}$, CoQ-deficient mice, reveal disease-specific cell populations

While the *in vitro* system allowed us to investigate mechanistic details of podocyte vulnerabilities in CoQ deficiency, it did not allow us to compare podocytes to other cell types in the kidney and understand the reasons underlying the specificity of podocyte injury. In particular, we sought to understand podocyte-specific reactions to CoQ deficiency in comparison to proximal tubular (PT) cells (the most energy-requiring cells of the kidney and the kidney cell type most frequently affected in mitochondrial cytopathies (Emma et al., 2012)). To answer this question, we used a mouse model of CoQ deficiency, *Pdss2*$^{kd/kd}$. By five months, *Pdss2*$^{kd/kd}$ (KDKD) mice had clear histological evidence of podocyte disease, including diffuse foot process effacement observed by electron microscopy **(Fig. S1.6A).**

To compare individual cell types at single cell resolution, we performed single nucleus RNA sequencing (sNuc-Seq) on five-month old KDKD mice versus age-matched controls (CTRL) (**Fig. S1.6B,C**). We profiled 37,336 nuclei across three CTRL (16,708 nuclei) and three KDKD

(20,628 nuclei) mice and performed unsupervised graph-based clustering followed by *post-hoc* annotation based on canonical marker genes for kidney cell types (**Table S1.7**), including a smaller podocyte and five proximal tubule clusters (**Fig. 2.4A, S1.6D, S1.7A**). While there is a known immune cell infiltrate in this disease (Sibalic et al., 1997), an immune cell cluster (marker genes: Ptprc, Cd74) was not found (**Fig. S1.7A**); this absence is consistent with prior findings that immune cells are not well represented in kidney sNuc-Seq samples (Wu et al., 2019). Podocyte injury in KDKD mice was evidenced by decreased expression of genes critical to podocyte function: Synpo, Wt1, and Plce1 (**Fig. 2.4B**).

Kidney cell types were equally represented across both KDKD and CTRL with the exception of two KDKD-specific clusters: a Dock10/Vcam1+ cluster, named for top enriched genes, and a mixed thick ascending limb (TAL) and distal convoluted tubule (DCT) (Mixed–TAL/DCT) cluster (**Fig. 2.4C**, **S1.7B**). Given that these clusters were KDKD-specific, we hypothesized that they represent disease-associated cell populations. While the Mixed–TAL/DCT cluster contained markers of both TAL (Slc12a1) and DCT (Slc12a3) (**Fig. S1.7A**), upon further analysis, there were separate populations of Slc12a1+ and Slc12a3+ cells which shared common expression of Dcdc2a, the top enriched gene (**Fig. S1.7C, Table S1.7**). Dcdc2a is a ciliary gene mutated in hereditary nephronophthisis (Schueler et al., 2015), that has not been previously described as a marker of tubular injury.

The novel disease-specific Dock10/Vcam1+ cluster was more difficult to classify, because it lacked strong expression of canonical kidney markers (**Fig. S1.7A**), but had high expression of genes involved in cytoskeleton regulation (Dock10), cell adhesion (Vcam1), and inflammation (Cxcl1) (**Fig. 2.4D, Table S1.8**). We performed GSEA on the marker gene list for this cluster followed by hierarchical and k-means clustering of the leading-edge genes (see methods), which revealed three sets of pathways (**Fig. S1.8A, Table S1.8**). One set had high representation of actin cytoskeleton genes at the leading edge (Rhoa, Rock2, Actg1, Actb), one

Figure 2.4. sNuc-Seq from CoQ-deficient mouse kidney tissue reveals patterns of injury with single cell resolution. A. T-distributed stochastic neighbor embedding (t-SNE) visualization of single nucleus transcriptomic profiles from three five-month-old *Pdss2*$^{kd/kd}$ mice (KDKD) and three age-matched control mice (CTRL) with cell type clusters as identified by canonical marker genes. **B.** Gene expression of canonical podocyte marker genes (Synaptopodin (Synpo), Wt1, Plce1) in podocytes from control and *Pdss2*$^{kd/kd}$ mice. **C.** Proportions of clusters across control and *Pdss2*$^{kd/kd}$ mice (left) with corresponding cell numbers (right), and *Pdss2*$^{kd/kd}$-specific clusters indicated with black arrows. **D.** Volcano plot of genes based on enrichment in Dock10/Vcam1+ cluster colored by significance (darker blue, p-adj. < 0.05, Wilcox rank sum test) and selected genes (red) based on GSEA. **E.** Dot plot representation of gene expression of canonical marker genes for immune cells and parietal epithelial cells (PECs). Note Dock10/Vcam1+ cells uniquely co-express the PEC markers CD44, Pax8 and Cldn1. **F.** Correlation plot of average gene expression across clusters show Dock10/Vcam1+ cells most similar to proximal tubule (PT) cells. **G.** Proportion of cycling cells in control and *Pdss2*$^{kd/kd}$ mice, with order and colors of bars as indicated, show increased numbers of cycling cells in *Pdss2*$^{kd/kd}$-specific clusters (Dock10/Vcam1+) and proximal tubular cells.

Figure 2.4 (Continued).

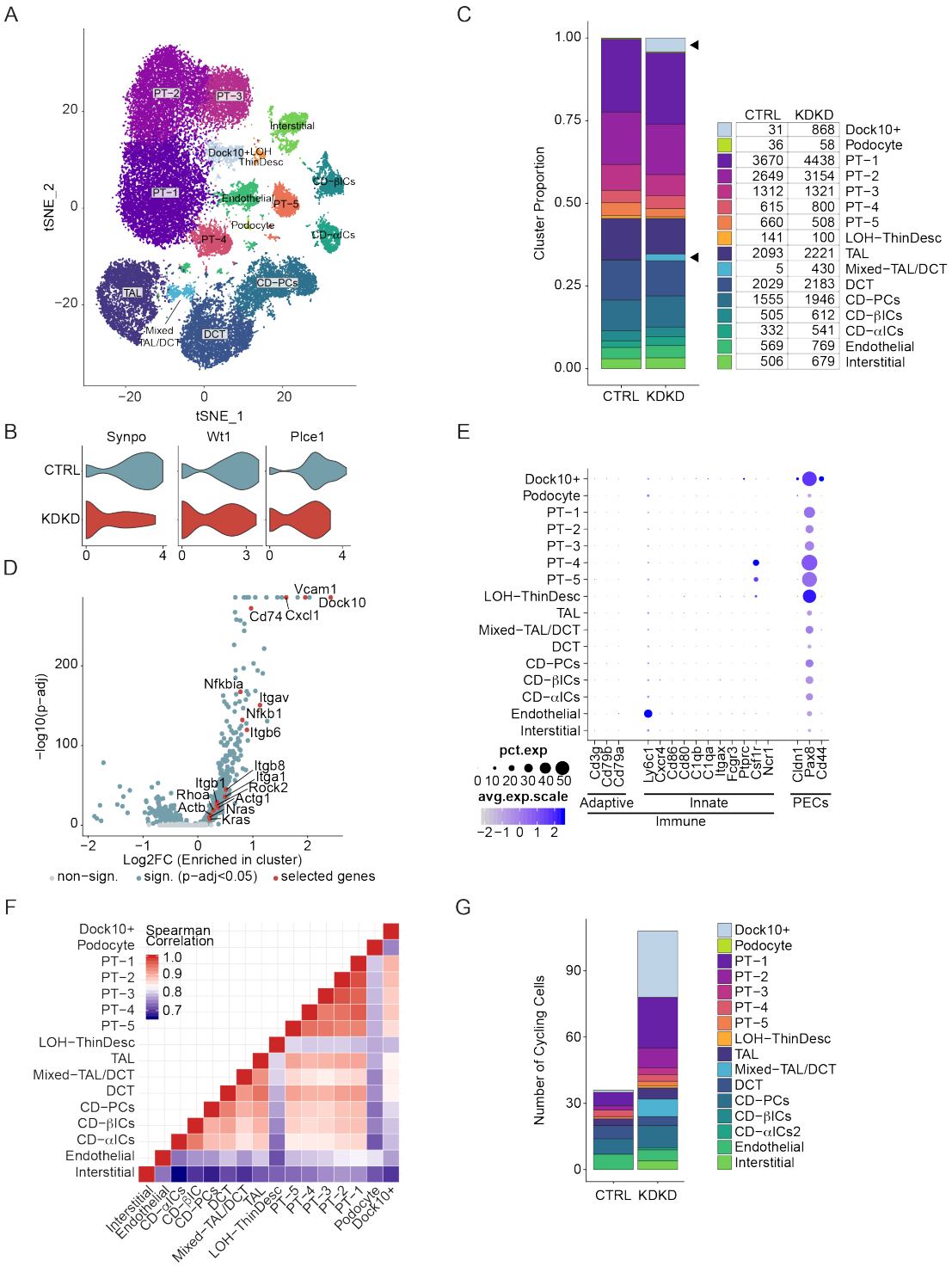

cluster had high representation of integrin adhesion genes, and a third had high representation of inflammatory genes (Ikbkb, Nfkb1, Nfkbia) (**Fig. 2.4D, S1.8A**). To rule out activated and migrating immune cells, we checked a broader panel of adaptive and innate immune cell markers, which were all negative, decreasing the likelihood that this cluster represented an immune cell population (**Fig. 2.4E**).

We subsequently hypothesized that the novel Dock10/Vcam1+ cluster might represent an activated population of parietal epithelial cells (PECs) of Bowman's capsule. While PECs have been difficult to detect by single cell transcriptomics (Boltengagen et al., 2018), this Dock10/Vcam1+ cluster expressed Cldn1 (Gharib et al., 2014) and Pax8, consistent with prior work showing that these genes are associated with a "cuboidal" PT-like PEC sub-population (**Fig. S1.8B**) (Kuppe et al., 2019). This cluster was also enriched for Cd44 which has been previously reported to be expressed *de novo* in parietal epithelial cells (PECs) of Bowman's capsule in the setting of podocyte injury (**Fig. S1.8B**) (Smeets et al., 2009). A PT-like, proliferative population has recently been reported in single cell analysis of a mouse model of unilateral ureteral obstruction (UUO) positive for similar marker genes (Vcam1, Cxcl1, **Fig. 2.4D**) (Wu et al., 2019). To assess the cell type to which this cluster was most similar in an unbiased manner, we calculated the Spearman correlation coefficient between all clusters, and found that the Dock10/Vcam1+ cluster was most similar to PT cells (**Fig. 2.4F**). This correlation was consistent with assigning the Dock10/Vcam1+ cells to PECs, in particular in mice where PT-like cuboidal PECs extend into Bowman's capsule (Haensly et al., 1982). Activated PECs, expressing Cd44, would also be expected to be proliferative; thus, we calculated S- and G2M-cell cycle scores, and set a threshold to classify "cycling cells" (**Fig. S1.8B**) (Rodman et al., 2016). Cycling cells were more abundant in KDKD mice and were predominantly found in Dock10/Vcam1+ and PT-1 clusters (**Fig. 2.4G**).

We localized the Dock10/Vcam1+ population using immunofluorescence to determine Vcam1 expression relative to PT cells (megalin, Lrp2) and podocytes (synaptopodin, Synpo). At low magnification, increased Vcam1 expression was observed in KDKD tissue (**Fig. 2.5A**, left). At higher magnification, PT cells were noted to have apical Lrp2 and basolateral expression of Vcam1+, indicating that glomerular injury could be potentially extending into the early proximal tubular compartment (**Fig. 2.5A**, right, **S1.9**). Additionally, Vcam1+ cells were present in cells surrounding podocytes, thus cells in Bowman's capsule, consistent with the idea that the Dock10/Vcam1+ cluster represents a sub-population of PECs (**Fig. 2.5B**). We assessed Vcam1 and Dock10 co-localization in cells surrounding podocytes (Nphs2) by an independent method (*in situ* chain reaction hybridization (HCR) (Choi et al., 2018), an advanced version of fluorescence *in situ* hybridization (FISH); see methods). We noted co-expression of Vcam1 and Dock10 in cells adjacent to Nphs2+ podocytes, consistent with PEC-localization (**Fig. 2.5C**). Finally, PEC activation in glomeruli of KDKD mice was histologically evident by PAS staining, as indicated by increased numbers of PECs in Bowman's capsule, with more prominent nucleoli (**Fig. 2.5D**). Thus, we discovered novel markers illuminating a newly identified, activated PEC population in response to podocyte injury.

sNuc-Seq provides insight into podocyte-specific disease state and associated pathways

Turning our focus to the podocyte, and based on our mechanistic work *in vitro* (**Figs 2.1-3**), we sought to validate transcriptomic readouts of lipid perturbations *in vivo*. We first assessed expression levels of Pla2 enzymes and Dgat2. A number of Pla2 enzymes (Pla2g16, Pla2g7, Pla2g6, Pla2g3, but not Pla2g12a) and Dgat2 were specifically elevated in podocytes compared to PT cells (either when grouped together or by individual cluster, **Fig. 2.6A**, **S1.10A**). As an indirect readout of elevated PUFAs, we used transcriptomic signatures derived from an *in vitro* screen of 65 biologically relevant fatty acids in a Min6 cell line (unpublished data, N. Wieder, Greka lab). Using this dataset gave us gene signatures of both up- (PUFA.up) and down-

Figure 2.5. A newly defined Dock10/Vcam1+ PEC population identified in CoQ-deficient mice. A. Immunofluorescence staining for PT (Lrp2) and Vcam1 in CTRL versus KDKD mice shows increased Vcam1 expression in KDKD (left; scale bars, 500 μm). Higher magnification shows Vcam1 co-localization with Lrp2+ PT cells (right; scale bars, 50 μm). **B.** Immunofluorescence staining for podocytes (Synpo) and Vcam1 in CTRL versus KDKD mice shows BC localization surrounding Synpo+ glomeruli; scale bars, 50 μm. **C.** *In situ* hybridization chain reaction shows co-localization of Dock10 and Vcam1 mRNA in cells surrounding podocytes (Nphs2), scale bars, 20 μm. **D.** Periodic acid–Schiff (PAS) staining of kidneys from CTRL and KDKD mice showing proteinuric casts in tubules of KDKD mice (*) and activation of PECs (arrowheads) at higher magnification, as seen by increased numbers and more prominent nucleoli.

Figure 2.5 (Continued).

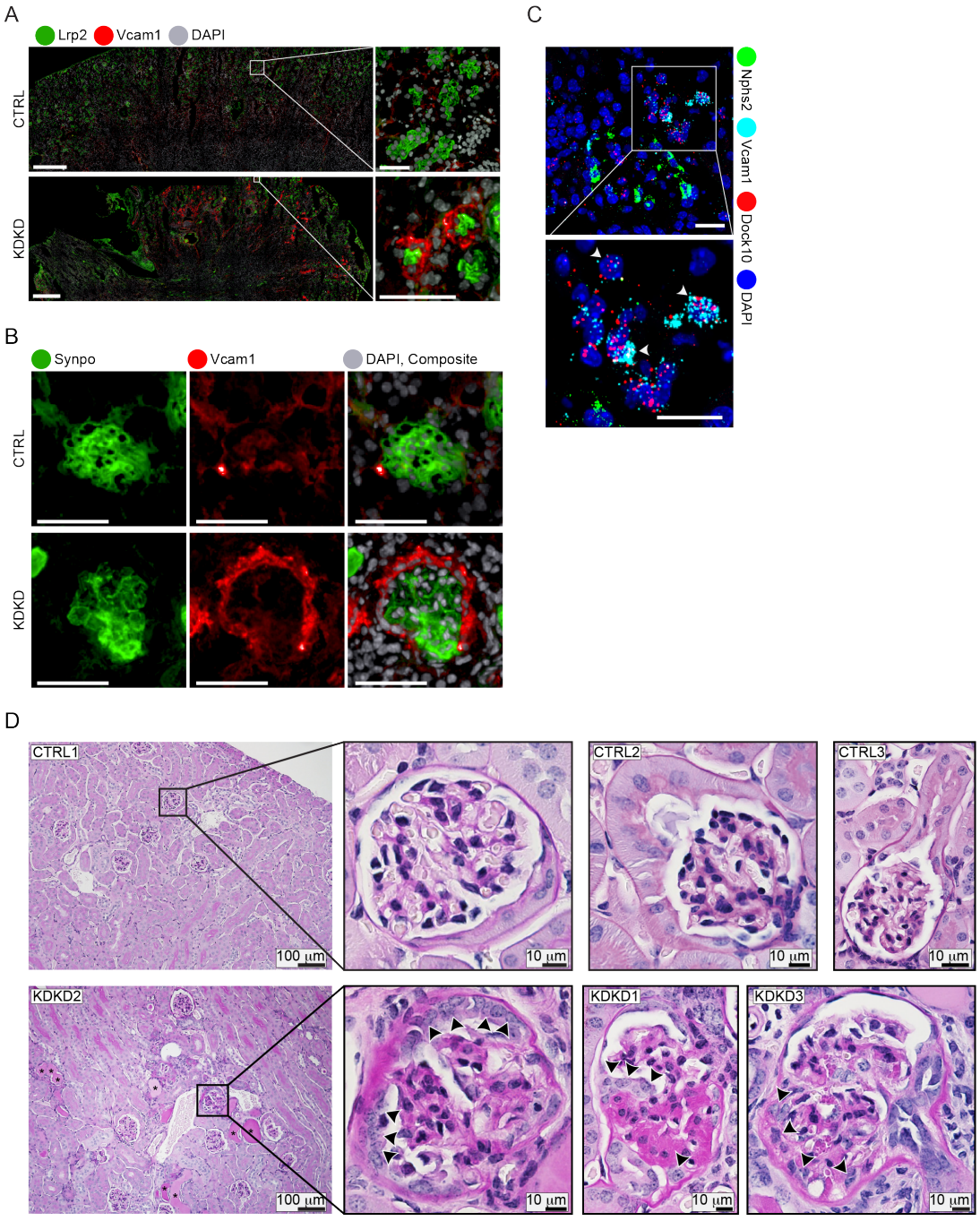

Figure 2.6. Single cell genomics analysis in CoQ-deficient mice reveals podocyte-specific changes in PUFA-related genes and therapeutically-targetable Mapk/Braf pathway. A. Dot plot representation of gene expression across various phospholipase A2 (Pla2) and Dgat2 enzymes in podocytes and all proximal tubule (PT) clusters combined. **B.** Violin plot of polyunsaturated fatty acid (PUFA) gene signatures (PUFA.up: upregulated genes associated with PUFA treatment; PUFA.down: downregulated genes associated with PUFA genes) in podocytes and all proximal tubule (PT) clusters combined. **C.** Mean-shift in PUFA gene signatures across all clusters with significance determined by a one-tailed Wilcox rank sum test (alternative hypothesis that CTRL is left-shifted compared to *Pdss2*$^{kd/kd}$ for PUFA.up signature; alternative hypothesis that CTRL is right-shifted compared to *Pdss2*$^{kd/kd}$ for PUFA.down signature). **D.** Analysis of leading edge genes (see methods) from GSEA on differential expression between control and *Pdss2*$^{kd/kd}$ podocytes (|log2fc| > 0.25), show three clusters of pathways, one driven by ETC genes (e.g. Uqcr11, Cox5a, Uqcrq, Uqcrc1, Cox7a2), and one driven by Mapk pathway genes (e.g. Raf1, Nras, Mapk1, Braf). **E.** Heatmap of average gene expression of Mapk pathway genes identified by podocyte GSEA across podocyte and combined PT clusters in CTRL versus KDKD mice. **F.** Heatmap of gene expression of Mapk pathway genes identified by *in vivo* podocyte GSEA in bulk RNAseq from CoQ-deficient podocytes compared to scrambled controls, n=3. **G.** Quantification of apoptosis after treatment with GDC-0879 (1 week), in CoQ-deficient podocytes and scrambled controls, n=4, two-way ANOVA, Tukey multiple comparison test. **H.** Live cell fluorescence imaging of cellular ROS (blue) and apoptosis (green) in cells treated with GDC-0879 (10 μM) for 1 week; scale bars, 100 μm.

Figure 2.6 (Continued).

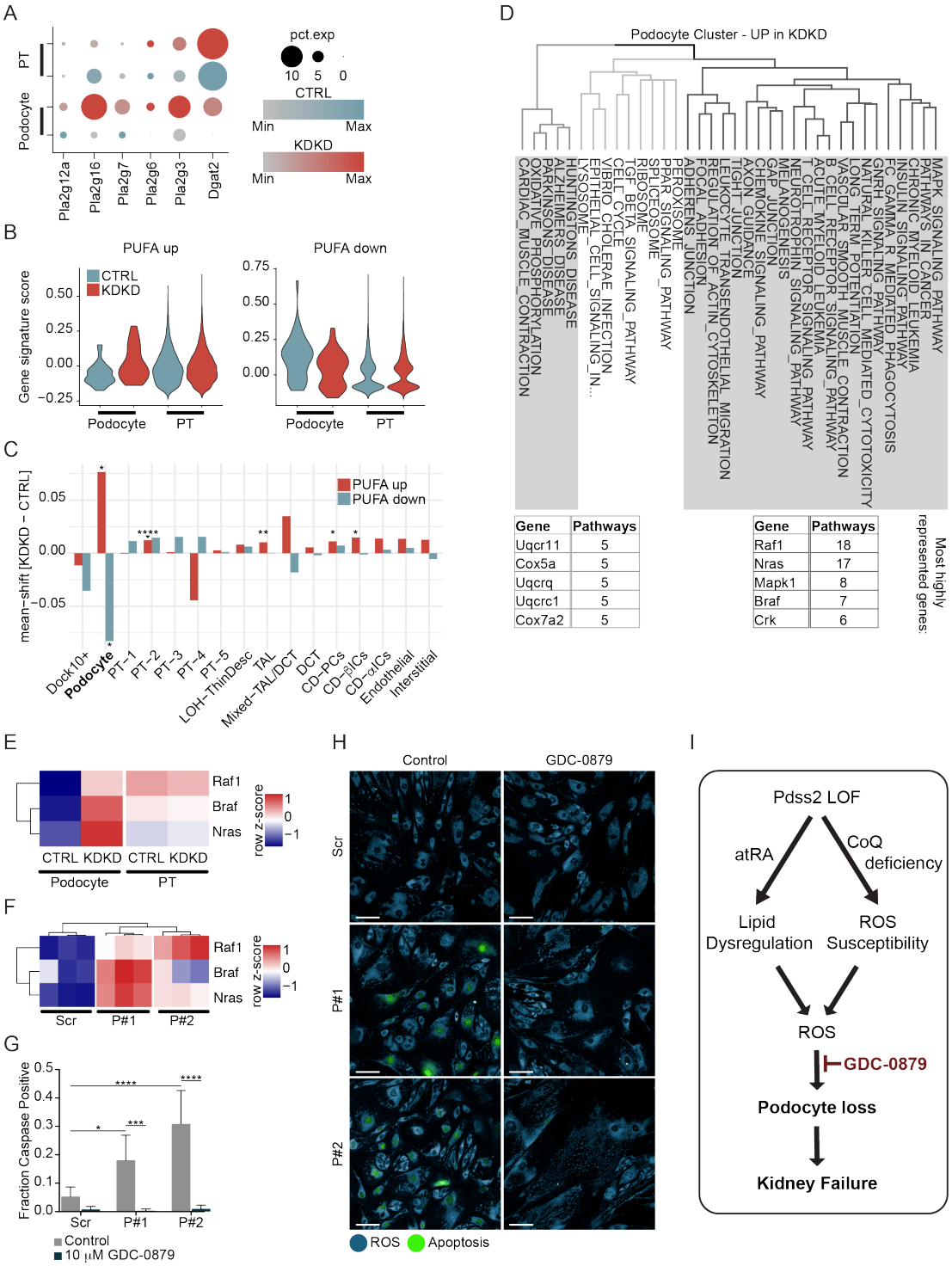

(PUFA.down) regulated genes sensitive and specific for PUFAs relative to other fatty acid families, including saturated and monounsaturated fatty acids. Calculating these gene signature scores in podocytes compared to PT cells *in vivo* showed both an increase in expression of the PUFA.up signature and a decrease of the PUFA.down signature specifically in the podocyte cluster (**Fig. 2.6B, S1.10B**, see methods). Furthermore, when using a Wilcox rank sum test to test for the one-tailed alternative hypothesis that the PUFA.up signature was increased in KDKD mice and the PUFA.down signature was decreased in KDKD mice, only the podocyte cluster showed a significant shift in mean for both signatures; it also had the largest mean-shift in both directions of all clusters (**Fig. 2.6C**). While these were not direct readouts of lipidomic perturbations at the single cell level, the sNuc-Seq data provided indirect transcriptomic validation, and suggested podocyte specificity of the proposed mechanism (**Fig. 2.3A**) *in vivo*.

To take an unbiased approach to characterizing podocyte pathways activated in disease, we performed GSEA on the podocyte cluster comparing CTRL versus KDKD podocytes, followed by hierarchical and k-means clustering of the leading-edge genes (see methods), which gave three pathway sets of up-regulated genes in KDKD podocytes (**Table S1.9**). One set was comprised of pathways which shared ETC genes at their leading edge (**Fig. 2.6D**). We hypothesized that the increased expression of ETC genes was likely not a podocyte-specific phenomenon, since CoQ-deficient cells are likely to compensate by upregulating ETC genes. We looked at a broad panel of ETC genes in podocytes and PT cells comparing CTRL and KDKD: as expected, both cell types showed increased expression of ETC genes in KDKD cells (**Fig. S1.11**).

Importantly, we noted a second set of pathways that showed increased expression of Mapk pathway genes (Raf1, Nras, Mapk1, Braf). We found this to be of interest due to prior work showing that the BRAF-targeted agent, GDC-0879, protects podocytes from a wide array of cellular stressors (Sieber et al., 2018). When comparing gene expression of these genes in comparison to PT cells, gene expression changes between CTRL and KDKD was specific to

podocytes (**Fig. 2.6E**). To explore this further mechanistically, we returned to the *in vitro* system. In agreement with the *in vivo* sNuc-Seq data, RNA-seq showed upregulation of Mapk pathway genes in CoQ-deficient podocytes relative to scrambled controls (**Fig. 2.6F**). The final critical experiment was treatment with BRAF-targeted GDC-0879: CoQ-deficient podocytes treated with GDC-0879 were rescued from apoptosis (**Fig. 2.6G,H**).

Discussion

In this study we investigated the mechanism of a genetically-defined mitochondrial cytopathy, CoQ-deficiency-associated kidney disease, in an effort to understand both basic podocyte biology and podocyte-specific disease pathways for targeted therapeutic intervention. Podocyte dysfunction is implicated in both genetic (Akchurin and Reidy, 2015) and acquired kidney diseases, including diabetic kidney disease (Brosius and Coward, 2014; Meyer et al., 1999; Pagtalunan et al., 1997), a leading cause of chronic kidney disease (CKD) worldwide (Jha et al., 2013). CKD affects over 500 million people worldwide (Jha et al., 2013), but despite this disease burden, therapeutic development has lagged (Inrig et al., 2014), with patients progressing to kidney failure requiring either dialysis (associated with 58% 5-year mortality (Saran et al., 2019)), or, more rarely available transplants. In this context, our approach in this study, a combination of hypothesis-driven mechanistic work and targeted deployment of "-omics" technologies, has led us to several important biological findings.

First, we conclude that of CoQ's functions (ETC, antioxidant, MPTP regulation, and co-factor for DHODH), it is the loss of CoQ's antioxidant function that is most injurious to podocytes. This is consistent with prior *in vivo* work which showed that ROS injury is specific to affected tissues in CoQ deficiency (Quinzii et al., 2013). While prior mechanistic studies on this disease have attempted to understand the consequence of CoQ deficiency, many studies have relied on patient fibroblast models (Ashraf et al., 2013; Lopez-Martin et al., 2007; Quinzii et al., 2008, 2010) and have not systematically evaluated all functions (Ashraf et al., 2013; Heeringa et al., 2011). By assessing baseline functions of (**Fig. S1.2**) and chemical susceptibility to each function (**Fig. 2.1, S1.3**), we were able to dissect a specific susceptibility of CoQ-deficient podocytes to oxidative stress injury that is rescued by either a radical scavenger, mitoTEMPO, or mitoQ (**Fig. 2.1**). Specifically, we showed that podocyte ETC function is robust despite CoQ deficiency, as measured by OCR (**Fig. S1.2**), and remarkably, viability is resistant to loss of podocyte ETC

function, through chemical inhibition by oligomycin (**Fig. S1.3**). These data provide evidence that kidney injury in CoQ deficiency is not driven by a lack of ATP production (as observed in mitochondrial cytopathies affecting tubular epithelial cells but not podocytes) (Au et al., 2007; Morris et al., 1995; Pitchon et al., 2007; Tzoufi et al., 2013).

Second, we describe for the first time a perturbation of PUFAs in the setting of podocyte CoQ deficiency: an increased abundance of PUFAs in conditioned media and a shift from the PL to TG fraction in cell lysates (**Fig. 2.1**). Further, we use RNA-Seq to measure transcriptomic changes that were subsequently integrated with measured metabolomic changes (**Fig. 2.3**). While metabolomics has been previously performed from kidneys, brain, and plasma of *Pdss2*$^{kd/kd}$ mice (Kleiner et al., 2018), the low percentage of podocytes in the kidney may have made it difficult in the past to detect podocyte-specific changes from bulk tissue measurements. Harnessing the power of single cell (or single nuclei) RNA-Seq has allowed us to overcome these previous limitations and confirm a role for podocyte Dgat2 and Pla2g in cellular injury. These findings were consistent with prior observations of PUFA-mediated injury in CoQ-deficient yeast (Do et al., 1996; Poon et al., 1997). We extended these findings by pointing to transcriptional regulation of PUFA metabolism through RA (**Fig. 2.3**). Idebenone, a CoQ analog, has been shown to decrease AA metabolism in astrocytes (Civenni et al., 1999), and AA has been shown to increase CoQ content in yeast (Cheng et al., 2010). Thus, this study illuminates lipid dysregulation in the setting of CoQ deficiency as a significant contributor to injury and disease progression.

Third, we propose an injury pathway driven by GGdP accumulation leading to elevated Rar-mediated transcriptional and downstream metabolomic changes (**Fig. 2.3A**). Increased Pla2 activity in the setting of atRA treatment has been previously described (Antony et al., 2003; Farooqui et al., 2004; Levine, 2001; Moon et al., 1986; Petroni et al., 1996). However, in the setting of podocyte injury, atRA has only been described to ameliorate injury through decreasing podocyte proliferation and promoting differentiation (He et al., 2007a; Li et al., 2014b; Vaughan

et al., 2005). Consistent with increased Rar-mediated transcription, CoQ-deficient podocytes downregulate pro-proliferation pathways (**Fig. 2.2**). However, this model suggests that de-differentiation and cell-cycle re-entry is not the only mechanism of podocyte injury, and that there might be disease states in which this pro-differentiation pathway becomes injurious. Specifically, we propose that it is the combination of (a) ROS-generating PUFAs, the result of upregulated Rar transcriptional programs, and (b) susceptibility to ROS injury which promote podocyte death in the setting of CoQ deficiency.

Fourth, we characterized the *Pdss2*$^{kd/kd}$ mouse model at the single cell level, which revealed novel markers for a newly-defined activated PEC cell population. Increased Vcam1 expression (previously described in the damaged tubules of *Pdss2*$^{kd/kd}$ mice (Sibalic et al., 1997)) led us to the discovery of a disease-specific Dock10/Vcam1+ cell population, transcriptionally similar to PTs but localized to BC, suggesting that an activated, proliferating PEC population leads to progressive glomerular injury in CoQ-mediated podocytopathies, and possibly in other proteinuric kidney diseases (**Fig. 2.4,2.5**). Furthermore, we validated podocyte-specific transcriptomic changes consistent with the lipidomic changes observed *in vitro* (in contrast to ETC gene alterations, for example, that were found across multiple cell types) (**Fig. 2.6**). Thus, the transcriptomic changes in specific cell types in the kidney revealed by sNuc-Seq illuminated with unprecedented resolution the podocyte-specific effects of CoQ deficiency.

The consistency of the transcriptomic changes between the *in vivo* and *in vitro* podocytes validated the *in vitro* podocytes as a model to understand *in vivo* mechanisms of injury. Of interest, *in vivo*, we observed a podocyte-specific alteration in Braf-Mapk pathway genes, which we found to also be consistent *in vitro*. This finding was of particular interest due to our prior work showing that the BRAFV600E inhibitor, GDC-0879, rescues podocytes from a wide array of cellular stressors, including fatty acid injury with palmitic acid (Sieber et al., 2018). Thus, we also tested the effect of GDC-0879 on CoQ-deficient podocytes, and found that it robustly reversed apoptosis

(**Fig. 6**). This result suggests that CoQ deficiency may share a final common end-injury pathway with other forms of podocyte injury, pointing to the Braf-Mapk pathway as a putative target for podocyte survival (**Fig. 6I**). While podocyte injury has been associated with cell cycle re-entry (Liapis et al., 2013), we suggest here a model in which the retinoic acid pathway promotes apoptosis and injury, while the Mapk pathway, traditionally thought of as a pro-proliferation pathway, promotes cell survival in post-mitotic podocytes.

In conclusion, we propose that podocyte injury in the setting of CoQ deficiency is mediated by a two-hit mechanism in which ROS susceptibility is exacerbated by a RA-mediated release of ROS-generating PUFAs (**Fig. 2.3A**). This pathway may be upstream of a common podocyte-injury pathway, rescued by GDC-0879 (**Fig. 2.6I**). Single cell genomics in the *Pdss2*$^{kd/kd}$ mouse revealed the podocyte-specific mechanisms leading to disease progression, though arguably a podocyte-specific *Pdss2* knockout mouse model might have allowed us to discern which aspects of tubular injury were directly related to CoQ deficiency versus indirect sequelae of podocyte injury. Regardless, the simplest explanation of the data suggest that podocytes lead the initiation and progression of injury in CoQ-deficiency kidney disease. sNuc-Seq analyses also revealed a novel Dock10/Vcam1+ PEC population that contributes to glomerular injury *in vivo*. It is important to note that, while this work has focused on mechanisms of glomerular kidney injury (the *Pdss2*$^{kdk/kd}$ mouse has isolated kidney disease(Peng et al., 2008)), patients with CoQ deficiency frequently present with extra-renal symptoms including encephalopathy (Diomedi-Camassei et al., 2007; Emmanuele et al., 2012; Heeringa et al., 2011; Jakobs et al., 2013; López et al., 2006; Ozaltin, 2014; Salviati et al., 2005). In fact, neurological involvement is frequent in mitochondrial cytopathies, thought to be driven by ETC dysfunction. We speculate that aspects of ROS-generating mechanisms and pathways identified here may be highly relevant to the neurologic features of these devastating diseases. Taken together, our studies combining transcriptomic and

metabolomic approaches *in vivo* and *in vitro* have allowed us to gain insight into the mechanism of a genetically-defined mitochondrial cytopathy and potential targets for therapeutic intervention.

Methods

Materials

Drug treatments: Oligomycin A (Sigma Aldrich, # 75351-5MG), Carbonyl cyanide 3-chlorophenylhydrazone (CCCP, Sigma-Aldrich, # C2759-100MG), Rotenone (Sigma Aldrich, # R8875-1G), Teriflunomide (Sigma-Aldrich, # SML0936-10MG), C_2-Ceramide (Sigma-Aldrich, # A7191-5MG), Paraquat (Sigma Aldrich, #36541-100MG), mitoQ (MedKoo Biosciences, # 317102), mitoTEMPO (Sigma-Aldrich, # SML0737-5MG), Arachidonic Acid (Sigma-Aldrich, # A3611-100MG), all-trans retinoic acid (Sigma-Aldrich, # R2625-100MG), Geranyl-geranyl pyrophosphate (Sigma-Aldrich, # G6025-1VL), GDC-0879 (R&D Systems, # 4453/10)

Live cell imaging dyes: CellEvent™ Caspase-3/7 Green Detection Reagent (Thermo Fisher Scientific, # C10423, 1:5000), DRAQ7 (VWR International, LLC, # 424001, 1:1000), MitoTracker™ Deep Red FM (Thermo Fisher Scientific, #M22426, 1:1000, 200 nM), Calcein-AM (Thermo Fisher Scientific, # C1430, 1 μM), Cobalt (II) Chloride ($CoCl_2$, Sigma-Aldrich, # 60818-50G, 2 mM), Tetramethylrhodamine, Methyl (TMRM, Thermo Fisher Scientific, # T668, 10 nM), CellROX™ Orange Reagent (Thermo Fisher Scientific, #C10443, 1:1000).

Antibodies: Pdss2 (Santa Cruz Biotechnology, #sc-515136, 1:100), Gapdh-HRP (Cell Signaling Technology, #8884S, 1:1000),Anti-mouse IgG, HRP-linked (Cell Signaling Technology, #7076, 1:2000), Synaptopodin (GeneTex, #GTX39067, 1:300), Megalin (Lrp2, Santa Cruz Biotechnology, #sc-515772, 1:100), Vcam1 (Cell Signaling Technology, #39036, 1:400), Anti-mouse IgG, Alexa Fluor 488 (Thermo Fisher Scientific, #A-11001, 1:1000), anti-rabbit IgG, Alexa Fluor 647 (Thermo Fisher Scientific, # A27040, 1:1000)

Primer sequences:

RARE-luciferase cloning: FWD: ctgcccaactggctcctgcaggCGAGCTCGGTGAACTTTC; REV: tgtaatccagaggttgattctcgagAACTTGTTTATTGCAGCTTATAATG

Pdss2 qPCR: FWD: GAGAGGCTCAAGAGAAAGGAAG; REV: TGGTAACGACACAGGTCAATAG

Pla2g12a qPCR: FWD: GCAGCGACGGATCGAAG; REV: ACTTGGTCAGGGAAGGGATA

Dgat2 qPCR: FWD: CCATCCAGCTGGTGAAGAC; REV: GCCTCTGTGCTGAAGTTACA

Gapdh qPCR: FWD: AGGCCGGTGCTGAGTATGTC; REV: TGCCTGCTTCACCACCTTCT

Cell culture

Conditionally immortalized mouse podocytes were cultured under permissive conditions (33^{o}C) in RPMI-1640 (Thermo Fisher Scientific, #11875135) with 10% FBS (Thermo Fisher Scientific, # 26140079), 100 U/ml penicillin and 100 mg/ml streptomycin (ThermoFisher Scientific, #15140) and interferon-γ (Cell Sciences, # CR2041B) on type I collagen (Corning, # 354236). Induction of differentiation is mediated by thermo-shift to 37^{o}C without interferon-γ. Lentivirus transduction was performed between days 5 to 10 of differentiation and assays were performed between days 10 to 17 of differentiation.

HEK293 cells were cultured in DMEM (ThermoFisher Scientific, #41965) supplemented with 10% FBS and penicillin/streptomycin.

Lentivirus Production

HEK293 cells (60-80% confluency in a 10-cm tissue culture dish) were triple-transfected with the two helper plasmids pCMV-dR8.91 (2 μg) and VSV-G (1 μg), and the shRNA-containing pLKO.1 (Sigma Aldrich, TRCN0000253052 (#1), TRCN0000253054 (#2)) or RARE-luciferase-containing vvPW plasmid (see below) (3 μg) using Lipofectamine 3000 (Thermo Fisher Scientific, #L3000001). Fresh antibiotic-containing media was added 20 hours post transfection. Virus was harvested 48 hours later, sterile filtered, aliquoted, and stored at -80^{o}C.

Podocytes were transduced with 20-30% virus, by volume, in the presence of 4μg/ml Polybrene for 20 hours and experiments were performed as described below.

Cloning of RARE-luciferase into lentivirus delivery plasmid

pGL3-RARE-luciferase was a gift from T. Michael Underhill (Addgene plasmid # 13458; http://n2t.net/addgene:13458 ; RRID:Addgene_13458). The RARE-luciferase promoter and open reading frame was sub-cloned into the vvPW lentivirus delivery plasmid by PCR amplification (Q5® Hot Start High-Fidelity 2X Master Mix, New England BioLabs, # M0494S) and digestion of the vvPW backbone (SbfI-HF, New England BioLabs, # R3642S; XhoI, New England BioLabs, # R0146S), followed by assembly and transformation into NEB 5-alpha competent cells (NEBuilder® HiFi DNA Assembly Cloning Kit, New England BioLabs, # E5520S). Transformants were validated by Sanger sequencing followed by whole plasmid sequencing.

Western Blotting

Proteins in lysis buffer (Cell Signaling Technology, # 9803) were separated in by 4-12% SDS-PAGE and transferred to nitrocellulose membranes. All washes were carried out with 0.1% Tween in PBS. Prior to primary antibody incubation (in blocking solution, 1 hour at room temperature) membranes were blocked for 1 hour at room temperature (5% nonfat dry milk in PBS containing 0.1% Tween). Secondary antibodies were applied for 1 hour at room temperature (in blocking solution). The immunoblots were detected using Super Signal West Pico or Femto (Thermo Fisher Scientific, # 34580, # 34096, respectively) using Gel imaging system:G:BOX Chemi XT4 (G:BOX-CHEMI-XT4, Syngene).

RNA isolation and quantitative real-time PCR

Podocytes were plated into 10-cm dishes (90K/plate) for differentiation, transduced with shRNA lentivirus on day 7 of differentiation and RNA was collected on day 14 of differentiation. Total RNA extraction was performed using RNeasy Mini Kit (Qiagen, #74106). RNA was eluted using

Nuclease-Free water and total yield and purity of RNA were assessed using NanoDrop™ 2000 (Thermo Fisher). For quantitative real-time PCR, cDNA library was synthesized according to the protocol using Maxima H Minus Reverse Transcriptase (Thermo Fisher Scientific, # EP0752). cDNA was diluted to 5 ng/μL and 20 ng per sample were used for qPCR reaction, with 0.5 μM primers, and PowerUp™ SYBR™ Green Master Mix (Thermo Fisher Scientific, # A25742) using Biorad CFX384™ Real-Time System. The qPCR was carried out with an initial denaturation at 95°C for 10 minutes, and 40 cycles of amplification (95 °C for 15 sec and 60°C for 1 min).

cDNA Library Construction

RNA from cells was quantified using the Quant-iTTM RiboGreen® RNA Assay Kit (Thermo Scientific #R11490) and normalized to 5 ng/μL. An automated variant of the Illumina TruSeqTM Stranded mRNA Sample Preparation Kit was used for library preparation from a 200 ng aliquot of RNA. This method preserves strand orientation of the RNA transcript and uses oligo dT beads to select mRNA from the total RNA sample. Following cDNA synthesis and enrichment, cDNA libraries were quantified with qPCR using KAPA Library Quantification Kit for Illumina Sequencing Platforms and then pooled equimolarly.

Illumina Sequencing

Pooled libraries were normalized to 2 nM and denatured using 0.1 N NaOH prior to sequencing. Flowcell cluster amplification and sequencing were performed according to the manufacturer's protocols using either the HiSeq 2000 or HiSeq 2500. Each run was a 101 bp paired-end with an eight-base index barcode read. Data was analyzed using the Broad Institute Picard Pipeline, which includes de-multiplexing and data aggregation.

Seahorse Flux Analyzer

Podocytes were plated onto 15-cm dishes (220K/plate) for differentiation. Podocytes were transferred to XF96 cell culture plates (Seahorse Bioscience, #) at a density of 50K/well on

differentiation day 6. Lentivirus transduction with shRNA was performed on differentiation day 7. Treatment with RPMI-1640 ± glucose was added on differentiation day 15, and the assay was performed on differentiation day 17. Oxygen consumption rate (OCR) and extracellular acidification rate (ECAR) measurements were performed using the XF96 Extracellular Flux Analyzer (Seahorse Bioscience). Prior to performing the assay, media was replaced with unbuffered RPMI-1640 and plates were placed in a 37°C, non-CO_2 incubator for 1 hour. Baseline OCR and ECAR were measured repeatedly with 8 minutes of mixing followed by 4 minutes of measuring, with 4 measurements before injection and 4 minutes following each injection: oligomycin (1 μM), CCCP (5 μM), Rotenone (1 μM). The OCR and ECAR were automatically recorded and calculated by the Seahorse XF-96 software.

High content imaging assays and image analysis

Podocytes were plated into CellCarrier-384 Ultra Microplates (125-150 cells/well, Perkin Elmer, # 6057300) for differentiation. Lentivirus transduction with shRNA virus was performed on differentiation day 6. Followed by drug treatments and imaging as follows:

Baseline apoptosis, rescue assays (mitoQ and GDC0879), and atRA treatment: An initial treatment was given immediately after lentivirus removal on differentiation day 7. On differentiation day 10, media was replaced, supplemented with rescue treatment and live cell imaging dyes. Live cell imaging was carried out daily from differentiation day 10 through differentiation day 14.

Cell viability susceptibility assays: Podocytes were maintained after lentiviral transduction until differentiation day 17 at which point podocytes were treated with Oligomycin A, Paraquat, C_2-ceramide, Teriflunomide, or Arachidonic Acid. For Oligomycin A, Paraquat, C_2-ceramide, Terflunomide time points were taken at 12, 16, 20, and 24 hours after treatment. For Arachidonic Acid, live cell imaging was performed once daily for 5 days. For rescue experiments, pre-

treatment (mitoQ, mitoTEMPO) was performed 12 hours prior to treatment with drugs and addition of dyes for live cell imaging.

All fluorescence imaging performed in this study was done using the imaging system Opera Phenix High-Content Screening System (HH14000000, Perkin Elmer). For fluorescence imaging of cells (live cell or fixed cell imaging), CellCarrier Ultra microplates were used and a minimum of nine fields were acquired per well. Image analysis for all imaging experiments was performed using Harmony software (PerkinElmer).

Caspase activation and DRAQ7 staining were used to calculate the fraction of cells going through apoptosis or cell death, respectively. Single nuclei were first identified using a combination of digital phase contrast and caspase and DRAQ7 changes and cell number was calculated. The entire cell body of the podocyte was identified using an additional dye, either TMRM or CellROX Orange. Threshold fluorescence was then determined and the fraction of cells that are positive for the staining was calculated. Further, large, podocyte-like cells were identified as having a cell area >3500 μm^2, based on higher expression of Synaptopodin (**Fig. S12A**) Mitochondrial membrane potential or ROS per cell were calculated from TMRM or CellROX Orange, respectively. For more detail on analysis sequence see **Fig. S12B**.

Luciferase Assay

Podocytes were plated into 96-well dishes (400-500 cells/well) for differentiation. Lentivirus transduction with RARE-luciferase virus was performed at differentiation day 5. For shRNA experiments, lentivirus transduction with shRNA virus and drug treatments were performed at differentiation day 9 and the luciferase assay (ONE-Glo™ EX Luciferase Assay System, Promega, # E8120) was performed after 28 hours. For drug treatments, luciferase assay was performed 5 to 8 days after delivery of RARE-luciferase virus and luminescence was measured 24 to 48 hours after treatment.

Metabolite extraction

For the metabolomics performed on the shRNA-lentivirus transduced podocytes, podocytes were plated into 10-cm dishes (90K/plate). Lentivirus transduction with shRNA virus was performed at differentiation day 7 and metabolite extraction was performed at differentiation day 14. For the atRA-treated podocytes, podocytes were plated into 6-well dishes (15K/well). Treatment was added on differentiation day 8 and metabolite extraction was performed at differentiation day 13. Media was profiled by snap-freezing 500 μL of conditioned media before beginning extraction. For non-polar metabolite extraction, cells were washed with cold PBS [no Mg^{2+}/no Ca^{2+}] followed by extraction using HPLC-grade 2-propanol (Sigma-Aldrich, # 34863. Cell extracts were incubated at 4°C for 1 hour, spun down (3500 rpm, 4°C, 10 minutes), and supernatant was transferred to new tubes. Polar metabolites were extracted in 80% HPLC-grade methanol (Sigma-Aldrich, # 34860), scraped from plates after incubation at -80°C for 15 minutes, spun down (3500 rpm, 4°C, 10 minutes), and supernatant was transferred to new tubes.

Metabolomics data acquisition:

Metabolites were profiled using four complimentary liquid chromatography tandem mass spectrometry (LC-MS) methods designed to measure polar metabolites, free fatty acids, and lipids as described previously (O'Sullivan et al., 2017; Paynter et al., 2018). Chromatography was done using Shimadzu Nexera X2 U-HPLC (Shimadzu Corp.; Marlborough, MA) and mass spectrometry using Q Exactive/Exactive Plus Instruments (Thermo Fisher Scientific; Waltham, MA).

For the measurement of water soluble metabolites methanol cell extracts were dried down under N_2 gas and resuspended in 10 µl of water. Metabolites from media and resuspended cell extracts (10 µl) were extracted with the addition of 90 µL of acetonitrile/methanol/formic acid (74.9/24.9/0.2; v/v/v) containing stable isotope-labeled internal standards (valine-d8, Sigma-Aldrich; St. Louis, MO; and phenylalanine-d8, Cambridge Isotope Laboratories; Andover, MA).

The samples were centrifuged (10 min, 9,000 x g, 4°C), and the supernatants (10 µL) were injected directly onto a 150 x 2 mm, 3 µm Atlantis HILIC column (Waters; Milford, MA). MS analyses were carried out using positive ion mode ionization using full scan analysis over 70-800 m/z.

For the measurement of polar metabolites that ionize in negative mode, methanol extracts were centrifuged (10 min, 9,000 x g, 4°C) and 10 µl of the supernatants were injected directly onto a 150 x 2.0 mm Luna NH2 column (Phenomenex; Torrance, CA). MS analyses were carried out using electrospray ionization in the negative ion mode using full scan analysis over m/z 60-750 at 70,000 resolution and 3 Hz data acquisition rate

For lipid profiling and coenzyme Q measurements, 200 µl of isopropanol cell extracts were dried under N_2. Both cell and media lipids were extracted with isopropanol containing 1,2-didodecanoyl-sn-glycero-3-phosphocholine (Avanti Polar Lipids; Alabaster, AL) either by directly resuspending dried cell extracts with 100 µl of solvent or 1:20 (vol media/vol solvent) extractions for media. After centrifugation, supernatants (2 µL) were injected directly onto a 100 x 2.1 mm, 1.7 µm ACQUITY BEH C8 column (Waters; Milford, MA). Eluting compounds were analyzed with a MS ionization in the positive ion mode using full scan analysis over 220–1100 m/z. Lipid identities were denoted by total acyl carbon number and total number of double bond number, the identity of coenzyme Qs was determined by matching the retention time and *m/z* of the authentic standards for Coenzyme Q9 (Cayman Chemical #16866) and Coenzyme Q10 (Sigma Aldrich, # C9538). For the measurement of free fatty acids and metabolites of intermediate polarity, media (30 µL) were extracted using 90 µL of methanol containing PGE2-d4 as an internal standard (Cayman Chemical Co.; Ann Arbor, MI) and centrifuged (10 min, 9,000 x g, 4°C). The supernatants of media and cell methanol extracts (10 µL) were injected onto a 150 x 2.1 mm ACQUITY BEH C18 column (Waters; Milford, MA). MS analyses were carried out using electrospray ionization in the negative

ion mode using full scan analysis over m/z 70-850 at 70,000 resolution and 3 Hz data acquisition rate.

Raw data were processed using TraceFinder 3.3 or 4.0 software (Thermo Fisher Scientific; Waltham, MA) and Progenesis QI (Nonlinear Dynamics; Newcastle upon Tyne, UK). For each method, metabolite identities were confirmed using authentic reference standards from an in-house collection of metabolites. HMDB identifiers were assigned to annotated compounds when available using version 3.0 of the HMDB library. For lipid families, based on the inability of the methods used in assigning the position of double bonds in the acyl chains, representative HMDB IDs were chosen instead.

Mice kidney immunofluorescence

Both kidneys were removed and rapidly frozen in Tissue-Tek® O.C.T. Compound, Sakura® Finetek (OCT) (VWR, #25608-930) using dry ice and methylbutane. 5 um-thick sagittal sections were obtained using a cryostat (Leica, # CM1950), thaw mounted on microscope slides (Fisherbrand™ Superfrost™ Plus, Fisher Scientific) and air dried for 15 min. Sections were fixed by immersion in 4% PFA (Electron Microscopy Sciences, #15710) at 4ºC for 10 min. All washes were carried out with PBS. Prior to staining, sections were incubated for 20 min at room temperature in PBS blocking solution containing 5% normal goat serum (Jackson ImmunoResearch, #005-000-121), 0.2% Triton X-100 (Sigma-Aldrich, # X100-100ML) and 2% bovine serum albumin (BSA) (Sigma-Aldrich, # A9576-50ML). Afterwards, sections were incubated at 4ºC overnight with primary antibodies diluted in the same blocking solution. Subsequently, sections were incubated with secondary antibodies diluted in PBS containing 0.1% Triton X-100 for 2 hr at room temperature. Following three washes of 10 min in PBS, sections were incubated with 1:10.000 DAPI solution (Thermo Fisher Scientific, #62248) in PBS for 5 min. Lastly, sections were air dried and mounted using ProLong™ Gold Antifade Mountant (Thermo Fisher Scientific, # P36930).

Kidney Histology

Kidney histology of 3 CTRL and 3 KDKD mice were assessed. Light microscopy images of periodic acid–Schiff (PAS), toluidine blue–stained sections as well as transmission electron micrographs were analyzed in a blinded fashion by A. Weins and classified using standard criteria.

***in situ* Hybridization Chain Reaction** (Choi et al., 2018)

All HCR v3 reagents (probes, hairpins, and buffers) were purchased from Molecular Technologies. Thin sections of tissue (10um) were mounted in 24 well glass bottom plates (82050-898, VWR) coated with a 1:50 dilution of APTES (440140, Sigma). The following solutions were added to the tissue: 10% formalin (100503-120, VWR) for 15min, 2 washes of 1x PBS (AM9625, ThermoFisher Scientific), ice cold 70% EtOH at -20 2 hours to overnight, 3 washes 5x SSCT (15557044, ThermoFisher Scientific with 0.2% Tween-20), Hybridization buffer (Molecular Technologies) for 10min, probes in Hybridization buffer overnight, 4 15min washes in Wash buffer (Molecular Technologies), 3 washes 5x SSCT, Amplification buffer (Molecular Technologies) for 10min, heat denatured hairpins in Amplification buffer overnight, 3 15min washes in 5x SSCT (1:10,000 DAPI TCA2412-5MG, VWR in the second wash), and storage/imaging in 5x SSCT. Imaging was performed on a spinning disk confocal (Yokogawa W1 on Nikon Eclipse Ti) operating NIS-elements AR software. Image analysis and processing was performed on ImageJ Fiji.

Single nuclei isolation for 10X genomics

Nuclei were isolated as previously described with modification (Wu et al., 2019). Briefly, nuclei were isolated with Nuclei EZ Lysis buffer (Sigma-Aldrich, #NUC-101) supplemented with protease inhibitor (Roche, #5892791001) and RNase inhibitor (Promega, # N2615; Life Technologies, #AM2696). Samples were cut into <2-mm pieces and homogenized with a Dounce homogenizer (Kimble Chase, #885300–0002) in 2 mL of ice-cold Nuclei EZ Lysis buffer, and then filtered through a 70 μm cell strainer (Corning, #352350). The samples were homogenized again, an

additional 2 mL of lysis buffer was added, and samples were incubated on ice for 5 minutes. The homogenate was then filtered through a 40 μm cell strainer (Corning, #352340) and centrifuged at 500xg for 5 minutes at 4°C. The pellet was resuspended and washed with 4 mL of the buffer, incubated on ice for 5 minutes, and centrifuged again. Finally, the pellet was resuspended in Nuclei Suspension Buffer (1XDPBS, 0.1% RNase inhibitor), filtered through a 30 μm cell strainer (Sysmex America, Inc., #04-004-2326), and counted.

Library preparation and single cell sequencing

Single nuclei were processed through the 10X Chromium 3' Single Cell Platform using the Chromium Single Cell 3' Library, Gel Bead and Chip Kits (10X Genomics, Pleasanton, CA), following the manufacturer's protocol. Briefly, 10,000 cells were added to each channel of a chip to be partitioned into Gel Beads in Emulsion (GEMs) in the Chromium instrument, followed by cell lysis and barcoded reverse transcription of RNA in the droplets. Breaking of the emulsion was followed by amplification, fragmentation and addition of adapter and sample index. Libraries were sequenced at a concentration of 1.8pM on a Nextseq with a 150 cycle v2 kit (TG-160-2002, Illumina) with a read structure of Read 1 26bp, Read 2 98bp, Index 1 8bp, and Index 2 0bp. One 10x lane was loaded per round of sequencing, resulting in 400M reads per sample.

Animal Experiments

B6/Pdss2$^{kd/kd}$ mice were purchased from Jackson laboratory. Pdss2$^{kd/kd}$ mice harbor a spontaneous mutation in the gene encoding the subunit 2 of polyprenyl-diphosphate synthase (Pdss2) and their phenotype was previously described (Peng et al, 2004; Quinzii et al, 2013). All experiments were performed according to a protocol approved by the Institutional Animal Care and Use Committee of the Columbia University Medical Center, and were consistent with the National Institutes of Health Guide for the Care and Use of Laboratory Animals. Mice were housed

and bred according to the international standard conditions, with a 12-h light/12-h dark cycle and free access to food and water.

Mutant and control animals were euthanized by rapid carbon dioxide narcosis followed by cervical dislocation after disease onset (5 months). Kidneys were quickly removed. For each animal, one kidney was frozen in the liquid phase of isopentane, pre-cooled toward its freezing point (-80°C) with dry ice and the second kidney was fixed in neutral buffered formalin. Experiments were performed in 3 mice for each group.

Quantification and Statistical Analysis

Statistical Analysis

Statistical analysis was performed, and results plotted using Graphpad Prism version 7.0 software. Data is presented as means ± standard deviation throughout the figures unless otherwise specified. Box plots are presented as the median with the lower and upper hinges corresponding to the first and third quartiles. The upper whisker extends from the hinge to the largest value at most 1.5*IQR from the hinge. The lower whisker extends from the hinge to the smallest value at most 1.5*IQR from the hinge. Data beyond the end of the whiskers are considered outliers and plotted individually. Statistical comparisons are as noted in figure legends. $*p < 0.05$ $**p < 0.01$ $***p < 0.001$ $****p < 0.0001$.

All other analysis was done in R/Bioconductor. Heatmaps were visualized using pheatmap, and boxplots were visualized using ggplot2.

Metabolomics analysis

To preprocess the data, metabolites that had missing values for more than 30% of the samples were filtered out, missing values were imputed with half of the minimum of the metabolite's intensity. All metabolite intensities were $\log_2$ transformed and samples were mean-centered. For

differential abundance (DA) analysis, only annotated peaks were selected, and a student t-test was performed (function: t.test) with either equal or unequal variances based on the results of an F test comparing variances (function: var.test). The p-values were then adjusted for multiple comparisons using Benjamini & Hochberg correction to calculate an FDR for each metabolite. Metabolites were selected as being DA if the FDR < 0.1 for at least one comparison (Scr vs. shRNA#1 or Scr vs. shRNA #2) and the $\log_2$ fold-change was in the same direction for both comparisons.

Abundances of different lipid groups were calculated by summing mean-normalized abundances of all lipids of class followed by calculating the $\log_2$ fold change relative to Scr samples. Statistics were performed using Graphpad Prism.

Bulk RNA sequencing analysis

Reads were aligned to the mm10 mouse genome using STAR aligner. RSEM v1.3.0 was used to estimate gene expression. FastQC was used to evaluate the quality of raw reads. Differential expression (DE) of individual genes was carried out using DESeq2 (Love et al., 2014) to compare Scr vs. shRNA#1 and Scr vs. shRNA#2 and shRNA#1 vs. shRNA#2. For downstream analysis with metabolomics data, genes were considered to be differentially expressed if p-adj < 0.05 for either comparison and non-significant between shRNA#1 and shRNA#2. For gene set enrichment analysis (GSEA), DE using DESeq2 was using to compare Scr to all other samples.

GSEA was carried out with the fgsea R package using KEGG pathways (http://software.broadinstitute.org/gsea/msigdb/collections.jsp). The rank list was generated from the DE analysis by calculating -log10(p-value)*SIGN(log2fc) for each gene.

Metabolomics-Transcriptomics integration using Human Metabolome Database (HMDB)

The human metabolome database for metabolites was downloaded as an .xml file (http://www.hmdb.ca/downloads). The XML R-package was used to read in the data

(xmlTreeParse). Metabolite accession numbers, names, and protein associations were extracted. DA metabolites and DE genes were determined as described above. DA metabolites were filtered for those with an annotated HMDB ID, and DE genes were filtered for those within the database. The HMDB metabolite-protein associations were used to determine associations between DA metabolites and DE genes. Using the pheatmap function, hierarchical clustering was performed on DE genes based on overlap of mapped metabolites.

Single nuclei sequencing analysis

Preprocessing of 10x droplet based sequencing output:

We used the Cellranger toolkit (v2.1.1) to perform de-multiplexing using the "cellranger mkfastq" command, and the "cellranger count" command for alignment to the mouse pre-mRNA transcriptome, cell barcode partitioning, collapsing unique molecular identifier (UMI) to transcripts, and gene-level quantification. We filtered genes to only include genes with expression in at least 5 cells. We filtered cells to only include cells expressing a minimum of 200 genes and a maximum of 4000 genes. Further, the percentage of reads mapping to mitochondrial genes was capped at 5%.

Unsupervised clustering and dimensionality reduction:

The default settings in the Seurat R package (Butler et al., 2018) (v2.3) were used for normalization (NormalizeData) of the gene expression counts and identifying highly variable genes (FindVariableGenes). Unwanted variation due to number of Genes was removed and default settings were used for scaling and centering using the highly variable genes (ScaleData). Dimensionality reduction was performed using Principal Component Analyses (RunPCA) on the highly variable genes computed previously. To distinguish principal components (PCs) for further analysis, we used the PCElbowPlot() function. We found 30 components to capture variance. We identified molecularly distinct clusters using the default parameters (FindClusters) and a

resolution of 0.4. We computed an embedding of the data in 2-D space using t-distributed stochastic neighbor embedding (tSNE) in the PC space for visualization (RunTSNE), independent of the clustering step.

Assignment of cell-identity

Cluster-enriched or marker genes were computed using the Wilcoxon-Rank sum test (FindAllMarkers) for differential expression of genes in the cluster cells vs all other cells, filtering for cells with a log2FC > 0.25. Cluster identities were assigned by comparing data-driven genes with a list of literature-curated genes for mature kidney cell types. For the Dock10/Vcam1+ cluster GSEA, a single list of enrichment of all genes was calculated with the default parameters with the exception that logfc.threshold was set to 0 (FindMarkers). A small podocyte cluster (94 cells) was identified by strong co-expression of canonical markers (Synpo, Nphs1, Wt1). Given the small number of podocytes retrieved by sNuc-Seq, glomerular enrichment prior to single cell transcriptomic profiling may be used in the future to increase podocyte numbers.

Differential gene expression analysis

To analyze differential expression between CTRL and KDKD samples, we performed pair-wise differential expression analysis in Seurat (FindMarkers) with default parameters.

Gene set enrichment analysis

GSEA was carried out as described above. For the Dock10/Vcam1+ and podocyte analyses, the gene lists were generated as described above. The leading-edge genes were extracted for each pathway and hierarchical clustering (hclust) was performed on the pathways based on the overlap of their leading-edge genes. K-means clustering (k=3) was performed on the resulting dendrogram (cutree) to generate pathway clusters, and a list of the most highly represented leading-edge genes in each cluster was generated.

Gene signatures

For cell cycling gene signatures, S-phase and G2M gene lists were taken from Tirosh *et. al*,(Tirosh et al., 2016) and a gene signature score was calculated for each cell (CellCycleScoring). For the PUFA gene signatures, up- and down-regulated genes were taken from a bulk RNAseq screen in Min6 cells treated with 65 biologically-relevant fatty acids (data not shown). The genes come from pathways up- and down-regulated specifically in PUFAs. A gene signature score was calculated for each cell (AddModuleScore). To determine statistically significant shifts in gene signature score, a Wilcoxon Rank Sum test was run with a one-tailed alternative hypothesis for the expected increased and decreased gene signature shift for PUFA.up and PUFA.down, respectively.

Contributions

Eriene-Heidi Sidhom and Anna Greka designed the study, interpreted the results, and wrote the manuscript. E-H.S. performed all experiments and computational analysis unless otherwise noted. Maria Alimova assisted with high content imaging. Julian Avila-Pacheco assisted with design of metabolomics experiments and acquired metabolomics data. Katherine Vernon assisted with single nuclei isolation and interpretation of single cell results. Jamie Marshall assisted with sequencing of single nuclei RNA libraries and performed *in situ* Hybridization Chain Reaction along with Elizabeth Grinkevich. Mice were provided by Catarina Quinzii and Giulio Kleiner. Estefanía Reyes-Bricio assisted with immunofluorescence validation of single nuclei analysis. Astrid Weins performed and analyzed histology of animals.

Also, we would like to thank Lan Nguyen assisted with single cell library preparation and the lab of Vamsi Mootha for assistance with and access to their Seahorse Flux Analyzer.

This work was funded by NIH grants DK095045, DK099465 (A.G.) and F30DK112477 (E-H.S) and an NDSEG fellowship (E-H.S.).

A.G. has a financial interest in Goldfinch Biopharma, which was reviewed and is managed by Brigham and Women's Hospital and Partners HealthCare and the Broad Institute of MIT and Harvard in accordance with their conflict of interest policies.

Chapter 3:

Kidney organoid reproducibility across multiple human iPSC lines and diminished off target cells after transplantation revealed by single cell transcriptomics

This chapter represents a manuscript available on *bioRxiv:*

A. Subramanian*, E.-H. Sidhom*, M. Emani*, N. Sahakian, K. Vernon, Y. Zhou, M. Kost-Alimova, A. Weins, M. Slyper, J. Waldman, D. Dionne, L. Nguyen, J. L. Marshall, O. Rozenblatt-Rosen, A. Regev, A. Greka, Kidney organoid reproducibility across multiple human iPSC lines and diminished off target cells after transplantation revealed by single cell transcriptomics, bioRxiv, 516807 (2019).

*These authors contributed equally.

Abstract

Human iPSC-derived kidney organoids have the potential to revolutionize discovery, but assessing their consistency and reproducibility across iPSC lines, and reducing the generation of off-target cells remain an open challenge. Here, we used single cell RNA-Seq (scRNA-Seq) to profile 415,775 cells to show that organoid composition and development are comparable to human fetal and adult kidneys. Although cell classes were largely reproducible across iPSC lines, time points, protocols, and replicates, cell proportions were variable between different iPSC lines. Off-target cell proportions were the most variable. Prolonged *in vitro* culture did not alter cell types, but organoid transplantation under the mouse kidney capsule diminished off-target cells. Our work shows how scRNA-seq can help score organoids for reproducibility, faithfulness and quality, that kidney organoids derived from different iPSC lines are comparable surrogates for human kidney, and that transplantation enhances their formation by diminishing off-target cells.

Introduction

Kidney diseases affect ~800 million people worldwide (Coresh et al., 2007). Despite the enormous disease burden, therapeutic innovation has lagged (Inrig et al., 2014), owing in part to the lack of appropriate models that reflect the cellular complexity of the human kidney. Technologies to generate kidney organoids from human induced pluripotent stem cells (iPSC) (Cruz et al., 2017; Forbes et al., 2018; Freedman et al., 2015; Morizane and Bonventre, 2017b; Morizane et al., 2015; Przepiorski et al., 2018; Taguchi and Nishinakamura, 2017; Taguchi et al., 2014; Takasato et al., 2015, 2016; Tanigawa et al., 2018) provide a promising avenue to further help advance our understanding of disease mechanisms and expedite therapeutic development.

To harness the full potential of iPSC derived kidney organoid technology, we must address critical unsolved questions about their reproducibility, faithfulness, and quality. First, we must establish organoid reproducibility: the comparability and range of variability in cellular composition and state between different iPSC lines from normal individuals across replicates and protocols (building on previous efforts to draw comparisons between iPSC and embryonic stem cell (ESC) derived organoids (Wu et al., 2018) or bulk RNASeq data comparing iPSC derived organoids (Phipson et al., 2019)). This is critically important, because individual patient iPSCs offer significant advantages over ESCs for precision medicine and drug development projects (Boreström et al., 2018; Burrows et al., 2016; Takasato et al., 2016). Second, we must define their faithfulness: how well organoids across many iPSC lines recapitulate kidney development and disease-associated genes at single cell resolution. Third, we need to define their quality. Since off-target cells interfere with organoid quality, we must understand how to drive their removal to more faithfully reproduce the human kidney (Wu et al., 2018).

Here, we address these critical questions by combining scRNA-Seq analysis of cellular composition with immunofluorescence validation to build a comprehensive atlas of human kidney

organoids across iPSC lines, replicates, differentiation protocols, and developmental time, and after organoid transplantation into mouse.

Result

A ~400K single cell census from 47 kidney organoid states derived from 4 human iPSC lines

To compare organoids at single cell resolution, we generated them according to two protocols, from each of four different human iPSC lines generated by different methods (episomal or Sendai virus; **Fig. S2.1A**), and at multiple time points along differentiation, and profiled them by droplet-based scRNA-seq (**Fig. 3.1A**). First, we used the ML protocol (Takasato et al., 2016) and generated organoids from each of two commercial lines (Thermo Fisher (ThF, female) and Alstem (AS, male)), and two obtained from human healthy donors (N1, female and N2, male) (**Fig. S2.1A**). We profiled single cells at the day 0 (D0) iPSC state, at two critical milestones, day 7 (D7; immediately prior to cells being plated for 3D self-organization and nephrogenesis), and day 15 (D15; when growth factor treatment ends), and finally, at day 29 (D29) when the organoids are mature. This allowed us to assess the reproducibility within a protocol and the impact of cell-line-specific differences in iPSC pluripotency and/or subsequent differentiation. Second, we generated kidney organoids using the JB protocol (Morizane and Bonventre, 2017b) from ThF iPSCs at D29 (**Fig. 3.1A**). To account for technical variability, we sequenced single cells from three different iPSC replicates (D15, D29, all lines) as well as an additional, independent passage (AS line at D7, D15, D29 and ThF at D7). We successfully profiled 382,465 single cells from organoids across all four iPSC lines (**Fig. 3.1B, S2.1B**) and compared them to 3,417 cells profiled from the unaffected kidney portion of a tumor nephrectomy from an adult male (with no known kidney diseases) (**Fig. 3.1C**). We determined the cellular composition of organoids using unsupervised graph-based clustering followed by *post-hoc* annotation (**Methods**) with signatures of cell types (**Fig. S2.2**, **Table S2.1**) and cell cycle genes (Kowalczyk et al., 2015).

Figure 3.1. Mature kidney organoids from four different human iPSC lines contain most major nephron cell classes. A. Schematic of differentiation protocols for kidney organoids derived from human iPSCs by the Bonventre (JB) and Little (ML) protocols. Single-cell sequencing time-points as shown. **B.** Table summarizing single cells profiled across four different human iPSC cell lines (AS, N1, N2, ThF) using two different protocols (ML, JB) across four time points (iPSC, Day 7 (D7), 15 (D15) and 29 (D29)). Replicates are indicated in parentheses. **C.** t-SNE plot of composite single cell transcriptomic profiles from all 4 iPSC D29 kidney organoids (left) and human adult kidney (right). Cluster color annotations as shown. **D.** (left) Violin plots showing expression of canonical adult human kidney markers used to identify nephron clusters in D29 organoids: podocyte (*NPHS2*), proximal tubule (PT; *LRP2*), thick ascending limb/distal nephron (TAL; *SLC12A1*) and immature distal nephron (*GATA3*+ DT). Mesenchymal and off-target cells were also detected. (right) Violin plots of data-derived tubular markers revealed *APOE* proximal to distal gradient of expression, proximal marker *SPP1*, and distal markers *WFDC2* and *MAL*. **(E-G)** Random forest classifier trained on D29 ML_ThF organoid gene expression profiles accurately predicted respective nephron cell classes in human **E.** first and **F.** second trimester fetal kidney as compared to adult kidney **G..** The Y-axis labels in each panel represents the assigned cell class in each human sample. The X-axis labels are cell classes at D29 (ML_ThF organoids). The size and intensity of the red dot represents the % of cells in the Y-axis cell-types classified as the corresponding X-axis cell-class, e.g., all human adult podocytes are correctly classified as podocytes, while distal convoluted tubule (DCT) is predicted to be most similar to the *GATA3*+ DT organoid cell class.

Figure 3.1 (Continued).

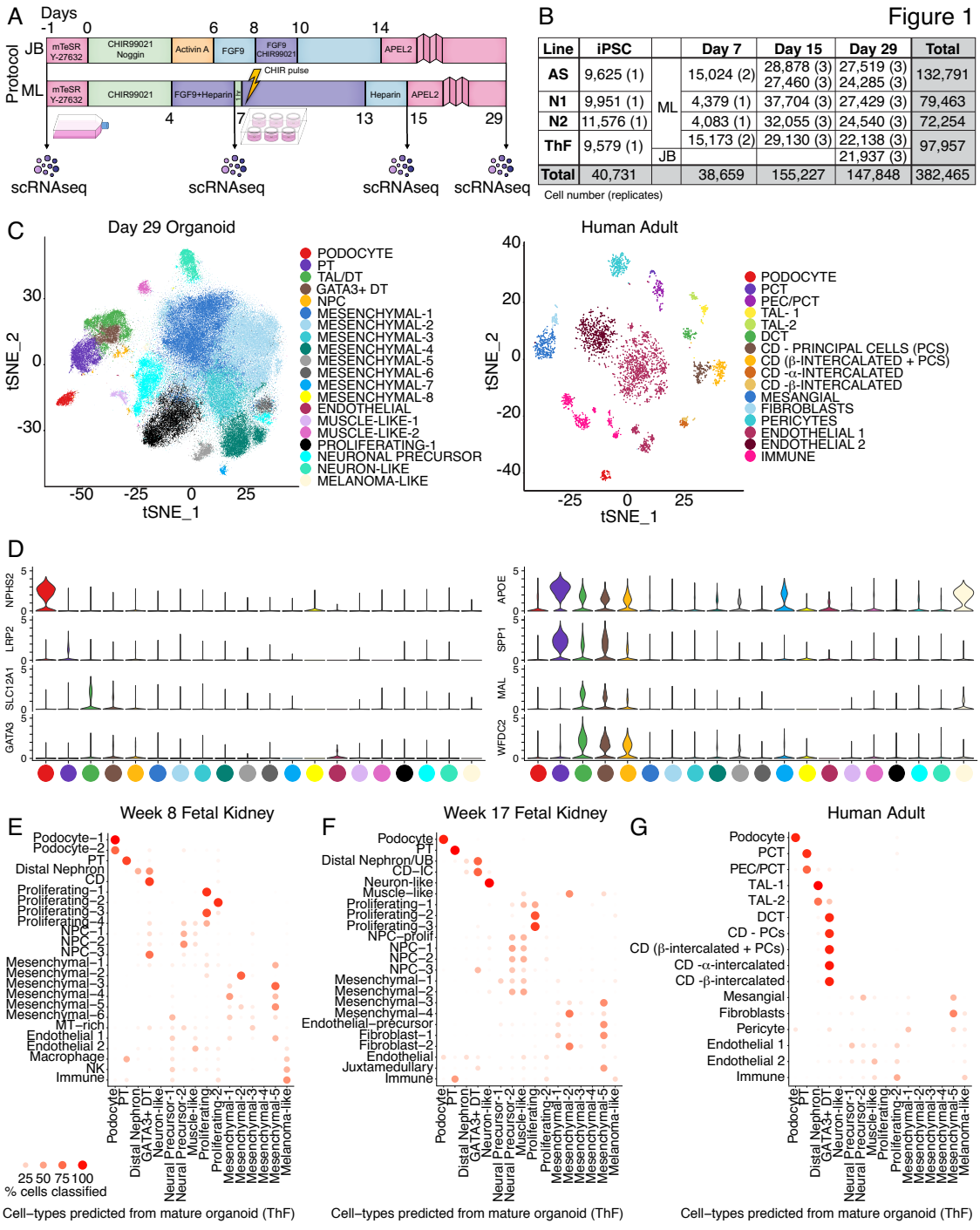

Line	iPSC		Day 7	Day 15	Day 29	Total
AS	9,625 (1)	ML	15,024 (2)	28,878 (3) 27,460 (3)	27,519 (3) 24,285 (3)	132,791
N1	9,951 (1)	ML	4,379 (1)	37,704 (3)	27,429 (3)	79,463
N2	11,576 (1)	ML	4,083 (1)	32,055 (3)	24,540 (3)	72,254
ThF	9,579 (1)	ML	15,173 (2)	29,130 (3)	22,138 (3)	97,957
		JB			21,937 (3)	
Total	40,731		38,659	155,227	147,848	382,465

Mature organoids from all iPSC lines contain predominant nephron cell classes

D29 organoids from all 4 iPSC lines contained cells representative of segments of a developing nephron (**Fig. 3.1C,D, S2.2)**: podocytes (*NPHS2*, podocin; *NPHS1*, nephrin; *SYNPO*, synaptopodin; *WT1*, Wilms Tumor 1), proximal tubular (PT) cells (*LRP2*, megalin), thick ascending limb (TAL; *SLC12A1*, Na-K-Cl cotransporter), and distal nephron cells (*CDH1*, E-cadherin; *AQP2*, aquaporin 2; *GATA3*). There was no cluster enriched for *SLC12A3* (Na-Cl symporter; **Fig. S2.2**), a canonical marker of the distal convoluted tubule (DCT). The organoid single cell profiles retained the proximal (podocyte) to distal axis of the human nephron (**Fig. 3.1C**, left) on visualization of the data using t-distributed Stochastic Nonlinear Embedding (tSNE), unlike the discrete clusters seen in adult kidney (**Fig. 3.1C**, right). We identified data-derived markers (**Table S2.2**), including osteopontin (*SPP1*) (Xie et al., 2001) in the proximal tubular cell cluster, and *WFDC2* (LeBleu et al., 2013) and *MAL* (Carmosino et al., 2010) in the distal nephron cluster (**Fig. 3.1D, S2.3A**), in line with single cell RNA-Seq studies of human adult and fetal kidney (Lindström et al., 2018a). In all 4 iPSC lines, we observed a novel proximal to distal tubular gradient of *APOE* (a gene associated with diabetic kidney disease (Araki, 2014))(**Fig. 3.1D**). Thus, D29 organoids reproducibly developed podocytes, proximal tubular cells, and cells consistent with the loop of Henle and distal nephron (but without a defined distal convoluted tubule (DCT) or collecting duct (CD) segment as seen in adult kidney).

D29 organoids also contained Nephron Progenitor Cells (NPC) enriched in *PAX2*, *LHX1* and *PAX8* (top cluster-specific differentially expressed (DE) genes). The majority of the organoid single cells (70% on average) were mesenchymal (**Fig. 3.1C**), grouped in 8 subsets (Mesenchymal 1-8) enriched for markers of progenitor and differentiating cell types (**Fig.3.1C, S2.2**). Prominent non-kidney off-target populations (Wu et al., 2018), absent in adult human kidney (**Fig. 3.1C, S2.2**), were found in D29 organoids, including melanoma-like cells (*PMEL*), *SOX2*-positive(+) neuronal precursors, *STMN2*+ neuron-like cells, and *MYOG*+ muscle-like cells,

as reported previously (Phipson et al., 2019; Wu et al., 2018). A rare population of endothelial cells was also observed (**Fig. 3.1C, S2.2**).

Mature organoids most closely resemble fetal kidney

We related the cell clusters from D29 human kidney organoids (ThF line) to human tissue by comparing them to fetal kidney from the first (8 weeks) and second (17 weeks) trimesters (Lindström et al., 2018b; Young et al., 2018), and to adult kidney (**Fig. 3.1C**, right). We used a classification based approach (random forest classifier) (Pandey et al., 2018) to assess the relation between each cell cluster in these tissues to each organoid cluster (**Fig. 3.1E-G, Methods**).

Overall, cells were most similar to those from first and second trimester fetal kidneys, largely consistent with previous studies using bulk RNA-Seq data (Takasato et al., 2015). All nephron lineages were accurately classified by the algorithm (**Fig. 3.1E-G**). Compared to those in adult human kidney (**Fig. 3.1C**), all organoids contained cells of human nephron segments, but with poorly differentiated distal tubular cells. In contrast, in the adult kidney, we identified distinct proximal, loop of Henle, DCT and CD sub-clusters, including principal cells (PC) and α- and β-intercalated cells (IC), as well as endothelial and immune cells (**Fig. 3.1C**, **S2.3B**).

Interestingly, some of the mesenchymal cell types in kidney organoids were predictive of cell types in fetal and adult kidney, suggesting that these are on-target mesenchymal cells. Fetal kidney cell types (mesenchymal, endothelial, and fibroblasts) were classified to mesenchymal-1, -2, and -5 clusters in organoids (**Fig. 3.1E,F, Table S2.2**), while mesangial cells, fibroblasts, and pericytes in adult kidney were classified to mesenchymal-1 and -5 in organoids (**Fig. 3.1G**). Of interest, mesenchymal-2 cells in organoids were enriched for *MGP*, *GAS2*, *PRDX2* and *FOXP2* (Wang et al., 2018), known markers of fetal mesangial cells in the developing kidney. Similarly, mesenchymal-5 cells in organoids were enriched for fetal stromal genes *SULTIE1*, *DKK1* (Iglesias

et al., 2007), *NR2F1* (Schwab et al., 2003), *ID3*, *ZEB2*, *COL6A3* (Menon et al., 2018) and *DCN*. In contrast, mesenchymal types that did not map to human kidney cell types included genes associated with cartilage formation (Ohba et al., 2015) (*ACAN*, *SOX9*, *MATN4*, *LECT1*, *EPYC*, *COL9A3* and *COL9A1*) (**Fig. 3.1E,F**).

We validated cell type markers using immunofluorescence (IF) staining (**Fig. 3.2A-C**, **S2.4, S2.5A**). Markers for podocyte (WT1), proximal tubule (LTL) and distal nephron (CDH1) were detected across all lines and protocols, although expression of GATA3, a marker of the developing ureteric bud, could only be detected in N2 and ThF (Lee et al., 2015; Takasato et al., 2016) (**Fig. 3.2C**). We also validated the markers used to annotate specific cell clusters: NPHS1(Greka and Mundel, 2012) (podocyte cluster), co-localized with the podocyte-specific marker synaptopodin (SYNPO) (Mundel et al., 1997) (**Fig. 3.2D**); LRP2 (Christensen and Birn, 2002) (proximal tubule cluster), co-localized with LTL, a lectin specific to the proximal tubule (**Fig. 3.2E**); CDH1 (Prozialeck et al., 2004) (distal tubular compartment) marked tubules distinctly from proximal LRP2/LTL positive tubular structures (**Fig. 3.2E**). We also validated MEIS1, a gene enriched in kidney mesenchymal cells, by IF staining, where it was shown to localize appropriately to the interstitium, defined as the cellular space outside laminin positive basement membrane structures (LAMA1) (**Fig. 3.2F**).

Cell proportions vary depending on iPSC line

Cell type proportions in mature D29 organoids were consistent between replicates of independent clones, but they varied between iPSC lines (**Fig. 3.3A, B**). We quantified the differences in cell proportions by computing the Jenson-Shannon Divergence (Yi-Rong Peng, Karthik Shekhar, Wenjun Yan, Dustin Herrmann, Anna Sappington, Greg S. Bryman, Tavé van Zyl, Michael Tri. H. Do, 2018) (JSD, a measure of compositional difference between 2 frequency vectors with a value between 0 and 1, where smaller values mean more similar) within- and between- iPSC lines (**Fig. 3.3C**). Differences between lines (average JSD=0.18, sd = 0.13)

Figure 3.2. IF validation of markers derived from the single cell data in mature kidney organoids. A. IF staining of an entire kidney organoid with segment specific markers as shown. **B.** Schematic of kidney nephron with major cell types and canonical markers annotated. **C.** Immunofluorescence staining of D29 kidney organoids for podocyte (WT1), proximal tubule (LTL), and distal tubule (CDH1 and GATA3) across two protocols (JB, ML) and four cell lines (AS, N1, N2, ThF). IF staining for validation of markers identified in the single cell data: **D.** NPHS1 co-localized with the podocyte-specific marker SYNPO and **E.** LRP2 co-localized with the proximal tubular marker LTL (bottom). **F.** IF staining validation for MEIS1-positive mesenchymal cells in D29 organoids. LAMA1 indicates basement membranes. MEIS1 staining of mesenchymal cells appropriately surrounds LAMA1-defined tubular nephron structures.

Figure 3.2 (Continued).

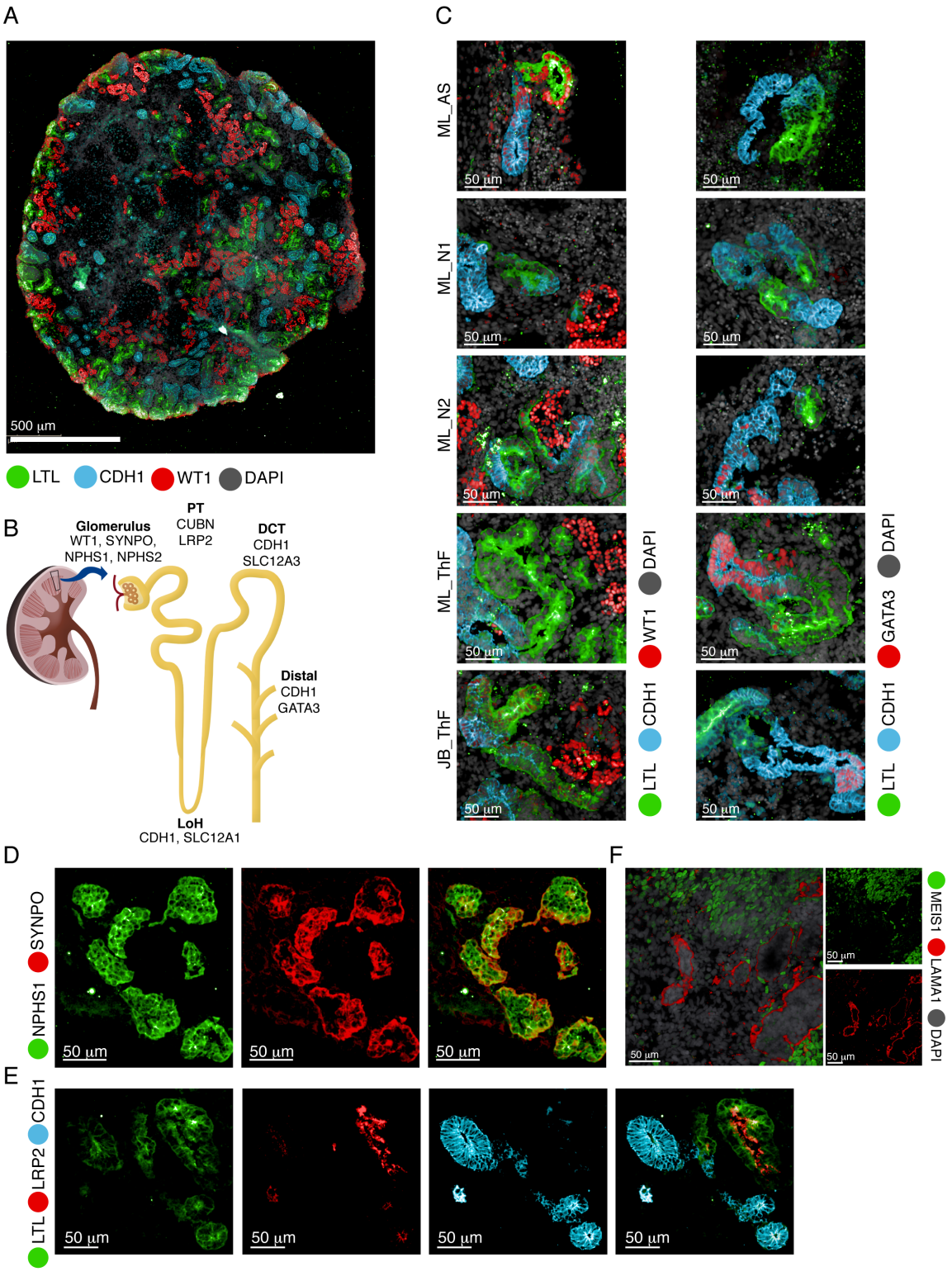

Figure 3.3. Variability in cell type proportions detected by scRNA-Seq at D15. (A, B) Relative proportions of endothelial, nephron, mesenchymal and off-target cell clusters across all replicates of D29 organoids. Annotations as shown. **(C, D)** Comparison of cell-type composition between D29 organoids as determined by boxplots of the Jenson-Shannon Divergence (JSD) method. Each point on the plot is a pair-wise (color) measure of JSD between 2 organoids. Legend indicates annotation for pairs of iPSC lines. **C.** Organoid compositional differences are greater between lines than between different protocols for the same line or between replicates of the same line and protocol (within lines). **D.** Organoid compositional heterogeneity is greatest in the off-target compartment followed by the mesenchyme and the nephron compartment in all three comparison groups (between lines, between protocols and within lines). t-SNE plot of single cells from **E.** iPSC, **F.** D7, and **G.** D15 of the organoid differentiation protocol. **H.** Comparison of relative cell type proportion across iPSC lines of cell clusters shown in **(E-G)**. **I.** Compartment specific cell-type proportions at D15 across all lines and replicates. **J.** Compositional differences are greatest between lines at D15 and the least at D7.

Figure 3.3 (Continued).

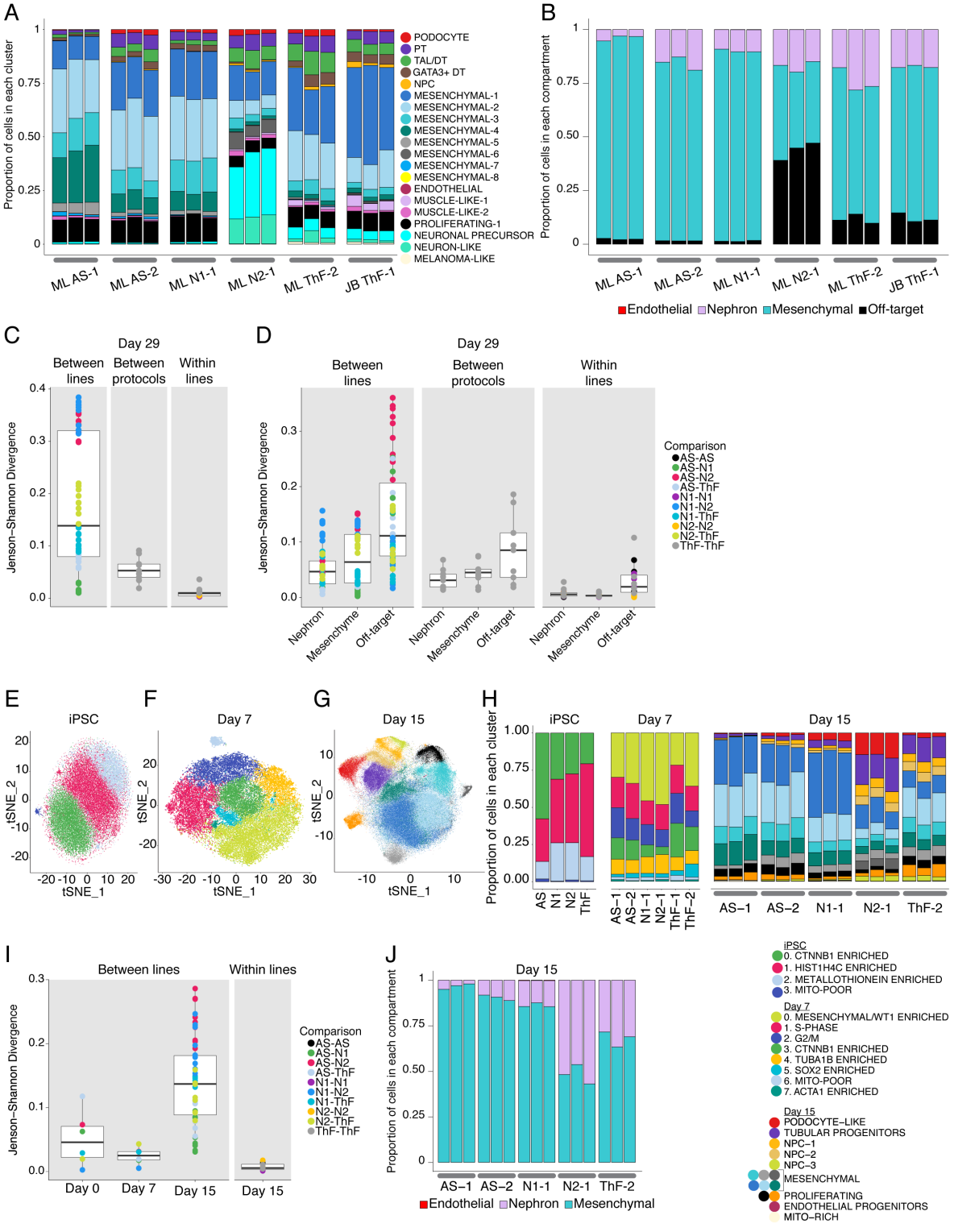

superseded differences between independent clones within the same line (average JSD 0.01, sd 0.01), and between different protocols for the same line (average JSD= 0.06, sd=0.02) (Fig. 3C). N2 was most different (divergent) from both AS and N1 iPSCs that were the most similar. For example, podocytes were captured across all experimental conditions (**Fig. 3.3A, S2.5B**), but varied between 1.33% (N1, averaged across replicates) to 2.58% (ThF) between lines on the ML protocol. AS, passage 1 (AS-1) was an outlier, with lower overall nephron numbers (0.3%). The JB protocol captured an average of 0.81% podocytes. Similarly, the distal nephron compartment (including TAL and *GATA3*+ distal nephron cells) ranged in average proportion from 2.34% (N1) to 6.95% (ThF), with an average 1.45-fold-change between protocols. In general, N1 organoids had the lowest average nephron cell proportions, followed by AS, N2 and ThF. *GATA3*+ distal-like cells were more abundant in ThF iPSCs, independent of protocol; GATA3 expression in AS and N1 was lower than in ThF and N2 (**Fig. S2.2**), as confirmed by IF (**Fig. 3.2C**).

To make higher level comparisons, we looked at 4 groups: nephron, mesenchymal, off-target and endothelial compartments (**Fig. 3.3B, Table S2.3**). The nephron compartment was on average 16.7%, of all cells (9.89% in N1 to 24.1% in ThF). The N1 line had the largest average relative proportion of endothelial cells (0.1%), with a global average of 0.05% across all lines. Mesenchymal cells were 82.8% of all cells in AS and 88.6% in N1 organoids, but only 64.2% in ThF and 39.2% in N2. Off-target cells varied markedly by iPSC line, from 1.6% in AS-1 and N1 to 43.7% in N2 (**Fig. 3.3B**). To determine variability within each compartment, we again computed the JSD (**Fig. 3.3D**). The nephron and mesenchymal compartments were consistent (nephron mean JSD between lines = 0.05, sd = 0.038; mesenchymal mean JSD = 0.07, sd = 0.05), whereas the off-target compartment was variable between lines (mean JSD = 0.14, SD = 0.09) and protocols (**Fig. 3.3D**). N2 organoids were most divergent from AS in off-target composition. Notably, the ratio of mesenchymal to nephron cells was inversely related (Spearman correlation ρ = -0.84) to the proportion of off-target cells. Higher proportion of off-targets (N2, ThF:11.7%, JB,

ThF: 12.2%) resulted in lower mesenchymal:nephron ratios (N2: 2.29, ThF: 2.66, JB ThF: 4.05) and vice-versa (Off-targets – N1, AS:1.59%; mesenchymal:nephron – N1: 8.96, AS: 5.31). In contrast, the mesenchyme proportions were lower in both adult and fetal kidney, both overall (15.7% in adult, 19.7% in fetal week 17) and relative to nephron cells (0.65 in adult, 0.47 in fetal). In summary, we noticed greater organoid heterogeneity between iPSC lines than between replicates within a line, or between protocols, with the off-target compartment contributing the most variability.

Variability in cell type proportions detected by scRNA Seq in D15 organoids

To explore whether the iPSC-line associated differences were associated with their basal state(Burrows et al., 2016; Féraud et al., 2016) at D0 or the process of differentiation, we compared the single cell profiles collected at D0,7, and 15 for each organoid culture.

Analysis of 42,433 single cells from the 4 undifferentiated iPSC lines at D0 (**Fig. 3.3E,H** and **Fig. S2.6A**), showed they were comparably pluripotent. To determine if there were clusters of cells primed towards a particular developmental germ layer, we scored organoids using known transcriptional signatures for the three germ layers. We did not observe sub-clusters with signatures for any specific germ layer (Tsankov et al., 2015), or primed for differentiation(Nguyen et al., 2018) (**Fig. S2.7A**). The four cell clusters had representation from each of the iPSC lines (avg JSD = 0.05, sd = 0.04, **Fig. 3.3H,I**), and from all cell-cycle phases (**Fig. S2.7B**).

Similarly, at D7, developing organoids from all iPSC lines expressed appropriate markers of mesodermal differentiation with actively proliferating cells (Kowalczyk et al., 2015) (**Fig. S2.7C, D**) and little variability between lines (**Fig. 3.3F,H**). Differences in proportions were small (avg JSD=0.02, sd=0.01, **Fig. 3.3I**). Notably, clusters 3, 5 and 0 appropriately expressed *CTNNB1* and *SOX11*, *SOX2*, and *WT1*, respectively, genes upregulated during the differentiation of intermediate mesoderm (IM) into the metanephric mesenchyme (MM) or the ureteric bud (UB)

(Kreidberg et al., 1993; Little and McMahon, 2012; Little et al., 2016) (**Fig. S2.6B**). We did not observe nephron cell types in D7 organoids.

At D15, organoids had multiple subsets of nephron progenitor cells (NPC) and a distinct population of epithelial cells broadly expressing tubular progenitor markers (*PAX2*, *LHX1*; **Fig. S2.8A**). Across all iPSC lines, we observed early patterning of the nephron (reflected by expression of proximal (*CUBN*) and distal (*MAL*, *WFDC2*, *POU3F3*) markers; **Fig. S2.8A**), proliferating cell populations (*e.g.*, cells in the Mesenchymal-4 cluster expressed *CTNNB1*, *PTPRS*, *CDC42*, and *SOX11*, similar to *CTNNB1*-expressing cells in clusters in the iPSCs and D7 organoids; **Fig. S2.8A**), and a distinct subset of podocyte-like cells (**Fig. 3.3G,H, S2.8A**). In contrast to D7 and D0 (**Fig. 3.3I**), there were notable differences in composition between iPSC lines (avg JSD = 0.14, sd = 0.07; **Fig. 3.3G,H,I**). Heterogeneity in endothelial progenitors was consistent with D29: N1 had the highest average relative proportions (0.32% vs 0.05% among other lines; **Fig. 3.3J**). The proportion of nephron-like cells ranged from 0.08% in AS to 56.9% in N2 D15 organoids (**Fig. 3.3H,J**). Although, no distinct off-target cells were found at D15, N2 and ThF organoids had a small population of cells expressing the neuronal progenitor *SOX2* within the mesenchymal compartment (**Fig. S2.8B**). The mesenchyme:nephron ratios were also lower in N2 and ThF D15 organoids (**Fig. 3.3J**). Hence, organoids with higher nephron proportions at D15 had a distinct pool of *SOX2*+ cells, and went on to develop a higher proportion of off-target cells at D29, associated in turn with lower D29 mesenchyme:nephron ratios (**Fig. 3.3B,J**). Taken together, variability in organoid differentiation was evident by D15.

Concordant expression of developmental programs across organoids from 4 human iPSC lines

Next, we tested whether known transcription factors (TFs) and critical genes involved in nephrogenesis (Little and McMahon, 2012; Little et al., 2016) are appropriately expressed in the respective clusters in organoids from 4 different iPSC lines, compared to adult kidney (**Fig. 3.4A,**

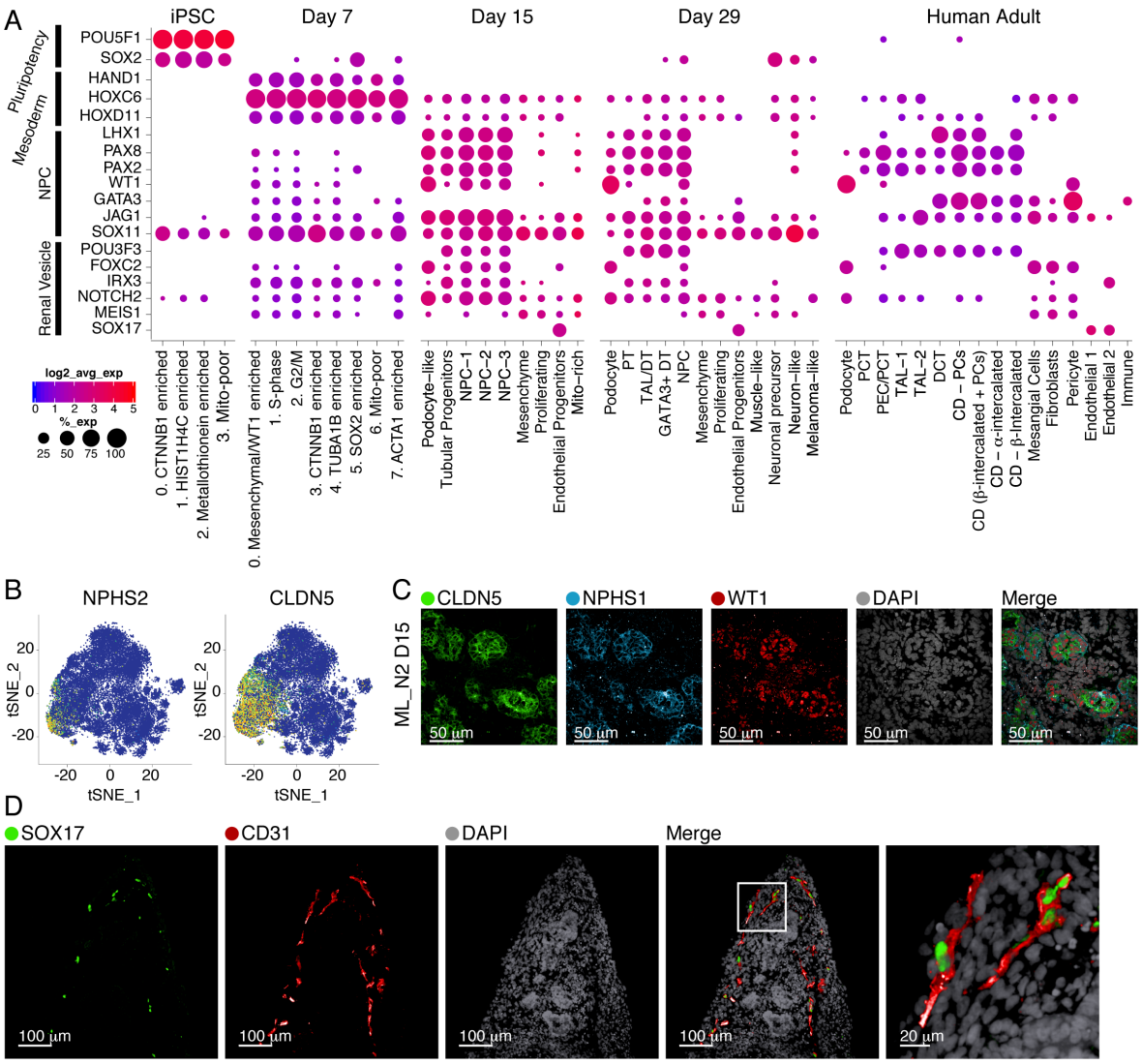

Figure 3.4. Concordant expression of developmental programs across organoids from 4 human iPSC lines. A. Dot plot comparison of expression patterns for major nephrogenesis markers across organoid differentiation time points (iPSC, D7, D15, and D29, averaged across four cell lines, ML protocol) and human adult kidney. The size of the dot represents the proportion of cells in the cluster that express the gene. Dots are shown only when the gene is expressed in at least 5% of the cells in the respective cluster. **B.** Canonical (NPHS2) and data-derived (CLDN5) podocyte marker genes superimposed in tSNE plots from D15 organoids (N2 line, ML protocol). **C.** IF staining of D15 kidney organoid (N2 line, ML protocol) for CLDN5 as a marker of early podocyte differentiation derived from the single cell data. Additional canonical podocyte markers (NPHS1, WT1) and DAPI staining as shown. **D.** IF staining of D29 kidney organoid (AS line, ML protocol) for SOX17 and CD31, markers of endothelial cells.

S2.9, S2.10). Overall, key developmental programs were expressed at expected time points and transitions, in a comparable manner across different iPSC-derived organoids (**Fig. 3.4A**, **S2.9, S2.10**). First, core pluripotency TFs were expressed during the iPSC stage and decreased subsequently (D7-D29). Notably, *SOX2*, a neuronal progenitor marker (Graham et al., 2003), re-appeared in D29 organoids in off-target neuron cells (**Fig. 3.4A**). Next, at D7, prior to the CHIR pulse (**Fig. 3.1A**), cells across all clusters had high expression of markers of mesoderm development, such as *HAND1* (Poh et al., 2014) and *HOX11* genes (Wellik et al., 2002). With organoid self-assembly between D7 and D15, IM inducing genes from D7 were downregulated in D15, while nephron progenitor genes were upregulated in a nephron-specific pattern: *JAG1*, *LHX1*, *PAX2*, *PAX8* in the epithelial clusters and WT1 in the nephron progenitor population and podocyte-like cells (**Fig. 3.4A**). At D15 we first observed a *SOX17*-positive endothelial progenitor cell population that persisted in D29 (**Fig. 3.4A, S2.9C**). Nephron patterning became more evident at D29: *FOXC2* and *WT1* were prominent in podocytes, whereas *IRX3* and *POU3F3* had a distinct distal pattern (**Fig. 3.4A**, **S2.10**). Developmental programs were comparable across all iPSC lines (**Fig. S2.9, S2.10**).

Of several data-derived markers enriched in the podocyte population at D15 (*CTGF*, *CLDN5*, *SOST*, *SPARC*; **Fig. 3.4B, S2.8C**), we validated CLDN5 (claudin 5, an integral membrane protein controlling tight junctions (Yuan et al., 2012) in many cells including podocytes (He et al., 2007b)) in nephrin- (NPHS1) and WT1-positive podocytes of D15 organoids (**Fig. 3.4C**). To validate the endothelial precursors identified in our analysis of D15 organoids, we stained for SOX17 (localized to endothelial cell nuclei) and showed that it co-localized with CD31, a classical endothelial marker (**Fig. 3.4D**).

Genes associated with kidney diseases are expressed in expected compartments across organoids from 4 human iPSC lines

To assess the applicability of kidney organoids from different iPSC lines for the study of genetic kidney diseases (Cruz et al., 2017; Forbes et al., 2018; Tanigawa et al., 2018), we determined the expression of genes causing congenital anomalies of the kidney and urinary tract (CAKUT), hereditary renal cystic (HRC) diseases and hereditary tumor syndromes (Brown et al., 2014; Hildebrandt, 2010; Vivante and Hildebrandt, 2016; Warejko et al., 2018) (**Fig. 3.5A,B, S2.11, S2.12**), as well as genes from Genome Wide Association Studies (GWAS) of chronic kidney disease (CKD) (Pattaro et al., 2016) (**Fig. S2.13**) and mendelian glomerular diseases (Ashraf et al., 2018) (**Fig. S2.14**).

Organoids from all lines reproducibly expressed the majority of genes associated with progressive kidney diseases (including adult onset diseases) in at least one compartment. Genes associated with embryonic and early childhood abnormalities (CAKUT and HRC) were broadly expressed in developing organoids from all iPSC lines as early as D7 (i.e. *CHD1L* (Brockschmidt et al., 2012) at D7). Appropriately, developmental genes enriched in organoids were absent in adult kidney (i.e. *RET*, *HPSE2*). Some genes achieved high levels of expression and cell-type specificity in mature organoids, in a pattern similar to adult kidney. For example, *PTPRO* (from CKD GWAS and monogenic glomerular diseases) was appropriately expressed in D29 and adult human podocytes (Wharram et al., 2000) (**Fig. S2.13, S2.14**). Similarly, *PAX2* and *MUC1* (from CAKUT and cystic diseases, respectively) were highly expressed in D29 distal tubules, similar to their human adult expression pattern (Leroy et al., 2002) (**Fig. 3.5A,B**,**S2.11,S2.12**). We validated these markers derived from scRNA-Seq analysis by IF staining, which confirmed the co-expression of *PAX2* and *MUC1* in CDH1+ distal tubular epithelial cells in mature organoid sections (**Fig. 3.5C**). In summary, kidney organoids from 4 different iPSC lines could serve as reasonably faithful surrogates of human kidney tissue for the study of a broad array of kidney diseases.

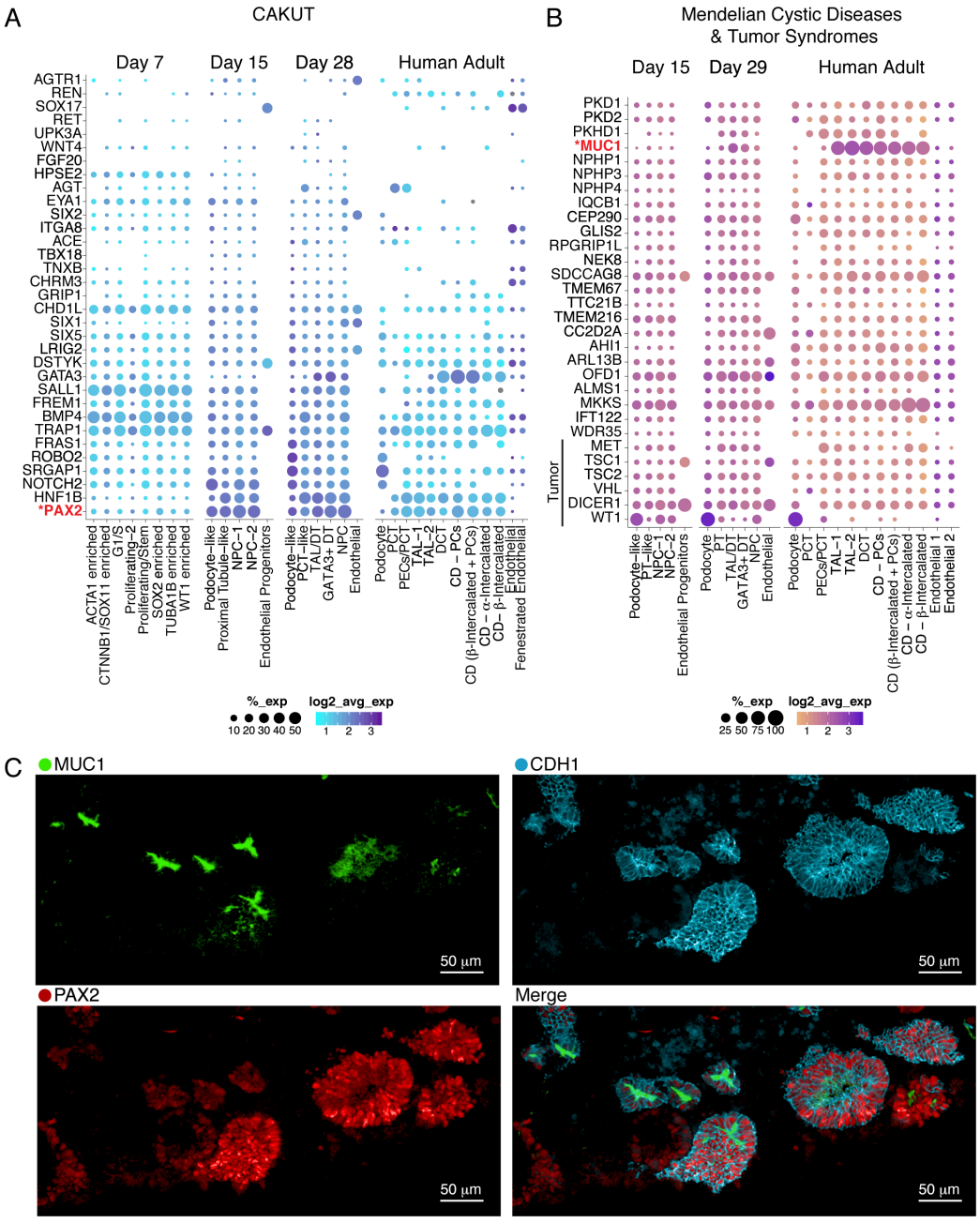

Figure 3.5. Genes associated with kidney diseases are expressed in expected compartments across organoids from 4 human iPSC lines. Dot plot comparison of cell type-specific gene expression (ThF line, ML protocol) in organoids and human adult kidney. Genes implicated in monogenic causes of **A.** congenital abnormalities of the kidney and urinary tract (CAKUT), and **B.** mendelian renal cystic diseases and tumor syndromes. **C.** IF staining validates the expression of MUC1 and PAX2 in the distal tubule in D29 kidney organoids. CDH1 serves a distal tubular marker. Note appropriate apical expression of MUC1 in distal tubular epithelial cells.

Organoid transplantation in mice diminishes off-target cells and enhances organoid quality and composition

We hypothesized that the reduction of off-target cells may improve organoid composition and overall quality. First, we determined that prolonged organoid culture *in vitro,* up to 51 days, did not reduce the portion of off-target cells, as assessed by scRNA-seq of organoids grown *in vitro* at day 32 (D32) and day 51 **(**D51) (**Fig. 3.6A,B, S2.15**). D32 and D51 organoids had most populations present in D29 organoids, including muscle, neuronal and melanoma off-target cell clusters. In particular, we noted 2 clusters of neuronal off-target cells at D29, D32 and D51: *STMN2*+ neuron-like cells (D29, D32) and *SOX2*+*NTRK2*+ neuronal-precursor cells (D29, D32, D51; **Fig. S2.2, S2.15B**).

Kidney development requires signaling from adjoining vasculature (Kitamoto et al., 1997), but endothelial cells were minimal in organoids grown *in vitro* (**Fig. 3.1C, 3.3A**). Organoid transplantation under the kidney capsule of immunodeficient mice allows mouse endothelial cells to infiltrate the transplanted kidney organoid and promote vascularization (Bantounas et al., 2018; van den Berg et al., 2018; Xinaris et al., 2012). We therefore hypothesized that organoid transplantation may improve organoid composition and reduce off-target cells.

To test our hypothesis, we transplanted D18 organoids (ThF line) under the mouse kidney capsule of immunodeficient mice, recovered them 14 days following transplantation ("D32 organoid transplants"), and profiled them by scRNA-Seq, along with D32 control organoids grown *in vitro* (**Fig. S2.16A-D**). We confirmed that transplanted human organoids were vascularized by mouse endothelial cells (Stan et al., 2012): IF showed mouse Plvap-positive endothelial cells apposed to human podocytes (NPHS1) (**Fig. 3.6C, Fig. S2.16B**). We distinguished the human from mouse cells by read alignment to the combined reference (**Methods**) and confirmed that the human nephron cells in D32 transplants (**Fig. S2.16D,E**) corresponded to D29 nephron clusters, with *VEGFA* and *ANGPT1* most highly expressed in podocytes (**Fig. 3.6D**). Correspondingly, the

Figure 3.6. Transplantation of human organoids into mouse diminishes off-target cells and improves organoid quality. t-SNE plots of organoids in prolonged *in vitro* culture reveal cell clusters in **A.** D32 and **B.** D51 organoids similar to clusters from D29 organoids. **C.** Transplanted and vascularized organoid. IF staining shows human podocytes (anti-human NPHS1 antibody) at the outer perimeter and mouse endothelial cells (anti-mouse Plvap antibody) lining the internal perimeter of a glomerular structure. Gray, human and mouse nuclei (DAPI). **D.** Dot plots indicating ligand and receptor pairs involved in putative cross-talk between human podocytes and mouse endothelial cells of transplanted organoids. **E.** Box plots of expression levels for *KLF6* and *HES1* in the distal *MAL*+ cluster from D29, D32 and D51 organoids grown *in vitro*, compared to D32 transplanted organoids. **F.** Box plots demonstrate that *PMEL*+ melanoma cells and *SOX2*+ neuronal cells were diminished after transplantation. *MYOG*+ muscle cells and *STMN2*+ neuron-like cells persisted. **G.** Random Forest Classifier shows the relation of cell clusters in transplant organoids compared to organoids grown *in vitro*. Melanoma and *SOX2*+ neuronal precursor cells are not detected in D32 transplant organoids. **H.** IF staining validation for SOX2 (green) in D32 control organoids compared to diminished abundance in D32 transplanted organoids. Human and mouse nuclei (DAPI, gray).

Figure 3.6 (Continued).

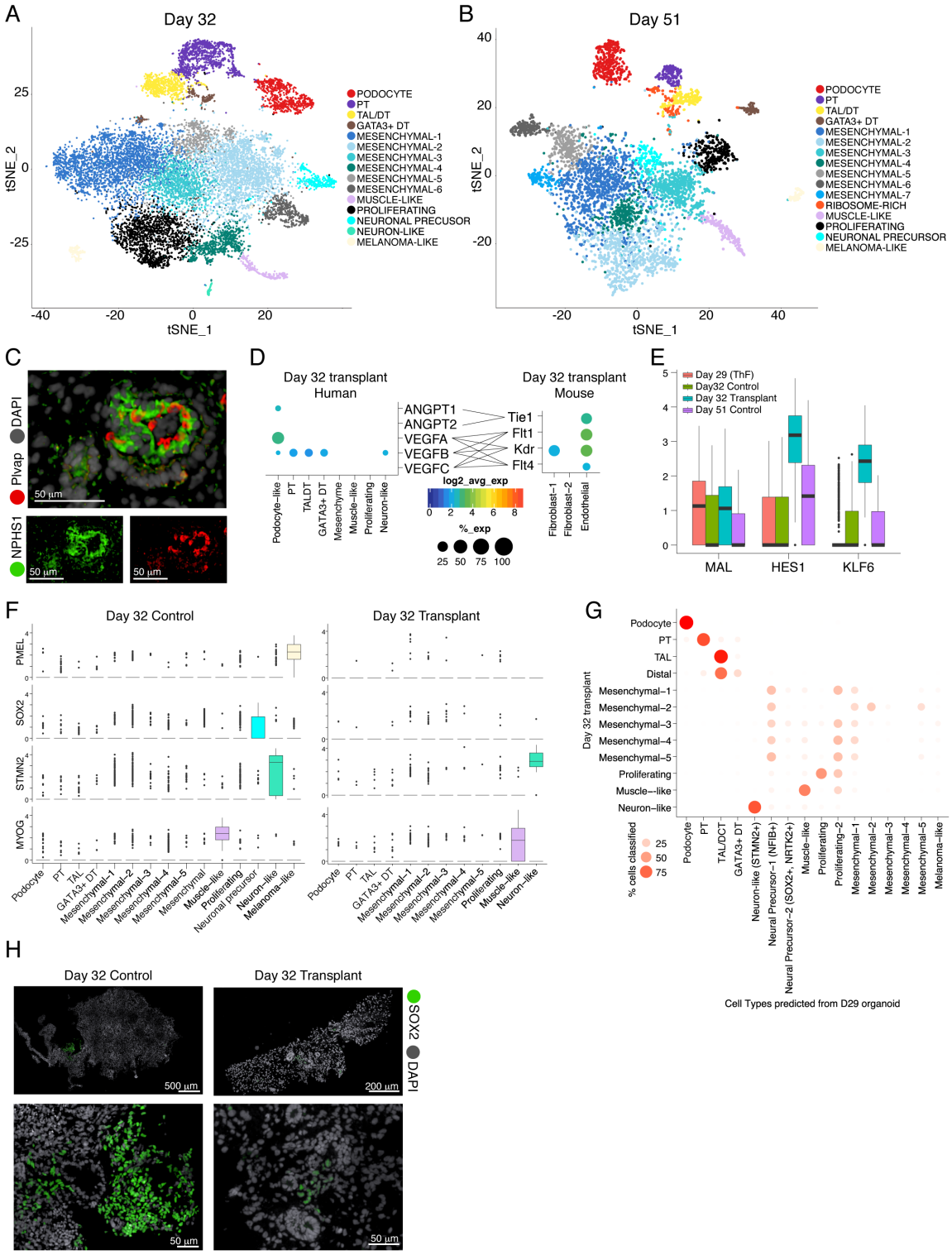

VEGF receptors *Flt1*, *Kdr* and *Flt4* (Ferrara, 1999; Kanno et al., 2000; Sharmin et al., 2016; Tufro et al., 1999) and the angiopoietin receptor *Tie1* were highly expressed in mouse Plvap-positive endothelial cells (**Fig. 3.6D**), suggesting that the cell types could interact.

The transplanted organoid epithelial cells had increased expression of genes suggestive of more mature states compared to *in vitro* D32, D29, or D51 controls. Specifically, both *KLF6*, a TF involved in the development of the ureteric bud and the kidney collecting duct (Fischer et al., 2001), and the Notch effector *HES1*, which plays a role in proximal to distal patterning in kidney nephrogenesis (Piscione et al., 2004), were upregulated in *MAL*+ distal cells from D32 transplanted organoids (**Fig. 3.6E**).

Strikingly, we found little off-target expression of *SOX2* (neuronal precursor cells) or PMEL (melanoma cells) in D32 transplanted organoids compared to controls, suggesting that transplantation diminished off-target cells (**Fig. 3.6F**, **S2.17A**). *MYOG* positive muscle cells persisted in D32 transplanted organoids (**Fig. 3.6F**, **S2.17A**). We also noted that a rare *STMN2*+ neuronal cluster persisted in D32 transplants. Interestingly, this cluster was uniquely and highly correlated with the neuronal cluster in week 17 fetal kidney (Spearman ρ = 0.82; **Fig. 3.1F, S2.17B**). A set of enriched genes (*GAL*, *CHGA*, *CHGB* (Dressler, 2006); **Fig. S2.18**) was shared between this cluster in fetal kidney and in D32 transplanted organoids (**Fig. S2.18A**). Further analysis revealed that in fact *CHGA* and *CHGB* were detectable in a small number of cells within the *STMN2*+ cluster in D29 control organoids (**Fig. S2.18B**) and transplantation selected for this *STMN2*+/*CHGA*+/*CHGB*+ cluster (**Fig. S2.18A**), suggestive of a more fetal-kidney-like state.

We applied a classifier to further assess the relation of all cell clusters in transplanted organoids to organoids grown *in vitro* (**Fig. 3.6G**). Consistently, no transplanted organoid cells corresponded to *SOX2*+*NTRK2*+ neural precursors or *PMEL*+ melanoma-like cells (**Fig. 3.6G**). In line with these findings, IF staining showed diminished SOX2 staining in D32 transplanted organoids compared to numerous SOX2 positive cells in controls (**Fig. 3.6H**). Taken together,

these data showed that transplantation reduced off-target cells, improving organoid maturity and quality.

Discussion

In this study, we present a comprehensive atlas of human kidney organoids in comparison to human adult and fetal kidneys at single cell resolution spanning multiple iPSC cell lines, time points, protocols, and replicates including transplantation into mice, at average sequencing depths of 10,000 reads per cell in a total of 415,775 cells. This analysis provided answers to several critical questions regarding organoid reproducibility, faithfulness and quality.

First, we compared kidney organoids derived from multiple iPSC lines with single cell resolution. The large number of cells and replicates sequenced across different conditions in this study afforded us the opportunity to retrieve numerous cell types and get robust results from statistics such as the Jenson-Shannon Divergence (Yi-Rong Peng, Karthik Shekhar, Wenjun Yan, Dustin Herrmann, Anna Sappington, Greg S. Bryman, Tavé van Zyl, Michael Tri. H. Do, 2018) to gain quantitative insights into organoid reproducibility. By comparison with adult and fetal human kidneys, major nephron cell types were identified in D29 human kidney organoids from all four iPSC lines. Podocytes and proximal tubular cells were well developed, whereas distal tubular cells were less differentiated. At single cell resolution, we also found that the iPSCs themselves had comparable pluripotency (at D0) and modest variability at D7. At D15, organoids showed greater variability in cell proportions and a distinct pool of *SOX2*+ cells, suggesting that variability in mature D29 organoids is likely derived from off-target programs at a point in organoid development between D7 and D15. The pattern of variability in cell composition was then maintained through D29, driven by the off-target compartment. Importantly, organoids with higher proportions of nephron progenitor cells at D15 went on to develop more off-target cells at D29. Hence, our data reveal that future improvements in organoid protocols should focus on the time interval between D7 and D15, aiming to reduce the persistence of progenitor cells that drive the development of off-target cell populations.

Second, the applicability and faithfulness of organoids as a tool for discovery was bolstered by the fact that the vast majority of genes associated with kidney diseases was expressed in organoids across all four iPSC lines in the expected, corresponding cell types. For example, we validated the expression of *MUC1* in the distal tubular compartment of D29 organoids. Mutations in *MUC1* are a cause of autosomal dominant tubulointerstitial kidney disease (Kirby et al., 2013; Živná et al., 2018), a rare kidney disease without a cure. Hence, efforts to find cures for genetically defined diseases may benefit greatly from our ability to study their mechanisms in patient iPSC-derived organoids, and this study provides an important foundational step in this direction. Specifically, our work suggests that organoids derived from individual patients can indeed be used as a tool to fuel biological discovery and therapeutics. However, single cell transcriptomics using comprehensive atlases such as this may be an essential reference when trying to make meaningful comparisons between iPSC-derived kidney organoids from different patients.

Finally, we addressed the critical question of organoid quality, with a focus on reduction of off-target cells. Recent reports focused on eliminating neuronal off-target cells from kidney organoids by using an NTRK2 blocker (Wu et al., 2018). However, NTRK2 is not only expressed in off-target neuronal cells, but it is also abundantly expressed in podocytes (Caroleo et al., 2015; Li et al., 2015) in both fetal human kidneys (Metsuyanim et al., 2009) and in developing organoids (**Fig. S2.18A**), raising the concern that NTRK2 blockers applied to organoid cultures may adversely affect podocyte differentiation and function. Here we identified organoid transplantation as an alternate approach to diminish off-target cells. Remarkably, organoid transplantation under the mouse kidney capsule diminished *SOX2*+ neuronal precursors and *PMEL*+ melanoma cells, in contrast to organoids grown *in vitro*, that retained a neuronal precursor *SOX2*+ off-target population. While some of these observations merit further studies, these data show that transplantation reduced off-target cells and improved organoid quality and maturity. Future

studies will be required to test if earlier organoid transplantation, as early as D7, may eliminate off-target cells and enhance organoid formation, especially ureteric bud and collecting duct development (building on gene programs such as uniquely upregulated *KLF6* and *HES1* in transplanted organoids). As it stands, our protocols may benefit from incorporating organoid transplantation into rodents. Since endothelial progenitors were identified in D15 organoids, and endothelial cells were detected in D29 organoids, we can further speculate that improved vascularization may be achieved by preserving and expanding human endothelial cells in organoids in the hopes of eliminating all off-target cells and generating even more faithful, adult-kidney-like organoids.

In conclusion, these studies provide unprecedented single cell resolution into iPSC-derived kidney organoids, illuminating their reproducibility, pinpointing the source of variability, and showing that transplantation is a novel method for reducing off-target cells and improving organoid quality. This comprehensive atlas, uniquely enabled by scRNA-Seq technology, should serve as a foundational resource for the community, fueling the development of much needed therapies for patients with kidney diseases.

Methods

Materials

Cell Culture and Chemicals: mTeSR1 (Stem Cell Technologies, no. 85870), Gentle Cell Dissociation Reagent (Stem Cell Technologies, no. 7174), ROCK Inhibitor Y-276*32* (Stem Cell Technologies, no. 72304*)*, STEMdiff™ APEL™2 (Stem Cell Technologies, no. 05270), Accutase (Stem Cell Technologies, no. 07920), Corning Matrigel (Stem Cell Technologies, no. 354277), 6-well transwell plate (Stem Cell Technologies, no. 3450), CHIR99021 (R&D systems, no. 4423/10), Activin A (R&D systems, no. 338-AC), Human recombinant FGF-9 (Peprotech, no. 100-23), NOGGIN (Peprotech, 120-10C) and Heparin (Sigma-Aldrich, no. H4784-250mg).

Antibodies, Immunofluorescence: WT1 (ThermoFisher, no. PA5-16879, 1:100), ECAD, SYNPO, MUC1 (Abcam, no. ab117702, 1:500), fluorescein labeled LTL (Vector Laboratories, no. FL-1321, 1:300), GATA3, SOX2 (Cell Signaling Technology, no. 5852, 3579 1:300), Laminin (Sigma-Aldrich, no. L9393, 1:500), MEIS1 (Activemotif, no. ATM39795, 1:300) CD31 (BD Pharmingen, no. 555444, 1:300), SOX17 (R&D Systems, no. AF1924, 1:300), LRP2 (Santa Cruz Biotechnology, no. 515772, 1:100), PAX2 (Zymed laboratories, no. 71-6000, 1:300). All donkey Alexa Fluor secondary antibodies were purchased from Invitrogen (1:1000). Human nuclei (Antibodies online, no. ABIN361360, 1:300), MECA-32 (BD Biosciences, no. 553849, 1:300), NPHS1 (R&D systems, no. AF4269, 1:300) and Claudin-5 Antibody (Novus Biologicals, no. NBP2-66783, 1:300).

iPSC culture:

Human Episomal iPSC Line (ThermoFisher, no. A18945, ALSTEM, no. iPS16). N1 line (S1930 CB A) N2 line (S1973 WR I) were derived from erythroblasts using CTS™ CytoTune™-iPS 2.1 Sendai Reprogramming Kit (ThermoFisher, no. A34546) at Harvard Stem Cell Institute (HSCI) iPS Core Facility. The N1 and N2 cell lines were characterized for pluripotency and spontaneous differentiation to the three germ layers using qPCR based on standard protocols at the HSCI Core

Facility. All iPSC cultures were maintained in mTeSR1 medium in T25 flasks coated with Matrigel. Cells were passaged using Gentle Cell Dissociation Reagent. All lines were confirmed to be karyotype normal and maintained below passage 15 and all the cell lines were routinely checked and were negative for mycoplasma.

Kidney Organoid Differentiation:

Kidney organoids were generated following the protocol described by Takasato et al., 2016(Takasato et al., 2016) or Morizane et al., 2017 (Morizane and Bonventre, 2017b) with slight modifications:

Takasato et al., 2016: 375K iPS cells were plated in a T25 flask in mTeSR1 media and ROCK Inhibitor, Y-27632 (10 uM). After 24 hours, cells were treated with CHIR99021 (8 uM) in APEL2 medium for four days, followed by recombinant human FGF-9 (200 ng/mL) and heparin (1 ug/mL) for an additional three days. At day seven, cells were dissociated into single cells using ACCUTASE^{TM}. 500K cells were pelleted at 350xg for 2 min (twice with 180^{o} flip) and transferred onto a 6-well transwell membrane. Pellets were incubated with CHIR99021 (5 uM) in APEL2 medium for one hour at 37^{o}C. After, the medium was changed to APEL2 supplemented with FGF-9 (200 ng/mL) and heparin (1 ug/mL) for an additional five days, and an additional two days with heparin (1 ug/mL). The organoids were maintained in APEL2 medium with no additional factors until day 29-51 for downstream experiments. Medium was changed every other day.

Morizane et al., 2017: iPS cells were plated as described above. After 24 hours, cells were treated with CHIR99021 (10 uM) and NOGGIN (5 ng/mL) in APEL2 medium for four days, followed by Activin A (10 ng/mL) for two days, and FGF-9 (10 ng/mL) for an additional two days. At day 8, the cells were dissociated and transferred to a 6-well transwell plate as described above. Pellets were incubated with CHIR99021 (3 uM) and FGF-9 (10 ng/mL) in APEL2 for two days, followed by four days with only FGF-9 (10 ng/mL). Organoids were maintained in APEL2 medium with no additional factors until harvest at day 25-28 for downstream experiments. Medium was changed every other day.

Single cell isolation for 10X genomics:

Day 28 mature kidney organoids were washed twice with PBS and incubated with Accumax (Stem Cell Technologies, no. 07921) for 10 minutes at 37°C and were dissociated into single cells using a 27G syringe (BD biosciences, no. 305540). Cells were spun down at 350xg for 5 minutes, resuspended in PBS, filtered through a 40µm filter (Corning, no. 352340), and checked for viability.

Library preparation and single cell sequencing:

Single cells were processed through the 10X Chromium 3' Single Cell Platform using the Chromium Single Cell 3' Library, Gel Bead and Chip Kits (10X Genomics, Pleasanton, CA), following the manufacturer's protocol. Briefly, 10,000 cells were added to each channel of a chip to be partitioned into Gel Beads in Emulsion (GEMs) in the Chromium instrument, followed by cell lysis and barcoded reverse transcription of RNA in the droplets. Breaking of the emulsion was followed by amplification, fragmentation and addition of adapter and sample index. Libraries were pooled together and sequenced on Illumina HiSeq.

Immunofluorescence:

Organoids were fixed in 4% paraformaldehyde (Alfa Aesar, no. J61899-AP), cryoprotected in 30% sucrose solution overnight, embedded in optimum cutting temperature (OCT) compound (VWR, no. 25608-930), flash frozen in dry ice with ethanol, and kept at -80°C overnight. Organoids were cryosectioned (Leica CM1950 Clinical Cryostat) at 6□m and mounted on Micro Slides, Superfrost™ Plus (VWR, 48311-703). Slides were washed with PBS (1 time, 5 minutes), blocked for 20 minutes (5% normal donkey serum, 1.5% Tween-20), and incubated overnight at 4°C with primary antibody (in blocking buffer). After, the slides were washed with PBS (3 times, 10 minutes each) and incubated with secondary antibody (PBS, 1.5% Tween-20) for two hours at room temperature. The slides were then washed with PBS (1 time, 10 minutes). For phalloidin staining,

the cells were incubated with Phalloidin-647 (ThermoFisher, no. A22287, 10U/mL in 1.5% Tween-20) for 20 minutes at room temperature and washed with PBS (1 time, 10 minutes). The sections were stained with DAPI (ThermoFisher, no. 62248, 1: 10,000 in PBS) for 5 minutes, washed with PBS (3 times, 10 minutes), and mounted using ProLong™ Gold antifade reagent (ThermoFisher, no. P36930). Images were obtained by confocal microscopy (PerkinElmer Opera Phenix High Content Screening System).

Animal Experiments:

Animal experiments were done at Custom contract research company Biomere (Biomedical Research Model company (https://biomere.com). Biomere has all the IACUC approval for animal experiments. Recipient mice (n = 8, NOD scid gamma (NSG) 8-week-old female mice, The Jackson Laboratory, no. Jax # 005557). Mice were anesthetized with ketamine/dexdomitor and for pain relief animals were injected with burenorphine. ThF kidney organoids generated using ML protocol (Day 7+11 and Day 7+18) were transplanted onto the left kidney capsule of mice as described in Cathelijne et al., 2018(van den Berg et al., 2018). Day 7+11 organoids were collected after 14 days of implantation and Day 7+18 organoids were collected after 26 days of implantation for single cell RNA sequencing, Immunohistochemistry and for Electron Microscope (EM) analysis.

Single cell isolation from human kidney tissue:

Samples of macroscopically normal cortex were obtained from a tumor nephrectomy specimen, distant from the tumor site and after appropriate patient consent, in accordance with IRB and institutional guidelines. Tissue was cut into 1mm x 1mm cubes and placed in 0.25mg/ml liberase TH (Roche Diagnostics, Indianapolis, USA) dissociation medium. Following further dissection, the tissue was incubated at 37C for 1 hour in a thermomixer at 600rpm. Samples were regularly triturated during the incubation period using a 1ml pipette, after which 10% heat-inactivated FBS RPMI was added to stop the digestion. Centrifugation at 500g for 5 minutes at room temperature

and removal of the supernatant was followed by the addition of ACK lysing buffer to remove erythrocytes (Thermo Fisher Scientific, Waltham, USA). Repeat addition of ACK lysing buffer was performed given the kidney was not perfused prior to removal. Following centrifugation, the resulting cell pellet was incubated with Accumax at 37C for 3 minutes (Innovative Cell Technologies Inc, San Diego, USA). 10% FBS RPMI was again used to neutralize the accumax and centrifugation was followed by resuspension of the cell pellet with 0.4% BSA/PBS. The single cell suspension was then filtered using a 30um CellTrics filter (Sysmex America Inc, Lincolnshire, USA) with the resulting cell concentration and viability determined using trypan blue. 10,000 cells were then loaded into the 10x Genomics microfluidic system according to the manufacturer's guidelines (10x Genomics, Pleasanton, USA).

Computational Methods for Data Analysis:

Study Design: Replicates from both sexes were incorporated wherever possible. Organoids were pooled on lanes using a randomized design to ensure that organoids replicates from an individual batch (donor, replicate, condition) were distributed across lanes.

Preprocessing of 10x droplet based sequencing outputs: We used the *Cellranger* toolkit (v2.1.1) to perform de-multiplexing using the "cellranger mkfastq" command, and the "cellranger count" command for alignment to the human transcriptome, cell barcode partitioning, collapsing unique-molecular identifier (UMI) to transcripts, and gene-level quantification.

Quality Control: We filtered cells to only include barcodes with minimum mapped UMIs of 1000, summarizing to at least 200 genes for downstream analysis. Further, the percentage of reads mapping to mitochondrial genes was capped at 20%.

Inferring cell-types from individual donor organoid, fetal and adult kidney cells: We used the default settings in the *Seurat* R package (Butler et al., 2018) (v2.3) for normalization (NormalizeData) of the gene expression counts and identifying variable genes

(FindVariableGenes). Briefly for normalization, UMI counts in each gene in a cell are divided by the total UMI count for the cell, divided by a factor of 100000 and log-transformed to obtain log(TPX+1) values. After mean-centering, we performed dimensionality reduction using Principal Component Analyses (RunPCA) on the highly variable genes computed in the previous step. We retained 50 PCs for unbiased clustering (FindClusters) by building a k-nearest neighbor graph and smart-moving local community detection algorithm. For iPSCs, the first 8 Principal Components sufficiently captured all the variance. The resolution parameter was adjusted as needed: for the human adult sample, resolution of 3 recovered expected renal cell compartments, for day 28 and 15, resolution of 1 was used. We computed an embedding of the data in 2-D space using t-distributed stochastic neighbor embedding (tSNE) in the PC space for visualization (RunTSNE), independent of the clustering step.

Assignment of cell-identity and gene-set signatures: Cluster-enriched or marker genes were computed using the Wilcoxon-Rank sum test (FindAllMarkers) for differential expression of genes in the cluster cells vs all other cells, and selecting those genes that pass the adjusted p-value (Benjamini-Hochberg(Benjamini et al., 1995) FDR) cutoff of 0.05 as cluster-representative. Cluster identity was assigned by comparing data-driven genes with a list of literature-curated genes for kidney developmental and mature cell types. Sub clustering was performed when a single cluster represented marker genes from multiple renal epithelial cell-types. We checked that cluster membership was not exclusive to a single replicate. Cells were scored for embryonic germ layer-specific gene signatures using Seurat's "AddModuleScore" function. Seurat's "CellCycleScoring" function was used to score cells for different stages of cell-cycles.

Curation of gene signatures: The cell-cycle signatures were obtained from Tirosh et al. The germ-layer signatures were obtained from Tsankov et al. 2015. Only those genes were included which passed the cutoff of. We curated a set of genes, both transcription factor or not, critical for early nephrogenesis from the kidney development literature.

Combined analyses of organoids from multiple donors: Clusters, particularly representing interstitial cell types, segregated by donor origin when default analyses as described above was performed. To identify similar cell types among organoids from multiple donors, we co-embedded the cells using canonical correlation analyses using Seurat's "MultiCCA" function. 20 canonical components were used for clustering. Clusters were assigned identity based on expression of literature-curated marker genes as well as verified by differential expression analysis for individual lines (AS or ThF).

Analysis of Mouse transplants: For cells from the mouse transplants, we aligned the sequenced reads to a reference combining the human and mouse transcriptomes using the Cellranger software as described before. Multimapped reads were discarded and two expression matrices, representing mouse and human barcodes were derived. In case of barcodes that remained in both matrices after quality filtering, we assigned their identities based on the transcriptome that yielded the higher number of total UMIs. Downstream analysis was performed as described above.

Analysis of human fetal data: Trimester 1 human fetal kidney single-cell transcriptomes were downloaded from the Data Supplement in Trimester 2 Human fetal kidney single-cell transcriptomes were downloaded from NCBI GEO GSE112570(Young et al., 2018). In both cases, the data were available in the format of gene expression count matrices which were directly plugged into cell-type identification and assignment routines as described above.

Assessment of compositional differences: The Jenson-Shannon Divergence was computed between any two vectors of cell-proportions using the "JSD" function in the *philentropy* R package, using the default log2 transformation. The AS, passage 1 (D7, D15, D29) was excluded when computing summary statistics as it was an outlier in terms of extremely low nephron numbers. ThF, passage 1 (D7) was also excluded as it did not undergo nephrogenesis.

Comparison of cell-types between organoids and human kidney cells: We used the R package randomForest(Liaw, A and Wiener, 2002) to train a multi-class Random Forest classifier (5000 trees) on the mature ThF organoids. The number of training cells per cell-type was set at 1000 or 70% of cluster membership, whichever was lower. The remaining cells comprised the test set. The classifier was then used to predict cell types in fetal kidney cells derived from individual kidneys at trimesters one and two, and adult human kidney cells. We inferred cell-types for fetal and adult cells using unbiased clustering as described earlier. Prediction outcomes and concordance of cell-types were visualized by a dotplot representation, where x-axis levels were ThF cell-types and y-axis levels were input (fetal or adult) cell-types. Each dot (size and color) represented the percentage of cells in the input (y-axis level) cell-types predicted to be a ThF (x-axis level) cell-types. The supervised classification analyses revealed high concordance between organoid and human kidney nephron epithelial and podocyte cell types.

Plotting and visualization: The R package *ggplot2* (Wickham, 2016) was used for visualization of tSNEs, cell-type proportions, boxplots and dotplots. In the dotplot representation, each dot size represented the percentage of cells and the color represented the average nonzero gene expression in log2 scale. For Fig 4A-C, we only display dots that represent expression in at least 5% of the respective cluster.

Contributions

A.S., E-H.S., M.E., and A.G. designed the study, interpreted the results, and wrote the manuscript. E-H.S. and M.E. performed all experiments unless otherwise noted. A.S. performed all computational analysis. N.S. assisted with organoid culture and immunofluorescence experiments. M.A. assisted with high content imaging. K.V. and M.S. performed single cell isolation of adult human kidney. J.W., D.D., and L.N. performed single cell library preparation and sequencing.

We thank our colleagues in the BWH Department of Urology, Drs. Steven Chang and Dimitar Zlatev for their generous assistance with recovery of tissue from tumor nephrectomies under IRB protocol 2011P002692. We thank Kendrah Kidd and Dr. Tony Bleyer at Wake Forest Medical School for assistance in obtaining blood samples for iPSC generation. We thank the Harvard Stem Cell Institute for assistance in the generation of the iPSC cell lines N1 and N2. N1 and N2 are covered under Broad ORSP-3414 and commercially purchased lines are covered by Broad NHSR-4998. We thank our colleagues Karthik Shekhar and Matan Hofree for helpful discussions.

This work was funded by NIH grants DK095045, DK099465 (A.G.) and F30DK112477 (E-H.S), the Slim Initiative for Genomic Medicine in the Americas (SIGMA), and an NDSEG fellowship (E-H.S.).

A.G. has a financial interest in Goldfinch Biopharma, which was reviewed and is managed by Brigham and Women's Hospital and Partners HealthCare and the Broad Institute of MIT and Harvard in accordance with their conflict of interest policies.

Chapter 4:

Conclusions

Chronic kidney diseases (CKD) is both a highly prevalent disease and a huge financial burden worldwide, and yet progress in understanding disease pathomechanism and development of targeted therapeutics has not kept pace with the increasing incidence and prevalence of kidney failure (ESRD) (Inrig et al., 2014; Jha et al., 2013). The multifactorial nature of DKD and other common etiologies of CKD combined with inadequate model systems have contributed to this lag in development. In this thesis we have sought to (i) demonstrate an approach to advancing therapeutic development through utilizing rare genetically-defined diseases to provide insight into cell-specific disease circuits, and (ii) comprehensively characterize kidney organoids at the single cell transcriptomic level to shed light on their utility for disease modeling.

CoQ and podocyte biology

The podocyte is a post-mitotic terminally differentiated cell of the kidney's glomerular filtration barrier (Greka and Mundel, 2012). Podocyte loss, which occurs both through acquired/environmental and genetically-driven podocyte dysfunction, is an irreversible process as there exists no known mechanism for podocyte regeneration *in vivo*. Thus, understanding the molecular circuits that drive podocyte injury is critical for designing targeted therapeutics to protect podocytes and thus prevent and reverse disease progression. Genetically defined rare diseases have previously provided insight to therapeutic targets for prevention of podocyte injury and loss, such as chemical inhibitors of TRP channels which modulate RHO GTPase activity and the downstream actin cytoskeleton (Zhou et al., 2017).

In chapter 2 we postulated that the unique presentation of podocyte dysfunction in the setting of CoQ deficiency (relative to other mitochondrial cytopathies) may provide insight into podocyte-specific disease pathways. We used a combination of hypothesis-driven mechanistic work and targeted deployment of "-omics" technologies to understand specific podocyte vulnerabilities in CoQ deficiency both *in vitro* and *in vivo*.

By systematically evaluating CoQ's functions (ETC, antioxidant, MPTP regulation, and co-factor for DHODH) we determined that it is the loss of CoQ's antioxidant function that is most injurious to podocytes. Through the combination of metabolomics and transcriptomics we described a perturbation in PUFAs and RA signaling in the setting of CoQ deficiency. While previous work had described PUFA susceptibility in the setting of CoQ deficiency and had also linked RA alterations to PUFA metabolism, this link had yet to be shown in the setting of disease and it was not previously known that this pathway is injurious to podocytes. Further, the characterization of the *Pdss2*$^{kd/kd}$ mouse at the single cell level led to the identification of a disease-specific activated PEC population, and involvement of a podocyte-specific Braf-Mapk disease circuit. Finally, the identification of BRAF-targeting compound GDC-0879, a previously studied cancer therapeutic (Hoeflich et al., 2009), as podocyte-protective in CoQ deficiency highlights how mechanistic insight into disease pathways can expedite targeted therapeutic development through drug repurposing.

While this work has provided insight into podocyte dysfunction in the setting of this rare disease, several questions remain. First, while PDSS1, PDSS2, COQ2, COQ6, and COQ8B/ADCK4 mutations lead to a podocytopathy, patients identified with COQ7 and COQ9 mutations have tubular dysfunction (Emma et al., 2016; Kwong et al., 2019). While these are very few patients, given that these mutations are in fact causal for disease, it presents an interesting conundrum of what is different between these two disease presentations. The fact that all of these patients have CoQ deficiency serves as an additional piece of evidence that podocyte dysfunction is not solely due to loss of the end metabolite, consistent with our observations in chapter 2. Additionally, PDSS1/2, COQ2, and COQ6 together mediate the first three committed steps of CoQ biosynthesis, while COQ7 mediates a step further downstream in this pathway (Acosta et al., 2016). Thus, perhaps as we suggest here, there may be differences in metabolite build-up leading to the two distinct clinical presentations. COQ7 and COQ9 have been found to functionally

interact, and this might explain why either of these mutations have a similar clinical presentation (Lohman et al., 2014).

Second, we provide evidence for the RAR as the transcriptional mediator of the observed lipidomic changes, and show podocyte-specificity *in vivo*, but what drives cell-type specificity remains unclear. Changes in PUFA metabolism after RA treatment have been observed in other cell types though outside the kidney (Antony et al., 2003; Farooqui et al., 2004; Levine, 2001; Moon et al., 1986; Petroni et al., 1996). Further, whether this pathway is contributory to other forms of podocyte injury is also yet to be determined. However, the convergence of multiple forms of podocyte injury on a downstream Braf-Mapk pathway suggests shared pathways to podocyte injury and thus shared therapeutic targets (Sieber et al., 2018).

Podocyte dysfunction ultimately causes more broad tubular injury and fibrosis. However, the mechanisms of progression of kidney disease and ultimately failure are poorly understood. Single cell transcriptomics can provide the resolution required to elucidate interactions among heterogeneous cell types. Our analysis of the *Pdss2*$^{kd/kd}$ mouse revealed two disease-specific populations: an activated PEC population and a tubule population (Mixed – TAL/DCT). It is difficult to know from this whole body CoQ deficiency model what aspects of these transcriptomic changes are due to reaction to CoQ deficiency versus a response to podocyte injury. In the future, comparisons between a podocyte-specific conditional knockout model could provide insight into how tubular cells detect and respond to kidney injury. Additionally, the activated PEC population, which is PT-like, has a different transcriptional signature from the more distal tubular cluster (Mixed – TAL/DCT); thus it will be potentially interesting to understand how different kidney tubular segments respond to podocyte injury. Finally, there is little tubular injury observed histologically and thus these observed transcriptional changes are likely markers of early tubular injury, which leads to further questions for future studies about how tubular injury progresses over time.

Kidney organoids as models for biology in health and disease

Kidney organoids derived from human induced pluripotent stem cells (iPSCs) are an emerging technology with the potential to both recapitulate the cellular diversity of the kidney and to further our understanding of disease mechanisms. Organoids provide a novel model system which combines several advantages of both *in vivo* and *in vitro* models: (i) they capture the cellular complexity of the nephron, as in mouse models, (ii) they are human-derived mini-tissue 3D models and (iii) they offer higher throughput capacity than mice, more similar to traditional 2D tissue culture systems.

In chapter 3 we built on prior research in understanding mammalian kidney development and utilized this knowledge to develop hiPSC-derived kidney organoids (Little et al., 2019; Morizane and Bonventre, 2017a). While, organoids are a promising model system for understanding human disease pathogenesis, understanding their reproducibility and quality across multiple samples, replicates and patients-donors is critical. Thus, we generated a 412,358 single cell census of 47 organoid and iPSC samples derived from four cell lines across four time points of differentiation and two previously established protocols.

First, comparison between lines and protocols showed that the largest differences in organoid generation occur between lines, not protocols, and that this difference is most pronounced in the presence and amount of off-target cell populations. Second, using comparisons to adult and fetal kidney single cell transcriptomics, confirmed prior work which characterized organoids to be most similar to first trimester fetal kidney. We found proximal structures (podocytes, proximal tubules, and loop of Henle) to be best developed with poorly developed distal tubules and variably present primitive CD-like, *GATA3*+ UB population. Third, to demonstrate utility of organoids for disease models we show broad expression of many kidney disease-associated genes, as well as appropriate patterning and sub-cellular localization of MUC1, a protein mutated in autosomal dominant tubulointerstitial kidney disease . Finally, to

demonstrate how organoid quality can be enhanced, we demonstrated that *in vivo* transplantation of organoids under the kidney capsule of immunodeficient mice led to vascularization, diminished off-target populations, and upregulation of genes associated with UB and CD development (*KLF6*, *HES1*) suggesting both enhanced quality and maturation of organoids can be achieved.

Although kidney organoids can presently be used for disease modeling, there remains room for further development. Based on our findings of the effects of *in vivo* transplantation, several interesting questions remain. First, while in our work we transplant kidney organoids underneath the kidney capsule, other groups have done *in vivo* transplantation at other locations (Bantounas et al., 2018; van den Berg et al., 2018; Garreta et al., 2019; Tanigawa et al., 2018). Thus, more can be learned about the effects of transplantation: whether the location of transplantation affects organoid development and how. We hypothesize that development is mediated through vascularization, but what factors precisely are mediating these effects and whether there are additional stromal factors which are contributory remains unknown. Second, just as our knowledge of kidney embryogenesis has informed development of organoid technology, as our models improve, the loop can be closed such that *in vitro* development can provide insight into *in vivo* embryogenesis. For example, Lindström and colleagues recently proposed a time-dependent cell fate acquisition that determines nephron patterning (Lindström et al., 2018b). If and how this is reflected in organoid development remains unknown. They hypothesize that distal progenitors are recruited ahead of proximal progenitors. However, in organoid systems, the proximal structures are further developed compared to distal structures (DCT and CD). While poor UB development likely affects nephron patterning, validation of such hypotheses can provide insight as to how to improve organoid quality.

While work still needs to be done on improving organoid maturation, organoids are currently well-suited to the study of congenital and early-onset diseases, such as NS. However, it remains to be seen how much insight can be presently gained through the study of late-onset

and slow-progressing pathologies. One such example is autosomal dominant polycystic kidney disease (ADPKD), a leading cause of ESRD, due to mutations in two genes, *PKD1* and *PKD2* (Polycystin 1/2) (Willey et al., 2016). Recent work in kidney organoids demonstrated that organoid cyst formation could be enhanced by full knockout of either *PKD1* or *PKD2* using CRISPR-Cas9 technology further enhanced through chemical and physical perturbations (Cruz et al., 2017). Organoid systems may still be limited in ability to capture changes associated with chronic disease, however, transcriptional profiling may still provide insight into early disease perturbations in the absence of obvious morphological changes.

A final note

There exist over 7,000 rare diseases and a growing number of monogenic kidney diseases; it is an insurmountable task, both due to financial limitations and the required person-years, to develop and characterize mouse models for each of these individually. However, organoids across many organ systems combined with other developing genomic technologies, like CRISPR-Cas9, are providing higher throughput systems for understanding disease and developing targeted technologies. In conclusion, this body of work demonstrates how deep mechanistic insight can facilitate the identification of drug targets. Additionally, the combination of mechanistic work with developing organoid systems can further enhance much needed therapeutic development in the kidney space.

References

Acosta, M.J., Vazquez Fonseca, L., Desbats, M.A., Cerqua, C., Zordan, R., Trevisson, E., and Salviati, L. (2016). Coenzyme Q biosynthesis in health and disease. Biochim. Biophys. Acta - Bioenerg.

Adam, M., Potter, A.S., and Potter, S.S. (2017). Psychrophilic proteases dramatically reduce single-cell RNA-seq artifacts: a molecular atlas of kidney development. Development *144*, 3625–3632.

Akchurin, O., and Reidy, K.J. (2015). Genetic causes of proteinuria and nephrotic syndrome: Impact on podocyte pathobiology. Pediatr. Nephrol. *30*, 221–233.

Antony, P., Freysz, L., Horrocks, L.A., and Farooqui, A.A. (2003). Ca2+-independent phospholipases A2 and production of arachidonic acid in nuclei of LA-N-1 cell cultures: a specific receptor activation mediated with retinoic acid. Brain Res. Mol. Brain Res. *115*, 187–195.

Araki, S.I. (2014). APOE polymorphism and diabetic nephropathy. Clin. Exp. Nephrol.

Araki, H., Shidoji, Y., Yamada, Y., Moriwaki, H., and Muto, Y. (1995). Retinoid Agonist Activities of Synthetic Geranyl Geranoic Acid Derivatives. Biochem. Biophys. Res. Commun. *209*, 66–72.

Ashraf, S., Gee, H.Y., Woerner, S., Xie, L.X., Vega-Warner, V., Lovric, S., Fang, H., Song, X., Cattran, D.C., Avila-Casado, C., et al. (2013). ADCK4 mutations promote steroid-resistant nephrotic syndrome through CoQ10 biosynthesis disruption. J. Clin. Invest. *123*, 5179–5189.

Ashraf, S., Kudo, H., Rao, J., Kikuchi, A., Widmeier, E., Lawson, J.A., Tan, W., Hermle, T., Warejko, J.K., Shril, S., et al. (2018). Mutations in six nephrosis genes delineate a pathogenic pathway amenable to treatment. Nat. Commun. *9*, 1960.

Au, K.M., Lau, S.C., Mak, Y.F., Lai, W.M., Chow, T.C., Chen, M.L., Chiu, M.C., and Chan, A.Y.W. (2007). Mitochondrial DNA deletion in a girl with Fanconi's syndrome. Pediatr. Nephrol. *22*, 136–140.

Bantounas, I., Ranjzad, P., Tengku, F., Silajdžić, E., Forster, D., Asselin, M.-C., Lewis, P., Lennon, R., Plagge, A., Wang, Q., et al. (2018). Generation of Functioning Nephrons by Implanting Human Pluripotent Stem Cell-Derived Kidney Progenitors. Stem Cell Reports *10*, 766–779.

Barak, H., Huh, S.-H., Chen, S., Jeanpierre, C., Martinovic, J., Parisot, M., Bole-Feysot, C., Nitschké, P., Salomon, R., Antignac, C., et al. (2012). FGF9 and FGF20 Maintain the Stemness of Nephron Progenitors in Mice and Man. Dev. Cell *22*, 1191–1207.

Barker, N., Huch, M., Kujala, P., van de Wetering, M., Snippert, H.J., van Es, J.H., Sato, T., Stange, D.E., Begthel, H., van den Born, M., et al. (2010). Lgr5+ve Stem Cells Drive Self-Renewal in the Stomach and Build Long-Lived Gastric Units In Vitro. Cell Stem Cell *6*, 25–36.

Barkoudah, E., Skali, H., Uno, H., Solomon, S.D., and Pfeffer, M.A. (2012). Mortality Rates in

Trials of Subjects With Type 2 Diabetes. J. Am. Heart Assoc. *1*, 8–15.

Barua, M., Brown, E.J., Charoonratana, V.T., Genovese, G., Sun, H., and Pollak, M.R. (2013). Mutations in the INF2 gene account for a significant proportion of familial but not sporadic focal and segmental glomerulosclerosis. Kidney Int. *83*, 316–322.

Beckerman, P., Bi-Karchin, J., Park, A.S.D., Qiu, C., Dummer, P.D., Soomro, I., Boustany-Kari, C.M., Pullen, S.S., Miner, J.H., Hu, C.-A.A., et al. (2017). Transgenic expression of human APOL1 risk variants in podocytes induces kidney disease in mice. Nat. Med. *23*, 429–438.

Belliere, J., Devun, F., Cottet-Rousselle, C., Batandier, C., Leverve, X., and Fontaine, E. (2012). Prerequisites for ubiquinone analogs to prevent mitochondrial permeability transition-induced cell death. J. Bioenerg. Biomembr. *44*, 207–212.

Belostotsky, R., Ben-Shalom, E., Rinat, C., Becker-Cohen, R., Feinstein, S., Zeligson, S., Segel, R., Elpeleg, O., Nassar, S., and Frishberg, Y. (2011). Mutations in the mitochondrial seryl-tRNA synthetase cause hyperuricemia, pulmonary hypertension, renal failure in infancy and alkalosis, HUPRA syndrome. Am. J. Hum. Genet. *88*, 193–200.

Beltcheva, O., Martin, P., Lenkkeri, U., and Tryggvason, K. (2001). Mutation spectrum in the nephrin gene (NPHS1) in congenital nephrotic syndrome. Hum. Mutat. *17*, 368–373.

Benjamini, Y., Hochberg, Y., and Benjamini, Yoav, H.Y. (1995). Benjamini and Y FDR.pdf. J. R. Stat. Soc. Ser. B *57*, 289–300.

van den Berg, C.W., Ritsma, L., Avramut, M.C., Wiersma, L.E., van den Berg, B.M., Leuning, D.G., Lievers, E., Koning, M., Vanslambrouck, J.M., Koster, A.J., et al. (2018). Renal Subcapsular Transplantation of PSC-Derived Kidney Organoids Induces Neo-vasculogenesis and Significant Glomerular and Tubular Maturation In Vivo. Stem Cell Reports *10*, 751–765.

Bhargava, P., and Schnellmann, R.G. (2017). Mitochondrial energetics in the kidney. Nat. Rev. Nephrol. *13*, 629–646.

Boj, S.F., Hwang, C.-I., Baker, L.A., Chio, I.I.C., Engle, D.D., Corbo, V., Jager, M., Ponz-Sarvise, M., Tiriac, H., Spector, M.S., et al. (2015). Organoid Models of Human and Mouse Ductal Pancreatic Cancer. Cell *160*, 324–338.

Boltengagen, A., Kann, M., Rajewsky, N., Kocks, C., Benzing, T., Liu, H., Rahmatollahi, M., Hoehne, M., Schermer, B., Karaiskos, N., et al. (2018). A Single-Cell Transcriptome Atlas of the Mouse Glomerulus. J. Am. Soc. Nephrol. *29*, 2060–2068.

Boreström, C., Jonebring, A., Guo, J., Palmgren, H., Cederblad, L., Forslöw, A., Svensson, A., Söderberg, M., Reznichenko, A., Nyström, J., et al. (2018). A CRISP(e)R view on kidney organoids allows generation of an induced pluripotent stem cell–derived kidney model for drug discovery. Kidney Int.

Bourdon, A., Minai, L., Serre, V., Jais, J.-P., Sarzi, E., Aubert, S., Chrétien, D., de Lonlay, P., Paquis-Flucklinger, V., Arakawa, H., et al. (2007). Mutation of RRM2B, encoding p53-controlled ribonucleotide reductase (p53R2), causes severe mitochondrial DNA depletion. Nat. Genet. *39*,

776–780.

Boute, N., Gribouval, O., Roselli, S., Benessy, F., Lee, H., Fuchshuber, A., Dahan, K., Gubler, M.C., Niaudet, P., and Antignac, C. (2000). NPHS2, encoding the glomerular protein podocin, is mutated in autosomal recessive steroid-resistant nephrotic syndrome. Nat. Genet. *24*, 349–354.

Boyer, O., Benoit, G., Gribouval, O., Nevo, F., Tête, M.-J., Dantal, J., Gilbert-Dussardier, B., Touchard, G., Karras, A., Presne, C., et al. (2011). Mutations in INF2 Are a Major Cause of Autosomal Dominant Focal Segmental Glomerulosclerosis . J. Am. Soc. Nephrol. *22*, 239–245.

Boyle, S., Misfeldt, A., Chandler, K.J., Deal, K.K., Southard-Smith, E.M., Mortlock, D.P., Baldwin, H.S., and de Caestecker, M. (2008). Fate mapping using Cited1-CreERT2 mice demonstrates that the cap mesenchyme contains self-renewing progenitor cells and gives rise exclusively to nephronic epithelia. Dev. Biol. *313*, 234–245.

Brockschmidt, A., Chung, B., Weber, S., Fischer, D.C., Kolatsi-Joannou, M., Christ, L., Heimbach, A., Shtiza, D., Klaus, G., Simonetti, G.D., et al. (2012). CHD1L: A new candidate gene for congenital anomalies of the kidneys and urinary tract (CAKUT). Nephrol. Dial. Transplant. *27*, 2355–2364.

Brosius, F.C., and Coward, R.J. (2014). Podocytes, signaling pathways, and vascular factors in diabetic kidney disease. Adv. Chronic Kidney Dis. *21*, 304–310.

Brown, E.J., Schlöndorff, J.S., Becker, D.J., Tsukaguchi, H., Uscinski, A.L., Higgs, H.N., Henderson, J.M., and Pollak, M.R. (2010). Mutations in the formin gene INF2 cause focal segmental glomerulosclerosis. Nat. Genet. *42*, 72–76.

Brown, E.J., Pollak, M.R., and Barua, M. (2014). Genetic testing for nephrotic syndrome and FSGS in the era of next-generation sequencing. Kidney Int. *85*, 1030–1038.

Bruce, S.J., Rea, R.W., Steptoe, A.L., Busslinger, M., Bertram, J.F., and Perkins, A.C. (2007). In vitro differentiation of murine embryonic stem cells toward a renal lineage. Differentiation *75*, 337–349.

Burrows, C.K., Banovich, N.E., Pavlovic, B.J., Patterson, K., Gallego Romero, I., Pritchard, J.K., and Gilad, Y. (2016). Genetic Variation, Not Cell Type of Origin, Underlies the Majority of Identifiable Regulatory Differences in iPSCs. PLoS Genet. *12*, e1005793.

Bus, J.S., and Gibson, J.E. (1984). Paraquat: model for oxidant-initiated toxicity. Environ. Health Perspect. *55*, 37–46.

Butler, A., Hoffman, P., Smibert, P., Papalexi, E., and Satija, R. (2018). Integrating single-cell transcriptomic data across different conditions, technologies, and species. Nat. Biotechnol. *36*, 411–420.

Cao, L., Gibson, J.D., Miyamoto, S., Sail, V., Verma, R., Rosenberg, D.W., Nelson, C.E., and Giardina, C. (2011). Intestinal lineage commitment of embryonic stem cells. Differentiation *81*, 1–10.

Carmosino, M., Rizzo, F., Procino, G., Basco, D., Valenti, G., Forbush, B., Schaeren-Wiemers, N., Caplan, M.J.J., and Svelto, M. (2010). MAL/VIP17, a new player in the regulation of NKCC2 in the kidney. Mol. Biol. Cell *21*, 3985–3997.

Caroleo, M.C., Carito, V., Pingitore, A., Perrotta, I.D., Perri, M., Mancuso, D., Russo, A., and Cione, E. (2015). Human kidney podocyte cell population as a novel biological target of nerve growth factor. Growth Factors.

Carrozzo, R., Dionisi-Vici, C., Steuerwald, U., Lucioli, S., Deodato, F., Di Giandomenico, S., Bertini, E., Franke, B., Kluijtmans, L.A.J., Meschini, M.C., et al. (2007). SUCLA2 mutations are associated with mild methylmalonic aciduria, Leigh-like encephalomyopathy, dystonia and deafness. Brain *130*, 862–874.

Chen, L., Lee, J.W., Chou, C.-L., Nair, A. V, Battistone, M.A., Păunescu, T.G., Merkulova, M., Breton, S., Verlander, J.W., Wall, S.M., et al. (2017). Transcriptomes of major renal collecting duct cell types in mouse identified by single-cell RNA-seq. Proc. Natl. Acad. Sci. *114*, E9989–E9998.

Cheng, B., Yuan, Q., Sun, X., and Li, W. (2010). Enhanced Production of Coenzyme Q10 by Overexpressing HMG-CoA Reductase and Induction with Arachidonic Acid in Schizosaccharomyces pombe. Appl. Biochem. Biotechnol. *160*, 523–531.

Choi, H.M.T., Schwarzkopf, M., Fornace, M.E., Acharya, A., Artavanis, G., Stegmaier, J., Cunha, A., and Pierce, N.A. (2018). Third-generation in situ hybridization chain reaction: multiplexed, quantitative, sensitive, versatile, robust. Development *145*, dev165753.

Christensen, E.I., and Birn, H. (2002). Megalin and cubilin: Multifunctional endocytic receptors. Nat. Rev. Mol. Cell Biol.

Chua, C.W., Shibata, M., Lei, M., Toivanen, R., Barlow, L.J., Bergren, S.K., Badani, K.K., McKiernan, J.M., Benson, M.C., Hibshoosh, H., et al. (2014). Single luminal epithelial progenitors can generate prostate organoids in culture. Nat. Cell Biol. *16*, 951–961.

Chun, J., Zhang, J.-Y., Wilkins, M.S., Subramanian, B., Riella, C., Magraner, J.M., Alper, S.L., Friedman, D.J., and Pollak, M.R. (2019). Recruitment of APOL1 kidney disease risk variants to lipid droplets attenuates cell toxicity. Proc. Natl. Acad. Sci. *116*, 3712–3721.

Civenni, G., Bezzi, P., Trotti, D., Volterra, A., and Racagni, G. (1999). Inhibitory effect of the neuroprotective agent idebenone on arachidonic acid metabolism in astrocytes. Eur. J. Pharmacol. *370*, 161–167.

Combes, A.N., Zappia, L., Er, P.X., Oshlack, A., and Little, M.H. (2019). Single-cell analysis reveals congruence between kidney organoids and human fetal kidney. Genome Med. *11*, 1–15.

Coresh, J., Selvin, E., Stevens, L.A., Manzi, J., Kusek, J.W., Eggers, P., Van Lente, F., and Levey, A.S. (2007). Prevalence of Chronic Kidney Disease in the United States. JAMA *298*, 2038.

Cruz, N.M., Song, X., Czerniecki, S.M., Gulieva, R.E., Churchill, A.J., Kim, Y.K., Winston, K., Tran, L.M., Diaz, M.A., Fu, H., et al. (2017). Organoid cystogenesis reveals a critical role of microenvironment in human polycystic kidney disease. Nat. Mater. *16*, 1112–1119.

Danhauser, K., Herebian, D., Haack, T.B., Rodenburg, R.J., Strom, T.M., Meitinger, T., Klee, D., Mayatepek, E., Prokisch, H., and Distelmaier, F. (2016). Fatal neonatal encephalopathy and lactic acidosis caused by a homozygous loss-of-function variant in COQ9. Eur. J. Hum. Genet. *24*, 450–454.

Davin, J.-C., and Rutjes, N.W. (2011). Nephrotic Syndrome in Children: From Bench to Treatment. Int. J. Nephrol. *2011*, 1–6.

Davis, J.P., Cain, G.A., Pitts, W.J., Magolda, R.L., and Copeland, R.A. (1996). The Immunosuppressive Metabolite of Leflunomide Is a Potent Inhibitor of Human Dihydroorotate Dehydrogenase. Biochemistry *35*, 1270–1273.

Dennis, E.A., Cao, J., Hsu, Y.-H., Magrioti, V., and Kokotos, G. (2011). Phospholipase A2 enzymes: physical structure, biological function, disease implication, chemical inhibition, and therapeutic intervention. Chem. Rev. *111*, 6130–6185.

Dimmock, D.P., Zhang, Q., Dionisi-Vici, C., Carrozzo, R., Shieh, J., Tang, L.-Y., Truong, C., Schmitt, E., Sifry-Platt, M., Lucioli, S., et al. (2008). Clinical and molecular features of mitochondrial DNA depletion due to mutations in deoxyguanosine kinase. Hum. Mutat. *29*, 330–331.

Diomedi-Camassei, F., Di Giandomenico, S., Santorelli, F.M., Caridi, G., Piemonte, F., Montini, G., Ghiggeri, G.M., Murer, L., Barisoni, L., Pastore, A., et al. (2007). COQ2 Nephropathy: A Newly Described Inherited Mitochondriopathy with Primary Renal Involvement. J. Am. Soc. Nephrol. *18*, 2773–2780.

Do, T.Q., Schultz, J.R., and Clarke, C.F. (1996). Enhanced sensitivity of ubiquinone-deficient mutants of Saccharomyces cerevisiae to products of autoxidized polyunsaturated fatty acids. Proc. Natl. Acad. Sci. U. S. A. *93*, 7534–7539.

Downie, M.L., Gallibois, C., Parekh, R.S., and Noone, D.G. (2017). Nephrotic syndrome in infants and children: pathophysiology and management. Paediatr. Int. Child Health *37*, 248–258.

Dressler, G.R. (2006). The Cellular Basis of Kidney Development. Annu. Rev. Cell Dev. Biol.

Duchateau, P.N., Pullinger, C.R., Orellana, R.E., Kunitake, S.T., Naya-Vigne, J., O'Connor, P.M., Malloy, M.J., and Kane, J.P. (1997). Apolipoprotein L, a New Human High Density Lipoprotein Apolipoprotein Expressed by the Pancreas. J. Biol. Chem. *272*, 25576–25582.

Duncan, A.J., Bitner-Glindzicz, M., Meunier, B., Costello, H., Hargreaves, I.P., López, L.C., Hirano, M., Quinzii, C.M., Sadowski, M.I., Hardy, J., et al. (2009). A Nonsense Mutation in COQ9 Causes Autosomal-Recessive Neonatal-Onset Primary Coenzyme Q10 Deficiency: A Potentially Treatable Form of Mitochondrial Disease. Am. J. Hum. Genet. *84*, 558–566.

Dye, B.R., Hill, D.R., Ferguson, M.A., Tsai, Y.-H., Nagy, M.S., Dyal, R., Wells, J.M., Mayhew, C.N., Nattiv, R., Klein, O.D., et al. (2015). In vitro generation of human pluripotent stem cell derived lung organoids. Elife *4*, 1–25.

Ebarasi, L., He, L., Hultenby, K., Takemoto, M., Betsholtz, C., Tryggvason, K., and Majumdar, A. (2009). A reverse genetic screen in the zebrafish identifies crb2b as a regulator of the glomerular filtration barrier. Dev. Biol. *334*, 1–9.

Ebarasi, L., Ashraf, S., Bierzynska, A., Gee, H.Y., McCarthy, H.J., Lovric, S., Sadowski, C.E., Pabst, W., Vega-Warner, V., Fang, H., et al. (2015). Defects of CRB2 cause steroid-resistant nephrotic syndrome. Am. J. Hum. Genet. *96*, 153–161.

El-Hattab, A.W., and Scaglia, F. (2013). Mitochondrial DNA depletion syndromes: review and updates of genetic basis, manifestations, and therapeutic options. Neurotherapeutics *10*, 186–198.

El-Hattab, A.W., and Scaglia, F. (2016). Mitochondrial cytopathies. Cell Calcium *60*, 199–206.

Emma, F., and Salviati, L. (2017). Mitochondrial cytopathies and the kidney. Néphrologie & Thérapeutique *13*, S23–S28.

Emma, F., Bertini, E., Salviati, L., and Montini, G. (2012). Renal involvement in mitochondrial cytopathies. Pediatr. Nephrol. *27*, 539–550.

Emma, F., Montini, G., Parikh, S.M., and Salviati, L. (2016). Mitochondrial dysfunction in inherited renal disease and acute kidney injury. Nat. Rev. Nephrol. *12*, 267–280.

Emmanuele, V., López, L.C., Berardo, A., Naini, A., Tadesse, S., Wen, B., D'Agostino, E., Solomon, M., DiMauro, S., Quinzii, C., et al. (2012). Heterogeneity of Coenzyme Q 10 Deficiency. Arch. Neurol. *69*, 978–983.

Farooqui, A.A., Antony, P., Ong, W.Y., Horrocks, L.A., and Freysz, L. (2004). Retinoic acid-mediated phospholipase A2 signaling in the nucleus. Brain Res. Rev. *45*, 179–195.

Féraud, O., Valogne, Y., Melkus, M.W., Zhang, Y., Oudrhiri, N., Haddad, R., Daury, A., Rocher, C., Larbi, A., Duquesnoy, P., et al. (2016). Donor dependent variations in hematopoietic differentiation among embryonic and induced pluripotent stem cell lines. PLoS One *11*, 1–22.

Ferrara, N. (1999). Role of vascular endothelial growth factor in the regulation of angiogenesis. Kidney Int. *56*, 794–814.

Fischer, E.A., Verpont, M.C., Garrett-Sinha, L.A., Ronco, P.M., and Rossert, J.A. (2001). Klf6 is a zinc finger protein expressed in a cell-specific manner during kidney development. J Am Soc Nephrol.

Forbes, T.A., Howden, S.E., Lawlor, K., Phipson, B., Maksimovic, J., Hale, L., Wilson, S., Quinlan, C., Ho, G., Holman, K., et al. (2018). Patient-iPSC-Derived Kidney Organoids Show Functional Validation of a Ciliopathic Renal Phenotype and Reveal Underlying Pathogenetic Mechanisms. Am. J. Hum. Genet. *102*, 816–831.

Fornoni, A., Sageshima, J., Wei, C., Merscher-Gomez, S., Aguillon-Prada, R., Jauregui, A.N., Li, J., Mattiazzi, A., Ciancio, G., Chen, L., et al. (2011). Rituximab Targets Podocytes in Recurrent Focal Segmental Glomerulosclerosis. Sci. Transl. Med. *3*, 85ra46-85ra46.

Freedman, B.S., Brooks, C.R., Lam, A.Q., Fu, H., Morizane, R., Agrawal, V., Saad, A.F., Li, M.K., Hughes, M.R., Werff, R. Vander, et al. (2015). Modelling kidney disease with CRISPR-mutant kidney organoids derived from human pluripotent epiblast spheroids. Nat. Commun. *6*, 1–13.

Frei, B., Kim, M.C., and Ames, B.N. (1990). Ubiquinol-10 is an effective lipid-soluble antioxidant at physiological concentrations. Proc. Natl. Acad. Sci. *87*, 4879–4883.

Gao, D., Vela, I., Sboner, A., Iaquinta, P.J., Karthaus, W.R., Gopalan, A., Dowling, C., Wanjala, J.N., Undvall, E.A., Arora, V.K., et al. (2014). Organoid Cultures Derived from Patients with Advanced Prostate Cancer. Cell *159*, 176–187.

Garg, P., Verma, R., Cook, L., Soofi, A., Venkatareddy, M., George, B., Mizuno, K., Gurniak, C., Witke, W., and Holzman, L.B. (2010). Actin-depolymerizing Factor Cofilin-1 Is Necessary in Maintaining Mature Podocyte Architecture. J. Biol. Chem. *285*, 22676–22688.

Garreta, E., Prado, P., Tarantino, C., Oria, R., Fanlo, L., Martí, E., Zalvidea, D., Trepat, X., Roca-Cusachs, P., Gavaldà-Navarro, A., et al. (2019). Fine tuning the extracellular environment accelerates the derivation of kidney organoids from human pluripotent stem cells. Nat. Mater. *18*, 397–405.

Gbadegesin, R.A., Lavin, P.J., Hall, G., Bartkowiak, B., Homstad, A., Jiang, R., Wu, G., Byrd, A., Lynn, K., Wolfish, N., et al. (2012). Inverted formin 2 mutations with variable expression in patients with sporadic and hereditary focal and segmental glomerulosclerosis. Kidney Int. *81*, 94–99.

Gee, H.Y., Saisawat, P., Ashraf, S., Hurd, T.W., Vega-Warner, V., Fang, H., Beck, B.B., Gribouval, O., Zhou, W., Diaz, K.A., et al. (2013). ARHGDIA mutations cause nephrotic syndrome via defective RHO GTPase signaling. J. Clin. Invest. *123*, 3243–3253.

Genovese, G., Friedman, D.J., Ross, M.D., Lecordier, L., Uzureau, P., Freedman, B.I., Bowden, D.W., Langefeld, C.D., Oleksyk, T.K., Knob, A.L.U., et al. (2010). Association of Trypanolytic ApoL1 African Americans. 67–68.

Georgas, K., Rumballe, B., Valerius, M.T., Chiu, H.S., Thiagarajan, R.D., Lesieur, E., Aronow, B.J., Brunskill, E.W., Combes, A.N., Tang, D., et al. (2009). Analysis of early nephron patterning reveals a role for distal RV proliferation in fusion to the ureteric tip via a cap mesenchyme-derived connecting segment. Dev. Biol. *332*, 273–286.

Gharib, S.A., Pippin, J.W., Ohse, T., Pickering, S.G., Krofft, R.D., and Shankland, S.J. (2014). Transcriptional landscape of glomerular parietal epithelial cells. PLoS One *9*.

Gigante, M., Pontrelli, P., Montemurno, E., Roca, L., Aucella, F., Penza, R., Caridi, G., Ranieri, E., Ghiggeri, G.M., and Gesualdo, L. (2009). CD2AP mutations are associated with sporadic nephrotic syndrome and focal segmental glomerulosclerosis (FSGS). Nephrol. Dial. Transplant. *24*, 1858–1864.

Gigante, M., Caridi, G., Montemurno, E., Soccio, M., D'Apolito, M., Cerullo, G., Aucella, F., Schirinzi, A., Emma, F., Massella, L., et al. (2011). TRPC6 Mutations in Children with Steroid-Resistant Nephrotic Syndrome and Atypical Phenotype. Clin. J. Am. Soc. Nephrol. *6*, 1626–1634.

Graham, V., Khudyakov, J., Ellis, P., and Pevny, L. (2003). SOX2 functions to maintain neural progenitor identity. Neuron *39*, 749–765.

Greggio, C., De Franceschi, F., Figueiredo-Larsen, M., Gobaa, S., Ranga, A., Semb, H., Lutolf, M., and Grapin-Botton, A. (2013). Artificial three-dimensional niches deconstruct pancreas development in vitro. Development *140*, 4452–4462.

Greka, A., and Mundel, P. (2012). Cell biology and pathology of podocytes. Annu. Rev. Physiol. *74*, 299–323.

Haensly, W.E., Granger, H.J., Morris, A.C., and Cioffe, C. (1982). Proximal-tubule-like epithelium in Bowman's capsule in spontaneously hypertensive rats. Changes with age. Am. J. Pathol. *107*, 92–97.

Harder, J.L., Menon, R., Otto, E.A., Zhou, J., Eddy, S., Wys, N.L., O'Connor, C., Luo, J., Nair, V., Cebrian, C., et al. (2019). Organoid single cell profiling identifies a transcriptional signature of glomerular disease. JCI Insight *4*.

Hartleben, B., Schweizer, H., Lübben, P., Bartram, M.P., Möller, C.C., Herr, R., Wei, C., Neumann-Haefelin, E., Schermer, B., Zentgraf, H., et al. (2008). Neph-Nephrin Proteins Bind the Par3-Par6-Atypical Protein Kinase C (aPKC) Complex to Regulate Podocyte Cell Polarity. J. Biol. Chem. *283*, 23033–23038.

Hartleben, B., Widmeier, E., Wanner, N., Schmidts, M., Kim, S.T., Schneider, L., Mayer, B., Kerjaschki, D., Miner, J.H., Walz, G., et al. (2012). Role of the Polarity Protein Scribble for Podocyte Differentiation and Maintenance. PLoS One *7*, e36705.

He, J.C., Lu, T.-C., Fleet, M., Sunamoto, M., Husain, M., Fang, W., Neves, S., Chen, Y., Shankland, S., Iyengar, R., et al. (2007a). Retinoic Acid Inhibits HIV-1-Induced Podocyte Proliferation through the cAMP Pathway. J. Am. Soc. Nephrol. *18*, 93–102.

He, L., Sun, Y., Patrakka, J., Mostad, P., Norlin, J., Xiao, Z., Andrae, J., Tryggvason, K., Samuelsson, T., Betsholtz, C., et al. (2007b). Glomerulus-specific mRNA transcripts and proteins identified through kidney expressed sequence tag database analysis. Kidney Int. *71*, 889–900.

Heeringa, S.F., Chernin, G., Chaki, M., Zhou, W., Sloan, A.J., Ji, Z., Xie, L.X., Salviati, L., Hurd, T.W., Vega-Warner, V., et al. (2011). COQ6 mutations in human patients produce nephrotic syndrome with sensorineural deafness. J. Clin. Invest. *121*, 2013–2024.

Herebian, D., Seibt, A., Smits, S.H.J., Rodenburg, R.J., Mayatepek, E., and Distelmaier, F. (2017). 4-Hydroxybenzoic acid restores CoQ 10 biosynthesis in human COQ2 deficiency. Ann. Clin. Transl. Neurol. *4*, 902–908.

Herman-Edelstein, M., Scherzer, P., Tobar, A., Levi, M., and Gafter, U. (2014). Altered renal lipid metabolism and renal lipid accumulation in human diabetic nephropathy. J. Lipid Res. *55*, 561–572.

Hidalgo-Gutiérrez, A., Barriocanal-Casado, E., Bakkali, M., Díaz-Casado, M.E., Sánchez-Maldonado, L., Romero, M., Sayed, R.K., Prehn, C., Escames, G., Duarte, J., et al. (2019). β-RA reduces DMQ/CoQ ratio and rescues the encephalopathic phenotype in Coq9 R239X mice. EMBO Mol. Med. *11*, e9466.

Hildebrandt, F. (2010). Genetic kidney diseases. Lancet (London, England) *375*, 1287–1295.

Hinkes, B.G., Mucha, B., Vlangos, C.N., Gbadegesin, R., Liu, J., Hasselbacher, K., Hangan, D., Ozaltin, F., Zenker, M., and Hildebrandt, F. (2007). Nephrotic Syndrome in the First Year of Life: Two Thirds of Cases Are Caused by Mutations in 4 Genes (NPHS1, NPHS2, WT1, and LAMB2). Pediatrics *119*, e907–e919.

Hisha, H., Tanaka, T., Kanno, S., Tokuyama, Y., Komai, Y., Ohe, S., Yanai, H., Omachi, T., and Ueno, H. (2013). Establishment of a Novel Lingual Organoid Culture System: Generation of Organoids Having Mature Keratinized Epithelium from Adult Epithelial Stem Cells. Sci. Rep. *3*, 3224.

Hochane, M., van den Berg, P.R., Fan, X., Bérenger-Currias, N., Adegeest, E., Bialecka, M., Nieveen, M., Menschaart, M., Chuva de Sousa Lopes, S.M., and Semrau, S. (2019). Single-cell transcriptomics reveals gene expression dynamics of human fetal kidney development.

Hoeflich, K.P., Herter, S., Tien, J., Wong, L., Berry, L., Chan, J., O'Brien, C., Modrusan, Z., Seshagiri, S., Lackner, M., et al. (2009). Antitumor efficacy of the novel RAF inhibitor GDC-0879 is predicted by BRAF V600E mutational status and sustained extracellular signal-regulated kinase/mitogen-activated protein kinase pathway suppression. Cancer Res. *69*, 3042–3051.

Hoffman, L.M., Garcha, K., Karamboulas, K., Cowan, M.F., Drysdale, L.M., Horton, W.A., and Underhill, T.M. (2006). BMP action in skeletogenesis involves attenuation of retinoid signaling. J. Cell Biol. *174*, 101–113.

Huber, T.B. (2003). Molecular basis of the functionalpodocin-nephrin complex: mutations in the NPHS2 gene disrupt nephrin targeting to lipid raft microdomains. Hum. Mol. Genet. *12*, 3397–3405.

Huber, T.B., Köttgen, M., Schilling, B., Walz, G., and Benzing, T. (2001). Interaction with Podocin Facilitates Nephrin Signaling. J. Biol. Chem. *276*, 41543–41546.

Hughson, M., Farris, A.B., Douglas-Denton, R., Hoy, W.E., and Bertram, J.F. (2003). Glomerular number and size in autopsy kidneys: The relationship to birth weight. Kidney Int. *63*, 2113–2122.

Hull, R.P., and Goldsmith, D.J.A. (2008). Nephrotic syndrome in adults. BMJ *336*, 1185–1189.

Ichimura, K., Kurihara, H., and Sakai, T. (2007). Actin filament organization of foot processes in vertebrate glomerular podocytes. Cell Tissue Res. *329*, 541–557.

Iglesias, D.M., Hueber, P.-A., Chu, L., Campbell, R., Patenaude, A.-M., Dziarmaga, A.J., Quinlan, J., Mohamed, O., Dufort, D., and Goodyer, P.R. (2007). Canonical WNT signaling during kidney development. Am. J. Physiol. Physiol. *293*, F494–F500.

Inrig, J.K., Califf, R.M., Tasneem, A., Vegunta, R.K., Molina, C., Stanifer, J.W., Chiswell, K., and Patel, U.D. (2014). The landscape of clinical trials in nephrology: A systematic review of clinicaltrials.gov. Am. J. Kidney Dis. *63*, 771–780.

Jakobs, B.S., van den Heuvel, L.P., Smeets, R.J.P., de Vries, M.C., Hien, S., Schaible, T., Smeitink, J. a M., Wevers, R. a, Wortmann, S.B., and Rodenburg, R.J.T. (2013). A novel mutation in COQ2 leading to fatal infantile multisystem disease. J. Neurol. Sci. *326*, 24–28.

Jha, V., Garcia-Garcia, G., Iseki, K., Li, Z., Naicker, S., Plattner, B., Saran, R., Wang, A.Y.-M., and Yang, C.-W. (2013). Chronic kidney disease: global dimension and perspectives. Lancet (London, England) *382*, 260–272.

Jiang, L., Ding, J., Tsai, H., Li, L., Feng, Q., Miao, J., and Fan, Q. (2011). Over-expressing transient receptor potential cation channel 6 in podocytes induces cytoskeleton rearrangement through increases of intracellular Ca 2+ and RhoA activation. Exp. Biol. Med. *236*, 184–193.

Jiang, T., Wang, Z., Proctor, G., Moskowitz, S., Liebman, S.E., Rogers, T., Lucia, M.S., Li, J., and Levi, M. (2005). Diet-induced Obesity in C57BL/6J Mice Causes Increased Renal Lipid Accumulation and Glomerulosclerosis via a Sterol Regulatory Element-binding Protein-1c-dependent Pathway. J. Biol. Chem. *280*, 32317–32325.

Jones, N., Blasutig, I.M., Eremina, V., Ruston, J.M., Bladt, F., Li, H., Huang, H., Larose, L., Li, S.S.-C., Takano, T., et al. (2006). Nck adaptor proteins link nephrin to the actin cytoskeleton of kidney podocytes. Nature *440*, 818–823.

Kanno, S., Oda, N., Abe, M., Terai, Y., Ito, M., Shitara, K., Tabayashi, K., Shibuya, M., and Sato, Y. (2000). Roles of two VEGF receptors, Flt-1 and KDR, in the signal transduction of VEGF effects in human vascular endothelial cells. Oncogene *19*, 2138–2146.

Kao, W.H.L., Klag, M.J., Meoni, L.A., Reich, D., Berthier-Schaad, Y., Li, M., Coresh, J., Patterson, N., Tandon, A., Powe, N.R., et al. (2008). MYH9 is associated with nondiabetic end-stage renal disease in African Americans. Nat. Genet. *40*, 1185–1192.

Karaiskos, N., Rahmatollahi, M., Boltengagen, A., Liu, H., Hoehne, M., Rinschen, M., Schermer, B., Benzing, T., Rajewsky, N., Kocks, C., et al. (2018). A Single-Cell Transcriptome Atlas of the Mouse Glomerulus. J. Am. Soc. Nephrol. *29*, 2060–2068.

Karle, S.M., Uetz, B., Ronner, V., Glaeser, L., Hildebrandt, F., and Fuchshuber, A. (2002). Novel mutations in NPHS2 detected in both familial and sporadic steroid-resistant nephrotic syndrome. J. Am. Soc. Nephrol. *13*, 388–393.

Kawamukai, M. (2016). Biosynthesis of coenzyme Q in eukaryotes. Biosci. Biotechnol. Biochem. *80*, 23–33.

Kerjaschki, D. (2001). Caught flat-footed: podocyte damage and the molecular bases of focal

glomerulosclerosis. J. Clin. Invest. *108*, 1583–1587.

Kestilä, M., Lenkkeri, U., Männikkö, M., Lamerdin, J., McCready, P., Putaala, H., Ruotsalainen, V., Morita, T., Nissinen, M., Herva, R., et al. (1998). Positionally cloned gene for a novel glomerular protein--nephrin--is mutated in congenital nephrotic syndrome. Mol. Cell *1*, 575–582.

Kim, J.M. (2003). CD2-Associated Protein Haploinsufficiency Is Linked to Glomerular Disease Susceptibility. Science (80-.). *300*, 1298–1300.

Kim, D., and Dressler, G.R. (2005). Nephrogenic Factors Promote Differentiation of Mouse Embryonic Stem Cells into Renal Epithelia. J. Am. Soc. Nephrol. *16*, 3527–3534.

Kim, E.Y., Anderson, M., Wilson, C., Hagmann, H., Benzing, T., and Dryer, S.E. (2013). NOX2 interacts with podocyte TRPC6 channels and contributes to their activation by diacylglycerol: essential role of podocin in formation of this complex. Am. J. Physiol. Physiol. *305*, C960–C971.

Kirby, A., Gnirke, A., Jaffe, D.B., Barešová, V., Pochet, N., Blumenstiel, B., Ye, C., Aird, D., Stevens, C., Robinson, J.T., et al. (2013). Mutations causing medullary cystic kidney disease type 1 lie in a large VNTR in MUC1 missed by massively parallel sequencing. Nat. Genet.

Kiss, E., Kränzlin, B., Wagenblaβ, K., Bonrouhi, M., Thiery, J., Gröne, E., Nordström, V., Teupser, D., Gretz, N., Malle, E., et al. (2013). Lipid Droplet Accumulation Is Associated with an Increase in Hyperglycemia-Induced Renal Damage. Am. J. Pathol. *182*, 727–741.

Kitamoto, Y., Tokunaga, H., and Tomita, K. (1997). Vascular endothelial growth factor is an essential molecule for mouse kidney development: Glomerulogenesis and nephrogenesis. J. Clin. Invest. *99*, 2351–2357.

Kleiner, G., Barca, E., Ziosi, M., Emmanuele, V., Xu, Y., Hidalgo-Gutierrez, A., Qiao, C., Tadesse, S., Area-Gomez, E., Lopez, L.C., et al. (2018). CoQ10 supplementation rescues nephrotic syndrome through normalization of H2S oxidation pathway. Biochim. Biophys. Acta - Mol. Basis Dis. *1864*, 3708–3722.

Kobayashi, A., Valerius, M.T., Mugford, J.W., Carroll, T.J., Self, M., Oliver, G., and McMahon, A.P. (2008). Six2 Defines and Regulates a Multipotent Self-Renewing Nephron Progenitor Population throughout Mammalian Kidney Development. Cell Stem Cell *3*, 169–181.

Kobayashi, T., Tanaka, H., Kuwana, H., Inoshita, S., Teraoka, H., Sasaki, S., and Terada, Y. (2005). Wnt4-transformed mouse embryonic stem cells differentiate into renal tubular cells. Biochem. Biophys. Res. Commun. *336*, 585–595.

Königshausen, E., and Sellin, L. (2017). Recent Treatment Advances and New Trials in Adult Nephrotic Syndrome. Biomed Res. Int. *2017*, 1–9.

Kopp, J.B., Smith, M.W., Nelson, G.W., Johnson, R.C., Freedman, B.I., Bowden, D.W., Oleksyk, T., McKenzie, L.M., Kajiyama, H., Ahuja, T.S., et al. (2008). MYH9 is a major-effect risk gene for focal segmental glomerulosclerosis. Nat. Genet. *40*, 1175–1184.

Kowalczyk, M.S., Tirosh, I., Heckl, D., Rao, T.N., Dixit, A., Haas, B.J., Schneider, R.K., Wagers,

A.J., Ebert, B.L., and Regev, A. (2015). Single-cell RNA-seq reveals changes in cell cycle and differentiation programs upon aging of hematopoietic stem cells. Genome Res. *25*, 1860–1872.

Kramann, R., Kusaba, T., and Humphreys, B.D. (2015). Who regenerates the kidney tubule? Nephrol. Dial. Transplant. *30*, 903–910.

Kreidberg, J.A., Sariola, H., Loring, J.M., Maeda, M., Pelletier, J., Housman, D., and Jaenisch, R. (1993). WT-1 is required for early kidney development. Cell *74*, 679–691.

Kuppe, C., Leuchtle, K., Wagner, A., Kabgani, N., Saritas, T., Puelles, V.G., Smeets, B., Hakroush, S., van der Vlag, J., Boor, P., et al. (2019). Novel parietal epithelial cell subpopulations contribute to focal segmental glomerulosclerosis and glomerular tip lesions. Kidney Int.

Kusaba, T., Lalli, M., Kramann, R., Kobayashi, A., and Humphreys, B.D. (2014). Differentiated kidney epithelial cells repair injured proximal tubule. Proc. Natl. Acad. Sci. *111*, 1527–1532.

Kwong, A.K., Chiu, A.T., Tsang, M.H., Rodenburg, R.J.T., Smeitink, J., and Chung, B.H. (2019). A fatal case of COQ7 -associated primary coenzyme Q 10 deficiency. J. Inherit. Metab. Dis. 1–7.

Lake, B.B., Codeluppi, S., Yung, Y.C., Gao, D., Chun, J., Kharchenko, P. V., Linnarsson, S., and Zhang, K. (2017). A comparative strategy for single-nucleus and single-cell transcriptomes confirms accuracy in predicted cell-type expression from nuclear RNA. Sci. Rep. *7*, 6031.

Lam, A.Q., Freedman, B.S., Morizane, R., Lerou, P.H., Valerius, M.T., and Bonventre, J. V. (2014). Rapid and Efficient Differentiation of Human Pluripotent Stem Cells into Intermediate Mesoderm That Forms Tubules Expressing Kidney Proximal Tubular Markers. J. Am. Soc. Nephrol. *25*, 1211–1225.

Lancaster, M.A., Renner, M., Martin, C.-A., Wenzel, D., Bicknell, L.S., Hurles, M.E., Homfray, T., Penninger, J.M., Jackson, A.P., and Knoblich, J.A. (2013). Cerebral organoids model human brain development and microcephaly. Nature *501*, 373–379.

LeBleu, V.S.S., Teng, Y., O'Connell, J.T.T., Charytan, D., Müller, G.A.A., Müller, C.A.A., Sugimoto, H., and Kalluri, R. (2013). Identification of human epididymis protein-4 as a fibroblast-derived mediator of fibrosis. Nat. Med. *19*, 227–231.

Lee, J.W., Chou, C.-L., and Knepper, M.A. (2015). Deep Sequencing in Microdissected Renal Tubules Identifies Nephron Segment–Specific Transcriptomes. J. Am. Soc. Nephrol. *26*, 2669–2677.

Lee, Y.S., Yap, H.K., Barshop, B.A., Lee, Y.S., Rajalingam, S., and Loke, K.Y. (2001). Mitochondrial tubulopathy: the many faces of mitochondrial disorders. Pediatr. Nephrol. *16*, 710–712.

Leroy, X., Copin, M.C., Devisme, L., Buisine, M.P., Aubert, J.P., Gosselin, B., and Porchet, N. (2002). Expression of human mucin genes in normal kidney and renal cell carcinoma. Histopathology.

Levine, L. (2001). Stimulated release of arachidonic acid by agonists of the peroxisome proliferator-activated receptor and retinoic acid receptors. Prostaglandins, Leukot. Essent. Fat. Acids *65*, 229–232.

Li, M., Armelloni, S., Zennaro, C., Wei, C., Corbelli, A., Ikehata, M., Berra, S., Giardino, L., Mattinzoli, D., Watanabe, S., et al. (2015). BDNF repairs podocyte damage by microRNA-mediated increase of actin polymerization. J. Pathol.

Li, X., Nadauld, L., Ootani, A., Corney, D.C., Pai, R.K., Gevaert, O., Cantrell, M.A., Rack, P.G., Neal, J.T., Chan, C.W.M., et al. (2014a). Oncogenic transformation of diverse gastrointestinal tissues in primary organoid culture. Nat. Med. *20*, 769–777.

Li, X., Dai, Y., Chuang, P.Y., and He, J.C. (2014b). Induction of Retinol Dehydrogenase 9 Expression in Podocytes Attenuates Kidney Injury. J. Am. Soc. Nephrol. *25*, 1933–1941.

Liapis, H., Romagnani, P., and Anders, H.-J. (2013). New Insights into the Pathology of Podocyte Loss. Am. J. Pathol. *183*, 1364–1374.

Liaw, A and Wiener, M. (2002). Classification and Regression by randomForest. R News *2(3)*, 18--22.

Lindström, N.O., Guo, J., Kim, A.D., Tran, T., Guo, Q., De Sena Brandine, G., Ransick, A., Parvez, R.K., Thornton, M.E., Baskin, L., et al. (2018a). Conserved and Divergent Features of Mesenchymal Progenitor Cell Types within the Cortical Nephrogenic Niche of the Human and Mouse Kidney. J. Am. Soc. Nephrol. *29*, 806–824.

Lindström, N.O., De Sena Brandine, G., Tran, T., Ransick, A., Suh, G., Guo, J., Kim, A.D., Parvez, R.K., Ruffins, S.W., Rutledge, E.A., et al. (2018b). Progressive Recruitment of Mesenchymal Progenitors Reveals a Time-Dependent Process of Cell Fate Acquisition in Mouse and Human Nephrogenesis. Dev. Cell *45*, 651–660.e4.

Lipkowitz, M.S., Freedman, B.I., Langefeld, C.D., Comeau, M.E., Bowden, D.W., Kao, W.H.L., Astor, B.C., Bottinger, E.P., Iyengar, S.K., Klotman, P.E., et al. (2013). Apolipoprotein L1 gene variants associate with hypertension-attributed nephropathy and the rate of kidney function decline in African Americans. Kidney Int. *83*, 114–120.

Little, M.H., and McMahon, A.P. (2012). Mammalian kidney development: Principles, progress, and projections. Cold Spring Harb. Perspect. Biol. *4*, 3.

Little, M.H., Brennan, J., Georgas, K., Davies, J.A., Davidson, D.R., Baldock, R.A., Beverdam, A., Bertram, J.F., Capel, B., Chiu, H.S., et al. (2007). A high-resolution anatomical ontology of the developing murine genitourinary tract. Gene Expr. Patterns *7*, 680–699.

Little, M.H., Combes, A.N., and Takasato, M. (2016). Understanding kidney morphogenesis to guide renal tissue regeneration. Nat. Rev. Nephrol. *12*, 624–635.

Little, M.H., Hale, L.J., Howden, S.E., and Kumar, S. V (2019). Generating Kidney from Stem Cells. Annu. Rev. Physiol. *81*, 335–357.

Lohman, D.C., Forouhar, F., Beebe, E.T., Stefely, M.S., Minogue, C.E., Ulbrich, A., Stefely, J.A., Sukumar, S., Luna-Sanchez, M., Jochem, A., et al. (2014). Mitochondrial COQ9 is a lipid-binding protein that associates with COQ7 to enable coenzyme Q biosynthesis. Proc. Natl. Acad. Sci. *111*, E4697–E4705.

de Lonlay, P., Valnot, I., Barrientos, A., Gorbatyuk, M., Tzagoloff, A., Taanman, J.W., Benayoun, E., Chrétien, D., Kadhom, N., Lombès, A., et al. (2001). A mutant mitochondrial respiratory chain assembly protein causes complex III deficiency in patients with tubulopathy, encephalopathy and liver failure. Nat. Genet. *29*, 57–60.

Lopez-Martin, J.M., Salviati, L., Trevisson, E., Montini, G., DiMauro, S., Quinzii, C., Hirano, M., Rodriguez-Hernandez, A., Cordero, M.D., Sanchez-Alcazar, J.A., et al. (2007). Missense mutation of the COQ2 gene causes defects of bioenergetics and de novo pyrimidine synthesis. Hum. Mol. Genet. *16*, 1091–1097.

López, L.C., Schuelke, M., Quinzii, C.M., Kanki, T., Rodenburg, R.J.T., Naini, A., DiMauro, S., and Hirano, M. (2006). Leigh Syndrome with Nephropathy and CoQ10 Deficiency Due to decaprenyl diphosphate synthase subunit 2 (PDSS2) Mutations. Am. J. Hum. Genet. *79*, 1125–1129.

Love, M.I., Huber, W., and Anders, S. (2014). Moderated estimation of fold change and dispersion for RNA-seq data with DESeq2. Genome Biol. *15*, 1–21.

Lowik, M., Levtchenko, E., Westra, D., Groenen, P., Steenbergen, E., Weening, J., Lilien, M., Monnens, L., and Heuvel, L. Van Den (2008). Bigenic heterozygosity and the development of steroid-resistant focal segmental glomerulosclerosis. Nephrol. Dial. Transplant. *23*, 3146–3151.

Löwik, M.M., Groenen, P.J.T.A., Pronk, I., Lilien, M.R., Goldschmeding, R., Dijkman, H.B., Levtchenko, E.N., Monnens, L.A., and van den Heuvel, L.P. (2007). Focal segmental glomerulosclerosis in a patient homozygous for a CD2AP mutation. Kidney Int. *72*, 1198–1203.

Lyon, M.F., and Hulse, E. V (1971). An inherited kidney disease of mice resembling human nephronophthisis. J. Med. Genet. *8*, 41–48.

Madhavan, S.M., O'Toole, J.F., Konieczkowski, M., Ganesan, S., Bruggeman, L.A., and Sedor, J.R. (2011). APOL1 Localization in Normal Kidney and Nondiabetic Kidney Disease. J. Am. Soc. Nephrol. *22*, 2119–2128.

Mae, S.-I., Shirasawa, S., Yoshie, S., Sato, F., Kanoh, Y., Ichikawa, H., Yokoyama, T., Yue, F., Tomotsune, D., and Sasaki, K. (2010). Combination of small molecules enhances differentiation of mouse embryonic stem cells into intermediate mesoderm through BMP7-positive cells. Biochem. Biophys. Res. Commun. *393*, 877–882.

Magella, B., Adam, M., Potter, A.S., Venkatasubramanian, M., Chetal, K., Hay, S.B., Salomonis, N., and Potter, S.S. (2018). Cross-platform single cell analysis of kidney development shows stromal cells express Gdnf. Dev. Biol. *434*, 36–47.

Magner, M., Dvorakova, V., Tesarova, M., Mazurova, S., Hansikova, H., Zahorec, M., Brennerova, K., Bzduch, V., Spiegel, R., Horovitz, Y., et al. (2015). TMEM70 deficiency: long-term outcome of 48 patients. J. Inherit. Metab. Dis. *38*, 417–426.

McCracken, K.W., Catá, E.M., Crawford, C.M., Sinagoga, K.L., Schumacher, M., Rockich, B.E., Tsai, Y.-H., Mayhew, C.N., Spence, J.R., Zavros, Y., et al. (2014). Modelling human development and disease in pluripotent stem-cell-derived gastric organoids. Nature *516*, 400–404.

Mele, C., Iatropoulos, P., Donadelli, R., Calabria, A., Maranta, R., Cassis, P., Buelli, S., Tomasoni, S., Piras, R., Krendel, M., et al. (2011). MYO1E Mutations and Childhood Familial Focal Segmental Glomerulosclerosis. N. Engl. J. Med. *365*, 295–306.

Menon, R., Otto, E.A., Kokoruda, A., Zhou, J., Zhang, Z., Yoon, E., Chen, Y.-C., Troyanskaya, O., Spence, J.R., Kretzler, M., et al. (2018). Single-cell analysis of progenitor cell dynamics and lineage specification in the human fetal kidney. Development *145*, dev164038.

Merscher-Gomez, S., Guzman, J., Pedigo, C.E., Lehto, M., Aguillon-Prada, R., Mendez, A., Lassenius, M.I., Forsblom, C., Yoo, T., Villarreal, R., et al. (2013). Cyclodextrin Protects Podocytes in Diabetic Kidney Disease. Diabetes *62*, 3817–3827.

Metsuyanim, S., Harari-Steinberg, O., Buzhor, E., Omer, D., Pode-Shakked, N., Ben-, H., Hur, Halperin, R., Schneider, D., and Dekel, B. (2009). Expression of Stem Cell Markers in the Human Fetal Kidney. PLoS One *4*, e6709.

Meyer, T.W., Bennett, P.H., and Nelson, R.G. (1999). Podocyte number predicts long-term urinary albumin excretion in Pima Indians with Type II diabetes and microalbuminuria. Diabetologia *42*, 1341–1344.

Mollet, J., Giurgea, I., Schlemmer, D., Dallner, G., Chretien, D., Delahodde, A., Bacq, D., de Lonlay, P., Munnich, A., and Rötig, A. (2007). Prenyldiphosphate synthase, subunit 1 (PDSS1) and OH-benzoate polyprenyltransferase (COQ2) mutations in ubiquinone deficiency and oxidative phosphorylation disorders. J. Clin. Invest. *117*, 765–772.

Mondrinos, M.J., Jones, P.L., Finck, C.M., and Lelkes, P.I. (2014). Engineering De Novo Assembly of Fetal Pulmonary Organoids. Tissue Eng. Part A *20*, 2892–2907.

Montini, G., Malaventura, C., and Salviati, L. (2008). Early Coenzyme Q10 Supplementation in Primary Coenzyme Q10 Deficiency. N. Engl. J. Med. *358*, 2849–2850.

Moon, P.O., Chepenik, K.P., and Kochhar, D.M. (1986). Effects of retinoic acid treatment on release of arachidonic acid by chondrogenic cells in response to ionophore A23187. Life Sci. *38*, 1445–1450.

Morizane, R., and Bonventre, J. V. (2017a). Kidney Organoids: A Translational Journey. Trends Mol. Med. *23*, 246–263.

Morizane, R., and Bonventre, J. V (2017b). Generation of nephron progenitor cells and kidney organoids from human pluripotent stem cells. Nat. Protoc. *12*, 195–207.

Morizane, R., Monkawa, T., and Itoh, H. (2009). Differentiation of murine embryonic stem and induced pluripotent stem cells to renal lineage in vitro. Biochem. Biophys. Res. Commun. *390*, 1334–1339.

Morizane, R., Monkawa, T., Fujii, S., Yamaguchi, S., Homma, K., Matsuzaki, Y., Okano, H., and Itoh, H. (2013). Kidney Specific Protein-Positive Cells Derived from Embryonic Stem Cells Reproduce Tubular Structures In Vitro and Differentiate into Renal Tubular Cells. PLoS One *8*, e64843.

Morizane, R., Lam, A.Q., Freedman, B.S., Kishi, S., Valerius, M.T., and Bonventre, J. V. (2015). Nephron organoids derived from human pluripotent stem cells model kidney development and injury. Nat. Biotechnol. *33*, 1193–1200.

Morris, A.A.M., Taylor, R.W., Birch-Machin, M.A., Jackson, M.J., Coulthard, M.G., Bindoff, L.A., Welch, R.J., Howell, N., and Turnbull, D.M. (1995). Neonatal Fanconi syndrome due to deficiency of complex III of the respiratory chain. Pediatr. Nephrol. *9*, 407–411.

Mundel, P., Heid, H.W., Mundel, T.M., Krüger, M., Reiser, J., and Kriz, W. (1997). Synaptopodin: An Actin-associated Protein in Telencephalic Dendrites and Renal Podocytes. J. Cell Biol. *139*, 193–204.

Najafian, B., Svarstad, E., Bostad, L., Gubler, M.-C., Tøndel, C., Whitley, C., and Mauer, M. (2011). Progressive podocyte injury and globotriaosylceramide (GL-3) accumulation in young patients with Fabry disease. Kidney Int. *79*, 663–670.

Nakajima, J., Eminoglu, T.F., Vatansever, G., Nakashima, M., Tsurusaki, Y., Saitsu, H., Kawashima, H., Matsumoto, N., and Miyake, N. (2014). A novel homozygous YARS2 mutation causes severe myopathy, lactic acidosis, and sideroblastic anemia 2. J. Hum. Genet. *59*, 229–232.

Nanduri, L.S.Y., Baanstra, M., Faber, H., Rocchi, C., Zwart, E., de Haan, G., van Os, R., and Coppes, R.P. (2014). Purification and Ex Vivo Expansion of Fully Functional Salivary Gland Stem Cells. Stem Cell Reports *3*, 957–964.

Nguyen, Q.H., Lukowski, S.W., Chiu, H.S., Senabouth, A., Bruxner, T.J.C., Christ, A.N., Palpant, N.J., and Powell, J.E. (2018). Single-cell RNA-seq of human induced pluripotent stem cells reveals cellular heterogeneity and cell state transitions between subpopulations. Genome Res. *28*, 1053–1066.

Nishikawa, M., Yanagawa, N., Kojima, N., Yuri, S., Hauser, P. V., Jo, O.D., and Yanagawa, N. (2012). Stepwise renal lineage differentiation of mouse embryonic stem cells tracing in vivo development. Biochem. Biophys. Res. Commun. *417*, 897–902.

Novgorodov, S.A., Szulc, Z.M., Luberto, C., Jones, J.A., Bielawski, J., Bielawska, A., Hannun, Y.A., and Obeid, L.M. (2005). Positively Charged Ceramide Is a Potent Inducer of Mitochondrial Permeabilization. J. Biol. Chem. *280*, 16096–16105.

Noy, N. (2010). Between Death and Survival: Retinoic Acid in Regulation of Apoptosis. Annu. Rev. Nutr. *30*, 201–217.

O'Connor, P.M. (2006). Renal oxygen delivery: matching delivery to metabolic demand. Clin. Exp. Pharmacol. Physiol. *33*, 961–967.

O'Sullivan, J.F., Morningstar, J.E., Yang, Q., Zheng, B., Gao, Y., Jeanfavre, S., Scott, J., Fernandez, C., Zheng, H., O'Connor, S., et al. (2017). Dimethylguanidino valeric acid is a marker of liver fat and predicts diabetes. J. Clin. Invest. *127*, 4394–4402.

O'Toole, J. (2014). Renal manifestations of genetic mitochondrial disease. Int. J. Nephrol. Renovasc. Dis. *7*, 57.

Ohba, S., He, X., Hojo, H., and McMahon, A.P. (2015). Distinct Transcriptional Programs Underlie Sox9 Regulation of the Mammalian Chondrocyte. Cell Rep. *12*, 229–243.

Ozaltin, F. (2014). Primary coenzyme Q10 (CoQ10) deficiencies and related nephropathies. Pediatr. Nephrol. *29*, 961–969.

Ozeir, M., Mühlenhoff, U., Webert, H., Lill, R., Fontecave, M., and Pierrel, F. (2011). Coenzyme Q Biosynthesis: Coq6 Is Required for the C5-Hydroxylation Reaction and Substrate Analogs Rescue Coq6 Deficiency. Chem. Biol. *18*, 1134–1142.

Ozone, C., Suga, H., Eiraku, M., Kadoshima, T., Yonemura, S., Takata, N., Oiso, Y., Tsuji, T., and Sasai, Y. (2016). Functional anterior pituitary generated in self-organizing culture of human embryonic stem cells. Nat. Commun. *7*, 10351.

Pagtalunan, M.E., Miller, P.L., Jumping-Eagle, S., Nelson, R.G., Myers, B.D., Rennke, H.G., Coplon, N.S., Sun, L., and Meyer, T.W. (1997). Podocyte loss and progressive glomerular injury in type II diabetes. J. Clin. Invest. *99*, 342–348.

Pandey, S., Shekhar, K., Regev, A., and Schier, A.F. (2018). Comprehensive Identification and Spatial Mapping of Habenular Neuronal Types Using Single-Cell RNA-Seq. Curr. Biol. *28*, 1052–1065.e7.

Papucci, L., Schiavone, N., Witort, E., Donnini, M., Lapucci, A., Tempestini, A., Formigli, L., Zecchi-Orlandini, S., Orlandini, G., Carella, G., et al. (2003). Coenzyme Q10 Prevents Apoptosis by Inhibiting Mitochondrial Depolarization Independently of Its Free Radical Scavenging Property. J. Biol. Chem. *278*, 28220–28228.

Park, J., Shrestha, R., Qiu, C., Kondo, A., Huang, S., Werth, M., Li, M., Barasch, J., and Suszták, K. (2018). Single-cell transcriptomics of the mouse kidney reveals potential cellular targets of kidney disease. Science (80-.). *360*, 758–763.

Parsa, A., Kao, W.H.L., Xie, D., Astor, B.C., Li, M., Hsu, C., Feldman, H.I., Parekh, R.S., Kusek, J.W., Greene, T.H., et al. (2013). APOL1 Risk Variants, Race, and Progression of Chronic Kidney Disease . N. Engl. J. Med. *369*, 2183–2196.

Pattaro, C., Teumer, A., Gorski, M., Chu, A.Y., Li, M., Mijatovic, V., Garnaas, M., Tin, A., Sorice, R., Li, Y., et al. (2016). Genetic associations at 53 loci highlight cell types and biological pathways relevant for kidney function. Nat. Commun. *7*, 1–19.

Paynter, N.P., Balasubramanian, R., Giulianini, F., Wang, D.D., Tinker, L.F., Gopal, S., Deik, A.A., Bullock, K., Pierce, K.A., Scott, J., et al. (2018). Metabolic Predictors of Incident Coronary Heart Disease in Women. Circulation *137*, 841–853.

Peng, M., Jarett, L., Meade, R., Madaio, M.P., Hancock, W.W., George, A.L., Neilson, E.G., and Gasser, D.L. (2004). Mutant prenyltransferase-like mitochondrial protein (PLMP) and mitochondrial abnormalities in kd/kd mice. Kidney Int. *66*, 20–28.

Peng, M., Falk, M.J., Haase, V.H., King, R., Polyak, E., Selak, M., Yudkoff, M., Hancock, W.W., Meade, R., Saiki, R., et al. (2008). Primary Coenzyme Q Deficiency in Pdss2 Mutant Mice Causes Isolated Renal Disease. PLoS Genet. *4*, e1000061.

Petroni, A., Blasevich, M., Papini, N., La Spada, P., and Galli, C. (1996). Changes in arachidonic acid levels and formation and in lipid synthesis in the human neuroblastoma SK-N-BE during retinoic acid-induced differentiation. J. Neurochem. *67*, 549–556.

Phipson, B., Er, P.X., Combes, A.N., Forbes, T.A., Howden, S.E., Zappia, L., Yen, H.-J., Lawlor, K.T., Hale, L.J., Sun, J., et al. (2019). Evaluation of variability in human kidney organoids. Nat. Methods *16*, 79–87.

Pierrel, F. (2017). Impact of Chemical Analogs of 4-Hydroxybenzoic Acid on Coenzyme Q Biosynthesis: From Inhibition to Bypass of Coenzyme Q Deficiency. Front. Physiol. *8*, 1–7.

Piscione, T.D., Wu, M.Y.J., and Quaggin, S.E. (2004). Expression of Hairy/Enhancer of Split genes, Hes1 and Hes5, during murine nephron morphogenesis. Gene Expr. Patterns *4*, 707–711.

Pitchon, E., Cachat, F., Jacquemont, S., Hinard, C., Borruat, F.-X., Schorderet, D., Morris, M., and Munier, F. (2007). Patient with Fanconi Syndrome (FS) and Retinitis Pigmentosa (RP) Caused by a Deletion and Duplication of Mitochondrial DNA (mtDNA). Klin. Monbl. Augenheilkd. *224*, 340–343.

Poh, Y.C., Chen, J., Hong, Y., Yi, H., Zhang, S., Chen, J., Wu, D.C., Wang, L., Jia, Q., Singh, R., et al. (2014). Generation of organized germ layers from a single mouse embryonic stem cell. Nat. Commun. *5*, 1–12.

Poon, W.W., Do, T.Q., Marbois, B.N., and Clarke, C.F. (1997). Sensitivity to treatment with polyunsaturated fatty acids is a general characteristic of the ubiquinone-deficient yeast coq mutants. Mol. Aspects Med. *18 Suppl*, S121-7.

Prasad, C., Melançon, S.B., Rupar, C.A., Prasad, A.N., Nunez, L.D., Rosenblatt, D.S., and Majewski, J. (2013). Exome sequencing reveals a homozygous mutation in TWINKLE as the cause of multisystemic failure including renal tubulopathy in three siblings. Mol. Genet. Metab. *108*, 190–194.

Proctor, G., Jiang, T., Iwahashi, M., Wang, Z., Li, J., and Levi, M. (2006). Regulation of Renal Fatty Acid and Cholesterol Metabolism, Inflammation, and Fibrosis in Akita and OVE26 Mice With Type 1 Diabetes. Diabetes *55*, 2502–2509.

Prozialeck, W.C., Lamar, P.C., and Appelt, D.M. (2004). Differential expression of E-cadherin, N-cadherin and beta-catenin in proximal and distal segments of the rat nephron. BMC Physiol.

Przepiorski, A., Sander, V., Tran, T., Hollywood, J.A., Sorrenson, B., Shih, J.-H., Wolvetang,

E.J., McMahon, A.P., Holm, T.M., and Davidson, A.J. (2018). A Simple Bioreactor-Based Method to Generate Kidney Organoids from Pluripotent Stem Cells. Stem Cell Reports *11*, 1–15.

Quinzii, C., Naini, A., Salviati, L., Trevisson, E., Navas, P., Dimauro, S., and Hirano, M. (2006). A mutation in para-hydroxybenzoate-polyprenyl transferase (COQ2) causes primary coenzyme Q10 deficiency. Am. J. Hum. Genet. *78*, 345–349.

Quinzii, C.M., López, L.C., Von-Moltke, J., Naini, A., Krishna, S., Schuelke, M., Salviati, L., Navas, P., DiMauro, S., and Hirano, M. (2008). Respiratory chain dysfunction and oxidative stress correlate with severity of primary CoQ10 deficiency. FASEB J. *22*, 1874–1885.

Quinzii, C.M., Lopez, L.C., Gilkerson, R.W., Dorado, B., Coku, J., Naini, A.B., Lagier-Tourenne, C., Schuelke, M., Salviati, L., Carrozzo, R., et al. (2010). Reactive oxygen species, oxidative stress, and cell death correlate with level of CoQ10 deficiency. FASEB J. *24*, 3733–3743.

Quinzii, C.M., Garone, C., Emmanuele, V., Tadesse, S., Krishna, S., Dorado, B., and Hirano, M. (2013). Tissue-specific oxidative stress and loss of mitochondria in CoQ-deficient Pdss2 mutant mice. FASEB J. *27*, 612–621.

Reeves-Daniel, A.M., DePalma, J.A., Bleyer, A.J., Rocco, M. V., Murea, M., Adams, P.L., Langefeld, C.D., Bowden, D.W., Hicks, P.J., Stratta, R.J., et al. (2011). The APOL1 Gene and Allograft Survival after Kidney Transplantation. Am. J. Transplant. *11*, 1025–1030.

Reiser, J., Kriz, W., Kretzler, M., and Mundel, P. (2000). The glomerular slit diaphragm is a modified adherens junction. J. Am. Soc. Nephrol. *11*, 1–8.

Reiser, J., Polu, K.R., Möller, C.C., Kenlan, P., Altintas, M.M., Wei, C., Faul, C., Herbert, S., Villegas, I., Avila-Casado, C., et al. (2005). TRPC6 is a glomerular slit diaphragm-associated channel required for normal renal function. Nat. Genet. *37*, 739–744.

Robins, R., and Takano, T. (2014). Rho-GTPase Signalling in the Pathogenesis of Nephrotic Syndrome. Adv. Nephrol. *2014*, 1–11.

Rodman, C., Wadsworth, M.H., Sullivan, R.J., Andreev, A.Y., Dutton-Regester, K., Hughes, T.K., Ziegler, C.G.K., Rozenblatt-Rosen, O., Bertagnolli, M., Van Allen, E.M., et al. (2016). Dissecting the multicellular ecosystem of metastatic melanoma by single-cell RNA-seq. Science (80-.). *352*, 189–196.

Roselli, S., Gribouval, O., Boute, N., Sich, M., Benessy, F., Attié, T., Gubler, M.-C., and Antignac, C. (2002). Podocin Localizes in the Kidney to the Slit Diaphragm Area. Am. J. Pathol. *160*, 131–139.

Rötig, A., Appelkvist, E.-L., Geromel, V., Chretien, D., Kadhom, N., Edery, P., Lebideau, M., Dallner, G., Munnich, A., Ernster, L., et al. (2000). Quinone-responsive multiple respiratory-chain dysfunction due to widespread coenzyme Q10 deficiency. Lancet *356*, 391–395.

Rumballe, B.A., Georgas, K.M., Combes, A.N., Ju, A.L., Gilbert, T., and Little, M.H. (2011). Nephron formation adopts a novel spatial topology at cessation of nephrogenesis. Dev. Biol.

360, 110–122.

Ryan, D., Sutherland, M.R., Flores, T.J., Kent, A.L., Dahlstrom, J.E., Puelles, V.G., Bertram, J.F., McMahon, A.P., Little, M.H., Moore, L., et al. (2018). Development of the Human Fetal Kidney from Mid to Late Gestation in Male and Female Infants. EBioMedicine *27*, 275–283.

Saada, A., Shaag, A., Arnon, S., Dolfin, T., Miller, C., Fuchs-Telem, D., Lombes, A., and Elpeleg, O. (2007). Antenatal mitochondrial disease caused by mitochondrial ribosomal protein (MRPS22) mutation. J. Med. Genet. *44*, 784–786.

Salviati, L., Sacconi, S., Murer, L., Zacchello, G., Franceschini, L., Laverda, A.M., Basso, G., Quinzii, C., Angelini, C., Hirano, M., et al. (2005). Infantile encephalomyopathy and nephropathy with CoQ10 deficiency: A CoQ10-responsive condition. Neurology *65*, 606–608.

Saran, R., Robinson, B., Abbott, K.C., Agodoa, L.Y.C., Bragg-Gresham, J., Balkrishnan, R., Bhave, N., Dietrich, X., Ding, Z., Eggers, P.W., et al. (2019). US Renal Data System 2018 Annual Data Report: Epidemiology of Kidney Disease in the United States. Am. J. Kidney Dis. *73*, A7–A8.

Sato, T., Vries, R.G., Snippert, H.J., van de Wetering, M., Barker, N., Stange, D.E., van Es, J.H., Abo, A., Kujala, P., Peters, P.J., et al. (2009). Single Lgr5 stem cells build crypt-villus structures in vitro without a mesenchymal niche. Nature *459*, 262–265.

Satoh, D., Hirose, T., Harita, Y., Daimon, C., Harada, T., Kurihara, H., Yamashita, A., and Ohno, S. (2014). APKCλ maintains the integrity of the glomerular slit diaphragm through trafficking of nephrin to the cell surface. J. Biochem. *156*, 115–128.

Scalais, E., Chafai, R., Van Coster, R., Bindl, L., Nuttin, C., Panagiotaraki, C., Seneca, S., Lissens, W., Ribes, A., Geers, C., et al. (2013). Early myoclonic epilepsy, hypertrophic cardiomyopathy and subsequently a nephrotic syndrome in a patient with CoQ10 deficiency caused by mutations in para-hydroxybenzoate-polyprenyl transferase (COQ2). Eur. J. Paediatr. Neurol. *17*, 625–630.

Schueler, M., Braun, D.A., Chandrasekar, G., Gee, H.Y., Klasson, T.D., Halbritter, J., Bieder, A., Porath, J.D., Airik, R., Zhou, W., et al. (2015). DCDC2 mutations cause a renal-hepatic ciliopathy by disrupting Wnt signaling. Am. J. Hum. Genet. *96*, 81–92.

Schumacher, M.A., Aihara, E., Feng, R., Engevik, A., Shroyer, N.F., Ottemann, K.M., Worrell, R.T., Montrose, M.H., Shivdasani, R.A., and Zavros, Y. (2015). The use of murine-derived fundic organoids in studies of gastric physiology. J. Physiol. *593*, 1809–1827.

Schwab, K., Patterson, L.T., Aronow, B.J., Luckas, R., Liang, H.-C., and Potter, S.S. (2003). A catalogue of gene expression in the developing kidney. Kidney Int. *64*, 1588–1604.

Scott, R.P., and Quaggin, S.E. (2015). Beyond the cell: The cell biology of renal filtration. J. Cell Biol. *209*, 199–210.

Sharmin, S., Taguchi, A., Kaku, Y., Yoshimura, Y., Ohmori, T., Sakuma, T., Mukoyama, M., Yamamoto, T., Kurihara, H., and Nishinakamura, R. (2016). Human Induced Pluripotent Stem

Cell-Derived Podocytes Mature into Vascularized Glomeruli upon Experimental Transplantation. J. Am. Soc. Nephrol. *27*, 1778–1791.

Shi, H., Noguchi, N., and Niki, E. (1999). Comparative study on dynamics of antioxidative action of alpha-tocopheryl hydroquinone, ubiquinol, and alpha-tocopherol against lipid peroxidation. Free Radic. Biol. Med. *27*, 334–346.

Sibalic, V., Fan, X., and Wüthrich, R.P. (1997). Characterisation of cellular infiltration and adhesion molecule expression in CBA/CaH- kdkd mice with tubulointerstitial renal disease. Histochem. Cell Biol. *108*, 235–242.

Sieber, J., Wieder, N., Clark, A., Reitberger, M., Matan, S., Schoenfelder, J., Zhang, J., Mandinova, A., Bittker, J.A., Gutierrez, J., et al. (2018). GDC-0879, a BRAFV600E Inhibitor, Protects Kidney Podocytes from Death. Cell Chem. Biol. *25*, 175–184.e4.

Siskind, L.J., Kolesnick, R.N., and Colombini, M. (2006). Ceramide forms channels in mitochondrial outer membranes at physiologically relevant concentrations. Mitochondrion *6*, 118–125.

Slavotinek, A., Kaylor, J., Pierce, H., Cahr, M., DeWard, S.J., Schneidman-Duhovny, D., Alsadah, A., Salem, F., Schmajuk, G., and Mehta, L. (2015). CRB2 Mutations Produce a Phenotype Resembling Congenital Nephrosis, Finnish Type, with Cerebral Ventriculomegaly and Raised Alpha-Fetoprotein. Am. J. Hum. Genet. *96*, 162–169.

Smeets, B., Uhlig, S., Fuss, A., Mooren, F., Wetzels, J.F.M., Floege, J., and Moeller, M.J. (2009). Tracing the Origin of Glomerular Extracapillary Lesions from Parietal Epithelial Cells. J. Am. Soc. Nephrol. *20*, 2604–2615.

Smith, A.C., Ito, Y., Ahmed, A., Schwartzentruber, J.A., Beaulieu, C.L., Aberg, E., Majewski, J., Bulman, D.E., Horsting-Wethly, K., Koning, D.V., et al. (2018). A family segregating lethal neonatal coenzyme Q10 deficiency caused by mutations in COQ9. J. Inherit. Metab. Dis. *41*, 719–729.

Spence, J.R., Mayhew, C.N., Rankin, S.A., Kuhar, M.F., Vallance, J.E., Tolle, K., Hoskins, E.E., Kalinichenko, V. V., Wells, S.I., Zorn, A.M., et al. (2011). Directed differentiation of human pluripotent stem cells into intestinal tissue in vitro. Nature *470*, 105–109.

Stadler, K., Goldberg, I.J., and Susztak, K. (2015). The Evolving Understanding of the Contribution of Lipid Metabolism to Diabetic Kidney Disease. Curr. Diab. Rep. *15*, 40.

Stan, R. V., Tse, D., Deharvengt, S.J., Smits, N.C., Xu, Y., Luciano, M.R., McGarry, C.L., Buitendijk, M., Nemani, K. V., Elgueta, R., et al. (2012). The Diaphragms of Fenestrated Endothelia: Gatekeepers of Vascular Permeability and Blood Composition. Dev. Cell.

Tachibana, H., Ogawa, D., Matsushita, Y., Bruemmer, D., Wada, J., Teshigawara, S., Eguchi, J., Sato-Horiguchi, C., Uchida, H.A., Shikata, K., et al. (2012). Activation of Liver X Receptor Inhibits Osteopontin and Ameliorates Diabetic Nephropathy. J. Am. Soc. Nephrol. *23*, 1835–1846.

Taguchi, A., and Nishinakamura, R. (2017). Higher-Order Kidney Organogenesis from Pluripotent Stem Cells. Cell Stem Cell *21*, 730–746.e6.

Taguchi, A., Kaku, Y., Ohmori, T., Sharmin, S., Ogawa, M., Sasaki, H., and Nishinakamura, R. (2014). Redefining the in vivo origin of metanephric nephron progenitors enables generation of complex kidney structures from pluripotent stem cells. Cell Stem Cell *14*, 53–67.

Takasato, M., Er, P.X., Becroft, M., Vanslambrouck, J.M., Stanley, E.G., Elefanty, A.G., and Little, M.H. (2014). Directing human embryonic stem cell differentiation towards a renal lineage generates a self-organizing kidney. Nat. Cell Biol. *16*, 118–126.

Takasato, M., Er, P.X., Chiu, H.S., Maier, B., Baillie, G.J., Ferguson, C., Parton, R.G., Wolvetang, E.J., Roost, M.S., Chuva de Sousa Lopes, S.M., et al. (2015). Kidney organoids from human iPS cells contain multiple lineages and model human nephrogenesis. Nature *526*, 564–568.

Takasato, M., Er, P.X., Chiu, H.S., and Little, M.H. (2016). Generation of kidney organoids from human pluripotent stem cells. Nat. Protoc. *11*, 1681–1692.

Tanaka, A., Yamamoto, A., Murota, K., Tsujiuchi, T., Iwamori, M., and Fukushima, N. (2017). Polyunsaturated fatty acids induce ovarian cancer cell death through ROS-dependent MAP kinase activation. Biochem. Biophys. Res. Commun. *493*, 468–473.

Tanigawa, S., Islam, M., Sharmin, S., Naganuma, H., Yoshimura, Y., Haque, F., Era, T., Nakazato, H., Nakanishi, K., Sakuma, T., et al. (2018). Organoids from Nephrotic Disease-Derived iPSCs Identify Impaired NEPHRIN Localization and Slit Diaphragm Formation in Kidney Podocytes. Stem Cell Reports *11*, 727–740.

Tay, S.K.H., Sacconi, S., Akman, H.O., Morales, J.F., Morales, A., De Vivo, D.C., Shanske, S., Bonilla, E., and DiMauro, S. (2005). Unusual clinical presentations in four cases of Leigh disease, cytochrome C oxidase deficiency, and SURF1 gene mutations. J. Child Neurol. *20*, 670–674.

Tirosh, I., Izar, B., Prakadan, S.M., Wadsworth, M.H., Treacy, D., Trombetta, J.J., Rotem, A., Rodman, C., Lian, C., Murphy, G., et al. (2016). Dissecting the multicellular ecosystem of metastatic melanoma by single-cell RNA-seq. Science (80-.). *352*, 189–196.

Tsankov, A.M., Akopian, V., Pop, R., Chetty, S., Gifford, C.A., Daheron, L., Tsankova, N.M., and Meissner, A. (2015). A qPCR ScoreCard quantifies the differentiation potential of human pluripotent stem cells. Nat. Biotechnol. *33*, 1182–1192.

Tucker, E.J., Wanschers, B.F.J., Szklarczyk, R., Mountford, H.S., Wijeyeratne, X.W., van den Brand, M.A.M., Leenders, A.M., Rodenburg, R.J., Reljić, B., Compton, A.G., et al. (2013). Mutations in the UQCC1-interacting protein, UQCC2, cause human complex III deficiency associated with perturbed cytochrome b protein expression. PLoS Genet. *9*, e1004034.

Tufro, a, Norwood, V.F., Carey, R.M., and Gomez, R. a (1999). Vascular endothelial growth factor induces nephrogenesis and vasculogenesis. J. Am. Soc. Nephrol. *10*, 2125–2134.

Turunen, M., Wehlin, L., Sjöberg, M., Lundahl, J., Dallner, G., Brismar, K., and Sindelar, P.J. (2002). beta2-Integrin and lipid modifications indicate a non-antioxidant mechanism for the anti-atherogenic effect of dietary coenzyme Q10. Biochem. Biophys. Res. Commun. *296*, 255–260.

Turunen, M., Olsson, J., and Dallner, G. (2004). Metabolism and function of coenzyme Q. Biochim. Biophys. Acta - Biomembr. *1660*, 171–199.

Tzoufi, M., Makis, A., Chaliasos, N., Nakou, I., Siomou, E., Tsatsoulis, A., Zikou, A., Argyropoulou, M., Bonnefont, J.P., and Siamopoulou, A. (2013). A rare case report of simultaneous presentation of myopathy, Addison's disease, primary hypoparathyroidism, and Fanconi syndrome in a child diagnosed with Kearns–Sayre syndrome. Eur. J. Pediatr. *172*, 557–561.

Tzur, S., Rosset, S., Shemer, R., Yudkovsky, G., Selig, S., Tarekegn, A., Bekele, E., Bradman, N., Wasser, W.G., Behar, D.M., et al. (2010). Missense mutations in the APOL1 gene are highly associated with end stage kidney disease risk previously attributed to the MYH9 gene. Hum. Genet. *128*, 345–350.

Valnot, I., von Kleist-Retzow, J.C., Barrientos, A., Gorbatyuk, M., Taanman, J.W., Mehaye, B., Rustin, P., Tzagoloff, A., Munnich, A., and Rötig, A. (2000). A mutation in the human heme A:farnesyltransferase gene (COX10) causes cytochrome c oxidase deficiency. Hum. Mol. Genet. *9*, 1245–1249.

Vasta, V., Merritt, J.L., Saneto, R.P., and Hahn, S.H. (2012). Next-generation sequencing for mitochondrial diseases: A wide diagnostic spectrum. Pediatr. Int. *54*, 585–601.

Vaughan, M.R., Pippin, J.W., Griffin, S. V., Krofft, R., Fleet, M., Haseley, L., and Shankland, S.J. (2005). ATRA induces podocyte differentiation and alters nephrin and podocin expression in vitro and in vivo. Kidney Int. *68*, 133–144.

Vazquez, M.D., Bouchet, P., Mallet, J.L., Foliguet, B., Gérard, H., and LeHeup, B. (1998). 3D reconstruction of the mouse's mesonephros. Anat. Histol. Embryol. *27*, 283–287.

Verma, R., Kovari, I., Soofi, A., Nihalani, D., Patrie, K., and Holzman, L.B. (2006). Nephrin ectodomain engagement results in Src kinase activation, nephrin phosphorylation, Nck recruitment, and actin polymerization. J. Clin. Invest. *116*, 1346–1359.

Vigneau, C., Polgar, K., Striker, G., Elliott, J., Hyink, D., Weber, O., Fehling, H.-J., Keller, G., Burrow, C., and Wilson, P. (2007). Mouse Embryonic Stem Cell–Derived Embryoid Bodies Generate Progenitors That Integrate Long Term into Renal Proximal Tubules In Vivo. J. Am. Soc. Nephrol. *18*, 1709–1720.

Vivante, A., and Hildebrandt, F. (2016). Exploring the genetic basis of early-onset chronic kidney disease. Nat. Rev. Nephrol. *12*, 133–146.

de Vries, A.P.J., Ruggenenti, P., Ruan, X.Z., Praga, M., Cruzado, J.M., Bajema, I.M., D'Agati, V.D., Lamb, H.J., Barlovic, D.P., Hojs, R., et al. (2014). Fatty kidney: emerging role of ectopic lipid in obesity-related renal disease. Lancet Diabetes Endocrinol. *2*, 417–426.

Walter, L., Nogueira, V., Leverve, X., Heitz, M.-P., Bernardi, P., and Fontaine, E. (2000). Three Classes of Ubiquinone Analogs Regulate the Mitochondrial Permeability Transition Pore through a Common Site. J. Biol. Chem. *275*, 29521–29527.

Wang, P., Chen, Y., Yong, J., Cui, Y., Wang, R., Wen, L., Qiao, J., and Tang, F. (2018). Dissecting the Global Dynamic Molecular Profiles of Human Fetal Kidney Development by Single-Cell RNA Sequencing. Cell Rep. *24*, 3554–3567.e3.

Wang, X.X., Jiang, T., Shen, Y., Caldas, Y., Miyazaki-Anzai, S., Santamaria, H., Urbanek, C., Solis, N., Scherzer, P., Lewis, L., et al. (2010). Diabetic Nephropathy Is Accelerated by Farnesoid X Receptor Deficiency and Inhibited by Farnesoid X Receptor Activation in a Type 1 Diabetes Model. Diabetes *59*, 2916–2927.

Wang, Z., Jiang, T., Li, J., Proctor, G., McManaman, J.L., Lucia, S., Chua, S., and Levi, M. (2005). Regulation of renal lipid metabolism, lipid accumulation, and glomerulosclerosis in FVBdb/db mice with type 2 diabetes. Diabetes *54*, 2328–2335.

Warejko, J.K., Tan, W., Daga, A., Schapiro, D., Lawson, J.A., Shril, S., Lovric, S., Ashraf, S., Rao, J., Hermle, T., et al. (2018). Whole exome sequencing of patients with steroid-resistant nephrotic syndrome. Clin. J. Am. Soc. Nephrol. *13*, 53–62.

Warner, H., Wilson, B.J., and Caswell, P.T. (2019). Control of adhesion and protrusion in cell migration by Rho GTPases. Curr. Opin. Cell Biol. *56*, 64–70.

Watson, C.L., Mahe, M.M., Múnera, J., Howell, J.C., Sundaram, N., Poling, H.M., Schweitzer, J.I., Vallance, J.E., Mayhew, C.N., Sun, Y., et al. (2014). An in vivo model of human small intestine using pluripotent stem cells. Nat. Med. *20*, 1310–1314.

Weins, A., Kenlan, P., Herbert, S., Le, T.C., Villegas, I., Kaplan, B.S., Appel, G.B., and Pollak, M.R. (2005). Mutational and Biological Analysis of α-Actinin-4 in Focal Segmental Glomerulosclerosis. J. Am. Soc. Nephrol. *16*, 3694–3701.

Wellik, D.M., Hawkes, P.J., and Capecchi, M.R. (2002). Hox11 paralogous genes are essential for metanephric kidney induction. Genes Dev. *16*, 1423–1432.

Wen, H., Kumar, V., Lan, X., Shoshtari, S.S.M., Eng, J.M., Zhou, X., Wang, F., Wang, H., Skorecki, K., Xing, G., et al. (2018). APOL1 risk variants cause podocytes injury through enhancing endoplasmic reticulum stress. Biosci. Rep. *38*, BSR20171713.

Wharram, B.L., Goyal, M., Gillespie, P.J., Wiggins, J.E., Kershaw, D.B., Holzman, L.B., Dysko, R.C., Saunders, T.L., Samuelson, L.C., and Wiggins, R.C. (2000). Altered podocyte structure in GLEPP1 (Ptpro) -deficient mice associated with hypertension and low glomerular filtration rate. J. Clin. Invest. *106*, 1281–1290.

Wickham, H. (2016). ggplot2: Elegant Graphics for Data Analysis.

Widmeier, E., Airik, M., Hugo, H., Schapiro, D., Wedel, J., Ghosh, C.C., Nakayama, M., Schneider, R., Awad, A.M., Nag, A., et al. (2019). Treatment with 2,4-Dihydroxybenzoic Acid Prevents FSGS Progression and Renal Fibrosis in Podocyte-Specific Coq6 Knockout Mice. J.

Am. Soc. Nephrol. *30*, 393–405.

Willey, C.J., Blais, J.D., Hall, A.K., Krasa, H.B., Makin, A.J., and Czerwiec, F.S. (2016). Prevalence of autosomal dominant polycystic kidney disease in the European Union. Nephrol. Dial. Transplant. *32*, gfw240.

Winn, M.P., Conlon, P.J., Lynn, K.L., Farrington, M.K., Creazzo, T., Hawkins, A.F., Daskalakis, N., Kwan, S.Y., Ebersviller, S., Burchette, J.L., et al. (2005). A mutation in the TRPC6 cation channel causes familial focal segmental glomerulosclerosis. Science *308*, 1801–1804.

Wu, H., Uchimura, K., Donnelly, E.L., Kirita, Y., Morris, S.A., and Humphreys, B.D. (2018). Comparative Analysis and Refinement of Human PSC-Derived Kidney Organoid Differentiation with Single-Cell Transcriptomics. Cell Stem Cell *23*, 869–881.e8.

Wu, H., Kirita, Y., Donnelly, E.L., and Humphreys, B.D. (2019). Advantages of Single-Nucleus over Single-Cell RNA Sequencing of Adult Kidney: Rare Cell Types and Novel Cell States Revealed in Fibrosis. J. Am. Soc. Nephrol. *30*, 23–32.

Xie, Y., Sakatsume, M., Nishi, S., Narita, I., Arakawa, M., and Gejyo, F. (2001). Expression, roles, receptors, and regulation of osteopontin in the kidney. Kidney Int.

Xinaris, C., Benedetti, V., Rizzo, P., Abbate, M., Corna, D., Azzollini, N., Conti, S., Unbekandt, M., Davies, J.A., Morigi, M., et al. (2012). In Vivo Maturation of Functional Renal Organoids Formed from Embryonic Cell Suspensions. J. Am. Soc. Nephrol. *23*, 1857–1868.

Yamamoto, M., Cui, L., Johkura, K., Asanuma, K., Okouchi, Y., Ogiwara, N., and Sasaki, K. (2006). Branching ducts similar to mesonephric ducts or ureteric buds in teratomas originating from mouse embryonic stem cells. Am. J. Physiol. Physiol. *290*, F52–F60.

Yi-Rong Peng, Karthik Shekhar, Wenjun Yan, Dustin Herrmann, Anna Sappington, Greg S. Bryman, Tavé van Zyl, Michael Tri. H. Do, A.R. and J.R.S. (2018). MOLECULAR CLASSIFICATION AND COMPARATIVE TAXONOMICS OF FOVEAL AND PERIPHERAL CELLS IN PRIMATE RETINA. Bioarxiv.

Young, M.D., Mitchell, T.J., Vieira Braga, F.A., Tran, M.G.B., Stewart, B.J., Ferdinand, J.R., Collord, G., Botting, R.A., Popescu, D.M., Loudon, K.W., et al. (2018). Single-cell transcriptomes from human kidneys reveal the cellular identity of renal tumors. Science (80-.). *361*, 594–599.

Yuan, L., Le Bras, A., Sacharidou, A., Itagaki, K., Zhan, Y., Kondo, M., Carman, C. V., Davis, G.E., Aird, W.C., and Oettgen, P. (2012). ETS-related gene (ERG) controls endothelial cell permeability via transcriptional regulation of the claudin 5 (CLDN5) gene. J. Biol. Chem. *287*, 6582–6591.

Yui, S., Nakamura, T., Sato, T., Nemoto, Y., Mizutani, T., Zheng, X., Ichinose, S., Nagaishi, T., Okamoto, R., Tsuchiya, K., et al. (2012). Functional engraftment of colon epithelium expanded in vitro from a single adult Lgr5 + stem cell. Nat. Med. *18*, 618–623.

Zhou, Y., Castonguay, P., Sidhom, E.-H., Clark, A.R., Dvela-Levitt, M., Kim, S., Sieber, J.,

Wieder, N., Jung, J.Y., Andreeva, S., et al. (2017). A small-molecule inhibitor of TRPC5 ion channels suppresses progressive kidney disease in animal models. Science (80-.). *358*, 1332–1336.

Živná, M., Kidd, K., Přistoupilová, A., Barešová, V., DeFelice, M., Blumenstiel, B., Harden, M., Conlon, P., Lavin, P., Connaughton, D.M., et al. (2018). Noninvasive Immunohistochemical Diagnosis and Novel *MUC1* Mutations Causing Autosomal Dominant Tubulointerstitial Kidney Disease. J. Am. Soc. Nephrol.

Appendix 1:

Material Related to Chapter 2

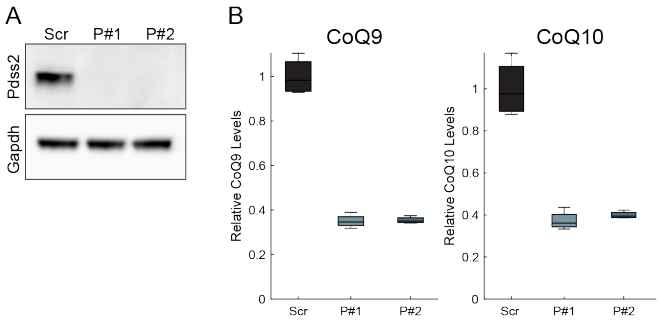

Figure S1.1. Pdss2 shRNAs deplete both protein and CoQ levels. A. Western blot from Pdss2 shRNA-infected podocytes or scrambled controls five days post-lentivirus infection. **B.** Log2 fold change of CoQ levels (CoQ9 and CoQ10) in Pdss2-shRNA infected podocytes compared to scrambled controls, n=4.

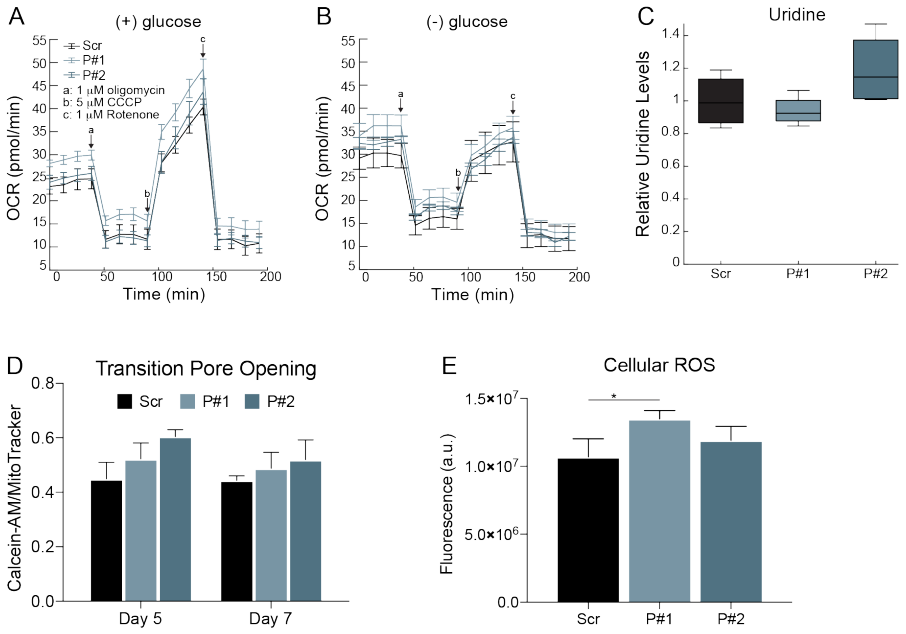

Figure S1.2. CoQ-deficient podocytes show minimal perturbation in CoQ functions at baseline. Mito-stress test to assess electron transport chain (ETC) function by oxygen consumption rate (OCR) with the Seahorse Flux Analyzer in Pdss2-shRNA infected podocytes and scrambled controls in **A.** full RPMI media (11.1 mM glucose, left) or **B.** glucose-free RPMI (right). **C.** Log2 fold change of uridine levels in Pdss2-shRNA infected podocytes compared to scrambled controls, n=4. **D.** Transition pore opening as measured by Calcein-AM in the presence of $CoCl_2$, normalized to total mitochondrial abundance, measured by MitoTracker Deep Red in Pdss2-shRNA infected podocytes and scrambled controls, n=4, one-way ANOVA, Tukey multiple comparison test. **E.** Cellular ROS as measured by the sum fluorescence of CellROX Orange dye in CoQ-deficient podocytes and scrambled controls, n=4, one-way ANOVA, Tukey multiple comparison test.

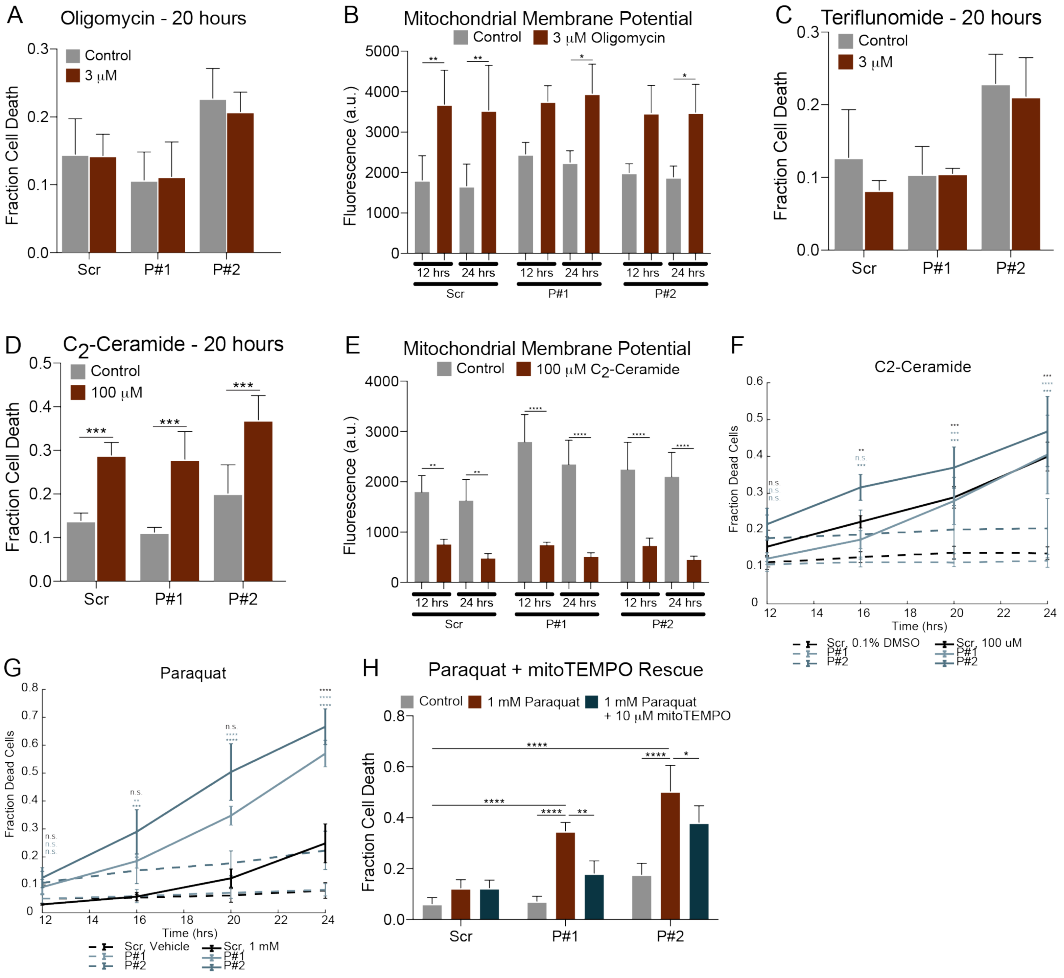

Figure S1.3. CoQ-deficient podocytes show susceptibility to ROS-mediated injury. A. Quantification of cell death after oligomycin treatment, n=4, one-way ANOVA, Sidak multiple comparison test. **B.** Quantification of mitochondrial membrane potential using Tetramethylrhodamine, Methyl (TMRM) dye with oligomycin treatment across experiment time course, n=4, one-way ANOVA, Tukey multiple comparison test. **C.** Quantification of cell death after teriflunomide treatment, n=4, one-way ANOVA, Sidak multiple comparison test. **D.** Quantification of cell death after teriflunomide treatment, n=4, one-way ANOVA, Sidak multiple comparison test. **E.** Quantification of mitochondrial membrane potential using Tetramethylrhodamine, Methyl (TMRM) dye with C_2-ceramide treatment across experiment time course, n=4, one-way ANOVA, Tukey multiple comparison test. **F.** Quantification of cell death after C_2-ceramide treatment across multiple time points, n=4, one-way ANOVA, Sidak multiple comparison test. **G.** Quantification of cell death after Paraquat treatment across multiple time points, n=4, one-way ANOVA, Sidak multiple comparison test. Rescue of Paraquat treatment with mitoTEMPO, n=4, two-way ANOVA, Tukey multiple comparison test.

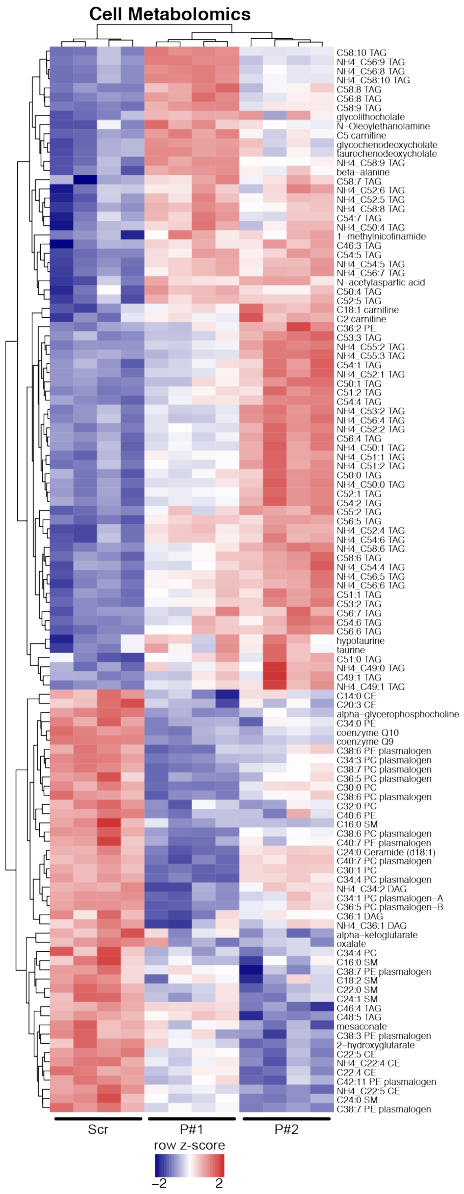

Figure S1.4. Metabolomics of CoQ-deficient podocytes show increased abundance of PU TGs and decreased abundance of PU PLs. Heatmap of statistically significant metabolites (FDR <10%, Benjamini-Hochberg correction on a student's t-test) from cell extracts of Pdss2 shRNA-infected podocytes compared to scrambled controls, n=4.

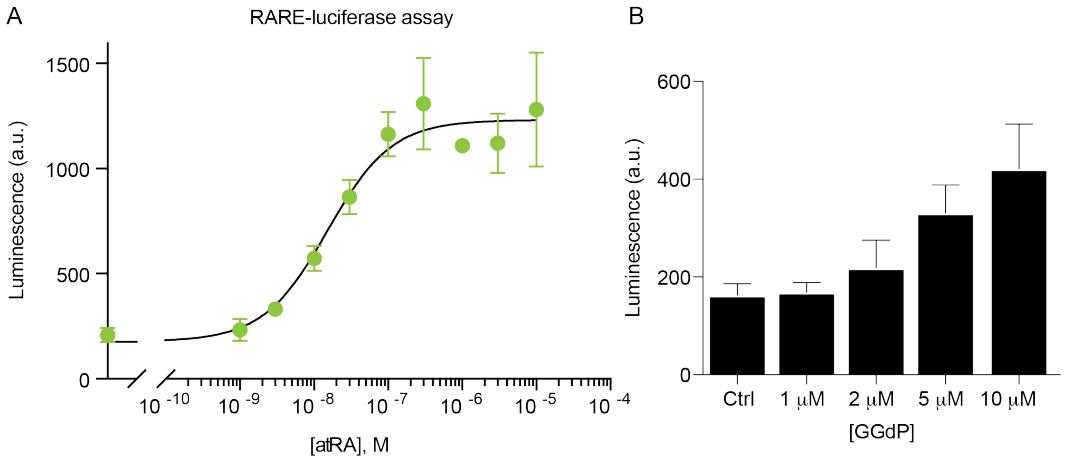

Figure S1.5. GGdP increases Rar-mediated transcription in a dose-responsive manner. Luminescence readout from a Retinoic Acid Receptor Element (RARE)-luciferase reporter assay following 24 hours of treatment with **A.** atRA or **B.** GGdP, showing that both increase Rar-mediated transcription in a dose-responsive manner, n=3.

A

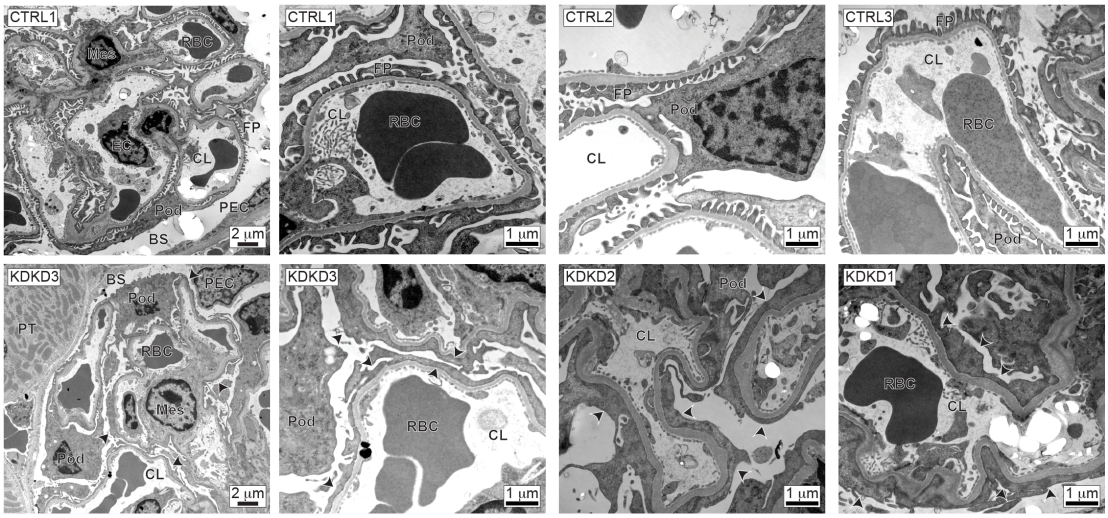

B

Sample	Sex	Genotype	Mean Reads/cell	Sequencing Saturation	Cells	After filtering		Median (nUMI)	Median (nGene)
CTRL1	Male	*Pdss2*$^{kd/wt}$	108,539	94.50%	5,369	5,367		1,140	775
CTRL2	Male	*Pdss2*$^{kd/wt}$	93,823	92.20%	4,755	4,746	16,708	1,606	1,018
CTRL3	Female	*Pdss2*$^{wt/wt}$	54,616	88.90%	6,604	6,595		1,345	875
KDKD1	Male	*Pdss2*$^{kd/kd}$	69,702	91.50%	7,308	7,295		1,136	804
KDKD2	Male	*Pdss2*$^{kd/kd}$	83,359	92.80%	6,497	6,485	20,628	1,579	998
KDKD3	Female	*Pdss2*$^{kd/kd}$	65,708	91.80%	6,855	6,848		1,428	884

C

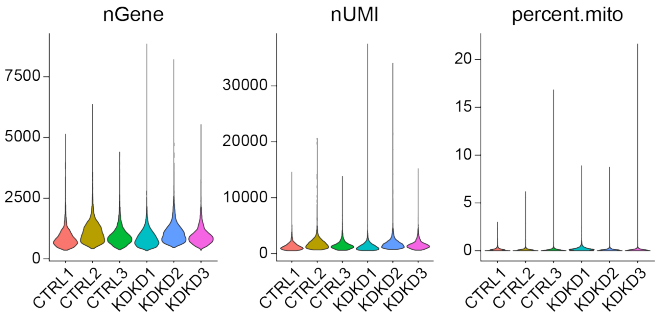

D

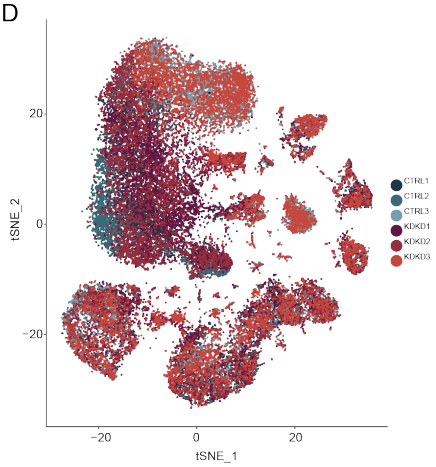

Figure S1.6. CoQ-deficient mice show evidence of histological kidney injury at five months. **A.** Electron microscopy of kidneys of CTRL and KDKD mice show diffuse podocyte foot process effacement (arrowheads) in glomeruli of KDKD mice; Pod, podocyte; PEC, parietal epithelial cell; Mes, mesangial cell; EC, endothelial cell; RBC, red blood cell; CL, capillary lumen; BS, Bowman's space; FP, podocyte foot processes. **B, C.** Quality control measures of sNuc-Seq by sample. **D.** t-SNE visualization of single nucleus transcriptomic profiles from three five-month-old *Pdss2*$^{kd/kd}$ mice (KDKD) and three age-matched control mice (CTRL) color-coded by sample.

Figure S1.7. sNuc-Seq of CoQ-deficient and age-control mice retrieve all expected major kidney cell types across samples. A. Dot plot representation of gene expression of canonical marker genes for different kidney cell types across all clusters, divided by control (CTRL) versus disease, *Pdss2*$^{kd/kd}$, (KDKD). **B.** Proportions of clusters by sample (left) with corresponding cell numbers (right). **C.** t-SNE visualization of all nuclei with expression of TAL (Slc12a1), DCT (Slc12a3) canonical markers with Dcdc2a superimposed (top), and expression of three genes only in Mixed–TAL/DCT cluster (bottom).

Figure S1.7 (Continued).

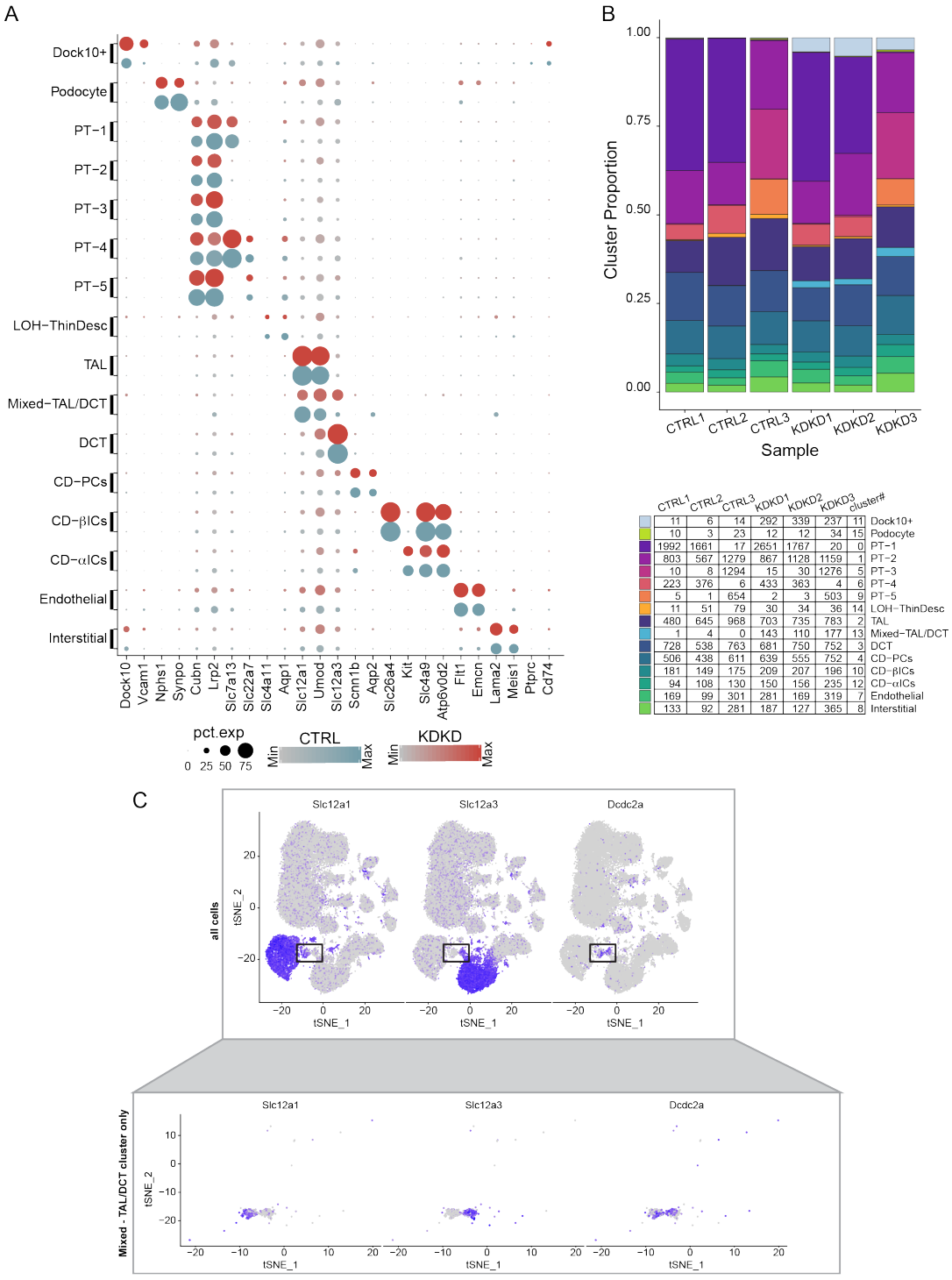

Figure S1.8. Dock10/Vcam1+ cells have increased expression of cytoskeleton- and inflammatory genes but lack other canonical immune-marker genes. A. Analysis on leading edge genes (see methods) from GSEA on Dock10/Vcam1+ marker gene list (|log2fc, enrichment| > 0.25), shows three clusters of pathways, one driven by cytoskeleton genes (e.g. Rhoa, Actg1, Actb), one driven by cell-adhesion genes (e.g. integrins), and one driven by inflammatory genes (e.g. Ikbkb, Nfkb1, Nfkbia). **B.** Scatter plot of cell cycle scores for all single nucleus transcriptomic profiles, with Dock10/Vcam1+ cells highlighted (red), and thresholds (black lines) indicated for determination of “cycling cells”.

Figure S1.8 (Continued).

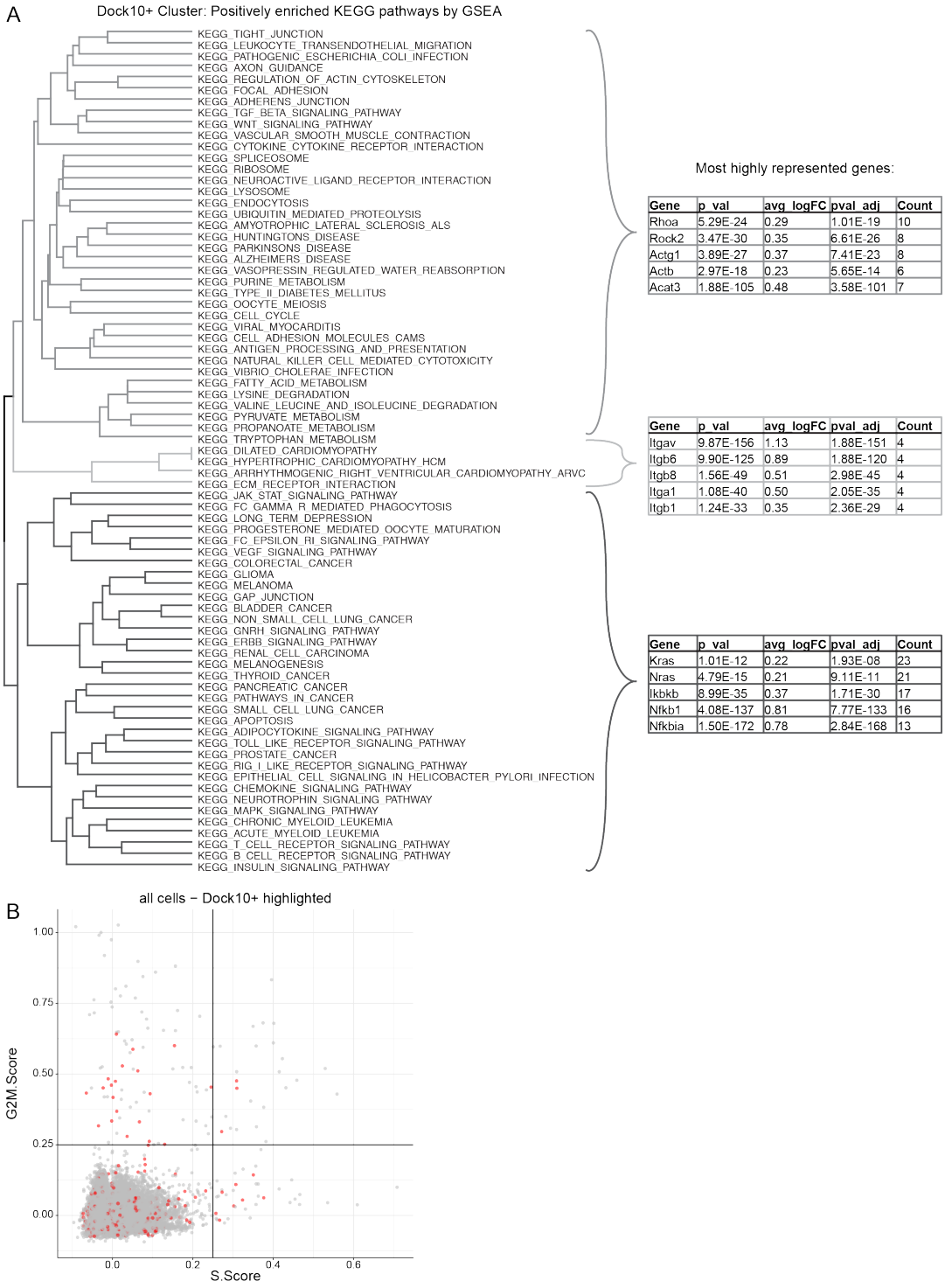

Gene	p_val	avg_logFC	pval_adj	Count
Rhoa	5.29E-24	0.29	1.01E-19	10
Rock2	3.47E-30	0.35	6.61E-26	8
Actg1	3.89E-27	0.37	7.41E-23	8
Actb	2.97E-18	0.23	5.65E-14	6
Acat3	1.88E-105	0.48	3.58E-101	7

Gene	p_val	avg_logFC	pval_adj	Count
Itgav	9.87E-156	1.13	1.88E-151	4
Itgb6	9.90E-125	0.89	1.88E-120	4
Itgb8	1.56E-49	0.51	2.98E-45	4
Itga1	1.08E-40	0.50	2.05E-35	4
Itgb1	1.24E-33	0.35	2.36E-29	4

Gene	p_val	avg_logFC	pval_adj	Count
Kras	1.01E-12	0.22	1.93E-08	23
Nras	4.79E-15	0.21	9.11E-11	21
Ikbkb	8.99E-35	0.37	1.71E-30	17
Nfkb1	4.08E-137	0.81	7.77E-133	16
Nfkbia	1.50E-172	0.78	2.84E-168	13

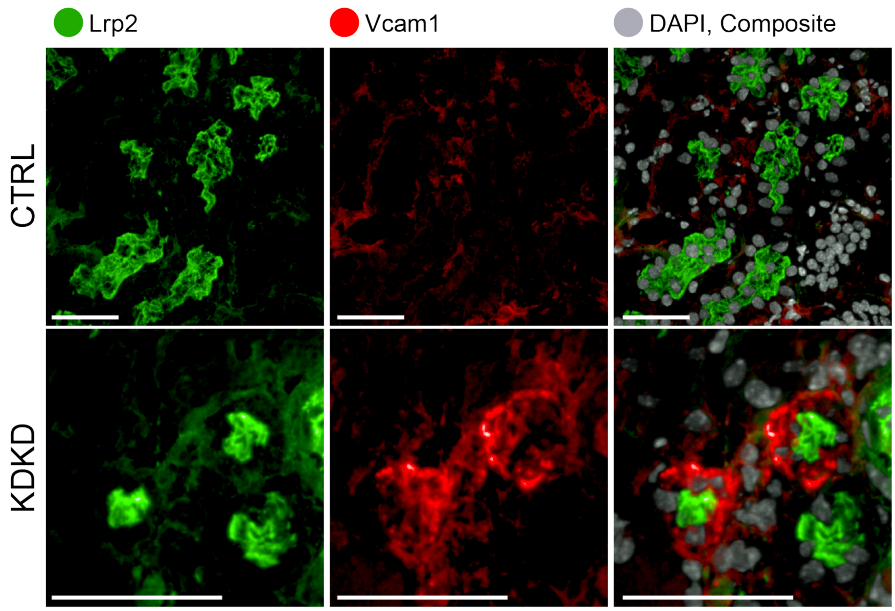

Figure S1.9. Dock10/Vcam1+ cells have increased expression of Vcam1 in cells surrounding proximal tubule. Immunofluorescence staining for PT (Lrp2) and Vcam1 in CTRL versus KDKD mice shows increased Vcam1 expression in KDKD with localization around Lrp2+ PT; scale bars, 50 μm.

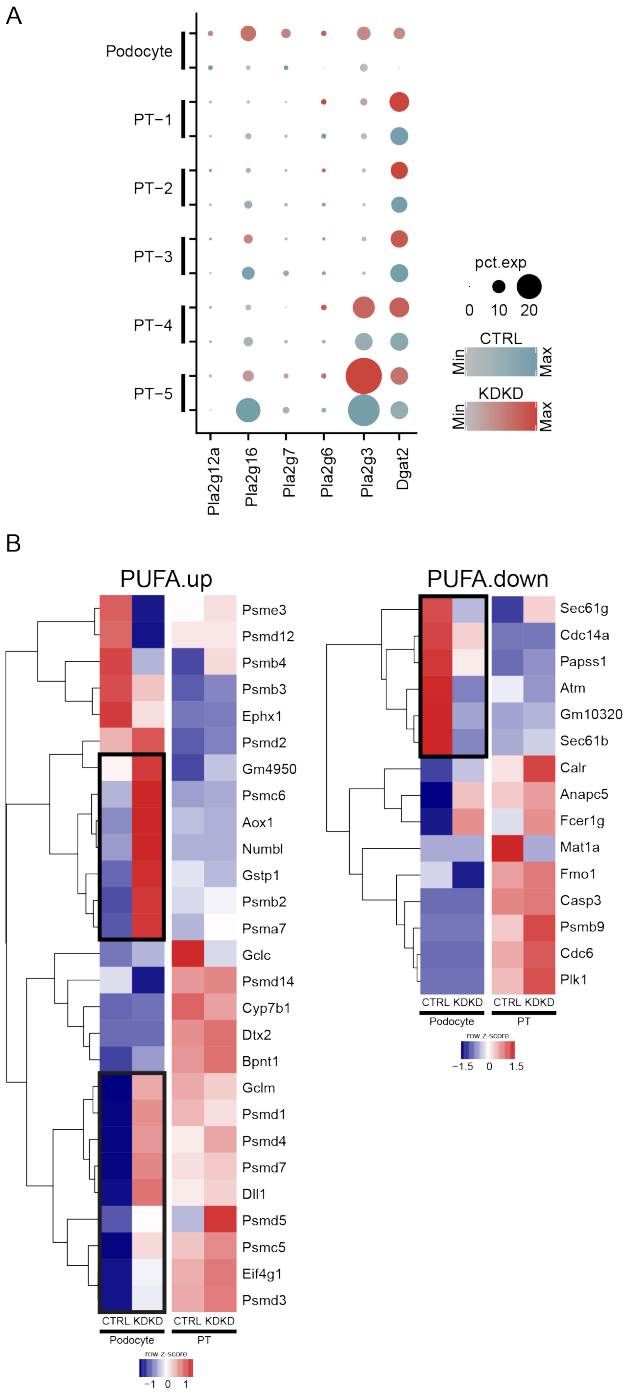

Figure S1.10. CoQ-deficient mice reveal podocyte-specific changes in PUFA-related genes. **A.** Dot plot representation of gene expression of selected Pla2 and Dgat2 enzymes across podocyte and proximal tubule clusters. **B.** Heatmap of average gene expression of genes used to create PUFA.up and PUFA.down gene signatures across podocyte and combined proximal tubules cells in control versus *Pdss2*$^{kd/kd}$ mice.

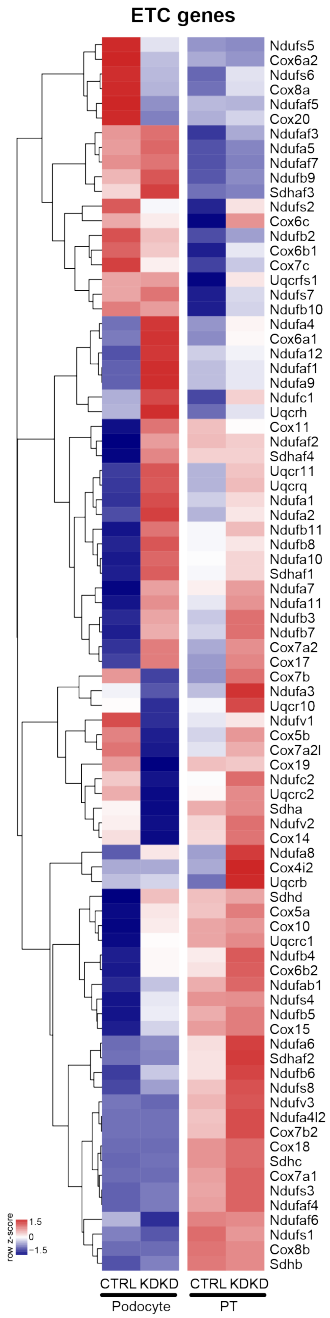

Figure S1.11. Increased expression of ETC genes is common to both podocytes and PT. Heatmap of average gene expression of electron transport genes (Complex I-IV) across podocyte and combined proximal tubules cells in CTRL versus KDKD mice.

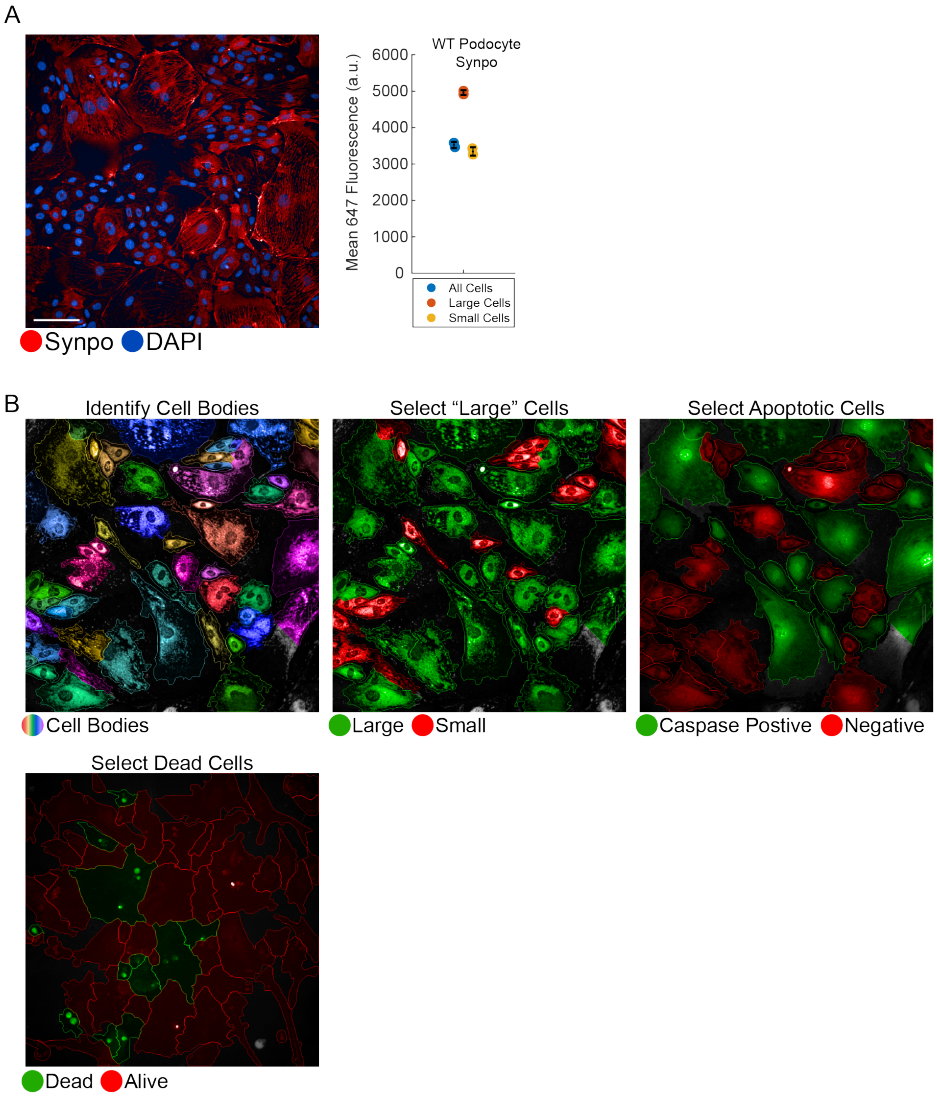

Figure S1.12. Image analysis using Opera Phenix High-Content Screening System and Harmony software. A. Immunofluorescence of synaptopodin (Synpo, red) with nuclei staining (DAPI, blue) and quantification by cell size showing larger cells have increased expression of synaptopodin (SYNPO) suggesting further podocyte maturation; scale bars, 100 μm. **B.** Analysis of live cell imaging by Harmony software demonstrating identification of cell bodies, selection of cells based on size, and selection of apoptotic (caspase positive) and dead cells.

Table S1.1. Differential expression data for all detected metabolites from conditioned media for scrambled and Pdss2 shRNAs with noted comparisons.

Metabolite	P1.v.Scr.fdr	P2.v.Scr.fdr	P1.v.P2.fdr	P1.v.Scr.log2fc	P2.v.Scr.log2fc
10-heptadecenoate	0.8519	0.9507	0.7080	0.0575	-0.0426
10-nonadecenoate	0.7737	0.8797	0.8142	0.1272	0.0912
11-HETE	0.6048	0.8331	0.2148	-0.1508	0.0730
12-HETE/8-HETE	0.8114	0.4783	0.3220	0.0521	-0.1683
13-docosenoate	0.9285	0.9951	0.9085	0.1123	-0.0062
13-HODE	0.7994	0.9507	0.7893	0.2778	0.0662
13-HpODE	0.9406	0.5320	0.5655	0.0167	-0.1719
15-HETE	0.9766	0.8636	0.7827	-0.0082	-0.1962
16-hydroxypalmitate	0.1919	0.4255	0.7427	0.3605	0.2844
16:0 PC(O)	0.4041	0.9292	0.0426	-0.1798	0.0326
17-Methylstearate	0.7226	0.9507	0.6084	0.1860	-0.0574
2-hydroxyhexadecanoate	0.7737	0.9507	0.9330	-0.0827	-0.0486
2-hydroxyoctanoate	0.8925	0.7352	0.6188	0.0279	-0.1194
3-hydroxydecanoate	0.1596	0.6047	0.0043	0.6264	-0.2005
3-hydroxyhexanoate	0.4041	0.0002	0.0014	-0.2231	0.5073
3-hydroxyoctanoate	0.0135	0.9507	0.0025	0.5874	-0.0229
3-methyladipate	0.8181	0.9507	0.9135	-0.1428	-0.0807
3-oxooctadecanoate	0.8277	0.9921	0.7080	-0.0353	0.0032
5-dodecenoate	0.9461	0.1243	0.0215	-0.0157	-1.5753
5-HETE	0.4041	0.0349	0.1251	0.2864	0.6743
5.6 diHETE	0.9209	0.9507	0.9845	0.0713	0.0575
9-cis-retinoic acid	0.9975	0.9921	0.9766	0.0012	-0.0099
9-HETE	0.9406	0.4741	0.2035	-0.0172	0.2493
9.10-diHOME	0.7226	0.5057	0.8720	0.0819	0.1061
adrenate	0.0135	0.0017	0.0069	0.5764	0.8331
alpha-linolenate	0.7677	0.0138	0.0021	0.1198	-0.8332
arachidate	0.9850	0.8925	0.7835	0.0072	-0.1125
arachidonate	0.0252	0.0295	0.7839	0.4753	0.5451
caprate	0.9461	0.8445	0.8720	-0.0136	-0.0489
carnosol	0.8428	0.9507	0.9551	-0.0931	-0.0596
chenodeoxycholate	0.8753	0.8445	0.9024	-0.0318	-0.0626
cholate	0.8270	0.9374	0.7498	0.0996	-0.1305
deoxycholate	0.6162	0.7957	0.9775	0.1464	0.1353
docosahexaenoate	0.6048	0.5320	0.9685	0.1781	0.1696
docosapentaenoate	0.0655	0.0247	0.6175	0.4341	0.5695
dodecanedioate	0.8681	0.9650	0.7678	-0.0185	0.0094
dodecanoate	0.6162	0.4207	0.9302	-0.0824	-0.0951
eicosadienoate	0.8270	0.2489	0.0069	-0.0678	0.3922
eicosanedioate	0.8250	0.9371	0.7632	0.0673	-0.0412
eicosapentaenoate	0.4517	0.8749	0.1008	0.2235	-0.0579
eicosatrienoate	0.3245	0.0373	0.2134	0.2892	0.6248
eicosenoate	0.4594	0.9096	0.7498	0.0986	0.0411
fructose/glucose/galactose	0.8231	0.9940	0.8690	0.0250	-0.0026
gamma-linolenate	0.1596	0.6621	0.3827	-0.3852	-0.1693
glycochenodeoxycholate	0.8059	0.8853	0.9890	0.0516	0.0490
glycocholate	0.8270	0.9860	0.8370	0.0413	0.0082
glycodeoxycholate	0.9517	0.9921	0.9469	0.0119	-0.0054
glycolithocholate	0.9364	0.7894	0.1251	-0.0120	0.0610
glycoursodeoxycholate	0.7994	0.9292	0.8774	-0.2110	-0.1152
heptadecanoate	0.7994	0.9650	0.5243	0.0740	-0.0155
hexadecanedioate	0.7737	0.8782	0.9812	0.0417	0.0452
hydroxymyristate	0.6048	0.4296	0.6187	-0.1033	-0.2357
levulinate	0.0020	0.0008	0.0000	-0.6312	0.6473
linoleate	0.7737	0.7856	0.8989	-0.0937	-0.1241
lipoxin A5	0.8133	0.9292	0.9618	-0.0615	-0.0519
lithocholate	0.8089	0.8853	0.9775	0.1111	0.1267
myristate	0.7737	0.9446	0.7498	-0.0615	-0.0108
myristoleate	0.1657	0.8445	0.1112	-0.5749	-0.1014
N-acetylalanine	0.9948	0.7957	0.7236	-0.0009	-0.0743

Table S1.1 (Continued).

nervonic acid	0.7044	0.9734	0.3320	-0.4367	-0.0448
nonadecanoate	0.7226	0.9719	0.6888	0.1370	-0.0225
oleate	0.7994	0.9507	0.7427	0.0757	0.0289
oxypurinol	0.8059	0.9258	0.7032	-0.0338	0.0349
palmitate	0.8324	0.4454	0.5521	-0.0218	-0.1016
palmitoleate	0.8720	0.5057	0.2818	0.0425	-0.2510
palmitoylethanolamide	0.6854	0.5360	0.8881	0.5699	0.4347
pentadecanoate	0.9850	0.9860	0.9551	0.0049	-0.0107
pentadecanol	0.8008	0.9343	0.7921	-0.3191	-0.0724
phytanate	0.7737	0.9446	0.8675	-0.1280	-0.0631
sebacate	0.8477	0.5320	0.7839	-0.0274	-0.0688
stearate	0.7994	0.9446	0.9302	-0.0662	-0.0427
taurochenodeoxycholate	0.9125	0.9951	0.8720	-0.0152	-0.0015
taurocholate	0.7631	0.8631	0.7839	0.0826	0.0474
taurodeoxycholate	0.8477	0.9507	0.9302	0.0375	0.0286
taurohyodeoxycholate/tauroursodeoxycholate	0.6410	0.8445	0.7632	0.0974	0.0445
taurolithocholate	0.8250	0.9650	0.9460	0.0270	0.0141
tetradecanedioate	0.8527	0.8031	0.6540	-0.0190	0.0740
undecanedionate	0.9417	0.9663	0.8903	0.0079	-0.0055
C14:0 CE	0.7226	0.5320	0.8224	-0.0494	-0.0646
C14:0 LPC	0.3245	0.6158	0.4075	-0.1977	-0.0746
C14:0 SM	0.7044	0.8899	0.6899	-0.0993	-0.0365
C16:0 CE	0.8925	0.9650	0.9460	-0.0151	-0.0074
C16:0 Ceramide (d18:1)	0.7737	0.9921	0.0072	-1.0585	-0.0458
C16:0 LPC	0.6048	0.8331	0.6600	-0.0995	-0.0388
C16:0 LPC_Na	0.5427	0.8303	0.6540	-0.0930	-0.0349
C16:0 LPE	0.7737	0.8445	0.9685	-0.3122	-0.3698
C16:0 SM	0.7823	0.9921	0.7367	-0.0512	0.0019
C16:1 CE	0.7737	0.7313	0.9024	-0.0360	-0.0432
C16:1 LPC	0.0135	0.4449	0.0029	-0.4721	0.1096
C16:1 MAG	0.8231	0.9446	0.6660	0.2425	-0.1086
C16:1 SM	0.7226	0.7957	0.9085	-0.0712	-0.0547
C18:0 CE	0.8008	0.9507	0.7779	-0.0447	-0.0171
C18:0 LPC	0.7253	0.5320	0.9330	-0.0695	-0.0811
C18:0 LPE	0.9850	0.4783	0.2854	0.0090	-0.3186
C18:0 MAG	0.6741	0.8989	0.9685	0.0895	0.0768
C18:0 SM	0.8270	0.9777	0.8720	-0.0337	-0.0072
C18:1 CE	0.9925	0.6502	0.7260	0.0010	0.0268
C18:1 LPC	0.4041	0.9650	0.1713	-0.1660	0.0080
C18:1 LPE	0.5685	0.4207	0.9685	-0.4991	-0.4702
C18:1 SM	0.7994	0.9621	0.7934	-0.0497	-0.0132
C18:2 CE	0.7737	0.9168	0.7934	-0.0335	-0.0123
C18:2 LPC	0.0252	0.8989	0.0187	-0.2762	0.0220
C18:3 CE	0.7994	0.9921	0.7839	-0.0303	-0.0025
C20:0 LPE	0.7944	0.9507	0.7839	-0.0518	-0.0095
C20:0 SM	0.9188	0.9411	0.9685	-0.0167	-0.0231
C20:3 CE	0.7944	0.9650	0.7498	-0.0348	-0.0069
C20:4 CE	0.8378	0.9444	0.9612	-0.0129	-0.0096
C20:4 LPC	0.1009	0.6646	0.1115	-0.3480	-0.0786
C20:5 CE	0.8445	0.9507	0.7839	-0.0211	0.0130
C20:5 LPC	0.4099	0.8797	0.2923	-0.4788	-0.1314
C22:0 Ceramide (d18:1)	0.7631	0.9040	0.4046	-0.8613	-0.3896
C22:0 LPE	0.9757	0.8031	0.5924	-0.0064	-0.0870
C22:0 SM	0.8045	0.9507	0.8664	-0.0446	-0.0175
C22:1 MAG	0.9940	0.4454	0.0869	-0.0276	-2.5710
C22:1 SM	0.8048	0.9730	0.7807	-0.0444	-0.0078
C22:4 CE	0.8250	0.9507	0.7232	-0.0333	0.0167
C22:5 CE	0.7468	0.9719	0.7427	-0.0400	-0.0047
C22:6 CE	0.8190	0.9860	0.7827	-0.0239	0.0032
C22:6 LPC	0.1009	0.9292	0.0417	-0.3530	-0.0218
C24:0 Ceramide (d18:1)	0.7333	0.8445	0.1391	-1.4473	-0.9083

Table S1.1 (Continued).

C24:0 SM	0.7994	0.9777	0.7537	-0.0551	-0.0065
C24:1 Ceramide (d18:1)	0.7652	0.5320	0.0553	-0.4861	0.6205
C24:1 SM	0.7994	0.9650	0.7984	-0.0449	-0.0112
C30:0 DAG	0.8059	0.9446	0.5025	0.4982	-0.2187
C30:0 PC	0.7226	0.8797	0.4061	-0.0872	0.0461
C30:1 PC	0.0135	0.9650	0.0041	-2.0826	0.0272
C32:0 DAG	0.7994	0.9507	0.5171	0.3740	-0.1145
C32:0 PC	0.8114	0.9185	0.7232	-0.0311	0.0274
C32:1 DAG	0.9693	0.8445	0.7367	-0.0892	-0.6646
C32:1 PC	0.4180	0.6323	0.1112	-0.1564	0.0874
C32:2 DAG	0.9813	0.8765	0.7002	0.1102	-1.0616
C32:2 PC	0.0033	0.3743	0.0005	-1.4611	0.3177
C34:0 DAG	0.6410	0.9921	0.5047	0.2578	-0.0085
C34:0 PC	0.9693	0.9909	0.9469	-0.0055	0.0037
C34:0 PE	0.9760	0.8634	0.7807	0.0054	0.0552
C34:1 DAG	0.9475	0.8797	0.7498	-0.0932	-0.3722
C34:1 PC	0.8378	0.9921	0.8346	-0.0302	0.0025
C34:1 PC plasmalogen-A	0.9209	0.9621	0.9989	-0.0105	-0.0106
C34:2 DAG	0.9604	0.8445	0.6889	-0.1178	-0.6689
C34:2 PC	0.8114	0.9507	0.7236	-0.0330	0.0152
C34:2 PC plasmalogen	0.9813	0.6512	0.6147	0.0031	0.0623
C34:2 PE plasmalogen	0.6854	0.8445	0.4046	1.0760	-0.3744
C34:3 DAG	0.9406	0.6621	0.4159	-0.2614	-1.7247
C34:3 PC	0.7737	0.9650	0.4118	-0.0977	0.0179
C34:3 PC plasmalogen	0.6410	0.9620	0.5981	-0.1191	-0.0198
C34:4 PC	0.8008	0.7894	0.5981	0.1415	-0.1854
C34:4 PC plasmalogen	0.7044	0.8876	0.0680	-0.3102	0.1371
C36:0 DAG	0.6741	0.8853	0.6919	0.1627	0.0461
C36:0 PC	0.8100	0.8445	0.9984	0.0972	0.0965
C36:0 PE	0.7994	0.9951	0.7613	-0.0520	0.0008
C36:1 DAG	0.9850	0.9176	0.8171	-0.0369	-0.3007
C36:1 PC	0.8925	0.9860	0.8660	-0.0186	0.0048
C36:1 PC plasmalogen	0.7737	0.8085	0.5427	0.1083	-0.1086
C36:1 PE	0.7737	0.9921	0.7236	0.4016	0.0116
C36:2 DAG	0.8527	0.8331	0.7080	-0.2382	-0.5294
C36:2 PC	0.8231	0.9571	0.8690	-0.0359	-0.0136
C36:2 PC plasmalogen	0.8270	0.9161	0.5427	-0.0397	0.0359
C36:2 PE	0.8477	0.6738	0.6899	0.1412	0.3884
C36:3 DAG	0.8428	0.8797	0.9685	-0.6817	-0.8147
C36:3 PC	0.8270	0.9161	0.9890	-0.0339	-0.0359
C36:3 PC plasmalogen	0.7737	0.9650	0.7498	-0.0770	-0.0116
C36:3 PE	0.6048	0.8853	0.3693	-0.1482	0.0576
C36:4 DAG	0.8008	0.9951	0.5410	-0.2342	0.0028
C36:4 PC plasmalogen	0.7226	0.9596	0.7232	-0.0583	-0.0151
C36:4 PC-B	0.8477	0.9951	0.8725	-0.0236	-0.0008
C36:4 PE	0.7044	0.9663	0.4100	-0.6139	0.0519
C36:5 PC plasmalogen-B	0.6579	0.0373	0.0072	-0.1139	0.3349
C36:5 PE plasmalogen	0.6854	0.0438	0.0030	-0.5724	1.7758
C38:2 PC	0.8048	0.9343	0.6540	-0.0422	0.0210
C38:2 PE	0.8609	0.9650	0.9685	-0.0297	-0.0205
C38:3 PC	0.9940	0.9161	0.9024	-0.0014	-0.0200
C38:3 PE plasmalogen	0.7737	0.5320	0.6889	-0.3031	-0.7085
C38:4 DAG	0.7044	0.0104	0.0029	0.1176	0.7465
C38:4 PC	0.8519	0.9719	0.9024	-0.0239	-0.0075
C38:4 PC plasmalogen	0.9978	0.9168	0.8171	0.0002	-0.0379
C38:4 PE	0.7677	0.4207	0.0458	-0.1502	0.4457
C38:5 PE	0.8114	0.5057	0.7571	-0.1351	-0.3271
C38:5 PE plasmalogen	0.7737	0.1243	0.0020	-0.3893	1.4796
C38:6 PC	0.8231	0.9292	0.9685	-0.0290	-0.0220
C38:6 PC plasmalogen	0.8008	0.2957	0.1340	-0.0590	0.1614
C38:6 PE plasmalogen	0.6741	0.0805	0.0014	-0.4850	1.3068
C38:7 PC plasmalogen	0.8190	0.8853	0.5047	-0.0477	0.0500

Table S1.1 (Continued).

C38:7 PE plasmalogen	0.7737	0.6261	0.2388	-0.4460	0.7160
C40:6 PC	0.8527	0.9951	0.8889	-0.0295	0.0014
C40:6 PE	0.8114	0.4207	0.0753	-0.0601	0.2382
C40:6 PS	0.7737	0.7856	0.9402	-0.1714	-0.2225
C40:7 PC plasmalogen	0.8925	0.9951	0.9228	-0.0263	-0.0021
C40:7 PE plasmalogen	0.7677	0.9507	0.6889	1.2273	0.2026
C40:9 PC	0.8250	0.9507	0.9514	-0.0205	-0.0128
C41:0 TAG	0.7226	0.9951	0.5981	0.9477	0.0073
C42:0 TAG	0.8008	0.9860	0.7498	0.2906	-0.0353
C43:0 TAG	0.7737	0.9507	0.5981	0.5071	-0.1546
C43:1 TAG	0.8270	0.8445	0.8345	-0.4294	-0.7054
C44:0 TAG	0.8094	0.9650	0.6977	0.2607	-0.0800
C44:1 TAG	0.8477	0.8846	0.8171	-0.2126	-0.3492
C44:2 TAG	0.8100	0.8445	0.9085	-0.5499	-0.6703
C45:0 TAG	0.7737	0.9650	0.5981	0.3848	-0.0785
C45:1 TAG	0.7737	0.8084	0.9847	-0.4215	-0.4101
C45:2 TAG	0.7737	0.9730	0.6791	-0.4112	-0.0629
C46:0 TAG	0.8008	0.9507	0.5981	0.2299	-0.0861
C46:1 TAG	0.8270	0.8765	0.8690	-0.1829	-0.2415
C46:2 TAG	0.8114	0.8853	0.9845	-0.2697	-0.2579
C47:0 TAG	0.8059	0.9507	0.6188	0.2726	-0.1084
C47:1 TAG	0.8270	0.8445	0.7849	-0.1924	-0.2975
C47:2 TAG	0.8114	0.8631	0.9845	-0.2850	-0.2980
C48:0 TAG	0.7737	0.9663	0.6600	0.2173	-0.0492
C48:1 TAG	0.8420	0.8097	0.6463	-0.0879	-0.1870
C48:2 TAG	0.8114	0.8797	0.9890	-0.1355	-0.1387
C48:3 TAG	0.8008	0.9168	0.8356	-0.1577	-0.1054
C48:4 TAG	0.9461	0.9446	0.9412	-0.0823	-0.1455
C49:0 TAG	0.7737	0.9446	0.5533	0.3003	-0.1195
C49:1 TAG	0.8231	0.8084	0.7401	-0.1596	-0.2577
C49:2 TAG	0.8270	0.8179	0.8142	-0.1602	-0.2632
C49:3 TAG	0.7790	0.8797	0.8348	-0.2955	-0.1945
C50:0 TAG	0.7226	0.9292	0.8013	0.5548	0.2118
C50:1 TAG	0.8753	0.8084	0.6564	-0.0261	-0.0762
C50:2 TAG	0.7737	0.8445	0.9085	-0.0924	-0.0795
C50:3 TAG	0.8190	0.8445	0.8937	-0.0566	-0.0770
C50:4 TAG	0.8270	0.8797	0.8720	-0.0461	-0.0682
C50:5 TAG	0.7994	0.9921	0.7498	-0.1754	-0.0145
C51:0 TAG	0.7226	0.9371	0.7852	0.6161	0.2087
C51:1 TAG	0.8250	0.8636	0.9302	-0.1046	-0.1283
C51:2 TAG	0.7737	0.8303	0.8937	-0.1590	-0.1323
C51:3 TAG	0.7226	0.6442	0.9810	-0.2221	-0.2146
C52:0 TAG	0.7018	0.8989	0.8123	1.1047	0.4894
C52:1 TAG	0.8315	0.8853	0.9315	-0.0687	-0.0902
C52:2 TAG	0.8543	0.9777	0.8690	-0.0235	-0.0079
C52:3 TAG	0.7226	0.8429	0.8224	-0.0877	-0.0659
C52:4 TAG	0.7994	0.9650	0.7236	-0.0457	-0.0120
C52:5 TAG	0.9978	0.8303	0.7736	-0.0003	0.0407
C52:6 TAG	0.6013	0.9091	0.7807	-0.1327	-0.0545
C53:2 TAG	0.9978	0.8429	0.7839	0.0002	0.0546
C53:3 TAG	0.6854	0.6502	0.6769	-0.3236	-0.2524
C54:1 TAG	0.8925	0.9446	0.9909	-0.0255	-0.0275
C54:2 TAG	0.6497	0.6887	0.9220	-0.0954	-0.0795
C54:3 TAG	0.7944	0.9446	0.8203	-0.0755	-0.0369
C54:4 TAG	0.8023	0.9446	0.5981	-0.0466	0.0230
C54:5 TAG	0.8190	0.9777	0.7632	-0.0396	0.0057
C54:6 TAG	0.7737	0.9650	0.7236	-0.0489	0.0105
C54:7 TAG	0.9081	0.8853	0.4869	-0.0245	0.0596
C54:8 TAG	0.7631	0.9781	0.8241	0.3105	0.0626
C56:1 TAG	0.9741	0.9921	0.9514	-0.0097	0.0080
C56:2 TAG	0.7737	0.9663	0.5981	0.0762	0.0140
C56:3 TAG	0.9679	0.9909	0.9460	0.0070	-0.0040

Table S1.1 (Continued).

C56:4 TAG	0.8114	0.6442	0.6451	-0.0353	0.0297
C56:5 TAG	0.9693	0.9446	0.9469	0.0039	0.0104
C56:6 TAG	0.9679	0.9099	0.7367	-0.0053	0.0245
C56:7 TAG	0.7994	0.7856	0.8937	-0.0959	-0.1261
C56:8 TAG	0.9679	0.8423	0.7849	0.0091	0.0747
C56:9 TAG	0.7141	0.9650	0.6051	-0.4514	-0.0751
C58:10 TAG	0.8270	0.9145	0.7498	-0.2185	0.1261
C58:6 TAG	0.9604	0.9948	0.9685	0.0157	0.0025
C58:7 TAG	0.7226	0.6442	0.9228	-0.1727	-0.2171
C58:8 TAG	0.4041	0.7094	0.7632	0.1240	0.0775
C58:9 TAG	0.9417	0.9921	0.9460	0.0373	0.0137
cholesterol	0.7226	0.9507	0.6214	-0.1556	-0.0382
coemzyme Q10	0.8477	0.8341	0.7934	-0.0882	-0.1846
N-Oleoylethanolamine	0.8464	0.9921	0.2827	0.4620	0.0467
NH4_C14:0 CE	0.7737	0.6680	0.5067	-0.1188	-0.1665
NH4_C16:0 CE	0.8270	0.9621	0.8889	-0.0334	-0.0143
NH4_C16:1 CE	0.7737	0.8189	0.9943	-0.0478	-0.0472
NH4_C18:0 CE	0.7983	0.8445	0.9135	-0.0778	-0.0616
NH4_C18:0 MAG	0.7226	0.8846	0.9917	0.0923	0.0952
NH4_C18:1 CE	0.9406	0.8445	0.7367	-0.0085	0.0262
NH4_C18:2 CE	0.7944	0.8797	0.8774	-0.0505	-0.0303
NH4_C18:3 CE	0.8519	0.9921	0.8720	-0.0226	-0.0026
NH4_C20:3 CE	0.7677	0.8631	0.8348	-0.0666	-0.0437
NH4_C20:4 CE	0.8114	0.9292	0.9024	-0.0361	-0.0229
NH4_C20:5 CE	0.8270	0.9650	0.7835	-0.0285	0.0113
NH4_C22:4 CE	0.7737	0.9040	0.8675	-0.0756	-0.0413
NH4_C22:5 CE	0.8008	0.9082	0.9085	-0.0408	-0.0260
NH4_C22:6 CE	0.8023	0.9719	0.7498	-0.0450	-0.0088
NH4_C30:0 DAG	0.8008	0.9663	0.5879	0.6840	-0.1569
NH4_C32:0 DAG	0.7994	0.9507	0.5410	0.4182	-0.1382
NH4_C32:1 DAG	0.7994	0.9951	0.7839	-0.1578	0.0025
NH4_C32:2 DAG	0.8428	0.6750	0.7081	-0.3284	-0.8474
NH4_C34:0 DAG	0.6677	0.9650	0.5981	0.2812	0.0287
NH4_C34:1 DAG	0.8114	0.9446	0.7272	-0.1042	0.0900
NH4_C34:2 DAG	0.9679	0.9650	0.7849	0.0755	-0.1492
NH4_C36:0 DAG	0.6850	0.7894	0.9373	0.1572	0.1255
NH4_C36:1 DAG	0.8925	0.8925	0.7088	-0.1898	0.3208
NH4_C36:2 DAG	0.8811	0.9176	0.9330	-0.3166	-0.4253
NH4_C38:4 DAG	0.8720	0.0258	0.0215	0.1091	1.4613
NH4_C42:0 TAG	0.8045	0.9446	0.6889	0.3592	-0.1786
NH4_C43:0 TAG	0.7737	0.9446	0.5770	0.6908	-0.2364
NH4_C43:1 TAG	0.9604	0.9719	0.7849	-0.1971	0.2136
NH4_C44:0 TAG	0.8045	0.9507	0.6600	0.3149	-0.1207
NH4_C44:1 TAG	0.9940	0.9446	0.7839	0.0157	-0.2841
NH4_C44:2 TAG	0.8304	0.9663	0.7427	-0.8427	0.2835
NH4_C45:0 TAG	0.7944	0.9650	0.5981	0.4206	-0.0874
NH4_C45:1 TAG	0.8720	0.9176	0.9103	-0.2912	-0.3928
NH4_C45:2 TAG	0.8114	0.8846	0.9847	-1.0304	-1.0819
NH4_C46:0 TAG	0.8114	0.9446	0.5981	0.2184	-0.1270
NH4_C46:1 TAG	0.8270	0.8853	0.9025	-0.2117	-0.2665
NH4_C46:2 TAG	0.9850	0.9292	0.7827	-0.0310	-0.3071
NH4_C47:0 TAG	0.8190	0.9446	0.6214	0.2332	-0.1260
NH4_C47:1 TAG	0.8246	0.8445	0.7498	-0.2804	-0.4291
NH4_C47:2 TAG	0.8114	0.8925	0.9775	-0.4699	-0.4389
NH4_C48:0 TAG	0.8231	0.9719	0.7427	0.1563	-0.0481
NH4_C48:1 TAG	0.8270	0.8445	0.7934	-0.1223	-0.1807
NH4_C48:2 TAG	0.8114	0.8797	0.9985	-0.1764	-0.1760
NH4_C48:3 TAG	0.7737	0.9168	0.6842	-0.5207	-0.2520
NH4_C49:0 TAG	0.7737	0.9800	0.5981	0.3168	-0.0382
NH4_C49:1 TAG	0.8190	0.8429	0.7839	-0.1767	-0.2547
NH4_C49:2 TAG	0.8720	0.8429	0.7232	-0.1307	-0.3338
NH4_C49:3 TAG	0.8114	0.9145	0.8837	-0.6963	-0.4080

Table S1.1 (Continued).

NH4_C50:0 TAG	0.7226	0.9446	0.7807	0.4453	0.1321
NH4_C50:1 TAG	0.8114	0.8076	0.8405	-0.0785	-0.1099
NH4_C50:2 TAG	0.8114	0.8797	0.9775	-0.0855	-0.0903
NH4_C50:3 TAG	0.8720	0.8947	0.7835	-0.0658	-0.1152
NH4_C50:4 TAG	0.8270	0.9951	0.8720	-0.1071	-0.0026
NH4_C50:5 TAG	0.8753	0.8631	0.8171	-0.9368	-2.4337
NH4_C51:1 TAG	0.8270	0.8445	0.7849	-0.0895	-0.1357
NH4_C51:2 TAG	0.8114	0.7435	0.7613	-0.1611	-0.2560
NH4_C51:3 TAG	0.8925	0.8445	0.4880	-0.0614	-0.1693
NH4_C52:0 TAG	0.7631	0.8853	0.8195	0.0697	0.0318
NH4_C52:1 TAG	0.8824	0.9343	0.4869	0.0144	-0.0184
NH4_C52:2 TAG	0.7677	0.8989	0.7537	-0.0871	-0.0465
NH4_C52:3 TAG	0.7666	0.8925	0.7089	-0.1167	-0.0673
NH4_C52:4 TAG	0.7737	0.8925	0.8427	-0.0783	-0.0529
NH4_C52:5 TAG	0.8114	0.8989	0.9311	-0.0635	-0.0413
NH4_C52:6 TAG	0.8114	0.8445	0.9943	-0.3274	-0.3347
NH4_C53:2 TAG	0.9417	0.4783	0.5242	-0.0197	-0.2239
NH4_C53:3 TAG	0.8270	0.9777	0.8171	-0.0542	-0.0108
NH4_C54:2 TAG	0.6854	0.9446	0.6888	-0.0315	-0.0090
NH4_C54:3 TAG	0.7044	0.9507	0.7447	-0.0656	-0.0196
NH4_C54:4 TAG	0.7737	0.9292	0.7849	0.0142	0.0042
NH4_C54:5 TAG	0.8707	0.9596	0.7498	-0.0232	0.0143
NH4_C54:6 TAG	0.8977	0.9343	0.7849	-0.0177	0.0231
NH4_C54:7 TAG	0.8270	0.8129	0.4046	0.1642	-0.3736
NH4_C54:8 TAG	0.8378	0.9951	0.8720	-0.5501	0.0252
NH4_C55:2 TAG	0.7677	0.8989	0.7537	0.2255	0.1041
NH4_C55:3 TAG	0.8925	0.5320	0.1093	-0.0470	-0.2601
NH4_C56:1 TAG	0.7737	0.9860	0.7498	-0.4883	0.0763
NH4_C56:2 TAG	0.8477	0.9921	0.8384	-0.4665	0.0677
NH4_C56:3 TAG	0.8925	0.8189	0.6791	0.0408	-0.1902
NH4_C56:4 TAG	0.9249	0.5798	0.7632	-0.0349	0.0833
NH4_C56:5 TAG	0.7226	0.9292	0.5981	-0.0534	0.0236
NH4_C56:6 TAG	0.8190	0.9292	0.9812	0.0229	0.0207
NH4_C56:7 TAG	0.8270	0.4296	0.7498	0.0199	0.0559
NH4_C56:8 TAG	0.7944	0.9596	0.7427	0.1267	-0.0636
NH4_C56:9 TAG	0.3245	0.5320	0.8224	0.6561	0.4960
NH4_C58:10 TAG	0.8527	0.8445	0.5981	0.0654	-0.1175
NH4_C58:11 TAG	0.8059	0.9860	0.7570	-0.1868	0.0270
NH4_C58:6 TAG	0.7226	0.5402	0.9402	-0.4059	-0.3509
NH4_C58:8 TAG	0.9052	0.9168	0.9391	-0.0088	-0.0153
NH4_C58:9 TAG	0.8445	0.4783	0.4550	-0.0442	-0.2139
NH4_C60:12 TAG	0.7226	0.9176	0.7613	0.3535	0.1466
palmithoylethanolamide	0.8008	0.8429	0.7562	-0.5993	-0.6628
sphingosine	0.7994	0.8797	0.9315	-0.6390	-0.5110
1-methylurate	0.7737	0.9650	0.7236	-0.8670	-0.0909
1-methylxanthine	0.6677	0.5320	0.9685	0.5032	0.4875
2-aminoadipate	0.7737	0.6352	0.9890	0.1552	0.1593
2-aminobutyrate	0.7413	0.5865	0.7934	0.0526	0.0690
2-aminoheptanoate	0.8882	0.4454	0.5981	0.0176	-0.0613
2-hydroxy-3-methylbutyrate/hydroxyisovalerate	0.5685	0.4449	0.9685	-0.0640	-0.0607
2-hydroxy-3-methylpentanoate/hydroxyisocaproate	0.6410	0.9621	0.5242	0.2722	-0.0494
2-hydroxyglutarate	0.7737	0.0921	0.4370	0.0275	0.0829
2-isopropylmalate	0.8464	0.9650	0.9103	0.0937	0.0486
3-4-dihydroxybenzylamine	0.8378	0.9371	0.9670	0.0153	0.0205
3-methyladipate/pimelate	0.6850	0.6282	0.9331	0.0936	0.0834
4-pyridoxate	0.9641	0.5279	0.4159	0.0035	0.0568
aconitate	0.8250	0.0662	0.0378	-0.0157	0.1528
adenine	0.8114	0.0503	0.0357	0.3096	1.8020
adipate/methylglutarate	0.6741	0.6198	0.8889	0.0947	0.0746
adonitol/arabitol	0.7411	0.5057	0.7498	0.0298	0.0437

Table S1.1 (Continued).

alpha-glycerophosphate	0.7226	0.0628	0.0378	-0.2552	0.6457
alpha-hydroxybutyrate/beta-hydroxybutyrate/hydroxyisobutyrate	0.8378	0.8925	0.8989	-0.0162	-0.0314
alpha-keto-beta-methylvalerate/alpha-ketoisocaproate	0.8270	0.9446	0.9460	0.1882	0.1279
alpha-ketoglutarate	0.1009	0.2918	0.0002	-0.4926	-0.2114
alpha-ketoisovalerate	0.8114	0.9145	0.9685	0.2272	0.1895
anhydroDglucose	0.7044	0.5279	0.7367	0.0619	0.1091
aspartate	0.8519	0.4296	0.4118	0.0159	0.0682
biotin	0.8270	0.9446	0.6540	-0.0296	0.0232
caffeate	0.7994	0.5211	0.8162	0.1012	0.1697
citrate/isocitrate	0.7562	0.5057	0.9847	0.0633	0.0658
cystathionine	0.9919	0.8965	0.7839	-0.0037	-0.0957
cytidine	0.6048	0.8989	0.7236	0.3101	0.1286
erythronate/threonate	0.8420	0.2031	0.1091	0.0109	0.0865
folate	0.8527	0.9200	0.9971	0.0154	0.0157
fructose/glucose/galactose	0.8190	0.9446	0.8999	-0.0218	-0.0146
fumarate/maleate	0.7737	0.4296	0.5981	0.0293	0.0806
glucuronate	0.9813	0.6158	0.1536	-0.0115	0.2453
glycerate	0.8114	0.3309	0.5047	0.0310	0.1072
guanine	0.6497	0.2489	0.4550	0.4229	0.7274
hexose monophosphate	0.5360	0.9921	0.8142	-0.1060	-0.0075
hippurate	0.8270	0.7894	0.8995	0.0149	0.0239
homovanillate	0.8477	0.5507	0.4646	-0.0108	0.0722
hypoxanthine	0.6435	0.9621	0.4118	0.3147	0.0452
indolelactate	0.9978	0.8989	0.7934	-0.0001	-0.0354
inosine	0.9813	0.9650	0.9228	-0.0117	0.0424
inositol	0.6854	0.4849	0.9810	0.0366	0.0377
isovalerate/valerate/methylbutyrate	0.8925	0.9777	0.9460	0.0669	0.0275
lactate	0.8231	0.3743	0.7498	0.0496	0.1245
malate	0.6741	0.1432	0.4550	0.0553	0.1293
malonate	0.7363	0.5320	0.8660	-0.1975	-0.2865
MDA	0.7226	0.6442	0.9085	0.1107	0.0878
mesaconate	0.8270	0.2957	0.3177	0.0125	0.0641
methylcysteine	0.9001	0.9921	0.9442	-0.0567	-0.0114
N-acetylcarnosine	0.8250	0.9650	0.7934	-0.1535	0.0357
N-acetylglutamate	0.8008	0.9371	0.6888	-0.0737	0.0300
norepinephrine	0.6579	0.2040	0.4118	0.0647	0.1198
oxalate	0.8882	0.6621	0.5248	-0.0125	0.0520
pantothenate	0.8925	0.9507	0.9775	-0.0127	-0.0103
pseudouridine	0.6048	0.2957	0.7613	0.0679	0.0910
quinolinate	0.8925	0.9507	0.7080	-0.0146	0.0164
riboflavin	0.9745	0.8445	0.7613	-0.0278	0.2544
salicylate	0.6677	0.9921	0.4869	1.1951	0.0206
salicylurate	0.4041	0.4983	0.9469	0.0827	0.0907
sebacate	0.8194	0.9749	0.7827	0.0350	-0.0084
sorbitol	0.7226	0.4207	0.7839	0.0471	0.0656
suberate	0.8477	0.5057	0.4880	0.1014	-0.3042
succinate	0.8008	0.8853	0.9916	0.0730	0.0746
sucrose/lactose/trehalose	0.3245	0.9176	0.3718	0.3854	-0.1129
taurodeoxycholate/taurochenodeoxycholate	0.8133	0.9082	0.9514	0.0980	0.0789
threitol	0.6677	0.4296	0.7427	0.0464	0.0623
thymine	0.7994	0.4922	0.2854	-0.0262	0.0401
uracil	0.5201	0.8631	0.1243	-0.0506	0.0154
urate	0.6497	0.5200	0.9685	0.1610	0.1745
uridine	0.6677	0.5360	0.9085	0.0786	0.0984
xanthine	0.8231	0.4089	0.4048	-0.0155	0.0442
xylose	0.7652	0.4454	0.6647	0.0535	0.0858
1-methyladenosine	0.5925	0.5360	0.5981	-0.4626	-0.1782
1-methylguanine	0.6497	0.9719	0.4773	-0.4440	0.0211
1-methylguanosine	0.4070	0.5360	0.6557	-0.3925	-0.2334
1-methylhistidine	0.9624	0.8477	0.7839	0.0350	0.1830

Table S1.1 (Continued).

1-methylnicotinamide	0.6741	0.9650	0.7236	0.1834	0.0341
1H-indole-3-acetamide	0.9406	0.8989	0.7260	0.3462	-1.1179
2-aminoheptanoic acid	0.6497	0.5057	0.9291	0.3147	0.3594
2-aminooctanate	0.8231	0.9860	0.7924	-0.2430	-0.0282
2-hydroxyphenethylamine	0.9940	0.8846	0.8085	-0.0191	0.3954
2'-deoxycytidine	0.6677	0.8303	0.7260	-0.3326	-0.1635
2'-O-methyladenosine	0.8288	0.9507	0.9685	-0.0773	-0.0582
3-aminoisobutyrate	0.7737	0.9650	0.7236	0.1160	-0.0332
3-chlorotyrosine	0.7677	0.9982	0.6888	-0.2834	0.0004
3-methylhistidine	0.8114	0.5320	0.7839	0.1757	0.3294
4-acetamidobenzoic acid	0.7994	0.6223	0.7212	-0.1626	-0.4683
4-acetamidobutanoate	0.8925	0.7957	0.5981	-0.0541	0.1602
4-aminohippuric acid	0.8114	0.9650	0.7839	0.0896	-0.0333
4-guanidinobutanoic acid	0.7226	0.9145	0.7601	-0.2333	-0.0843
4-hydroxyhippurate	0.7737	0.4296	0.7260	0.1595	0.2972
4-pyridoxate*	0.7652	0.6750	0.9612	-0.2255	-0.2005
5-acetylamino-6-amino-3-methyluracil	0.8008	0.8445	0.8660	-0.6252	-0.2922
5-alpha-cholestanol	0.8114	0.7893	0.8937	-0.1096	-0.1695
5-hydroxydopamine	0.7044	0.9663	0.5981	-0.2565	-0.0192
5-hydroxylysine	0.8270	0.8445	0.6230	0.0903	-0.1516
5-hydroxytryptophan	0.9890	0.5057	0.5427	-0.0066	-0.2526
5-hydroxytryptophol	0.7677	0.6223	0.8680	0.2400	0.3301
5-methylcytidine	0.3245	0.6750	0.6206	-0.4926	-0.2686
5-methylcytosine	0.6677	0.9446	0.4815	-1.6086	0.2083
6,8-dihydroxypurine	0.7226	0.7681	0.9612	0.1680	0.1445
7-methylguanine	0.3319	0.9176	0.2806	-0.4905	-0.0839
acetyl-galactosamine	0.5427	0.4454	0.9085	0.2239	0.2624
acetylcholine	0.7044	0.8445	0.7367	-0.1870	-0.0874
adenosine	0.8270	0.0628	0.1827	0.2079	1.2485
ADMA	0.9833	0.5200	0.4893	-0.0098	-0.2657
agmatine	0.8519	0.8429	0.2388	-0.1249	0.2725
ala-ala	0.8114	0.9082	0.9220	0.4060	0.2288
alanine	0.5318	0.5360	0.5981	-0.4647	-0.1869
allantoin	0.9162	0.6155	0.7236	0.0441	0.1927
alloisoleucine	0.8270	0.5057	0.5521	-0.0749	-0.2969
alpha-glycerophosphocholine	0.8114	0.8853	0.6116	-0.1180	0.1043
anserine	0.6579	0.9446	0.6540	0.2847	0.0594
arachidoyl ethanolamide	0.7226	0.9650	0.5981	-1.0752	-0.1194
arginine	0.4099	0.5320	0.7839	0.2715	0.1990
asparagine	0.7790	0.4845	0.9460	-0.1427	-0.1722
aspartate	0.9652	0.8253	0.2035	-0.0230	0.1832
barbituric acid	0.8048	0.9096	0.5540	0.8815	-0.7893
beta-alanine	0.5318	0.5320	0.8195	-0.3698	-0.2715
beta-guanidinopropionic acid	0.8674	0.9650	0.7236	0.0719	-0.0423
beta-leucine	0.7226	0.9824	0.5243	-0.4115	-0.0291
betaine	0.7737	0.4785	0.8370	0.1702	0.2426
biopterin	0.8231	0.9860	0.7839	-0.1450	-0.0202
biotin	0.9417	0.7828	0.5981	-0.0346	0.1767
butyrobetaine	0.6048	0.9650	0.6842	0.2158	0.0341
butyrylcarnitine	0.5318	0.7140	0.8680	-0.2777	-0.2089
C-glycosyltryptophan	0.9293	0.5320	0.6540	0.1647	0.9472
C14 carnitine	0.8250	0.9507	0.8346	-0.1799	-0.0811
C14:0 LPC	0.8114	0.8445	0.1291	-0.1728	0.2065
C14:0 SM	0.9406	0.8303	0.7357	0.0375	-0.1365
C14:1 carnitine	0.6741	0.5279	0.9519	-1.0123	-0.9073
C16 carnitine	0.3245	0.4747	0.7367	0.5662	0.3734
C16:0 ceramide (d18:1)	0.7809	0.6502	0.5981	0.6553	1.0199
C16:0 LPC_B	0.9489	0.5360	0.6600	0.0315	0.2239
C16:0 LPE	0.8720	0.5320	0.5950	-0.0430	-0.4094
C16:0 SM	0.9489	0.7083	0.7236	0.0258	0.1919
C16:1 LPC	0.7412	0.7957	0.4048	-0.2062	0.1476
C16:1 LPC plasmalogen	0.3319	0.9161	0.4019	-0.3957	-0.0898

Table S1.1 (Continued).

C16:1 SM	0.4624	0.6621	0.7844	0.2627	0.1736
C18 carnitine	0.9461	0.9507	0.9775	-0.0466	-0.0618
C18:0 LPC	0.8190	0.9200	0.3220	-0.1058	0.0851
C18:0 LPE	0.7737	0.4296	0.5981	-0.1611	-0.3774
C18:0 SM	0.5694	0.4296	0.7839	3.9408	4.2127
C18:1 carnitine	0.7737	0.5363	0.7839	0.2293	0.4244
C18:1 LPC	0.6677	0.5360	0.7447	-0.3494	-0.1682
C18:1 LPC plasmalogen	0.9367	0.5057	0.5171	0.0515	0.3497
C18:1 LPC plasmalogen_minor	0.9741	0.9951	0.9847	-0.0551	-0.0181
C18:1 LPE	0.4041	0.9446	0.2528	-0.4696	0.0615
C18:1 SM	0.7709	0.7083	0.9551	0.8145	0.9255
C18:2 carnitine	0.7141	0.8228	0.8352	-1.1833	-0.6925
C18:2 LPC	0.9940	0.4207	0.1482	0.0021	0.2669
C18:2 LPC_minor	0.7823	0.7632	0.9847	-0.1835	-0.1737
C18:2 SM	0.8114	0.7265	0.7934	0.5484	1.0259
C18:3 LPC	0.7994	0.6502	0.8632	-0.1568	-0.2346
C2 carnitine	0.6677	0.9921	0.5521	-0.2291	-0.0093
C20:0 LPE	0.8231	0.8989	0.9024	0.0907	0.1839
C20:0 SM	0.6854	0.6361	0.7498	-0.3008	-0.1515
C20:4 carnitine	0.7652	0.5320	0.6600	-0.2875	-0.8406
C20:4 LPC	0.3245	0.4783	0.7498	-0.4149	-0.3283
C20:4 LPE	0.4041	0.6261	0.1008	-1.2012	0.5509
C20:5 LPC	0.4099	0.9951	0.2806	-0.7687	0.0045
C22:1 SM	0.4876	0.8429	0.5981	-0.3091	-0.1401
C22:5 LPC	0.8445	0.5200	0.4736	0.0441	0.2239
C22:6 LPC	0.3245	0.4783	0.4159	-0.5594	-0.2213
C24:1 ceramide (d18:1)	0.8190	0.5057	0.3065	0.2462	0.7441
C3 carnitine	0.8925	0.4207	0.1713	0.0495	-0.3875
C3-DC-CH3 carnitine	0.7737	0.7435	0.2827	-0.1552	0.1546
C30:0 PC	0.8614	0.9507	0.7893	0.0657	-0.0578
C32:2 PC	0.3245	0.6621	0.0869	-2.8251	0.6873
C34:0 PE	0.8114	0.4207	0.7427	0.1526	0.3575
C34:1 DAG*	0.8231	0.9663	0.7534	0.6396	-0.1473
C34:2 PE plasmalogen	0.9606	0.4296	0.1315	0.0859	1.4884
C34:3 PC	0.8008	0.5320	0.1857	-0.3019	0.5564
C34:3 PC plasmalogen	0.8270	0.9982	0.8352	-0.1944	-0.0009
C36:2 PC	0.3086	0.4296	0.8224	0.2722	0.2262
C36:2 PE	0.7737	0.4454	0.8720	-0.3484	-0.5002
C36:4 PE	0.8008	0.4207	0.3450	0.6486	2.1280
C36:5 PC plasmalogen	0.9367	0.6621	0.7613	0.0441	0.1903
C36:5 PE plasmalogen	0.7044	0.0044	0.0048	-0.4868	2.0853
C38:4 PE	0.8008	0.1270	0.1827	0.2094	0.8715
C38:5 PE plasmalogen*	0.7944	0.0331	0.0043	-0.2372	1.3769
C38:6 PC plasmalogen	0.9143	0.4783	0.4118	0.0515	0.3750
C38:6 PE	0.9406	0.9650	0.9916	-0.1264	-0.1089
C38:6 PE plasmalogen*	0.9001	0.0021	0.0027	-0.0528	1.9802
C38:7 PC plasmalogen	0.7677	0.8989	0.8660	0.1497	0.0842
C38:7 PE plasmalogen	0.9693	0.2248	0.0753	0.0527	1.5380
C4-OH carnitine	0.6048	0.8429	0.6214	0.2780	0.0858
C40:6 PE	0.8477	0.8631	0.8774	-0.1383	-0.3042
C40:7 PE plasmalogen	0.8008	0.3743	0.1441	0.5735	1.9145
C5 carnitine	0.7994	0.3743	0.0869	0.1427	-0.4079
C5-DC carnitine	0.8008	0.8820	0.5981	-0.1276	0.0960
C5:1 carnitine	0.8464	0.9663	0.8345	0.0700	-0.0303
C6 carnitine	0.6741	0.0108	0.2528	-0.2770	-0.6962
C7 carnitine	0.8720	0.0132	0.0240	-0.0525	-0.9527
C9 carnitine	0.8190	0.7478	0.8296	-0.3255	-0.5734
caprylate	0.8934	0.8989	0.9103	0.1964	0.4230
carnitine	0.6497	0.8429	0.8171	0.2174	0.1292
carnosine	0.4180	0.8853	0.6888	-0.2828	-0.1055
choline	0.2796	0.5057	0.5067	0.3771	0.1930
cinnamoylglycine	0.6410	0.6502	0.7260	-0.3812	-0.2735

Table S1.1 (Continued).

citrulline	0.9162	0.8445	0.2302	-0.0425	0.1508
cotinine	0.8925	0.6158	0.6600	0.1656	0.9153
creatine	0.7044	0.9082	0.4550	-0.1852	0.0709
creatinine	0.7737	0.9734	0.7401	0.1269	-0.0261
cyclohexylamine	0.7737	0.6442	0.9685	-0.1835	-0.1671
cystine	0.9940	0.9650	0.9460	-0.0033	-0.0461
cytidine	0.6103	0.6964	0.7839	-0.3128	-0.2309
cytosine	0.6854	0.5821	0.2148	-0.2545	0.2274
dehydrophytosphingosine	0.5427	0.2040	0.5790	1.0827	1.3713
dihydrothymine	0.7994	0.8853	0.5981	0.5182	-0.3821
dihydrouracil	0.7666	0.8429	0.8720	0.6219	0.4362
dimethylglycine	0.7226	0.4296	0.9469	-0.1986	-0.1723
DMGV	0.8445	0.8119	0.0869	-0.0853	0.1851
ectoine	0.8926	0.9446	0.5981	0.1551	-0.1973
FAPy-adenine	0.5427	0.6502	0.5981	-0.4148	-0.2020
GABA	0.8977	0.9446	0.9612	-0.0542	-0.0820
geranyl acetoacetate	0.6741	0.8057	0.7613	-0.3072	-0.2027
glutamate	0.8231	0.5200	0.7236	0.1035	0.2473
glutamic acid amide	0.9693	0.3437	0.2003	-0.0156	-0.3703
glutamine	0.8519	0.8253	0.7839	0.0672	0.1588
glutamine_fragment1	0.3245	0.9507	0.5981	0.2722	0.0421
glycine	0.6048	0.8429	0.7498	-0.2537	-0.1309
glycocholate*	0.7055	0.5057	0.8296	0.2582	0.3355
glycodeoxycholate/glycochenodeoxycholate*	0.7044	0.8445	0.7248	-0.2764	-0.1045
guanidinoacetic acid	0.4041	0.0804	0.0005	-0.6093	0.7939
guanine	0.7631	0.0132	0.2035	0.5187	1.7872
guanosine	0.7944	0.0019	0.0171	0.4870	3.6818
hexanoylglycine	0.7737	0.9909	0.7498	0.2353	0.0206
hippurate*	0.7737	0.4296	0.9103	-0.2170	-0.2815
histamine	0.8114	0.7632	0.7849	0.1360	0.2065
histidine	0.9604	0.4296	0.3510	-0.0129	-0.2610
homoarginine	0.9679	0.8429	0.6692	-0.0179	0.1386
homocitrulline	0.7226	0.8989	0.7839	0.2229	0.0897
homocysteine	0.9679	0.9161	0.7839	0.0588	0.3103
homoserine	0.6854	0.3788	0.8720	0.2181	0.2690
hydroxyproline	0.7737	0.4280	0.9775	-0.1567	-0.1680
hypotaurine	0.8824	0.8853	0.8224	-0.1305	-0.6604
hypoxanthine	0.6677	0.8429	0.2806	0.2568	-0.1295
imidazole propionate	0.6048	0.9091	0.3518	-0.2198	0.0669
imidazoleacetic acid	0.6741	0.9176	0.7367	0.2822	0.1173
imidazolelactate	0.8008	0.7083	0.7447	0.3026	1.0185
inosine	0.9850	0.0033	0.0227	-0.0105	1.0767
isoleucine	0.9417	0.4296	0.2736	-0.0219	-0.3492
isoxanthopterin	0.7737	0.9176	0.2035	-0.3085	0.1584
kynurenic acid	0.9948	0.9446	0.9249	0.0039	0.0546
L-alpha-glutamyl-L-lysine	0.7666	0.9730	0.6780	-0.2613	0.0409
leucine	0.1717	0.5320	0.4046	0.3558	0.1706
linoleoyl ethanolamide	0.8270	0.8853	0.6540	-0.5749	0.8433
lysine	0.9176	0.8445	0.2594	-0.0414	0.1452
m-tyramine	0.8720	0.7047	0.5612	0.1110	-0.2667
methionine	0.7044	0.9200	0.4869	-0.2006	0.0689
methionine sulfoxide	0.7044	0.9921	0.6625	0.1711	-0.0063
methylguanidine	0.8925	0.7894	0.8171	-0.0490	-0.1486
methylimidazole acetic acid	0.8114	0.5360	0.7839	0.1196	0.2237
methylthioadenosine	0.6048	0.2054	0.0240	-0.5324	0.9743
myristoleate	0.7737	0.9429	0.5242	-0.2697	0.1275
N-acetylalanine	0.8008	0.7313	0.5758	0.1211	-0.1547
N-acetylaspartic acid	0.9683	0.5360	0.5981	0.0144	0.2777
N-acetylglutamic acid	0.6741	0.7083	0.8315	0.4432	0.7405
N-acetylhistidine	0.7737	0.4783	0.9469	-0.1759	-0.2042
N-acetylleucine	0.7737	0.5402	0.9157	0.3340	0.4369

Table S1.1 (Continued).

N-acetylornithine	0.8114	0.8445	0.4826	0.1113	-0.1301
N-acetylputrescine	0.7631	0.8445	0.5243	-0.2018	0.0886
N-acetylserine	0.8753	0.8846	0.7236	-0.0658	0.1549
N-acetyltryptophan	0.8250	0.5279	0.7934	-0.1181	-0.2265
N-alpha-acetylarginine	0.6125	0.0349	0.6463	0.2610	0.4373
N-lauroylglycine	0.7440	0.9176	0.7236	0.4776	0.0959
N-methylproline	0.9679	0.7828	0.4826	-0.0162	0.1652
N-methyltryptamine	0.6741	0.8445	0.9103	0.1921	0.1386
N1-acetylspermidine	0.3086	0.0186	0.0378	-0.5323	-1.1700
N2,N2-dimethylguanosine	0.9276	0.5360	0.5242	-0.0340	0.2565
N4-acetylcytidine	0.6677	0.6030	0.8428	-0.2923	-0.2030
N6-acetyllysine	0.8753	0.8429	0.2148	-0.0687	0.1721
N6,N6-dimethyllysine*	0.8270	0.8036	0.5242	0.0899	-0.1541
N6,N6,N6-trimethyllysine	0.6854	0.9096	0.3693	-0.2158	0.0662
niacinamide	0.7253	0.9951	0.7260	0.1567	-0.0050
nicotinic acid	0.7631	0.4849	0.9685	-0.4112	-0.3774
NMMA	0.8250	0.4420	0.6600	0.1006	0.2681
norleucine	0.7044	0.9446	0.6791	-0.6298	-0.0922
oleamide	0.8231	0.9446	0.8698	-0.7198	-0.3753
oleoyl glycine	0.8445	0.9446	0.9373	-0.3352	-0.2594
ornithine	0.5685	0.8445	0.7427	-0.2546	-0.1247
pantothenate*	0.6048	0.5057	0.9135	0.2641	0.2288
pantothenol	0.8114	0.9650	0.8720	-0.8063	-0.3113
phenylacetylglutamine	0.7652	0.7718	0.7934	0.1897	0.4044
phenylacetylglycine	0.9624	0.5279	0.5981	0.0234	-0.2232
phenylalanine	0.6854	0.9292	0.4075	-0.2137	0.0555
phosphocholine	0.8008	0.5057	0.4869	0.1767	0.4665
phytosphingosine	0.7759	0.9292	0.6600	1.0152	-0.5726
pipecolic acid	0.6099	0.5057	0.9326	0.2407	0.2110
pro-gly	0.8190	0.5057	0.2539	-0.1407	-0.3967
progesterone	0.3245	0.5279	0.7427	-2.2693	-1.5349
proline	0.6048	0.9429	0.6889	0.2266	0.0590
proline-betaine	0.6125	0.9161	0.6889	-0.2240	-0.0796
pseudouridine	0.7631	0.5853	0.8660	0.1502	0.2119
putrescine	0.8925	0.7572	0.6625	-0.0477	-0.1957
pyridoxal hydrochloride	0.8270	0.0732	0.0355	0.0827	0.7450
pyridoxamine	0.8250	0.7435	0.5047	0.0758	-0.1429
pyridoxine	0.6048	0.9921	0.4869	-0.2485	-0.0072
pyroglutamic acid	0.7226	0.9860	0.7498	0.1870	0.0190
ribothymidine	0.6741	0.9267	0.6767	-0.3624	-0.1078
S-methyl-L-cysteine-S-oxide	0.7737	0.4296	0.8261	0.1739	0.2571
sarcosine	0.6579	0.5488	0.7498	-0.5064	-0.2811
SDMA	0.8487	0.5320	0.5790	0.0988	0.3420
serine	0.6579	0.9621	0.7427	0.1844	0.0381
serotonin	0.6677	0.8084	0.8660	-0.3573	-0.2505
SM(d18:0/18:1(9Z))	0.7677	0.8989	0.9469	0.2485	0.1839
sphingosine	0.7226	0.8445	0.7839	-0.6093	-0.3435
sucrose	0.8190	0.8853	0.9469	0.3903	0.4688
taurine	0.9975	0.7435	0.6600	-0.0014	-0.1605
thiamine	0.6579	0.8846	0.3177	-0.2054	0.0756
threo-sphingosine	0.7055	0.9650	0.5981	2.5502	0.1378
threonine	0.8017	0.4542	0.8171	-0.1383	-0.2291
thymidine	0.8231	0.8303	0.3929	-0.1259	0.1971
thyroxine	0.5427	0.8853	0.5242	0.6453	0.2257
transvaccenic acid	0.8114	0.9860	0.6084	-0.3101	0.0364
triethanolamine	0.7044	0.5320	0.7849	0.2504	0.4298
trigonelline	0.7044	0.9596	0.6214	-0.2433	-0.0476
trimethylamine-N-oxide	0.4099	0.5057	0.7839	0.3213	0.2293
trimethylbenzene_isomer1	0.7677	0.9507	0.5242	-0.3090	0.0624
trimethylbenzene_isomer2	0.6677	0.4296	0.7849	0.6395	0.9354
tryptophan	0.8114	0.7894	0.4118	0.1081	-0.1593
tyramine	0.8100	0.9446	0.8142	-0.1882	-0.0465

Table S1.1 (Continued).

tyrosine	0.7018	0.9860	0.6276	0.1877	-0.0154
urate	0.6854	0.7359	0.7498	-0.5286	-0.2753
urocanic acid	0.8250	0.9797	0.8104	0.5563	0.1055
valine	0.8352	0.4241	0.2827	-0.0499	-0.3180
vanillylamine	0.7044	0.5320	0.8171	0.3668	0.4325
warfarin	0.9683	0.8989	0.8889	0.0463	0.2112
xanthine	0.5427	0.8989	0.6600	-0.2801	-0.0848
xanthopterin	0.9461	0.8631	0.9024	-0.0465	-0.1466
xanthosine	0.6854	0.8445	0.7236	-0.2352	-0.0937

Table S1.2. Differential expression data for all detected metabolites from cell extracts for scrambled and Pdss2 shRNAs with noted comparisons.

Metabolite	P1.v.Scr.fdr	P2.v.Scr.fdr	P1.v.P2.fdr	P1.v.Scr.log2fc	P2.v.Scr.log2fc
10-heptadecenoate	0.5809	0.4979	0.6619	-1.1624	-1.2881
10-nonadecenoate	0.5964	0.7258	0.5573	-1.2744	-0.7591
12-HETE/8-HETE	0.3232	0.7853	0.6955	-0.4653	-0.2056
13-docosenoate	0.3985	0.7389	0.3710	-1.6205	-0.4328
13-HODE	0.3829	0.4076	0.3949	-2.1150	-1.7785
13-HpODE	0.6707	0.5547	0.9702	0.0516	0.0555
16-hydroxypalmitate	0.5526	0.6767	0.2820	-0.0590	0.0374
16:0 PC(O)	0.1401	0.9021	0.1115	-0.4917	0.0248
17-Methylstearate	0.2426	0.6575	0.2382	-0.6027	-0.1370
2-hydroxyhexadecanoate	0.5340	0.5040	0.6541	-0.9647	-0.9267
3-hydroxydecanoate	0.6052	0.7510	0.6437	-0.1288	-0.0394
3-hydroxyhexanoate	0.7374	0.5320	0.2988	-0.1213	0.1705
3-hydroxyoctanoate	0.9660	0.6506	0.6528	-0.0093	0.0919
3-methyladipate	0.0404	0.8600	0.2300	-0.2978	-0.0375
3-oxooctadecanoate	0.7623	0.6575	0.9651	0.0751	0.0676
9-cis-retinoic acid	0.1324	0.5935	0.5761	0.1033	0.0500
9.10-diHOME	0.6815	0.2559	0.6955	-0.0642	-0.1242
adrenate	0.1354	0.0239	0.0656	0.3373	0.7261
alpha-linolenate	0.4836	0.2272	0.2144	-0.7809	-1.3115
arachidate	0.3486	0.3555	0.7604	-0.3999	-0.3328
arachidonate	0.4964	0.0504	0.1126	0.2371	0.8174
caprate	0.5336	0.0535	0.5240	-0.0713	-0.1395
carnosol	0.7432	0.9215	0.6528	0.1207	0.0279
docosahexaenoate	0.8769	0.2079	0.1773	0.0573	0.5996
docosapentaenoate	0.4130	0.0527	0.0883	0.3130	0.8672
dodecanedioate	0.6323	0.9001	0.3270	-0.0490	0.0105
dodecanoate	0.8688	0.7760	0.4141	0.0403	-0.0505
eicosadienoate	0.4348	0.8082	0.0258	-1.9577	-0.5155
eicosanedioate	0.9098	0.7301	0.6541	0.0418	-0.0923
eicosapentaenoate	0.5439	0.3064	0.4845	0.1413	0.2632
eicosatrienoate	0.6457	0.8480	0.0288	-0.7494	0.2739
eicosenoate	0.4480	0.5691	0.4097	-0.9925	-0.6919
fructose/glucose/galactose	0.5277	0.5900	0.0656	-0.4479	0.3583
gamma-linolenate	0.1915	0.7510	0.0051	-3.2549	-0.5932
glycochenodeoxycholate	0.0165	0.0883	0.0872	1.5896	0.8138
glycocholate	0.2862	0.3067	0.8834	0.6932	0.7584
glycodeoxycholate	0.1246	0.2593	0.7135	0.8899	0.7323
glycolithocholate	0.0014	0.0755	0.5200	2.3578	1.8254
heptadecanoate	0.6213	0.5947	0.8333	-0.3641	-0.3336
hexadecanedioate	0.7678	0.6097	0.8247	0.0285	0.0472
hydroxymyristate	0.5182	0.4972	0.8152	-0.4128	-0.3832
levulinate	0.5182	0.2245	0.0274	-0.2217	0.4484
linoleate	0.4816	0.4413	0.8123	-1.3096	-1.2615
lipoxin A5	0.6700	0.0519	0.4013	-0.0410	-0.1172
myristate	0.5744	0.5347	0.9596	-0.3013	-0.2958
myristoleate	0.5391	0.4152	0.4316	-0.9650	-1.1648
nervonic acid	0.1832	0.4421	0.0091	-1.3052	0.6964
nonadecanoate	0.4964	0.5900	0.3296	-0.7493	-0.4980
oleate	0.5289	0.5410	0.4996	-0.7321	-0.6205
oxypurinol	0.3978	0.9326	0.1078	-2.0685	0.1668
palmitate	0.9648	0.7742	0.7418	-0.0133	-0.0597

Table S1.2 (Continued).

palmitoleate	0.5560	0.4805	0.6194	-0.9773	-1.0562
palmitoylethanolamide	0.3908	0.4419	0.5436	-1.2977	-0.6014
pentadecanoate	0.6491	0.5836	0.9652	-0.5033	-0.5135
pentadecanol	0.9956	0.9283	0.8212	0.0052	0.1148
phytanate	0.6160	0.4592	0.1959	-1.0539	0.9077
sebacate	0.7677	0.9982	0.6221	-0.0672	-0.0003
stearate	0.5002	0.3064	0.9631	-0.0603	-0.0638
taurochenodeoxycholate	0.0114	0.0784	0.0441	1.7423	0.7942
taurocholate	0.3161	0.3781	0.9104	0.5661	0.6286
taurodeoxycholate	0.2329	0.2829	0.9247	0.5514	0.5854
taurohyodeoxycholate/tauroursodeoxycholate	0.5340	0.2971	0.4520	0.9247	1.5612
taurolithocholate	0.0693	0.2537	0.3791	1.0838	0.7426
tetradecanedioate	0.6209	0.6767	0.9985	0.0483	0.0482
undecanedionate	0.6604	0.4375	0.8333	-0.0603	-0.0880
C14:0 CE	0.0130	0.0504	0.1126	-0.5142	-0.2593
C14:0 LPC	0.3616	0.3064	0.9238	-0.2095	-0.2284
C14:0 SM	0.3070	0.0640	0.1695	-0.1440	-0.2973
C16:0 CE	0.7551	0.5223	0.8117	-0.0639	-0.0978
C16:0 Ceramide (d18:1)	0.0013	0.0021	0.0002	-0.5386	0.6932
C16:0 LPC	0.6663	0.2795	0.4624	-0.0948	-0.1953
C16:0 LPC_Na	0.6323	0.4066	0.6437	-0.1160	-0.1928
C16:0 LPE	0.3161	0.2277	0.9702	-0.3044	-0.3111
C16:0 SM	0.0114	0.0412	0.8123	-0.3535	-0.3411
C16:1 CE	0.2373	0.2752	0.7525	-0.1504	-0.1158
C16:1 LPC	0.0440	0.6007	0.0258	-0.5066	-0.1050
C16:1 MAG	0.1110	0.9654	0.2174	0.4120	-0.0110
C16:1 SM	0.2331	0.0243	0.0529	-0.1331	-0.3543
C18:0 CE	0.6530	0.9326	0.6512	-0.1327	-0.0162
C18:0 LPC	0.7677	0.2079	0.2258	-0.0608	-0.2586
C18:0 LPE	0.0436	0.3066	0.0348	-0.4053	-0.1763
C18:0 MAG	0.5277	0.0738	0.2546	0.2938	-0.1972
C18:0 SM	0.7955	0.5471	0.2545	0.0519	-0.1012
C18:1 CE	0.9098	0.4972	0.6447	-0.0283	-0.1250
C18:1 LPC	0.5734	0.5054	0.9783	-0.1586	-0.1631
C18:1 LPE	0.6068	0.6542	0.2378	0.2580	-0.1798
C18:1 SM	0.8227	0.2082	0.0258	0.0309	-0.1855
C18:2 CE	0.9743	0.5433	0.4924	0.0078	-0.1260
C18:2 LPC	0.8781	0.3900	0.7437	-0.0577	-0.1495
C18:3 CE	0.9098	0.5377	0.5107	0.0365	-0.1451
C20:0 LPE	0.9782	0.6528	0.6330	0.0022	-0.0444
C20:0 SM	0.2373	0.0286	0.0775	-0.1283	-0.2504
C20:3 CE	0.0201	0.0527	0.3270	-0.4013	-0.2945
C20:4 CE	0.5560	0.1366	0.0288	0.0832	-0.2187
C20:4 LPC	0.2426	0.1798	0.8272	-0.3720	-0.4085
C20:4 LPE	0.7346	0.7550	0.9013	-0.3382	-0.2497
C20:5 CE	0.7799	0.0539	0.0847	-0.0775	-0.6079
C20:5 LPC	0.3335	0.3900	0.8641	-0.2505	-0.2230
C22:0 Ceramide (d18:1)	0.0017	0.1255	0.0007	-0.6845	0.2187
C22:0 LPE	0.9496	0.0983	0.0451	-0.0113	-0.2324
C22:0 SM	0.0106	0.0036	0.2240	-0.3107	-0.4249
C22:1 MAG	0.0168	0.0016	0.0000	0.3095	-0.6112
C22:1 SM	0.6700	0.0329	0.0021	-0.0479	-0.2833

Table S1.2 (Continued).

C22:4 CE	0.0107	0.0021	0.0480	-0.4211	-0.7361
C22:5 CE	0.0015	0.0010	0.0242	-0.5559	-0.9278
C22:6 CE	0.2613	0.0218	0.1333	-0.2296	-0.5428
C22:6 LPC	0.2115	0.3080	0.4357	-0.3663	-0.2400
C22:6 LPE	0.9574	0.3389	0.3184	-0.0611	-0.7659
C24:0 Ceramide (d18:1)	0.0004	0.0919	0.0001	-1.2688	-0.2669
C24:0 SM	0.0130	0.0025	0.0182	-0.4577	-0.7082
C24:1 Ceramide (d18:1)	0.0004	0.1981	0.0002	-0.9273	0.1846
C24:1 SM	0.0213	0.0085	0.4404	-0.3617	-0.4497
C30:0 DAG	0.5809	0.9001	0.6221	-0.3908	-0.0913
C30:0 PC	0.0002	0.0202	0.0007	-0.6303	-0.2495
C30:1 PC	0.0001	0.0430	0.0000	-1.4337	-0.2150
C32:0 DAG	0.1107	0.3422	0.6541	-0.2932	-0.1977
C32:0 PC	0.0116	0.0152	0.5899	-0.3067	-0.2567
C32:0 PE	0.0021	0.2180	0.0246	-0.5908	-0.1842
C32:1 DAG	0.7652	0.5307	0.6461	-0.1065	-0.3241
C32:1 PC	0.0004	0.7615	0.0000	-1.0216	-0.0332
C32:1 PE	0.0028	0.2363	0.0000	-1.1816	-0.1367
C32:2 DAG	0.8103	0.5130	0.1289	-0.7711	1.6802
C32:2 PC	0.0001	0.3422	0.0000	-1.3701	0.0952
C34:0 DAG	0.4416	0.2881	0.7346	0.2899	0.1825
C34:0 PC	0.0854	0.3942	0.0470	0.1789	-0.0921
C34:0 PE	0.0015	0.0347	0.3903	-0.2335	-0.1824
C34:0 PS	0.2154	0.0089	0.0026	-0.1655	0.3918
C34:1 DAG	0.0250	0.2125	0.3027	-0.2727	-0.1589
C34:1 PC	0.7277	0.0417	0.0274	-0.0254	0.2074
C34:1 PC plasmalogen-A	0.0004	0.0417	0.0247	-0.5535	-0.2421
C34:2 DAG	0.0302	0.4473	0.0234	-2.3183	-0.3452
C34:2 PC	0.0025	0.0066	0.0000	-0.5261	0.3991
C34:2 PC plasmalogen	0.1976	0.0293	0.0006	0.1555	-0.3108
C34:2 PE	0.0015	0.0054	0.0000	-0.5565	0.4432
C34:2 PE plasmalogen	0.0020	0.0329	0.0008	0.3997	-0.2676
C34:3 PC	0.0012	0.0819	0.0006	-0.7143	0.2310
C34:3 PC plasmalogen	0.0004	0.0025	0.0453	-0.5899	-0.3956
C34:3 PE plasmalogen	0.1922	0.0087	0.0568	-0.1330	-0.3455
C34:4 PC	0.0196	0.0243	0.9128	-0.2178	-0.2229
C34:4 PC plasmalogen	0.0002	0.0210	0.0001	-0.8891	-0.2164
C34:5 PC plasmalogen	0.0015	0.2046	0.0283	-0.3839	-0.1372
C36:0 DAG	0.3232	0.2126	0.5251	0.3680	0.1548
C36:0 PC	0.3985	0.3350	0.1144	0.1027	-0.1228
C36:0 PE	0.0205	0.9021	0.0034	0.3377	0.0114
C36:1 DAG	0.0465	0.0707	0.2240	-0.2114	-0.1036
C36:1 PC	0.2406	0.4442	0.2794	-0.1341	-0.0741
C36:1 PC plasmalogen	0.0004	0.4084	0.0007	-0.8993	-0.1085
C36:1 PE	0.2350	0.2451	0.0510	-0.1714	0.1694
C36:1 PE plasmalogen	0.4934	0.0318	0.0453	-0.0575	-0.3349
C36:2 DAG	0.0630	0.5850	0.0437	-0.2830	0.0740
C36:2 PC	0.1858	0.0013	0.0001	-0.1284	0.5681
C36:2 PC plasmalogen	0.0001	0.6097	0.0000	-0.7315	-0.0321
C36:2 PE	0.0657	0.0031	0.0216	0.1911	0.5728
C36:2 PE plasmalogen	0.2809	0.0217	0.0137	0.1058	-0.3134
C36:3 DAG	0.0160	0.8496	0.0033	-0.9878	0.0505
C36:3 PC	0.4606	0.0750	0.0002	-0.1557	0.5128

Table S1.2 (Continued).

C36:3 PC plasmalogen	0.0021	0.3331	0.0008	-0.6038	-0.1196
C36:3 PE	0.0290	0.3092	0.0408	-0.2486	-0.0944
C36:3 PE plasmalogen	0.0264	0.0493	0.0031	0.2846	-0.2450
C36:4 DAG	0.7058	0.2020	0.5588	-0.2393	-0.6101
C36:4 hydroxy-PC-B	0.2487	0.6074	0.1123	-0.3801	0.1100
C36:4 PC plasmalogen	0.0002	0.5320	0.0000	-0.7902	0.0423
C36:4 PC-B	0.5439	0.6137	0.1201	-0.0551	0.0350
C36:4 PE	0.0015	0.3251	0.0003	-0.4140	0.0809
C36:4 PE plasmalogen	0.0003	0.5850	0.0002	-0.8140	0.0625
C36:5 PC plasmalogen-B	0.0002	0.0146	0.0055	-0.6738	-0.2761
C36:5 PE plasmalogen	0.0009	0.3715	0.0030	-0.4925	-0.0781
C38:2 PC	0.0051	0.0228	0.0002	-0.4546	0.2795
C38:2 PE	0.9222	0.0016	0.0001	0.0130	0.6600
C38:3 PC	0.0302	0.0193	0.0005	-0.3680	0.3853
C38:3 PE plasmalogen	0.0657	0.0066	0.1144	-0.1853	-0.3344
C38:4 DAG	0.6709	0.2593	0.5432	-0.1017	-0.2649
C38:4 PC	0.3557	0.1021	0.0453	0.0722	-0.1391
C38:4 PC plasmalogen	0.0002	0.6531	0.0000	-0.9664	0.0418
C38:4 PE	0.0213	0.0286	0.0002	-0.2269	0.1789
C38:4 PI	0.4266	0.1377	0.1666	0.5807	1.2748
C38:5 DAG	0.7705	0.8600	0.8803	-0.0600	-0.0312
C38:5 PE	0.9574	0.0032	0.0132	0.0065	0.3712
C38:5 PE plasmalogen	0.0009	0.1669	0.0106	-0.6112	-0.1850
C38:6 PC	0.1966	0.8496	0.0184	-0.3561	0.0439
C38:6 PC plasmalogen	0.0005	0.0043	0.0007	-0.9181	-0.5061
C38:6 PE	0.3056	0.1981	0.5573	-0.1231	-0.1586
C38:6 PE plasmalogen	0.0027	0.0417	0.0620	-0.4717	-0.2395
C38:6 PS	0.0009	0.4498	0.0003	-0.5994	0.0620
C38:7 PC plasmalogen	0.0002	0.0031	0.0032	-0.8049	-0.4171
C38:7 PE plasmalogen	0.0038	0.0009	0.0032	-0.3304	-0.5417
C40:10 PC	0.0235	0.0471	0.0006	-0.1846	0.1515
C40:6 PC	0.3636	0.2020	0.0258	-0.0973	0.1076
C40:6 PE	0.0020	0.0727	0.4097	-0.3524	-0.2540
C40:6 PS	0.2329	0.1307	0.5319	0.1775	0.2316
C40:7 PC plasmalogen	0.0002	0.0800	0.0002	-0.9824	-0.1630
C40:7 PE plasmalogen	0.0066	0.0550	0.0416	-0.4700	-0.2713
C40:9 PC	0.5809	0.2752	0.4177	0.0782	0.1471
C41:0 TAG	0.6707	0.2741	0.4012	0.2714	1.0896
C42:0 TAG	0.8893	0.3422	0.3401	0.0545	0.4919
C42:11 PE plasmalogen	0.0146	0.0036	0.1496	-0.3308	-0.5279
C43:0 TAG	0.6031	0.3067	0.4070	0.2089	0.7997
C43:1 TAG	0.5980	0.4255	0.6221	0.5491	1.2948
C44:0 TAG	0.6059	0.2673	0.1899	-0.1080	0.4853
C44:1 TAG	0.4751	0.2611	0.1350	-0.2290	0.6729
C44:13 PE plasmalogen	0.0107	0.8464	0.0034	0.3203	0.0185
C44:2 TAG	0.7563	0.3592	0.4845	0.1834	0.7747
C45:0 TAG	0.5023	0.2906	0.3382	0.1507	0.6098
C45:1 TAG	0.4416	0.3538	0.4742	0.2508	0.7745
C45:2 TAG	0.6223	0.3092	0.5439	0.3493	0.8978
C46:0 TAG	0.5627	0.0393	0.0183	-0.0853	0.5605
C46:1 TAG	0.0535	0.0789	0.0173	-0.3247	0.5208
C46:2 TAG	0.0252	0.2342	0.0227	-0.5029	0.4076
C46:3 TAG	0.0253	0.0211	0.4628	1.1606	1.3335

Table S1.2 (Continued).

C46:4 TAG	0.0522	0.0016	0.0203	-0.3348	-1.4974
C47:0 TAG	0.3917	0.2272	0.3457	0.2023	0.5882
C47:1 TAG	0.5336	0.2353	0.2382	0.1455	0.7522
C47:2 TAG	0.6840	0.2287	0.2388	0.1235	0.7401
C48:0 TAG	0.3671	0.0473	0.0606	0.1415	0.5694
C48:1 TAG	0.4135	0.0037	0.0064	-0.1365	0.6335
C48:2 TAG	0.0088	0.0103	0.0002	-0.3766	0.4516
C48:3 TAG	0.0630	0.1131	0.0007	-0.2548	0.2291
C48:4 TAG	0.4816	0.0886	0.0007	0.0789	-0.1930
C48:5 TAG	0.0480	0.0019	0.0048	-0.2394	-0.9559
C49:0 TAG	0.1983	0.0747	0.4002	0.4348	0.7338
C49:1 TAG	0.0945	0.0919	0.2350	0.3122	0.6629
C49:2 TAG	0.4135	0.0417	0.0752	0.1469	0.7345
C49:3 TAG	0.4836	0.1223	0.0775	0.0622	0.5312
C50:0 TAG	0.0198	0.0029	0.0281	0.4200	0.8580
C50:1 TAG	0.0633	0.0017	0.0326	0.3016	0.7666
C50:2 TAG	0.4831	0.0211	0.0049	-0.0982	0.5647
C50:3 TAG	0.1698	0.0031	0.0015	-0.1564	0.4730
C50:4 TAG	0.0176	0.0550	0.0546	0.3225	0.2371
C50:5 TAG	0.0737	0.5900	0.0019	0.2594	0.0677
C50:6 TAG	0.0302	0.2248	0.0005	0.2946	-0.1581
C51:0 TAG	0.0605	0.0494	0.5322	0.7131	0.9096
C51:1 TAG	0.0087	0.0024	0.1109	0.4874	0.7710
C51:2 TAG	0.0080	0.0194	0.0474	0.3435	0.7050
C51:3 TAG	0.4130	0.0026	0.0022	0.0830	0.6691
C52:0 TAG	0.2731	0.0512	0.5144	0.4988	0.7508
C52:1 TAG	0.0232	0.0015	0.0240	0.3262	0.7375
C52:2 TAG	0.1103	0.0070	0.0108	0.2450	0.7471
C52:3 TAG	0.8073	0.0016	0.0016	-0.0240	0.6235
C52:4 TAG	0.2401	0.0393	0.4073	0.1471	0.2638
C52:5 TAG	0.0069	0.0070	0.7167	0.4314	0.4143
C52:6 TAG	0.1065	0.1649	0.8165	0.2225	0.2311
C52:7 TAG	0.0109	0.3111	0.0000	0.7312	-0.1191
C53:2 TAG	0.0010	0.0014	0.0409	0.5110	0.8371
C53:3 TAG	0.0843	0.0014	0.0055	0.3167	1.1078
C54:1 TAG	0.0665	0.0048	0.0307	0.2633	0.6827
C54:2 TAG	0.0114	0.0016	0.0028	0.2418	0.6496
C54:3 TAG	0.4831	0.0009	0.0001	0.0623	0.7918
C54:4 TAG	0.0148	0.0014	0.0235	0.3354	0.6810
C54:5 TAG	0.0029	0.0026	0.9291	0.5464	0.5576
C54:6 TAG	0.0224	0.0052	0.2361	0.3344	0.5205
C54:7 TAG	0.0154	0.0996	0.1212	0.3514	0.2133
C54:8 TAG	0.0015	0.6360	0.0000	0.8173	0.0636
C54:9 TAG	0.0168	0.0295	0.0000	0.9286	-0.4983
C55:2 TAG	0.0130	0.0009	0.0547	0.4126	0.6824
C56:1 TAG	0.3881	0.0128	0.0444	0.1627	0.6235
C56:10 TAG	0.0006	0.7112	0.0001	1.1381	-0.0598
C56:2 TAG	0.3796	0.0047	0.0110	0.0984	0.6069
C56:3 TAG	0.9565	0.0009	0.0002	-0.0058	0.7693
C56:4 TAG	0.0155	0.0013	0.0011	0.2613	0.7760
C56:5 TAG	0.0004	0.0010	0.1647	0.5025	0.6194
C56:6 TAG	0.0039	0.0014	0.1666	0.4685	0.6395
C56:7 TAG	0.0693	0.0046	0.3472	0.3291	0.4851

Table S1.2 (Continued).

C56:8 TAG	0.0003	0.0074	0.0050	1.0483	0.4765
C56:9 TAG	0.0007	0.2041	0.0000	1.0275	0.2284
C58:10 TAG	0.0004	0.0650	0.0000	0.9928	0.3533
C58:11 TAG	0.0069	0.1928	0.0000	1.0037	0.1921
C58:6 TAG	0.0107	0.0016	0.0449	0.3896	0.6947
C58:7 TAG	0.0292	0.0595	0.4578	0.7865	0.6400
C58:8 TAG	0.0010	0.0275	0.0436	0.7764	0.3774
C58:9 TAG	0.0001	0.0014	0.0053	1.0690	0.6041
C60:12 TAG	0.0001	0.1082	0.0000	1.2183	0.1647
campesterol	0.3298	0.2152	0.5322	-0.1177	-0.1900
cholesterol	0.4836	0.2435	0.5728	-0.1040	-0.1702
coemzyme Q10	0.0009	0.0016	0.1610	-1.4403	-1.1228
coenzyme Q9	0.0002	0.0004	0.1342	-1.5352	-1.3034
N-Oleoylethanolamine	0.0121	0.0747	0.0277	0.7431	0.3913
NH4_C14:0 CE	0.0949	0.2309	0.2713	-0.5007	-0.2391
NH4_C16:0 CE	0.8680	0.8716	0.9370	-0.0438	-0.0287
NH4_C16:1 CE	0.7551	0.6137	0.9128	-0.0565	-0.0717
NH4_C18:0 CE	0.6139	0.5151	0.1717	-0.1267	0.1338
NH4_C18:0 MAG	0.5238	0.0290	0.2420	0.3367	-0.2403
NH4_C18:1 CE	0.9928	0.8199	0.8508	0.0019	-0.0374
NH4_C18:2 CE	0.8026	0.9369	0.7173	0.0931	-0.0207
NH4_C18:3 CE	0.7649	0.6339	0.4141	0.1194	-0.1426
NH4_C20:3 CE	0.1152	0.3073	0.2391	-0.3178	-0.1697
NH4_C20:4 CE	0.5439	0.2816	0.0581	0.1285	-0.2152
NH4_C20:5 CE	0.8967	0.0445	0.0283	-0.0381	-0.5692
NH4_C22:4 CE	0.0043	0.0016	0.0319	-0.3999	-0.6750
NH4_C22:5 CE	0.0029	0.0011	0.0064	-0.4974	-0.8432
NH4_C22:6 CE	0.5980	0.0937	0.2144	-0.1651	-0.5512
NH4_C30:0 DAG	0.1205	0.5320	0.2027	-1.2458	-0.3398
NH4_C32:0 DAG	0.0452	0.3064	0.1588	-0.5537	-0.1852
NH4_C32:1 DAG	0.0829	0.3227	0.5240	-0.6153	-0.3749
NH4_C32:2 DAG	0.0456	0.3422	0.5784	-2.4699	-1.5588
NH4_C34:0 DAG	0.8567	0.6520	0.9370	0.0762	0.0510
NH4_C34:1 DAG	0.0106	0.3227	0.1977	-0.2928	-0.1249
NH4_C34:2 DAG	0.0017	0.0588	0.0082	-1.7337	-0.4850
NH4_C36:0 DAG	0.3759	0.9624	0.3155	0.3117	-0.0055
NH4_C36:1 DAG	0.0484	0.0959	0.2388	-0.3619	-0.1761
NH4_C36:2 DAG	0.0179	0.3781	0.0087	-0.4321	0.0673
NH4_C36:3 DAG	0.0043	0.8489	0.0019	-1.3676	0.0544
NH4_C36:4 DAG	0.1687	0.0025	0.2984	-0.3834	-0.6088
NH4_C38:4 DAG	0.5035	0.2554	0.8123	-0.2084	-0.2857
NH4_C38:5 DAG	0.4098	0.4421	0.8124	-0.3180	-0.2205
NH4_C42:0 TAG	0.9782	0.4955	0.4337	-0.0122	0.4310
NH4_C43:0 TAG	0.8763	0.3250	0.3364	0.0910	0.9190
NH4_C43:1 TAG	0.8117	0.4084	0.5728	0.4123	1.6152
NH4_C44:0 TAG	0.5072	0.2281	0.1197	-0.1278	0.5443
NH4_C44:1 TAG	0.4480	0.2511	0.1269	-0.2950	0.6808
NH4_C44:2 TAG	0.8309	0.3555	0.3555	-0.2736	1.0376
NH4_C45:0 TAG	0.4582	0.3073	0.3949	0.1873	0.6528
NH4_C45:1 TAG	0.5182	0.3092	0.4073	0.3094	1.0749
NH4_C45:2 TAG	0.3983	0.4036	0.7504	0.9525	1.5214
NH4_C46:0 TAG	0.9032	0.0276	0.0222	0.0197	0.5864
NH4_C46:1 TAG	0.0630	0.0890	0.0227	-0.3098	0.5516

Table S1.2 (Continued).

NH4_C46:2 TAG	0.1013	0.2179	0.0268	-0.5142	0.4898
NH4_C46:3 TAG	0.3390	0.9522	0.5104	-0.2126	0.0169
NH4_C47:0 TAG	0.0630	0.1497	0.3771	0.2902	0.6614
NH4_C47:1 TAG	0.1324	0.2256	0.2977	0.2941	0.8394
NH4_C47:2 TAG	0.6469	0.2361	0.2563	0.1737	0.9117
NH4_C48:0 TAG	0.1064	0.0036	0.0149	0.1999	0.7024
NH4_C48:1 TAG	0.4130	0.0048	0.0034	-0.0992	0.6087
NH4_C48:2 TAG	0.0288	0.0114	0.0008	-0.3694	0.4806
NH4_C48:3 TAG	0.2176	0.1415	0.0007	-0.2426	0.2736
NH4_C48:4 TAG	0.6530	0.1023	0.0026	0.0662	-0.2418
NH4_C49:0 TAG	0.0223	0.0275	0.2420	0.4135	0.6995
NH4_C49:1 TAG	0.0082	0.0393	0.1104	0.4336	0.8397
NH4_C49:2 TAG	0.3984	0.0271	0.0811	0.1657	0.7366
NH4_C49:3 TAG	0.2373	0.0504	0.1115	0.1689	0.6602
NH4_C50:0 TAG	0.0156	0.0023	0.0137	0.4323	1.0652
NH4_C50:1 TAG	0.0269	0.0021	0.0027	0.2645	0.7728
NH4_C50:2 TAG	0.9699	0.0021	0.0002	-0.0047	0.6825
NH4_C50:3 TAG	0.3897	0.0075	0.0005	-0.1364	0.5456
NH4_C50:4 TAG	0.0237	0.0993	0.3540	0.3586	0.2575
NH4_C50:5 TAG	0.1293	0.8775	0.0608	0.2546	0.0218
NH4_C50:6 TAG	0.3040	0.5707	0.0409	0.3036	-0.1614
NH4_C51:1 TAG	0.0080	0.0018	0.0062	0.4369	0.8648
NH4_C51:2 TAG	0.0168	0.0016	0.0029	0.3475	0.8547
NH4_C51:3 TAG	0.2542	0.0032	0.0029	0.1720	0.6963
NH4_C52:0 TAG	0.5340	0.0511	0.4593	0.0865	0.1854
NH4_C52:1 TAG	0.0171	0.0020	0.0087	0.3234	0.9463
NH4_C52:2 TAG	0.0028	0.0009	0.0015	0.3172	0.8461
NH4_C52:3 TAG	0.6223	0.0014	0.0003	0.0583	0.7795
NH4_C52:4 TAG	0.0046	0.0026	0.1846	0.5012	0.6011
NH4_C52:5 TAG	0.0147	0.0221	0.4097	0.4956	0.4205
NH4_C52:6 TAG	0.0456	0.0904	0.9370	0.2854	0.2947
NH4_C52:7 TAG	0.0063	0.3067	0.0007	0.7502	-0.2015
NH4_C53:2 TAG	0.0258	0.0009	0.0001	0.2724	0.9114
NH4_C53:3 TAG	0.1698	0.0010	0.0001	0.1765	0.9093
NH4_C54:2 TAG	0.1217	0.0018	0.0011	0.2274	0.7975
NH4_C54:3 TAG	0.1108	0.0009	0.0005	0.1720	0.9878
NH4_C54:4 TAG	0.0296	0.0031	0.0258	0.2766	0.5930
NH4_C54:5 TAG	0.0009	0.0020	0.8249	0.6708	0.6943
NH4_C54:6 TAG	0.0072	0.0050	0.1804	0.3861	0.4972
NH4_C54:7 TAG	0.0106	0.1889	0.0243	0.3830	0.1737
NH4_C54:8 TAG	0.0005	0.4066	0.0001	0.9317	0.1027
NH4_C55:2 TAG	0.0034	0.0004	0.0003	0.3680	1.1566
NH4_C55:3 TAG	0.0414	0.0009	0.0009	0.2620	1.3145
NH4_C56:1 TAG	0.6622	0.0043	0.0117	0.0822	0.7856
NH4_C56:2 TAG	0.7403	0.0024	0.0003	0.0594	0.8739
NH4_C56:3 TAG	0.9098	0.0009	0.0000	0.0184	1.1404
NH4_C56:4 TAG	0.0694	0.0010	0.0003	0.2999	1.1232
NH4_C56:5 TAG	0.0016	0.0019	0.1081	0.5463	0.7623
NH4_C56:6 TAG	0.0048	0.0024	0.1038	0.5536	0.7751
NH4_C56:7 TAG	0.0028	0.0032	0.6419	0.5407	0.5912
NH4_C56:8 TAG	0.0002	0.0128	0.0001	1.1919	0.4396
NH4_C56:9 TAG	0.0042	0.0535	0.0000	1.1321	0.2946
NH4_C58:10 TAG	0.0002	0.0111	0.0000	1.0482	0.3904

Table S1.2 (Continued).

NH4_C58:11 TAG	0.0005	0.2906	0.0004	1.1443	0.1936
NH4_C58:6 TAG	0.0050	0.0009	0.0034	0.4685	0.9705
NH4_C58:8 TAG	0.0017	0.0104	0.0613	0.7269	0.5086
NH4_C58:9 TAG	0.0009	0.0412	0.0002	1.0811	0.5714
NH4_C60:12 TAG	0.0014	0.4358	0.0001	1.3795	0.1851
palmithoylethanolamide	0.2614	0.1174	0.0637	0.2579	-0.1658
sphingosine	0.8161	0.0217	0.6736	0.7114	-0.3551
1-methylxanthine	0.0179	0.4152	0.1356	-1.3111	-0.4333
2-hydroxy-3-methylbutyrate/hydroxyisovalerate	0.8893	0.3318	0.1414	0.0742	0.4016
2-hydroxy-3-methylpentanoate/hydroxyisocaproate	0.3796	0.9762	0.2606	0.5670	-0.0168
2-hydroxyglutarate	0.0294	0.0021	0.0235	-0.2617	-0.4925
3-methyladipate/pimelate	0.1882	0.0852	0.5728	0.2716	0.3734
4-pyridoxate	0.3214	0.8702	0.1757	-1.7424	0.3011
aconitate	0.6996	0.0895	0.0388	-0.0802	0.4077
adenine	0.9002	0.1682	0.1144	-0.2228	1.5573
adipate/methylglutarate	0.0234	0.1981	0.4810	0.4729	0.3185
adonitol/arabitol	0.9098	0.8840	0.9783	-0.0406	-0.0357
ADP	0.5041	0.6254	0.7747	-0.3831	-0.2376
alpha-glycerophosphate	0.5778	0.0112	0.0014	0.2475	1.3863
alpha-hydroxybutyrate/beta-hydroxybutyrate/hydroxyisobutyrate	0.4130	0.8230	0.5841	-0.3014	-0.0882
alpha-keto-beta-methylvalerate/alpha-ketoisocaproate	0.0428	0.4136	0.0146	-1.0270	0.4794
alpha-ketoglutarate	0.0755	0.0058	0.1752	-0.3123	-0.4940
anhydroDglucose	0.0198	0.1757	0.1986	-0.3807	-0.2358
aspartate	0.0036	0.4617	0.0131	-0.9175	-0.1584
ATP	0.2679	0.1002	0.0274	-0.7133	1.0680
caffeate	0.7548	0.2783	0.6081	0.0488	0.1127
citrate/isocitrate	0.9699	0.0394	0.0583	0.0075	0.4853
erythronate/threonate	0.1909	0.6578	0.2890	-0.8385	-0.3073
folate	0.5708	0.3389	0.1087	-0.6256	0.8411
fructose/glucose/galactose	0.9289	0.3900	0.2383	-0.0343	0.3687
fumarate/maleate	0.7854	0.1596	0.0980	-0.0560	-0.2826
glutathione reduced	0.0010	0.1125	0.0001	-0.6304	0.1684
glycerate	0.1607	0.5191	0.2137	-1.4858	-0.5631
hexose diphosphate	0.6602	0.2125	0.0749	-0.5405	1.4212
hexose monophosphate	0.2252	0.6125	0.4761	-0.4667	-0.2246
hippurate	0.5435	0.4326	0.1043	-0.3035	0.4248
hydroquinone/pyrocatechol	0.3338	0.0218	0.1695	0.3376	0.7375
hypoxanthine	0.9095	0.3302	0.2119	0.0722	0.6140
inositol	0.3389	0.1834	0.4681	-0.1747	-0.3591
lactate	0.9671	0.2414	0.1532	0.0167	0.4911
malate	0.9574	0.1884	0.1122	0.0094	-0.2169
malonate	0.4135	0.9326	0.3032	0.1082	0.0073
MDA	0.9284	0.2041	0.1959	0.0648	0.6922
mesaconate	0.0532	0.0041	0.0552	-0.3332	-0.6478
norepinephrine	0.4253	0.6339	0.1023	-0.3354	0.1942
oxalate	0.0797	0.0026	0.8361	-0.3104	-0.3400
pantothenate	0.0334	0.4668	0.1123	-0.6130	-0.1792
phosphocreatine	0.1976	0.9522	0.1757	-1.7924	0.0323
pseudouridine	0.6491	0.3111	0.0656	-0.2584	0.5787
salicylate	0.2508	0.5320	0.4218	1.0817	0.4223

Table S1.2 (Continued).

sebacate	0.0449	0.9762	0.0749	0.2626	0.0030
sorbitol	0.9518	0.2872	0.1123	-0.0308	0.4209
suberate	0.2325	0.6339	0.3270	0.4674	0.1414
succinate	0.6599	0.2761	0.3160	0.0810	0.3031
threitol	0.6068	0.6097	0.1641	-0.4292	0.4047
thymine	0.4234	0.7689	0.2644	-0.1582	0.0689
UDP-galactose/UDP-glucose	0.5035	0.8861	0.4855	-0.1353	-0.0241
uracil	0.6809	0.3719	0.0127	-0.1630	0.3302
urate	0.2809	0.6575	0.0721	-0.6732	0.2790
uridine	0.2178	0.2364	0.0091	-0.5994	0.5519
xanthine	0.8134	0.2593	0.0749	-0.1331	0.5895
xylose	0.2809	0.5935	0.1144	-0.3507	0.2223
1-methyladenosine	0.0044	0.1212	0.0012	-0.6540	0.3268
1-methylguanine	0.5128	0.6423	0.7513	-0.6506	-0.3848
1-methylguanosine	0.9574	0.4066	0.3310	0.0375	0.4319
1-methylhistidine	0.2884	0.4189	0.1960	-0.1883	0.2795
1-methylnicotinamide	0.0290	0.0183	0.9576	0.4820	0.4740
1H-indole-3-acetamide	0.5600	0.7484	0.7684	-1.0309	-0.5500
2-aminoheptanoic acid	0.0630	0.4152	0.7370	0.9166	0.6504
2-aminooctanate	0.8781	0.9326	0.8803	0.1224	0.0412
2-hydroxyphenethylamine	0.9782	0.2795	0.2027	0.0132	0.4147
2'-deoxyadenosine	0.9574	0.5734	0.5899	0.0797	-0.5369
2'-deoxycytidine	0.3131	0.4350	0.0987	-0.4710	0.4651
2'-O-methyladenosine	0.5182	0.8600	0.5319	-1.5115	-0.3137
3-aminoisobutyrate	0.9709	0.9689	0.9272	0.0187	-0.0161
3-methylhistidine	0.8523	0.0883	0.0749	0.0842	0.8531
4-acetamidobenzoic acid	0.8419	0.4633	0.1334	-0.2489	0.7286
4-acetamidobutanoate	0.9782	0.3555	0.2977	0.0081	0.4519
4-aminohippuric acid	0.6392	0.5333	0.1717	-0.5207	0.7356
4-guanidinobutanoic acid	0.5526	0.8449	0.4557	-0.5375	-0.1390
4-pyridoxate*	0.3881	0.8449	0.5980	-1.3631	-0.3313
5-acetylamino-6-amino-3-methyluracil	0.4130	0.9376	0.3270	-0.6300	0.0523
5-alpha-cholestanol	0.7652	0.3851	0.3566	-0.2780	-0.6648
5-hydroxydopamine	0.3796	0.7972	0.1717	-0.5678	0.1645
5-hydroxylysine	0.7705	0.4413	0.1411	-0.5177	1.2702
5-hydroxytryptophol	0.8134	0.5777	0.2144	-0.2317	0.4178
5-methylcytidine	0.2096	0.5926	0.0862	-1.9093	0.5815
5-methylcytosine	0.1017	0.5795	0.2637	-2.1177	-0.7108
6,8-dihydroxypurine	0.4202	0.4152	0.0409	-0.7376	0.7388
7-methylguanine	0.1698	0.6101	0.1123	-0.4831	0.2414
acetyl-galactosamine	0.5526	0.1457	0.2240	0.2766	0.9606
acetylcholine	0.6700	0.6139	0.9576	-0.3457	-0.3754
adenosine	0.2614	0.9115	0.6437	-0.2261	-0.0435
ADMA	0.9098	0.2978	0.3154	0.0788	0.6042
agmatine	0.9660	0.4442	0.4557	0.0566	0.6780
alanine	0.0843	0.7550	0.0656	-0.7070	0.1170
allantoin	0.6469	0.3935	0.2680	-0.1535	0.5302
alloisoleucine	0.7969	0.4431	0.2314	-0.1300	0.2641
alpha-glycerophosphocholine	0.0002	0.0016	0.0529	-1.3132	-0.9913
anserine	0.5160	0.4189	0.7609	1.1074	1.7466
arachidoyl ethanolamide	0.9660	0.1763	0.0896	0.0414	-1.8325
arginine	0.8134	0.2893	0.1126	-0.0813	0.4632
asparagine	0.2305	0.3124	0.0749	-0.2730	0.3792

Table S1.2 (Continued).

aspartate	0.1936	0.5675	0.2644	-0.5451	-0.1977
barbituric acid	0.3985	0.8600	0.4845	-1.8690	-0.4003
beta-alanine	0.0010	0.0144	0.0158	0.4445	0.2754
beta-guanidinopropionic acid	0.6222	0.1693	0.2137	0.1903	0.4889
beta-leucine	0.6700	0.8489	0.5291	-0.1345	0.0524
betaine	0.9518	0.2948	0.2749	0.0191	0.3061
biotin	0.6290	0.4926	0.2144	-0.2015	0.3477
butyrobetaine	0.7532	0.0374	0.0503	0.0693	0.4203
butyrylcarnitine	0.1644	0.6304	0.0761	-0.5607	0.1826
C-glycosyltryptophan	0.8680	0.7615	0.8333	-0.1917	-0.3444
C12 carnitine	0.9098	0.3422	0.2432	0.1564	-1.0301
C14 carnitine	0.8028	0.2263	0.2492	-0.0825	0.2873
C14:0 LPC	0.4204	0.9059	0.2802	-0.2929	-0.0378
C14:0 SM	0.1976	0.2112	0.6437	-0.7213	-0.5641
C14:1 carnitine	0.0154	0.7550	0.0130	-0.9507	0.0958
C16 carnitine	0.2068	0.0223	0.0326	0.2398	0.6082
C16:0 ceramide (d18:1)	0.2900	0.7816	0.4357	-1.0335	-0.2137
C16:0 LPC_B	0.3347	0.6701	0.2660	-0.2509	0.1036
C16:0 LPE	0.2101	0.5433	0.1837	-0.4666	-0.1662
C16:0 SM	0.0287	0.0786	0.8212	-0.7307	-0.7977
C16:1 LPC	0.1511	0.2673	0.0416	-0.4948	0.4160
C16:1 LPC plasmalogen	0.5083	0.5686	0.7945	-0.2154	-0.1596
C16:1 LPE	0.5285	0.9010	0.5240	-0.9915	-0.1277
C16:1 SM	0.1501	0.1450	0.7506	-0.5622	-0.4809
C18 carnitine	0.9098	0.5054	0.3617	-0.0686	0.2882
C18:0 LPC	0.3317	0.4902	0.5240	-0.4673	-0.2337
C18:0 LPE	0.0095	0.2014	0.0086	-0.7378	-0.2615
C18:1 carnitine	0.0290	0.0077	0.0451	0.5751	0.9445
C18:1 LPC	0.3632	0.8600	0.2820	-0.4199	0.0614
C18:1 LPC plasmalogen	0.3577	0.3741	0.1126	-0.2976	0.2622
C18:1 LPC plasmalogen_minor	0.2341	0.8711	0.0752	-0.6232	0.0621
C18:1 LPE	0.3341	0.9522	0.1846	-0.2287	0.0131
C18:1 SM	0.1753	0.0800	0.8272	-1.6083	-1.8499
C18:2 carnitine	0.1891	0.0032	0.0126	0.6350	1.8414
C18:2 LPC	0.2325	0.4023	0.1123	-0.2118	0.1114
C18:2 LPC_minor	0.6599	0.8600	0.6221	-0.0835	0.0355
C18:2 SM	0.0743	0.0724	0.6603	-1.6373	-2.1086
C18:3 LPC	0.3161	0.9073	0.3122	-0.4789	-0.0346
C2 carnitine	0.0633	0.0152	0.0497	0.2356	0.4353
C20 carnitine	0.1846	0.2076	0.0268	-1.0082	0.6331
C20:0 LPE	0.3910	0.7616	0.4588	-0.4382	-0.1164
C20:0 SM	0.1511	0.2037	0.7370	-2.2924	-1.7761
C20:4 carnitine	0.0290	0.1350	0.0687	3.0931	1.4923
C20:4 LPC	0.4073	0.7058	0.0146	-0.2848	-0.1068
C20:4 LPE	0.2022	0.5433	0.5947	-0.4908	-0.2393
C20:5 LPC	0.7432	0.3111	0.1078	-0.1551	0.4657
C22:1 SM	0.2252	0.1272	0.2802	-0.3851	-0.8411
C22:5 LPC	0.3486	0.4350	0.1619	-0.2994	0.1914
C22:6 LPC	0.3796	0.8476	0.1738	-0.3380	0.0626
C22:6 LPE	0.5083	0.0923	0.0911	-0.4357	-1.1071
C24:1 ceramide (d18:1)	0.0743	0.3122	0.6048	-1.1085	-1.9420
C3 carnitine	0.2115	0.3454	0.8165	0.3453	0.2857
C3-DC-CH3 carnitine	0.8090	0.2364	0.2141	0.2592	1.1979

Table S1.2 (Continued).

C30:0 PC	0.0353	0.3422	0.4863	-0.7951	-0.4674
C32:2 PC	0.0002	0.2593	0.0001	-1.5165	0.2326
C34:0 PE	0.1641	0.2342	0.6644	-0.4593	-0.6798
C34:1 DAG*	0.3160	0.8222	0.1722	-0.7680	0.1434
C34:2 PE	0.0436	0.9073	0.2391	-0.5852	-0.0484
C34:2 PE plasmalogen	0.6230	0.1484	0.0749	0.2014	-1.1144
C34:3 PC	0.0147	0.2537	0.0025	-0.9020	0.3352
C34:3 PC plasmalogen	0.0146	0.2342	0.4070	-0.8190	-0.4925
C34:3 PE plasmalogen	0.2881	0.1811	0.6233	-0.5623	-0.7385
C36:2 PC	0.0828	0.2364	0.0626	-0.3915	0.3658
C36:2 PE	0.7072	0.6836	0.8536	0.1117	0.1920
C36:3 PE plasmalogen	0.9817	0.1484	0.0850	-0.0107	-0.9129
C36:4 PE	0.1983	0.5392	0.5600	-0.4655	-0.2458
C36:5 PC plasmalogen	0.0042	0.0722	0.0325	-0.9570	-0.5177
C36:5 PE plasmalogen	0.0200	0.1790	0.6955	-0.6300	-0.5192
C38:4 PE	0.5439	0.5850	0.8785	-0.2405	-0.3301
C38:5 PE plasmalogen*	0.0829	0.2554	0.4644	-0.3547	-0.7167
C38:6 PC plasmalogen	0.0006	0.0329	0.0065	-1.0231	-0.4586
C38:6 PE	0.7346	0.2046	0.2606	-0.1472	-0.5195
C38:6 PE plasmalogen*	0.1112	0.2364	0.9935	-0.5328	-0.5358
C38:7 PC plasmalogen	0.0114	0.1482	0.0464	-1.2031	-0.5445
C38:7 PE plasmalogen	0.0436	0.0285	0.1240	-0.3819	-0.7905
C4-OH carnitine	0.2679	0.5223	0.5240	0.7829	0.3853
C40:6 PE	0.7343	0.3277	0.5244	-0.2159	-0.5331
C40:7 PE plasmalogen	0.1641	0.2277	0.7173	-0.3681	-0.4868
C5 carnitine	0.0004	0.0134	0.0038	0.7979	0.3793
C5:1 carnitine	0.1967	0.5442	0.3055	1.2409	0.5882
C6 carnitine	0.2836	0.0244	0.0902	0.5194	1.3063
C7 carnitine	0.5182	0.6007	0.9128	-0.8309	-0.6758
C9 carnitine	0.3236	0.3715	0.8651	0.8176	0.9975
caprylate	0.4964	0.8397	0.3637	0.2960	-0.1127
carnitine	0.5421	0.0883	0.2408	0.2218	0.5793
carnosine	0.8967	0.3900	0.2545	-0.0673	0.4803
choline	0.8073	0.1811	0.0656	-0.0750	0.3951
citrulline	0.9098	0.2158	0.1008	0.0470	0.5741
cotinine	0.6489	0.9490	0.5784	-0.5843	0.0558
creatine	0.6714	0.4023	0.2382	-0.0926	0.2209
creatinine	0.5128	0.3935	0.0837	-0.2019	0.3173
cyclohexylamine	0.8130	0.2118	0.1342	0.0243	-0.1576
cystine	0.6880	0.5900	0.8790	0.4340	0.5585
cytidine	0.6068	0.4633	0.1060	-0.3969	0.6019
cytosine	0.4453	0.3422	0.0712	-0.4767	0.6459
dehydrophytosphingosine	0.3618	0.6540	0.7053	-0.7857	-0.4579
dihydrothymine	0.9701	0.5686	0.8155	-0.0502	-0.3187
dihydrouracil	0.2069	0.3808	0.5432	-0.8990	-0.4501
dimethylglycine	0.7346	0.3715	0.1109	-0.0915	0.2504
DMGV	0.6135	0.4032	0.6257	0.4281	0.9817
ectoine	0.7854	0.8197	0.4855	-0.3920	0.2344
FAPy-adenine	0.9782	0.4498	0.3791	-0.0137	0.3386
GABA	0.3586	0.4498	0.7133	-0.1318	-0.0840
geranyl acetoacetate	0.9660	0.5407	0.5416	-0.0154	-0.1832
glutamate	0.3335	0.8430	0.2382	-0.3356	0.0709
glutamic acid amide	0.2784	0.7857	0.0409	-0.8402	0.2077

Table S1.2 (Continued).

glutamine	0.7969	0.2648	0.1327	-0.0835	0.4995
glutamine_fragment1	0.6491	0.3422	0.1550	-0.1413	0.4575
glycine	0.8362	0.0484	0.0498	0.0804	0.7826
glycodeoxycholate/glycochenodeoxycholate *	0.0607	0.5433	0.2027	3.9784	1.2780
guanidinoacetic acid	0.0021	0.0043	0.0001	-1.1215	1.3393
guanine	0.5072	0.0650	0.0718	0.3279	1.1999
guanosine	0.1065	0.2786	0.0472	-0.9001	0.6969
hexanoylglycine	0.9574	0.2936	0.2297	-0.0227	0.5853
hippurate*	0.4673	0.3796	0.0527	-0.3967	0.5356
histamine	0.9189	0.4028	0.1209	0.0660	0.4509
histidine	0.8268	0.1497	0.1327	0.0781	0.6668
homoarginine	0.9098	0.4365	0.1560	-0.0759	0.4331
homoserine	0.7677	0.7962	0.6221	-0.0691	0.0746
hydroxyproline	0.1001	0.1858	0.0212	-0.3874	0.4947
hypotaurine	0.0788	0.0633	0.8227	0.6100	0.6693
hypoxanthine	0.4311	0.1900	0.3180	0.3866	1.2304
imidazole propionate	0.7013	0.5484	0.7874	0.1571	0.2614
imidazoleacetic acid	0.4943	0.2554	0.3915	0.1303	0.3965
inosine	0.6679	0.4028	0.6437	1.0460	2.5448
isoleucine	0.9648	0.2277	0.1641	0.0210	0.5618
isoxanthopterin	0.4135	0.3389	0.7158	-2.4474	-2.8433
kynurenic acid	0.5964	0.7853	0.4761	-0.7838	-0.3577
leucine	0.9098	0.2363	0.2151	0.0574	0.6064
linoleoyl ethanolamide	0.1570	0.2537	0.5322	-2.1574	-1.5990
lysine	0.6545	0.2847	0.0711	-0.1910	0.5881
m-tyramine	0.6604	0.9001	0.8212	0.1048	0.0334
methionine	0.9723	0.5245	0.2122	-0.0244	0.4237
methionine sulfoxide	0.1293	0.3302	0.0775	-0.3724	0.4019
methylguanidine	0.9782	0.2125	0.2704	0.0108	0.5677
methylimidazole acetic acid	0.8606	0.4066	0.1753	-0.0779	0.3989
methylthioadenosine	0.2154	0.6575	0.0294	-0.7152	0.2174
myristoleate	0.9059	0.9021	0.7970	-0.0475	0.0377
N-acetylalanine	0.5839	0.3796	0.5947	-0.1730	-0.3818
N-acetylaspartic acid	0.0121	0.0071	0.3687	1.1755	1.3747
N-acetylglutamic acid	0.7034	0.3745	0.6693	0.1252	0.2740
N-acetylhistidine	0.6822	0.3067	0.2994	0.3372	0.9052
N-acetylleucine	0.6409	0.8716	0.5436	-0.1436	0.0668
N-acetylornithine	0.6700	0.3584	0.1641	-0.1895	0.5433
N-acetylputrescine	0.5305	0.8545	0.5728	0.2744	0.0724
N-acetylserine	0.8680	0.6304	0.7167	0.1430	0.4172
N-acetyltryptophan	0.8769	0.5093	0.3092	0.3352	1.2028
N-alpha-acetylarginine	0.7374	0.8199	0.9195	-0.5103	-0.3855
N-lauroylglycine	0.1739	0.6472	0.2361	-0.5583	-0.1206
N-methylproline	0.8236	0.2364	0.1566	-0.0641	0.4288
N-methyltryptamine	0.8763	0.4421	0.4855	-0.0810	-0.5086
N1-acetylspermidine	0.2176	0.0009	0.0003	-0.1807	-1.3911
N2,N2-dimethylguanosine	0.7072	0.2906	0.1487	-0.6884	1.4506
N4-acetylcytidine	0.9098	0.7816	0.6934	-0.2743	0.4219
N6-acetyllysine	0.8560	0.4498	0.5240	0.3919	1.3567
N6,N6-dimethyllysine*	0.7346	0.2752	0.1078	-0.1423	0.6091
N6,N6,N6-trimethyllysine	0.9944	0.3592	0.1566	0.0035	0.5308
niacinamide	0.3632	0.5223	0.1438	-0.4048	0.3539

Table S1.2 (Continued).

nicotinic acid	0.8657	0.3900	0.2915	-0.0662	-0.2690
NMMA	0.8954	0.2364	0.1701	0.1230	0.9957
oleamide	0.2537	0.2783	0.7439	-1.2346	-1.0014
oleoyl glycine	0.9222	0.6497	0.6886	-0.0693	-0.3054
ornithine	0.6707	0.3227	0.0811	-0.1715	0.5060
pantothenate*	0.2350	0.7615	0.6070	-0.4126	-0.1639
pantothenol	0.6815	0.1649	0.3153	0.5431	1.9018
phenylacetylglutamine	0.4751	0.2306	0.8116	-1.8161	-2.4658
phenylacetylglycine	0.5734	0.4252	0.1790	-0.2841	0.5263
phenylalanine	0.6323	0.3139	0.1082	-0.1683	0.4563
phosphocholine	0.6644	0.6471	0.9651	0.1318	0.1446
phytosphingosine	0.7193	0.6574	0.4893	-0.3297	0.4216
pipecolic acid	0.7532	0.7389	0.9510	0.0707	0.0813
pro-gly	0.5855	0.3389	0.7848	0.3641	0.4980
progesterone	0.5600	0.4621	0.9328	-1.0496	-0.9127
proline	0.7705	0.1497	0.0911	-0.0913	0.6081
proline-betaine	0.0651	0.8464	0.4555	-0.2879	-0.0624
pseudouridine	0.6599	0.6360	0.3210	-0.1926	0.2622
putrescine	0.5336	0.5572	0.2080	0.2073	-0.1899
pyridoxal hydrochloride	0.9098	0.1868	0.1038	0.0595	0.7623
pyridoxamine	0.9648	0.2420	0.0998	-0.0287	0.7084
pyridoxine	0.6323	0.3741	0.1419	-0.1719	0.4237
pyroglutamic acid	0.8649	0.3318	0.1636	0.1338	0.6044
S-adenosylhomocysteine	0.9352	0.2566	0.1419	-0.0666	0.7195
s-adenosylmethionine	0.3835	0.0004	0.0001	-0.0746	0.7252
S-methyl-L-cysteine-S-oxide	0.2350	0.7725	0.2997	-0.2217	-0.0600
sarcosine	0.1114	0.6097	0.1008	-0.6758	-0.1302
SDMA	0.7657	0.2158	0.1825	0.1264	0.7613
serine	0.1324	0.6097	0.0883	-0.3089	0.1330
sphinganine	0.2350	0.9376	0.1419	-0.9216	-0.0401
sphingosine	0.7432	0.7615	0.4154	0.2400	-0.2277
taurine	0.0890	0.0650	0.8552	0.4047	0.4418
thiamine	0.9254	0.2125	0.0902	-0.0438	0.6417
threo-sphingosine	0.7603	0.7853	0.8803	-0.4714	-0.2807
threonine	0.9574	0.5159	0.3382	-0.0340	0.2832
transvaccenic acid	0.4751	0.5223	0.6070	-0.3523	-0.1555
triethanolamine	0.8309	0.8711	0.7509	-0.1260	0.1443
trigonelline	0.9599	0.9021	0.9411	-0.0147	-0.0426
trimethylamine-N-oxide	0.7295	0.9592	0.6955	-0.1275	-0.0128
trimethylbenzene_isomer1	0.5809	0.6339	0.2416	-0.1654	0.1269
trimethylbenzene_isomer2	0.3070	0.5020	0.6592	-0.5063	-0.3235
tryptophan	0.9671	0.3818	0.1327	-0.0234	0.4715
tyramine	0.5600	0.5935	0.8745	0.2711	0.2212
tyrosine	0.9921	0.4028	0.1689	0.0052	0.4277
urate	0.5182	0.6854	0.4681	-1.3280	-0.7159
urocanic acid	0.6203	0.7844	0.8552	-0.4891	-0.2795
valine	0.9515	0.5795	0.3217	-0.0474	0.2899
vanillylamine	0.0591	0.4807	0.0283	-2.1287	0.5510
xanthine	0.9574	0.4028	0.2644	-0.0286	0.4784
xanthosine	0.2333	0.4028	0.1087	-1.1383	0.4666

Table S1.3. HMDB association between DE genes and DA metabolites.

gene	scr.v.p1.padj	scr.v.p1.log2fc	scr.v.p2.padj	scr.v.p2.log2fc	met.names
Nat8l	7.01E-05	-1.54E+00	3.80E-05	-1.5893	N-acetylaspartic acid
Adhfe1	7.05E-07	-1.32E+00	9.07E-05	-1.0662	alpha-ketoglutarate,2-hydroxyglutarate
Plcb4	5.69E-20	-7.72E-01	2.43E-14	-0.6481	C36:1 DAG
Dgat2	2.45E-02	-6.03E-01	4.19E-05	-1.0250	C50:0 TAG,C50:1 TAG,C51:2 TAG,C52:1 TAG,C54:4 TAG,C52:5 TAG,C54:5 TAG,C54:6 TAG,C56:8 TAG,C54:1 TAG,C56:4 TAG,C54:2 TAG,C56:5 TAG,C58:8 TAG,C50:4 TAG,C54:7 TAG,C56:6 TAG,C58:6 TAG,C56:7 TAG,C58:9 TAG,C58:7 TAG,C58:10 TAG,C36:1 DAG,C49:1 TAG,C51:1 TAG,C53:2 TAG,C55:2 TAG,C53:3 TAG
Prkcd	1.12E-30	-5.61E-01	2.67E-28	-0.5376	C36:1 DAG
Nceh1	2.73E-10	-5.16E-01	3.37E-06	-0.3867	C14:0 CE,C22:4 CE,C20:3 CE,C22:5 CE
Pla2g12a	7.31E-09	-5.06E-01	7.97E-12	-0.5915	C30:0 PC,C30:1 PC,C32:0 PC,C34:1 PC plasmalogen-A,C34:3 PC plasmalogen,C34:4 PC plasmalogen,C36:5 PC plasmalogen-B,C36:5 PC plasmalogen,C38:7 PC plasmalogen,C40:7 PC plasmalogen,C38:6 PC plasmalogen
Plscr3	1.37E-09	-4.49E-01	1.10E-04	-0.2955	C30:0 PC,C30:1 PC,C32:0 PC,C34:0 PE,C36:2 PE,C40:6 PE,C34:1 PC plasmalogen-A,C34:3 PC plasmalogen,C34:4 PC plasmalogen,C36:5 PC plasmalogen-B,C36:5 PC plasmalogen,C38:7 PC plasmalogen,C40:7 PC plasmalogen,C38:6 PC plasmalogen,C38:3 PE plasmalogen,C38:6 PE plasmalogen,C40:7 PE plasmalogen,C38:7 PE plasmalogen
Prkci	3.83E-13	-4.12E-01	3.66E-15	-0.4438	C36:1 DAG
Prkce	4.82E-09	-3.95E-01	2.69E-11	-0.4453	C36:1 DAG
Pigh	6.17E-04	-3.78E-01	3.77E-05	-0.4480	C24:0 Ceramide (d18:1),C16:0 SM,C24:0 SM,C22:0 SM,C24:1 SM
Plekhm1	2.17E-07	-3.61E-01	7.48E-10	-0.4234	C36:1 DAG
Egln2	1.18E-03	-3.50E-01	1.41E-02	-0.2736	alpha-ketoglutarate
Phf8	7.04E-09	-3.47E-01	6.23E-13	-0.4258	alpha-ketoglutarate
Asph	5.62E-04	-3.24E-01	2.87E-02	-0.2161	alpha-ketoglutarate
Chn2	2.24E-04	-3.02E-01	3.76E-05	-0.3345	C36:1 DAG

Table S1.3 (Continued).

Agk	5.45E-04	-3.01E-01	6.86E-05	-0.3436	C36:1 DAG
Pctp	2.48E-03	-3.01E-01	3.86E-07	-0.4838	C30:0 PC,C30:1 PC,C32:0 PC,C34:1 PC plasmalogen-A,C34:3 PC plasmalogen,C34:4 PC plasmalogen,C36:5 PC plasmalogen-B,C36:5 PC plasmalogen,C38:7 PC plasmalogen,C40:7 PC plasmalogen,C38:6 PC plasmalogen
Smpd4	3.65E-03	-1.96E-01	1.37E-03	-0.2152	C24:0 Ceramide (d18:1),C16:0 SM,C24:0 SM,C22:0 SM,C24:1 SM
Cpt2	1.87E-02	-1.80E-01	9.01E-03	-0.1988	C50:0 TAG,C50:1 TAG,C51:2 TAG,C52:1 TAG,C54:4 TAG,C52:5 TAG,C54:5 TAG,C54:6 TAG,C56:8 TAG,C54:1 TAG,C56:4 TAG,C54:2 TAG,C56:5 TAG,C58:8 TAG,C50:4 TAG,C54:7 TAG,C56:6 TAG,C58:6 TAG,C56:7 TAG,C58:9 TAG,C58:7 TAG,C58:10 TAG,C51:1 TAG,C53:2 TAG,C55:2 TAG,C53:3 TAG
Arfgap1	2.85E-02	-1.56E-01	1.01E-03	-0.2255	C30:0 PC,C30:1 PC,C32:0 PC,C34:1 PC plasmalogen-A,C34:3 PC plasmalogen,C34:4 PC plasmalogen,C36:5 PC plasmalogen-B,C36:5 PC plasmalogen,C38:7 PC plasmalogen,C40:7 PC plasmalogen,C38:6 PC plasmalogen
Pitpna	4.85E-05	2.61E-01	6.09E-04	0.2233	C30:0 PC,C30:1 PC,C32:0 PC,C34:1 PC plasmalogen-A,C34:3 PC plasmalogen,C34:4 PC plasmalogen,C36:5 PC plasmalogen-B,C36:5 PC plasmalogen,C38:7 PC plasmalogen,C40:7 PC plasmalogen,C38:6 PC plasmalogen
Csad	8.57E-08	3.41E-01	4.18E-09	0.3729	taurine,hypotaurine
Aldh3a2	3.41E-12	3.80E-01	6.38E-08	0.2989	beta-alanine,alpha-ketoglutarate
Rassf1	1.31E-08	4.57E-01	3.92E-04	0.2944	C36:1 DAG
Pitpnm1	1.86E-11	4.79E-01	2.43E-06	0.3417	C36:1 DAG,C30:0 PC,C30:1 PC,C32:0 PC,C34:1 PC plasmalogen-A,C34:3 PC plasmalogen,C34:4 PC plasmalogen,C36:5 PC plasmalogen-B,C36:5 PC plasmalogen,C38:7 PC plasmalogen,C40:7 PC plasmalogen,C38:6 PC plasmalogen

Table S1.3 (Continued).

Gpt	3.12E-02	5.30E-01	1.87E-02	0.5770	alpha-ketoglutarate
Lbp	8.01E-05	7.82E-01	3.12E-03	0.6008	C24:0 Ceramide (d18:1),C16:0 SM,C24:0 SM,C22:0 SM,C24:1 SM
Atp10d	4.67E-15	8.66E-01	8.73E-11	0.7180	C30:0 PC,C30:1 PC,C32:0 PC,C34:0 PE,C36:2 PE,C40:6 PE,C34:1 PC plasmalogen-A,C34:3 PC plasmalogen,C34:4 PC plasmalogen,C36:5 PC plasmalogen-B,C36:5 PC plasmalogen,C38:7 PC plasmalogen,C40:7 PC plasmalogen,C38:6 PC plasmalogen,C38:3 PE plasmalogen,C38:6 PE plasmalogen,C40:7 PE plasmalogen,C38:7 PE plasmalogen
Plce1	6.98E-16	9.06E-01	1.32E-19	1.0106	C36:1 DAG
Sphk1	2.72E-05	1.12E+00	9.59E-05	1.0407	C24:0 Ceramide (d18:1)

Table S1.4. Gene set enrichment analysis on Scr versus Pdss2 shRNA gene list.

pathway	pval	padj	ES	NES	nMoreExtreme	size	leadingEdge
KEGG_RIBOSOME	2.42E-04	1.49E-02	6.63E-01	2.28E+00	0	59	RPL3 FAU RPLP1 RPS23 RPS8 RPL18A RPL5 RPL29 RPL28 RPL38 RPL26 RPL27 RPS9 RPS7 RPL14 RPS5 RPL35 RPS18 RPS17 RPS27A RPL6 RPL10A RPS3A UBA52 RPL11 RPS24 RPL24 RPL12 RPL8 RPL23A RPL13A RPL22L1 RPLP2 RPL36AL RPS28 RPS12 RPS16 RPL39 RPSA RPL18 RPL15 RPL23 RPL27A RPS19
KEGG_DNA_REPLICATION	2.34E-04	1.49E-02	7.64E-01	2.36E+00	0	34	RFC1 PCNA MCM5 RFC5 MCM4 MCM6 MCM3 RNASEH2A PRIM2 LIG1 POLD1 RFC3 POLA2 MCM7 MCM2 POLA1 PRIM1 RNASEH2C RFC4 RFC2 RPA2 RNASEH1 POLE4 DNA2 RPA3 POLE3 POLE POLE2
KEGG_CELL_CYCLE	2.64E-04	1.49E-02	4.95E-01	1.92E+00	0	119	PCNA MCM5 MCM4 CDK1 CDK4 MCM6 MAD2L1 ESPL1 ORC6 CDC45 MCM3 PKMYT1 CDC20 YWHAH ANAPC4 CCNB1 CCNE2 CCNB2 CCNA2 ORC1 CHEK1 PLK1 CDC7 CDC27 CHEK2 MYC BUB1 MCM7 CDK2 SKP2 CDC6 MCM2 CCND3 CCNE1 TGFB3 TP53 BUB3 BUB1B CDC25B ORC4 E2F1 DBF4 ORC2 TGFB1
KEGG_RETINOL_METABOLISM	8.72E-04	2.53E-02	-6.40E-01	-1.88E+00	4	33	RDH11 RDH10 DHRS3 DHRS9 ALDH1A2 DGAT2 CYP26B1 UGT1A4 RETSAT
KEGG_SPLICEOSOME	1.05E-03	2.53E-02	4.48E-01	1.72E+00	3	110	PRPF18 HNRNPA3 HSPA1L SNRPB MAGOHB LSM6 SRSF8 TRA2A SNRPB2 DDX39B SNRPA CDC40 PQBP1 SRSF7 SRSF6 SRSF1 SF3A3 DHX15 TRA2B SNRNP40 EFTUD2 HNRNPM SNRPA1 SF3B4 NCBP1 PHF5A U2AF1 PLRG1 PCBP1 SRSF9 SNRPD1 PRPF19 DHX38 SRSF3 SF3A2 EIF4A3 ACIN1 SRSF10 THOC1 HNRNPU DDX42

Table S1.4 (Continued).

KEGG_MISMATCH_REPAIR	9.08E-04	2.53E-02	6.80E-01	1.88E+00	3	21	RFC1 PCNA RFC5 LIG1 POLD1 EXO1 RFC3 PMS2 MSH3 MLH3 MSH2 RFC4 RFC2 RPA2 RPA3
KEGG_PROGESTERONE_MEDIATED_OOCYTE_MATURATION	7.54E-04	2.53E-02	4.84E-01	1.76E+00	2	79	MAPK11 CDK1 MAD2L1 HSP90AA1 PKMYT1 ANAPC4 CCNB1 CCNB2 CCNA2 ADCY7 MAPK3 PIK3R2 PLK1 MAPK8 CDC27 RPS6KA2 BUB1 CDK2 CDC25B PIK3CD KRAS RPS6KA1 AKT1 CDC25C MAPK12 ANAPC10
KEGG_OOCYTE_MEIOSIS	1.55E-03	3.27E-02	4.53E-01	1.70E+00	5	97	CDK1 PPP3R1 MAD2L1 FBXW11 ESPL1 PPP2R5B PKMYT1 CDC20 YWHAH AURKA ANAPC4 CCNB1 CCNE2 CCNB2 ADCY7 MAPK3 PLK1 FBXO5 CDC27 RPS6KA2 BUB1 CDK2 PPP3CA PPP1CA CCNE1 ITPR2
KEGG_GLYCOLYSIS_GLUCONEOGENESIS	2.62E-03	4.92E-02	5.18E-01	1.74E+00	10	51	PGK1 ALDOA LDHA ALDH3A2 BPGM ENO1 FBP2 HK1 ENO3 TPI1 PGAM2 HK2 PFKL ENO2 DLD ALDH9A1 PFKP PGAM1 ALDH7A1 ALDH2 GPI PFKM

Table S1.5. Rar and Rxr predicted binding sites in 1000 bp upstream of Pla2g12a and Dgat2 gene in mouse genome. Pla2g12a (Chr10:43220486,43221485); Dgat2 (Chr7:99152663,99153662)

Pla2g12a							
Matrix ID	**Name**	**Score**	**Relative score**	**Start**	**End**	**Strand**	**Predicted sequence**
MA0512.1	Rxra	9.31709	0.89853318	226	236	-	tagaggccagg
MA0512.1	Rxra	8.1222	0.88132206	281	291	+	ctaggttcaca
MA0512.1	Rxra	6.53776	0.85849974	15	25	+	ctcaggccact
MA0512.1	Rxra	5.51775	0.84380761	832	842	+	caaagggcgga
PB0161.1	Rxra_2	7.5417	0.83423966	829	844	+	tgccaaagggcggaca
MA0512.1	Rxra	4.12254	0.82371105	423	433	-	atgagtgcatt
MA0512.1	Rxra	4.0924	0.82327692	548	558	+	cagggctcagc
PB0057.1	Rxra_1	7.92004	0.81275934	788	804	+	tgcagagaccccgagag
MA0512.1	Rxra	2.91451	0.80631055	757	767	-	cagagtgaagc
Dgat2							
Matrix ID	**Name**	**Score**	**Relative score**	**Start**	**End**	**Strand**	**Predicted sequence**
MA0512.1	Rxra	12.8754	0.94978629	162	172	+	ccaaggtcagt
MA0512.1	Rxra	12.6018	0.94584649	18	28	+	caaagggcaca
MA0512.1	Rxra	6.62535	0.85976145	804	814	+	caaaggtccta
PB0053.1	Rara_1	10.8495	0.843662	15	30	+	aagcaaagggcacagg
MA0512.1	Rxra	5.23907	0.83979346	254	264	+	tacagggcaag
MA0512.1	Rxra	4.99764	0.8363159	683	693	+	tcgaggccagc
MA0512.1	Rxra	4.26729	0.82579605	183	193	-	caaaagccaca
MA0512.1	Rxra	4.23874	0.82538475	938	948	-	cacaggacaaa
MA0512.1	Rxra	3.99846	0.82192378	273	283	-	cggaggccacc
PB0053.1	Rara_1	9.68828	0.82070316	159	174	+	ttcccaaggtcagtta
PB0161.1	Rxra_2	7.01986	0.81956745	819	834	-	ttaagaaggttggctg
MA0512.1	Rxra	3.38454	0.81308098	906	916	+	caaggttgagg
MA0512.1	Rxra	3.2024	0.81045732	677	687	+	ctgagttcgag
PB0161.1	Rxra_2	6.67843	0.80996767	801	816	+	aaacaaaggtcctaaa
PB0161.1	Rxra_2	6.66398	0.80956144	15	30	+	aagcaaagggcacagg

Table S1.6. Differential expression data for all detected metabolites from condition media with atRA versus DMSO comparison.

Metabolite	fdr	log2fc
10-heptadecenoate	0.9916	-0.0673
12-HETE/8-HETE	0.9916	-0.0513
15-HETE	0.9916	0.0937
16-hydroxypalmitate	0.1702	0.7247
16:0 PC(O)	0.9916	-0.1357
2-hydroxyhexadecanoate	0.9916	0.4563
3-hydroxydecanoate	0.9916	-0.1967
3-hydroxyhexanoate	0.9916	-0.5164
3-hydroxyoctanoate	0.9916	0.3346
9-cis-retinoic acid	0.9916	0.3551
adrenate	0.9916	0.2793
alpha-linolenate	0.9916	0.3436
arachidate	0.9916	-0.2758
arachidonate	0.9916	0.1073
arachidonate	0.9916	0.2343
docosahexaenoate	0.2877	0.3287
docosapentaenoate	0.9916	0.3751
dodecanedioate	0.9916	0.2417
dodecanoate	0.9916	-0.0734
eicosanedioate	0.9916	-0.5626
eicosapentaenoate	0.9916	0.0863
eicosatrienoate	0.8850	0.2996
eicosenoate	0.9916	0.2012
fructose/glucose/galactose	0.9916	-0.0649
gamma-linolenate	0.9916	0.0449
glycochenodeoxycholate	0.9916	-0.1502
glycocholate	0.9916	0.0504
glycodeoxycholate	0.4369	0.3357
glycolithocholate	0.9916	0.1040
heptadecanoate	0.9916	0.1763
hexadecanedioate	0.9916	-0.1811
hydroxymyristate	0.9916	-0.1643
levulinate	0.9916	0.1276
linoleate	0.0785	0.6468
myristate	0.9916	0.4927
myristoleate	0.9916	0.4332
oleate	0.9916	-0.0510
palmitate	0.9916	-0.0339
palmitoleate	0.9448	0.6928
palmitoylethanolamide	0.9339	0.7646
pentadecanoate	0.9916	0.0267
porphobilinogen	0.9916	0.3490
ribothymidine	0.1402	-0.7325

Table S1.6 (Continued).

sebacate	0.9916	-0.2271
stearate	0.9916	0.0806
tauro-alpha-muricholate/tauro-beta-muricholate	0.9916	0.2952
taurochenodeoxycholate	0.9916	0.1173
taurocholate	0.9916	0.0626
taurodeoxycholate	0.9916	0.4720
taurohyodeoxycholate/tauroursodeoxycholate	0.9916	-0.2771
tetradecanedioate	0.9916	0.3257
undecanedionate	0.9916	0.3890
C14:0 CE	0.9916	0.0077
C14:0 SM	0.9916	-0.0789
C16:0 CE	0.9959	0.0018
C16:0 Ceramide (d18:1)	0.9916	1.0512
C16:0 LPE	0.9916	-0.0970
C16:1 CE	0.9916	-0.0875
C16:1 SM	0.9916	-0.1082
C18:0 CE	0.9959	-0.0009
C18:0 LPE	0.9916	-0.1225
C18:0 MAG	0.9916	-0.0437
C18:0 SM	0.9916	-0.0863
C18:1 CE	0.9916	0.0090
C18:1 LPC	0.0293	-0.4972
C18:1 LPE	0.9916	-0.3480
C18:1 SM	0.9916	-0.0365
C18:2 CE	0.9916	-0.0496
C18:3 CE	0.9916	-0.0313
C20:0 LPE	0.9916	-0.0398
C20:0 SM	0.9916	-0.0427
C20:3 CE	0.9916	-0.0545
C20:3 LPC	0.0274	-1.6982
C20:3 LPC isomer	0.0293	-1.3777
C20:4 CE	0.9448	-0.1079
C20:4 LPC	0.0022	-0.8936
C20:5 CE	0.9916	-0.0704
C22:0 Ceramide (d18:1)	0.9916	0.7689
C22:0 LPE	0.9916	-0.0854
C22:0 SM	0.9916	-0.0284
C22:1 SM	0.9916	-0.0641
C22:4 CE	0.9916	0.0160
C22:4 PC	0.0007	-1.3548
C22:5 CE	0.9916	-0.0735
C22:5 PC	0.0293	-1.1486
C22:6 CE	0.9916	-0.0242
C22:6 PC	0.1402	-1.4194

Table S1.6 (Continued).

C24:0 Ceramide (d18:1)	0.9916	1.0717
C24:0 SM	0.9916	-0.0468
C24:1 SM	0.9916	-0.0233
C30:0 PC	0.9916	-0.0210
C30:1 PC	0.9916	-0.0794
C32:0 PC	0.9916	-0.0586
C32:0 PE	0.9916	-0.2376
C32:1 PC	0.9959	-0.0060
C32:2 PC	0.9916	-0.0321
C34:0 PC	0.9916	-0.0435
C34:0 PE	0.9959	0.0022
C34:1 PC	0.9916	-0.0708
C34:1 PC plasmalogen	0.9916	-0.0115
C34:2 PC	0.9952	0.0074
C34:2 PE	0.9916	0.0277
C34:2 PE plasmalogen	0.9916	-0.0841
C34:3 PC	0.9916	-0.1788
C34:4 PC	0.1402	-0.5756
C36:0 PC	0.9916	-0.0640
C36:0 PE	0.9916	-0.1216
C36:1 DAG	0.9916	0.2862
C36:1 PC	0.9916	-0.0746
C36:1 PC plasmalogen	0.9916	-0.0314
C36:1 PE	0.9959	-0.0040
C36:2 PC	0.9916	-0.0383
C36:2 PC plasmalogen	0.9916	-0.0484
C36:2 PE	0.9916	0.0356
C36:2 PE plasmalogen	0.9916	0.2089
C36:3 PC	0.9916	-0.0501
C36:3 PE plasmalogen	0.9916	-0.1781
C36:4 DAG	0.9916	0.0384
C36:4 PC	0.9916	-0.0154
C36:4 PC plasmalogen	0.9916	0.0670
C36:4 PE	0.9916	0.0629
C36:5 PC plasmalogen	0.9916	0.0284
C36:5 PE plasmalogen	0.9916	0.0431
C37:2 PC	0.9916	-0.0718
C38:2 PC	0.9916	-0.1197
C38:2 PE	0.9916	-0.0803
C38:3 PC	0.9916	-0.0616
C38:4 PC	0.9916	-0.0718
C38:4 PE	0.9916	0.0453
C38:5 DAG	0.9916	0.0930
C38:5 PE	0.9916	-0.0250

Table S1.6 (Continued).

C38:6 PC	0.9916	0.0194
C38:6 PC plasmalogen	0.9916	-0.0186
C38:6 PE	0.9916	-0.1790
C38:6 PE plasmalogen	0.9916	-0.0489
C38:7 PE plasmalogen	0.9916	-0.3749
C40:5 PC	0.9916	-0.0726
C40:5 PE plasmalogen	0.9959	-0.0090
C40:6 PE	0.9916	-0.0624
C40:6 PS	0.9916	0.0698
C40:9 PC	0.9916	-0.1040
C42:0 TAG	0.9916	0.0321
C43:0 TAG	0.9916	-0.0651
C44:0 TAG	0.9959	-0.0014
C44:1 TAG	0.9916	0.0273
C46:0 TAG	0.9916	0.0184
C46:1 TAG	0.9916	0.0081
C47:1 TAG	0.9916	0.1197
C47:2 TAG	0.9916	0.1524
C48:0 TAG	0.9916	-0.0111
C48:2 TAG	0.9916	0.0561
C48:3 TAG	0.9916	0.0985
C48:4 TAG	0.9916	-0.5698
C49:1 TAG	0.9916	0.0571
C49:2 TAG	0.9916	0.1694
C49:3 TAG	0.9916	-0.0289
C50:0 TAG	0.9916	-0.0231
C50:1 TAG	0.9916	-0.0165
C50:2 TAG	0.9916	0.0578
C50:3 TAG	0.9916	0.1524
C50:4 TAG	0.9916	-0.2432
C50:5 TAG	0.9916	-0.0334
C51:2 TAG	0.9916	0.1995
C51:3 TAG	0.9916	0.5146
C52:1 TAG	0.9916	0.0822
C52:2 TAG	0.9916	0.1692
C52:3 TAG	0.9916	0.2200
C52:6 TAG	0.9959	-0.0045
C53:2 TAG	0.9916	0.2127
C54:1 TAG	0.9916	0.2088
C54:2 TAG	0.9916	0.1745
C54:3 TAG	0.9916	0.2893
C54:5 TAG	0.9916	0.0482
C54:6 TAG	0.9916	0.0307
C54:7 TAG	0.9916	-0.4188

Table S1.6 (Continued).

C54:8 TAG	0.9916	-0.5497
C55:3 TAG	0.9916	0.1884
C56:1 TAG	0.9916	-0.6571
C56:2 TAG	0.9916	0.3231
C56:5 TAG	0.9916	0.0653
C56:6 TAG	0.9916	0.0667
C56:7 TAG	0.9916	-0.0894
C56:8 TAG	0.9916	0.2938
C56:9 TAG	0.9916	-0.1815
C58:8 TAG	0.1402	1.6227
C58:9 TAG	0.9916	0.0719

Table S1.7. Top 25 differentially enriched genes per cluster. Clusters as annotated in Fig. S1.7B.

p_val	avg_logFC	pct.1	pct.2	p_val_adj	cluster	gene
0	1.472	0.892	0.282	0	0	Slc22a30
0	1.387	0.762	0.186	0	0	Cyp2j13
0	1.339	0.854	0.288	0	0	Cyp4b1
0	1.267	0.596	0.128	0	0	Slc7a13
0	1.243	0.783	0.256	0	0	Atp11a
0	1.187	0.967	0.484	0	0	Acsm2
0	1.176	0.323	0.035	0	0	Slco1a1
0	1.123	0.808	0.442	0	0	Fbxw2
0	1.119	0.317	0.059	0	0	Cntnap5a
0	1.105	0.723	0.25	0	0	Gm11128
0	1.09	0.528	0.144	0	0	Ces1f
0	1.079	0.677	0.249	0	0	Acy3
0	1.071	0.717	0.259	0	0	Slc17a3
0	1.052	0.775	0.311	0	0	Slco1a6
0	1.049	0.677	0.257	0	0	Them7
0	1.031	0.733	0.313	0	0	Smarca2
0	1.021	0.878	0.398	0	0	Acsm1
0	1.018	0.737	0.273	0	0	Slc22a28
0	0.998	0.629	0.228	0	0	Erc2
0	0.991	0.282	0.036	0	0	0610031O16Rik
0	0.991	0.467	0.124	0	0	Ugt8a
0	0.985	0.662	0.246	0	0	Slc13a3
0	0.981	0.861	0.353	0	0	RP24-362L9.2
0	0.976	0.622	0.234	0	0	Tmem150a
0	0.972	0.479	0.148	0	0	Slc22a12
0	2.205	0.958	0.231	0	1	Slc5a12
0	1.789	0.949	0.38	0	1	Nox4
0	1.549	0.66	0.129	0	1	Slc5a2
0	1.488	0.492	0.085	0	1	Slc7a7
0	1.449	0.587	0.129	0	1	Gatm
0	1.316	0.419	0.072	0	1	Adra1a
0	1.184	0.484	0.16	0	1	Gm37245
0	1.181	0.492	0.134	0	1	Alpl
0	1.163	0.489	0.133	0	1	Gldc
0	1.158	0.412	0.108	0	1	Unc5c
0	1.139	0.98	0.607	0	1	Fut9
0	1.116	0.339	0.117	0	1	Cyp2d12
0	1.108	0.384	0.103	0	1	Slc16a14
0	1.105	0.696	0.304	0	1	Maf
0	1.103	0.241	0.027	0	1	Gabrb3
0	1.053	0.377	0.093	0	1	Angpt1
0	1.048	0.25	0.035	0	1	Clec2h
0	1.041	0.444	0.141	0	1	Slc6a19
0	1.033	0.972	0.567	0	1	Dab2
0	1.027	0.336	0.086	0	1	Slc7a8
0	1.025	0.456	0.141	0	1	Prodh2

Table S1.7 (Continued).

0	0.996	0.842	0.465	0	1	Nhs
0	0.992	0.527	0.196	0	1	Pik3c2g
0	0.989	0.816	0.412	0	1	Auts2
0	0.987	0.845	0.448	0	1	Slc4a4
0	3.527	0.998	0.176	0	2	Slc12a1
0	2.54	0.94	0.288	0	2	Egf
0	2.396	0.992	0.331	0	2	Erbb4
0	1.878	0.914	0.347	0	2	Umod
0	1.831	0.38	0.028	0	2	Tenm2
0	1.757	0.422	0.042	0	2	Ptger3
0	1.588	0.419	0.045	0	2	Casr
0	1.568	0.325	0.04	0	2	Enox1
0	1.503	0.672	0.193	0	2	Cacnb4
0	1.484	0.582	0.118	0	2	Ppp1r1a
0	1.458	0.809	0.263	0	2	Kng2
0	1.456	0.208	0.007	0	2	Tmem207
0	1.41	0.3	0.039	0	2	Lrrc31
0	1.378	0.303	0.097	0	2	Sgcz
0	1.348	0.391	0.086	0	2	St3gal4
0	1.332	0.287	0.027	0	2	Slc2a13
0	1.294	0.392	0.07	0	2	Plekhg1
0	1.275	0.766	0.265	0	2	Slit2
0	1.256	0.521	0.145	0	2	Pdgfd
0	1.25	0.376	0.076	0	2	Mrps6
0	1.213	0.285	0.033	0	2	Chst9
0	1.19	0.641	0.283	0	2	Arhgap6
0	1.188	0.618	0.276	0	2	Cgnl1
0	1.169	0.274	0.037	0	2	Ephb2
0	1.134	0.487	0.182	0	2	Bckdhb
0	3.612	0.996	0.202	0	3	Slc12a3
0	2.422	0.748	0.041	0	3	Trpm6
0	2.332	0.715	0.264	0	3	Slc8a1
0	2.33	0.852	0.154	0	3	Abca13
0	2.186	0.972	0.361	0	3	Wnk1
0	1.898	0.656	0.076	0	3	Klhl3
0	1.794	0.729	0.187	0	3	Sgms2
0	1.707	0.444	0.113	0	3	Calb1
0	1.628	0.454	0.036	0	3	Cwh43
0	1.491	0.462	0.052	0	3	Tox3
0	1.464	0.697	0.175	0	3	Cadps2
0	1.434	0.837	0.406	0	3	Trpm7
0	1.413	0.664	0.23	0	3	Defb1
0	1.394	0.619	0.16	0	3	Tsc22d1
0	1.318	0.562	0.133	0	3	Prkd1
0	1.312	0.522	0.119	0	3	Tdrd3
0	1.298	0.573	0.132	0	3	Slc16a7
0	1.249	0.962	0.372	0	3	Mecom
0	1.226	0.329	0.043	0	3	Lhx1
0	1.225	0.749	0.184	0	3	Cacnb4
0	1.179	0.392	0.073	0	3	Acss3

Table S1.7 (Continued).

0	1.17	0.338	0.055	0	3	Ier3
0	1.17	0.417	0.074	0	3	Cdk14
0	1.168	0.229	0.026	0	3	Gm21847
0	1.166	0.424	0.074	0	3	Esrrb
0	2.574	0.644	0.078	0	4	Frmpd4
0	2.406	0.962	0.167	0	4	Phactr1
0	2.275	0.449	0.031	0	4	Fxyd4
0	2.109	0.287	0.029	0	4	Egfem1
0	2.083	0.324	0.041	0	4	Mgat4c
0	1.838	0.483	0.032	0	4	Scnn1b
0	1.8	0.464	0.056	0	4	Slc2a9
0	1.689	0.526	0.136	0	4	Tbck
0	1.664	0.431	0.045	0	4	Hsd11b2
0	1.663	0.353	0.033	0	4	Aqp2
0	1.582	0.427	0.06	0	4	AI838599
0	1.52	0.829	0.261	0	4	Slc8a1
0	1.488	0.437	0.057	0	4	Bmpr1b
0	1.487	0.465	0.074	0	4	Rhcg
0	1.44	0.365	0.055	0	4	Tmem45b
0	1.396	0.712	0.247	0	4	Nr3c2
0	1.378	0.477	0.117	0	4	Abr
0	1.372	0.241	0.007	0	4	Col26a1
0	1.363	0.283	0.036	0	4	Apela
0	1.343	0.451	0.109	0	4	Cacnb2
0	1.334	0.29	0.034	0	4	Aim1
0	1.322	0.435	0.106	0	4	Sdk1
0	1.31	0.469	0.189	0	4	Gpc5
0	1.301	0.266	0.011	0	4	Scnn1g
0	1.293	0.232	0.013	0	4	Kif26b
0	1.568	0.478	0.046	0	5	Cyp4a14
0	1.533	0.973	0.308	0	5	Xist
0	1.307	0.407	0.1	0	5	Fam83g
0	1.245	0.491	0.086	0	5	Kynu
0	1.235	0.479	0.088	0	5	BC089597
0	1.179	0.607	0.157	0	5	Gldc
0	1.108	0.318	0.067	0	5	Slc2a5
0	1.084	0.449	0.122	0	5	Abcc4
0	1.053	0.515	0.116	0	5	Tsix
0	1.024	0.417	0.122	0	5	Hacl1
0	0.972	0.439	0.14	0	5	Tkfc
0	0.97	0.647	0.283	0	5	Acaa1b
0	0.96	0.919	0.498	0	5	Keg1
0	0.953	0.311	0.048	0	5	Prlr
0	0.946	0.221	0.027	0	5	Hmgcs2
0	0.923	0.863	0.435	0	5	Slc13a1
0	0.918	0.546	0.177	0	5	Slc22a8
0	0.913	0.283	0.047	0	5	Slc22a29
0	0.911	0.228	0.036	0	5	Pklr
0	0.874	0.528	0.215	0	5	Ces1d
0	0.874	0.92	0.434	0	5	Nox4

Table S1.7 (Continued).

0	0.865	0.975	0.662	0	5	Miox
0	0.843	0.621	0.27	0	5	Phyhipl
0	0.835	0.472	0.182	0	5	Acnat1
0	0.824	0.87	0.445	0	5	Auts2
0	2.994	0.876	0.056	0	6	Cyp7b1
0	1.904	0.98	0.433	0	6	Gramd1b
0	1.869	0.932	0.225	0	6	Fgf1
0	1.858	0.927	0.202	0	6	Slc7a13
0	1.821	0.823	0.135	0	6	Rnf24
0	1.696	0.423	0.016	0	6	Bcat1
0	1.561	0.999	0.796	0	6	Ghr
0	1.47	0.617	0.105	0	6	Slc6a15
0	1.406	0.783	0.214	0	6	Aadat
0	1.35	0.975	0.588	0	6	Spag5
0	1.338	0.971	0.347	0	6	Atp11a
0	1.334	0.491	0.036	0	6	Mep1b
0	1.33	0.583	0.082	0	6	Acsm3
0	1.325	0.855	0.227	0	6	Napsa
0	1.323	0.676	0.133	0	6	Gm853
0	1.285	0.86	0.242	0	6	Slc6a18
0	1.281	0.729	0.179	0	6	Slc9a8
0	1.281	0.604	0.103	0	6	Gpm6a
0	1.264	0.96	0.518	0	6	Mat2a
0	1.257	0.649	0.091	0	6	Chrm3
0	1.241	0.767	0.268	0	6	Gm28153
0	1.238	0.76	0.229	0	6	Snhg11
0	1.236	0.686	0.156	0	6	Crot
0	1.23	0.722	0.174	0	6	Wdr17
0	1.225	0.927	0.402	0	6	Osbpl8
0	2.683	0.842	0.113	0	7	Meis2
0	2.627	0.658	0.035	0	7	Adgrl4
0	2.43	0.699	0.056	0	7	Plpp1
0	2.405	0.7	0.061	0	7	Flt1
0	2.32	0.624	0.043	0	7	Emcn
0	2.231	0.694	0.068	0	7	Ldb2
0	2.016	0.546	0.067	0	7	Tek
0	1.996	0.463	0.057	0	7	Inpp4b
0	1.986	0.572	0.057	0	7	Ebf1
0	1.948	0.534	0.049	0	7	Rapgef4
0	1.876	0.917	0.526	0	7	Pbx1
0	1.859	0.367	0.022	0	7	Rgcc
0	1.819	0.606	0.116	0	7	Ptprm
0	1.805	0.383	0.017	0	7	Cyyr1
0	1.745	0.403	0.022	0	7	Exoc3l2
0	1.708	0.434	0.033	0	7	Eng
0	1.702	0.312	0.021	0	7	Tll1
0	1.691	0.339	0.023	0	7	Rapgef5
0	1.673	0.381	0.037	0	7	Arhgap31
0	1.66	0.467	0.088	0	7	Plpp3
0	1.642	0.444	0.068	0	7	Ptprb

Table S1.7 (Continued).

0	1.636	0.445	0.08	0	7	Heg1
0	1.624	0.274	0.024	0	7	D5Ertd615e
0	1.623	0.359	0.032	0	7	Plvap
0	1.575	0.381	0.064	0	7	Samd12
0	3.039	0.812	0.033	0	8	Cfh
0	2.767	0.846	0.071	0	8	Tshz2
0	2.741	0.694	0.043	0	8	Robo2
0	2.713	0.868	0.104	0	8	Prkg1
0	2.635	0.635	0.011	0	8	Gm2163
0	2.613	0.56	0.111	0	8	Csmd1
0	2.602	0.831	0.096	0	8	Rbms3
0	2.315	0.588	0.013	0	8	Pde3a
0	2.278	0.696	0.055	0	8	Dlc1
0	2.256	0.633	0.031	0	8	Cald1
0	2.218	0.605	0.03	0	8	Cped1
0	2.2	0.455	0.008	0	8	4930578G10Rik
0	2.197	0.576	0.04	0	8	Lama2
0	2.185	0.532	0.036	0	8	B3galt1
0	2.183	0.538	0.019	0	8	Kcnt2
0	2.173	0.655	0.057	0	8	Ebf1
0	2.159	0.533	0.026	0	8	Hsd11b1
0	2.154	0.5	0.011	0	8	Fhl2
0	2.147	0.662	0.072	0	8	Ldb2
0	2.121	0.539	0.054	0	8	Gpc6
0	2.081	0.464	0.047	0	8	Mgp
0	2.076	0.435	0.007	0	8	Abca8a
0	2.025	0.451	0.015	0	8	Fbln5
0	1.923	0.619	0.085	0	8	Fbxl7
0	1.919	0.415	0.035	0	8	Igfbp3
0	3.08	0.957	0.026	0	9	Slc7a12
0	2.952	0.985	0.211	0	9	Aadat
0	2.311	0.859	0.103	0	9	Gm20400
0	2.128	0.975	0.228	0	9	Napsa
0	2.023	0.842	0.14	0	9	Rnf24
0	1.954	0.947	0.171	0	9	Wdr17
0	1.923	0.69	0.046	0	9	Prlr
0	1.874	0.75	0.028	0	9	Slc22a19
0	1.782	0.786	0.107	0	9	Gm4450
0	1.78	0.72	0.064	0	9	A330033J07Rik
0	1.747	0.997	0.436	0	9	Gramd1b
0	1.735	0.888	0.228	0	9	Snhg11
0	1.653	0.826	0.234	0	9	Fgf1
0	1.573	0.618	0.032	0	9	Mro
0	1.501	0.827	0.171	0	9	Nceh1
0	1.46	0.582	0.061	0	9	Adgrb3
0	1.407	1	0.797	0	9	Ghr
0	1.406	0.92	0.244	0	9	Slc6a18
0	1.378	0.546	0.033	0	9	Cbr1
0	1.376	0.834	0.156	0	9	4930533I22Rik
0	1.366	0.803	0.152	0	9	Slc23a1

Table S1.7 (Continued).

0	1.346	0.603	0.101	0	9	Acy1
0	1.325	0.562	0.065	0	9	Bdh1
0	1.318	0.665	0.104	0	9	Gpm6a
0	1.313	0.582	0.056	0	9	Ccbl2
0	3.821	0.975	0.018	0	10	Slc26a4
0	3.419	0.939	0.153	0	10	Lsamp
0	3.012	0.962	0.027	0	10	Slc4a9
0	2.731	0.987	0.157	0	10	Tmem117
0	2.397	0.88	0.098	0	10	Pde4b
0	2.379	0.902	0.287	0	10	Car12
0	2.224	0.788	0.033	0	10	Atp6v1c2
0	2.19	0.794	0.037	0	10	Atp6v0d2
0	2.064	0.647	0.007	0	10	Insrr
0	1.966	0.577	0.029	0	10	Tmem163
0	1.949	0.856	0.204	0	10	Nbea
0	1.946	0.569	0.024	0	10	Syn2
0	1.944	0.633	0.088	0	10	Malrd1
0	1.838	0.672	0.047	0	10	Atp6v1g3
0	1.803	0.627	0.039	0	10	Rcan2
0	1.797	0.65	0.099	0	10	Zcchc16
0	1.649	0.878	0.354	0	10	Ralgapa2
0	1.611	0.452	0.03	0	10	Tshr
0	1.603	0.585	0.067	0	10	Irs1
0	1.574	0.437	0.01	0	10	Hepacam2
0	1.567	0.879	0.357	0	10	Dmxl1
0	1.521	0.827	0.203	0	10	Pde1a
0	1.519	0.441	0.025	0	10	Plcg2
0	1.493	0.624	0.077	0	10	Bmpr1b
0	1.467	0.408	0.052	0	10	Thsd7a
0	2.419	0.682	0.04	0	11	Dock10
0	2.033	0.467	0.078	0	11	Kcnip4
0	1.956	0.392	0.014	0	11	Vcam1
0	1.817	0.63	0.117	0	11	Il34
0	1.609	0.314	0.012	0	11	Cxcl1
0	1.528	0.491	0.063	0	11	Cp
0	1.45	0.455	0.058	0	11	Sytl2
0	1.447	0.251	0.019	0	11	Sorcs1
0	1.249	0.311	0.011	0	11	Creb5
0	1.047	0.211	0.01	0	11	Kcnh8
0	1.046	0.326	0.039	0	11	Birc3
0	0.928	0.281	0.028	0	11	Klf6
0	0.926	0.21	0.009	0	11	C3
0	0.903	0.209	0.007	0	11	Havcr1
0	0.902	0.271	0.029	0	11	Prickle2
0	0.873	0.22	0.01	0	11	Ngf
0	0.837	0.168	0.005	0	11	Cd44
0	0.683	0.102	0.002	0	11	Cxcl2
2.18E-277	0.97	0.247	0.029	4.16E-273	11	Cd74
2.00E-272	0.677	0.176	0.015	3.81E-268	11	Relb
3.45E-263	0.701	0.135	0.009	6.57E-259	11	Edn1

Table S1.7 (Continued).

3.79E-262	0.772	0.194	0.019	7.21E-258	11	Pdgfb
5.85E-258	0.847	0.241	0.03	1.11E-253	11	Icam1
4.63E-249	0.844	0.294	0.044	8.81E-245	11	Nfkbiz
2.09E-231	0.661	0.167	0.016	3.98E-227	11	Aoc1
0	2.315	0.95	0.163	0	12	Tmem117
0	2.117	0.658	0.042	0	12	Rcan2
0	1.996	0.643	0.045	0	12	Atp6v0d2
0	1.988	0.706	0.078	0	12	Bmpr1b
0	1.973	0.653	0.092	0	12	Malrd1
0	1.969	0.496	0.007	0	12	Aqp6
0	1.946	0.488	0.007	0	12	Kit
0	1.836	0.608	0.041	0	12	Slc4a9
0	1.805	0.691	0.108	0	12	Pde4b
0	1.78	0.57	0.078	0	12	Alcam
0	1.753	0.929	0.451	0	12	Pam
0	1.702	0.694	0.128	0	12	Cacnb2
0	1.695	0.42	0.033	0	12	Tshr
0	1.676	0.523	0.045	0	12	Atp6v1c2
0	1.674	0.416	0.015	0	12	Clnk
0	1.612	0.411	0.018	0	12	Adgrf5
0	1.581	0.391	0.018	0	12	Cpsf4l
0	1.574	0.467	0.092	0	12	Trpm3
0	1.567	0.471	0.056	0	12	Atp6v1g3
0	1.563	0.451	0.035	0	12	Rhbg
0	1.509	0.416	0.03	0	12	Epb41l2
0	1.499	0.772	0.261	0	12	Itpr2
0	1.486	0.616	0.14	0	12	Abr
0	1.474	0.399	0.032	0	12	Syn2
0	1.469	0.181	0.007	0	12	Rorb
0	2.094	0.614	0.033	0	13	Dcdc2a
3.82E-277	0.951	0.159	0.006	7.26E-273	13	Lcn2
1.15E-242	0.81	0.161	0.007	2.19E-238	13	Samd5
1.06E-229	1.094	0.177	0.01	2.02E-225	13	Edn1
3.67E-227	1.674	0.515	0.087	6.99E-223	13	Clu
4.19E-220	1.79	0.949	0.401	7.97E-216	13	Erbb4
1.02E-212	1.934	0.554	0.107	1.95E-208	13	Nrxn3
3.01E-211	1.871	0.876	0.343	5.72E-207	13	Spp1
6.23E-164	1.438	0.6	0.151	1.19E-159	13	Efna5
1.82E-126	1.299	0.494	0.125	3.45E-122	13	Kctd1
6.47E-125	1.104	0.349	0.065	1.23E-120	13	Sytl2
7.04E-118	0.862	0.237	0.033	1.34E-113	13	Dysf
3.00E-101	0.679	0.117	0.01	5.71E-97	13	Ifitm10
3.94E-94	0.682	0.133	0.013	7.50E-90	13	Osmr
2.91E-86	-1.085	0.747	0.893	5.55E-82	13	Pde4d
3.80E-85	0.939	0.251	0.048	7.23E-81	13	Nfkbiz
9.27E-78	-1.666	0.267	0.669	1.76E-73	13	Fut9
4.99E-76	0.709	0.874	0.434	9.49E-72	13	Mecom
3.46E-74	0.947	0.586	0.234	6.58E-70	13	Rgs6
1.42E-73	1.128	0.561	0.235	2.69E-69	13	Gm13247
9.60E-71	0.817	0.189	0.033	1.83E-66	13	Srgap1

Table S1.7 (Continued).

8.13E-70	1.041	0.372	0.112	1.55E-65	13	Rtn4
3.88E-69	-1.592	0.237	0.635	7.39E-65	13	Dab2
2.10E-68	0.927	0.126	0.016	3.99E-64	13	Kcnh1
3.91E-68	0.608	0.122	0.015	7.45E-64	13	Slco4a1
0	2.064	0.793	0.091	0	14	Tshz2
0	1.783	0.32	0.01	0	14	Ncam1
0	1.5	0.212	0.001	0	14	Fst
0	1.351	0.174	0.003	0	14	Tnc
0	0.975	0.158	0.002	0	14	Bst1
4.64E-308	1.309	0.203	0.005	8.84E-304	14	Slc4a11
9.42E-222	2.114	0.689	0.101	1.79E-217	14	Tbc1d4
3.55E-210	1.241	0.282	0.016	6.76E-206	14	Gm26883
8.43E-194	1.25	0.261	0.015	1.60E-189	14	Pgm5
5.58E-181	1.799	0.68	0.115	1.06E-176	14	Rbms3
3.85E-165	1.718	0.394	0.042	7.32E-161	14	Akap12
8.30E-157	1.211	0.274	0.021	1.58E-152	14	Spon1
8.62E-145	1.208	0.22	0.015	1.64E-140	14	Platr22
2.52E-143	1.1	0.174	0.009	4.80E-139	14	Scel
1.33E-134	1.83	0.315	0.032	2.54E-130	14	Cdh13
7.24E-122	1.451	0.249	0.022	1.38E-117	14	Stk32a
9.94E-121	1.361	0.365	0.047	1.89E-116	14	Ptpn14
6.77E-107	1.692	0.427	0.071	1.29E-102	14	Cp
4.67E-104	1.048	0.199	0.016	8.89E-100	14	Proser2
6.96E-104	1.633	0.452	0.084	1.32E-99	14	Chn2
1.16E-102	1.006	0.133	0.007	2.21E-98	14	Angpt2
1.79E-100	1.125	0.191	0.016	3.41E-96	14	Ccnjl
9.91E-99	0.947	0.166	0.012	1.89E-94	14	Arhgap28
3.35E-95	1.041	0.158	0.011	6.38E-91	14	Rasl11b
6.99E-93	1.567	0.332	0.049	1.33E-88	14	Cdh6
0	2.836	0.809	0.006	0	15	Ptpro
0	2.792	0.904	0.028	0	15	Podxl
0	2.532	0.83	0.033	0	15	Srgap1
0	2.391	0.617	0.011	0	15	Synpo
0	2.355	0.798	0.03	0	15	Plce1
0	2.339	0.66	0.013	0	15	Nebl
0	2.304	0.617	0.003	0	15	Nphs1
0	2.28	0.67	0.003	0	15	Wt1
0	2.261	0.649	0.011	0	15	Arhgap28
0	2.048	0.574	0.016	0	15	C1qtnf7
0	1.85	0.489	0.007	0	15	Wt1os
0	1.844	0.5	0.01	0	15	Sncaip
0	1.843	0.372	0.004	0	15	Cdkn1c
0	1.719	0.394	0.003	0	15	Nphs2
0	1.312	0.287	0.003	0	15	Lmx1b
0	1.289	0.319	0.001	0	15	Myom2
0	1.27	0.319	0.005	0	15	Tdrd5
0	1.106	0.277	0.001	0	15	Clic3
0	0.962	0.16	0	0	15	Gm12709
0	0.917	0.128	0	0	15	Ddn
0	0.55	0.117	0.001	0	15	Cdsn

Table S1.7 (Continued).

2.97E-306	1.38	0.298	0.005	5.65E-302	15	Sema3g
1.07E-292	0.953	0.202	0.002	2.03E-288	15	Gm4128
1.63E-287	0.976	0.17	0.002	3.10E-283	15	Gm13814
1.46E-262	2.761	0.904	0.061	2.77E-258	15	Robo2

Table S1.8. Gene set enrichment analysis on Dock10/Vcam1+ cluster marker list.

pathway	pval	padj	ES	NES	nMoreExtreme	size	leadingEdge
KEGG_CITRATE_CYCLE_TCA_CYCLE	8.34E-04	6.42E-02	-0.7842	-2.0569	0	19	PCK1 PC MDH1 ACO2 OGDH IDH2 DLAT SDHB PDHB
KEGG_CELL_ADHESION_MOLECULES_CAMS	1.41E-03	6.42E-02	0.8812	1.5080	12	27	VCAM1 ICAM1 ITGAV HLADQB1 PVR HLAE HLAA ITGB8 ITGB1
KEGG_FOCAL_ADHESION	2.52E-03	7.65E-02	0.7945	1.4002	24	72	BIRC3 PDGFB SPP1 ACTN1 ITGAV ITGB6 BIRC2 JUN PDGFD PAK1 ITGB8 VCL COL4A1 LAMA5 ITGA1 ITGB1 ROCK2 ACTG1 RHOA FLNB MET EGFR CAPN2
KEGG_ECM_RECEPTOR_INTERACTION	3.95E-03	8.98E-02	0.8908	1.5029	34	20	CD44 SPP1 ITGAV ITGB6 CD47 AGRN ITGB8 COL4A1 LAMA5 ITGA1 ITGB1
KEGG_APOPTOSIS	6.02E-03	9.15E-02	0.8643	1.4747	54	25	BIRC3 NGF NFKBIA NFKB1 BIRC2 APAF1 MAP3K14 IKBKB BCL2L1 CFLAR CAPN2
KEGG_ALDOSTERONE_REGULATED_SODIUM_REABSORPTION	6.03E-03	9.15E-02	-0.7640	-1.8776	8	15	NR3C2 ATP1B1 ATP1A1 FXYD2 SCNN1A PIK3R3
KEGG_PEROXISOME	8.55E-03	9.68E-02	-0.5477	-1.6757	3	38	PECR ACAA1 ACOX1 SLC27A2 IDH2 NUDT19 ABCD3 MPV17L ACOX3 PHYH AMACR
KEGG_LEUKOCYTE_TRANSENDOTHELIAL_MIGRATION	8.36E-03	9.68E-02	0.8140	1.4160	79	40	VCAM1 ICAM1 ACTN1 MSN VCL ITGB1 ROCK2 ACTG1 RHOA ACTB F11R EZR MYL12B GNAI2 CYBA GNAI3 CLDN2
KEGG_SMALL_CELL_LUNG_CANCER	9.57E-03	9.68E-02	0.8293	1.4322	89	33	BIRC3 NFKBIA ITGAV NFKB1 CDK6 BIRC2 COL4A1 APAF1 LAMA5 IKBKB ITGB1 BCL2L1
KEGG_NATURAL_KILLER_CELL_MEDIATED_CYTOTOXICITY	1.11E-02	1.01E-01	0.8448	1.4427	101	26	ICAM1 HLAE HLAA PAK1 NFAT5
KEGG_REGULATION_OF_ACTIN_CYTOSKELETON	1.39E-02	1.05E-01	0.7492	1.3192	137	81	PDGFB ACTN1 ITGAV ITGB6 MSN PDGFD SCIN MYH9 PAK1 ITGB8 VCL ITGA1 ITGB1 RRAS2 ROCK2 ACTG1 WASF2 RHOA EGFR ACTB EZR PFN1 MYL12B NRAS GNG12
KEGG_PATHWAYS_IN_CANCER	1.32E-02	1.05E-01	0.7290	1.2852	131	111	BIRC3 PDGFB RUNX1 NFKBIA ITGAV NFKB1 CDK6 BIRC2 JUN PAX8 TGFBR2 COL4A1 RALB LAMA5 RASSF1 IKBKB ITGB1 SMAD2 TPM3 STAT3 RHOA BCL2L1 MET EGFR

Table S1.8 (Continued).

KEGG_VIRAL_MYOCARDITIS	1.99E-02	1.39E-01	0.8814	1.4589	168	15	ICAM1 HLADQB1 HLAE HLAA MYH9 ACTG1 ACTB
KEGG_PROSTATE_CANCER	2.47E-02	1.61E-01	0.7743	1.3555	239	48	CREB5 PDGFB NFKBIA NFKB1 PDGFD IKBKB
KEGG_ANTIGEN_PROCESSING_AND_PRESENTATION	3.00E-02	1.82E-01	0.8690	1.4384	254	15	CD74 HLADQB1 HLAE HLAA B2M TAP2 LGMN
KEGG_TOLL_LIKE_RECEPTOR_SIGNALING_PATHWAY	3.33E-02	1.89E-01	0.8264	1.4047	300	23	SPP1 NFKBIA NFKB1 JUN IKBKB
KEGG_B_CELL_RECEPTOR_SIGNALING_PATHWAY	4.42E-02	2.37E-01	0.7969	1.3684	409	29	NFKBIA NFKB1 JUN MALT1 NFAT5 IKBKB NRAS KRAS
KEGG_INOSITOL_PHOSPHATE_METABOLISM	6.23E-02	2.38E-01	-0.5930	-1.5023	82	17	MIOX PIK3C2G PLCB1 ALDH6A1
KEGG_GLYCEROPHOSPHOLIPID_METABOLISM	5.00E-02	2.38E-01	-0.5787	-1.5179	59	19	PCYT2 CHPT1 PLA2G3
KEGG_PPAR_SIGNALING_PATHWAY	6.41E-02	2.38E-01	-0.5142	-1.4269	55	25	PCK1 ACAA1 ACOX1 LPL SLC27A2 SLC27A1 ACOX3 CD36
KEGG_WNT_SIGNALING_PATHWAY	4.93E-02	2.38E-01	0.7612	1.3277	473	43	PRICKLE2 JUN NFAT5 ROCK2 SMAD2 TBL1X RHOA
KEGG_RIG_I_LIKE_RECEPTOR_SIGNALING_PATHWAY	6.30E-02	2.38E-01	0.8228	1.3800	549	18	NFKBIA NFKB1 MAP3K1 DDX58 IKBKB TRAF3 CYLD RELA CASP8
KEGG_T_CELL_RECEPTOR_SIGNALING_PATHWAY	6.54E-02	2.38E-01	0.7575	1.3176	625	40	NFKBIA NFKB1 JUN PAK1 MAP3K14 MALT1 NFAT5 IKBKB RHOA NCK2 NRAS KRAS
KEGG_NEUROTROPHIN_SIGNALING_PATHWAY	6.52E-02	2.38E-01	0.7443	1.3023	630	47	NGF NFKBIA NFKB1 JUN MAP3K1 IKBKB RHOA NRAS YWHAQ KRAS MAPKAPK2 YWHAE IRAK2 MAP3K5 RELA
KEGG_EPITHELIAL_CELL_SIGNALING_IN_HELICOBACTER_PYLORI_INFECTION	5.60E-02	2.38E-01	0.7836	1.3464	520	30	NFKBIA NFKB1 JUN PAK1 MAP3K14 IKBKB MET EGFR ATP6V1C1 ADAM10 F11R
KEGG_ADHERENS_JUNCTION	6.90E-02	2.42E-01	0.7585	1.3169	657	38	ACTN1 TGFBR2 VCL SMAD2 ACTG1 WASF2 RHOA MET EGFR PTPRJ ACTB
KEGG_CARDIAC_MUSCLE_CONTRACTION	7.97E-02	2.69E-01	-0.4833	-1.3736	59	28	CACNB4 ATP1B1 ATP1A1 FXYD2 CACNB2 SLC8A1

Table S1.8 (Continued).

KEGG_GLYCOLYSIS_GLUCONEOGENESIS	8.34E-02	2.71E-01	-0.5511	-1.4455	99	19	PCK1 ACSS1 G6PC FBP1 HK1
KEGG_CHEMOKINE_SIGNALING_PATHWAY	9.00E-02	2.73E-01	0.7278	1.2743	873	49	NFKBIA NFKB1 CXCL16 PAK1 IKBKB ROCK2 STAT3 RHOA GRK5 GNB1 FGR GNAI2 NRAS GNG12 GNAI3 KRAS
KEGG_VASOPRESSIN_REGULATED_WATER_REABSORPTION	8.72E-02	2.73E-01	0.8074	1.3541	760	18	CREB5 DYNLL1
KEGG_ACUTE_MYELOID_LEUKEMIA	9.90E-02	2.91E-01	0.7639	1.3087	915	28	RUNX1 NFKB1 IKBKB STAT3 ZBTB16 NRAS KRAS
KEGG_MAPK_SIGNALING_PATHWAY	1.05E-01	2.99E-01	0.6915	1.2181	1043	77	NGF RELB PDGFB NFKB1 JUN MAP3K1 PAK1 TAOK3 TGFBR2 MAP3K14 IKBKB RRAS2 MAP4K4 FLNB RASA2 EGFR MAP3K13 CACNA2D4 NRAS DUSP16 GNG12 KRAS DDIT3 MAPKAPK2
KEGG_CYTOKINE_CYTOKINE_RECEPTOR_INTERACTION	1.14E-01	3.14E-01	0.8036	1.3392	979	16	PDGFB TNFRSF12A CXCL16 TGFBR2 MET EGFR
KEGG_AXON_GUIDANCE	1.42E-01	3.39E-01	0.7137	1.2448	1362	44	SEMA3C SEMA5A SEMA6A SRGAP1 PAK1 NFAT5 ITGB1 ROCK2 RHOA MET NCK2 PLXNA2 GNAI2 NRAS GNAI3 KRAS NTN1 NRP1
KEGG_RENAL_CELL_CARCINOMA	1.30E-01	3.39E-01	0.7423	1.2755	1206	30	PDGFB JUN PAK1 MET NRAS KRAS
KEGG_HYPERTROPHIC_CARDIOMYOPATHY_HCM	1.36E-01	3.39E-01	0.7744	1.3065	1207	20	ITGAV ITGB6 ITGB8 TPM1 ITGA1 ITGB1 TPM3 ACTG1 LMNA ACTB CACNA2D4
KEGG_ARRHYTHMOGENIC_RIGHT_VENTRICULAR_CARDIOMYOPATHY_ARVC	1.41E-01	3.39E-01	0.7530	1.2847	1290	25	ACTN1 ITGAV ITGB6 ITGB8 ITGA1 ITGB1 ACTG1 LMNA ACTB CACNA2D4
KEGG_DILATED_CARDIOMYOPATHY	1.41E-01	3.39E-01	0.7723	1.3031	1247	20	ITGAV ITGB6 ITGB8 TPM1 ITGA1 ITGB1 TPM3 ACTG1 LMNA ACTB CACNA2D4
KEGG_OXIDATIVE_PHOSPHORYLATION	1.68E-01	3.79E-01	-0.3618	-1.1658	45	50	ATP6V0A4 ATP6V1A COX7B CYC1 NDUFS1 SDHB ATP6V1H NDUFB3 NDUFV3 UQCRC2 NDUFS3
KEGG_UBIQUITIN_MEDIATED_PROTEOLYSIS	1.71E-01	3.79E-01	0.6850	1.2033	1673	57	BIRC3 BIRC2 MAP3K1 MID1 UBE2E2 MDM2 HUWE1 UBE2I TRIM37 UBE2D2 NEDD4 UBE2D3

Table S1.8 (Continued).

KEGG_CHRONIC_MYELOID_LEUKEMIA	1.70E-01	3.79E-01	0.7105	1.2334	1623	38	RUNX1 NFKBIA NFKB1 CDK6 TGFBR2 IKBKB BCL2L1 NRAS MDM2 KRAS
KEGG_TGF_BETA_SIGNALING_PATHWAY	1.84E-01	3.91E-01	0.7331	1.2508	1682	25	BMP6 TGFBR2 ROCK2 SMAD2 RHOA BMP4 ID3 SP1 SMAD3 SMURF1 ROCK1
KEGG_PANCREATIC_CANCER	1.85E-01	3.91E-01	0.7172	1.2350	1726	31	NFKB1 CDK6 TGFBR2 RALB IKBKB SMAD2 STAT3 BCL2L1 EGFR
KEGG_MELANOMA	1.95E-01	4.04E-01	0.7230	1.2372	1797	27	PDGFB CDK6 PDGFD MET EGFR NRAS MDM2 KRAS
KEGG_PHOSPHATIDYLINOSITOL_SIGNALING_SYSTEM	2.19E-01	4.42E-01	-0.4300	-1.1932	190	25	PIK3C2G PLCB1 ITPR2 PIK3R3 ITPR1
KEGG_CELL_CYCLE	2.40E-01	4.65E-01	0.6930	1.1948	2250	32	CDK6 SMAD2 WEE1 STAG1 MDM2 YWHAQ YWHAE
KEGG_TIGHT_JUNCTION	2.39E-01	4.65E-01	0.6731	1.1778	2309	47	ACTN1 MYH9 MAGI2 RRAS2 ACTG1 TJP2 RHOA SPTAN1 ACTB F11R MAGI3 MYL12B GNAI2 NRAS GNAI3 KRAS CLDN2
KEGG_MELANOGENESIS	2.52E-01	4.68E-01	0.7027	1.2001	2305	26	EDN1 GNAI2 NRAS GNAI3 KRAS
KEGG_GLIOMA	2.52E-01	4.68E-01	0.7027	1.2002	2305	26	PDGFB CDK6 EGFR NRAS MDM2 KRAS
KEGG_THYROID_CANCER	2.67E-01	4.87E-01	0.7302	1.2087	2274	15	PAX8 TPM3 NRAS KRAS
KEGG_PATHOGENIC_ESCHERICHIA_COLI_INFECTION	2.75E-01	4.90E-01	0.7130	1.1998	2417	19	ITGB1 ROCK2 ACTG1 RHOA NCK2 ACTB EZR YWHAQ ARPC2 CTTN NCK1 ROCK1 ARHGEF2
KEGG_ADIPOCYTOKINE_SIGNALING_PATHWAY	3.15E-01	5.50E-01	0.6840	1.1627	2849	23	NFKBIA NFKB1 IKBKB STAT3
KEGG_VIBRIO_CHOLERAE_INFECTION	3.20E-01	5.50E-01	0.6796	1.1574	2909	24	CFTR ACTG1 TJP2 ATP6V1C1 ACTB
KEGG_GAP_JUNCTION	3.39E-01	5.71E-01	0.6632	1.1388	3139	29	PDGFB PDGFD EGFR GNAI2 NRAS GNAI3 KRAS
KEGG_FC_GAMMA_R_MEDIATED_PHAGOCYTOSIS	4.09E-01	6.77E-01	0.6369	1.0937	3792	29	SCIN PAK1 WASF2 ASAP1 ARPC2 PRKCD GAB2 AKT3 CFL2 LYN MAP2K1 PIK3CA
KEGG_TRYPTOPHAN_METABOLISM	4.56E-01	6.80E-01	0.6371	1.0546	3880	15	ACAT2 DDC WARS2
KEGG_ERBB_SIGNALING_PATHWAY	4.56E-01	6.80E-01	0.6078	1.0572	4362	40	NRG1 JUN PAK1 EGFR NCK2 NRAS KRAS

Table S1.8 (Continued).

KEGG_LONG_TERM_POTENTIATION	4.52E-01	6.80E-01	-0.3566	-0.9896	394	25	PPP1R1A PLCB1 ITPR2 ITPR1
KEGG_TYPE_II_DIABETES_MELLITUS	4.35E-01	6.80E-01	0.6467	1.0704	3698	15	SOCS2 IKBKB PKLR PRKCD
KEGG_HUNTINGTONS_DISEASE	4.24E-01	6.80E-01	0.6026	1.0601	4180	65	CREB5 APAF1 TGM2 GPX1 CLTC
KEGG_COLORECTAL_CANCER	4.44E-01	6.80E-01	0.6231	1.0676	4104	28	JUN TGFBR2 SMAD2 RHOA KRAS SMAD3 AKT3 APPL1 GSK3B MAP2K1 PIK3CA
KEGG_LYSINE_DEGRADATION	4.94E-01	7.20E-01	0.6124	1.0271	4306	18	ACAT2 TMLHE
KEGG_AMYOTROPHIC_LATERAL_SCLEROSIS_ALS	4.98E-01	7.20E-01	0.6123	1.0204	4285	16	APAF1 BCL2L1 GPX1 MAP3K5
KEGG_NEUROACTIVE_LIGAND_RECEPTOR_INTERACTION	5.16E-01	7.33E-01	0.6033	1.0054	4436	16	GRID1 GRIA3 P2RX4
KEGG_CALCIUM_SIGNALING_PATHWAY	5.33E-01	7.35E-01	-0.3335	-0.9451	422	27	PLCB1 SLC8A1 ITPR2 PDE1A ITPR1 ERBB4
KEGG_JAK_STAT_SIGNALING_PATHWAY	5.26E-01	7.35E-01	0.5892	1.0035	4772	24	SOCS2 STAT3 BCL2L1 AKT3 JAK1 PIK3CA
KEGG_ENDOCYTOSIS	5.45E-01	7.41E-01	0.5676	0.9970	5348	57	HLAE HLAA ASAP1 MET EGFR PSD3 GRK5 EPN2 CLTC MDM2 AP2B1 IGF1R SH3GLB1 NEDD4 SH3GL1 RABEP1 ARAP2 AGAP1 SMURF1
KEGG_FATTY_ACID_METABOLISM	5.85E-01	7.71E-01	0.5655	0.9515	5145	19	ACAT2 ACSL4
KEGG_PROPANOATE_METABOLISM	5.79E-01	7.71E-01	0.5681	0.9559	5092	19	ACAT2 LDHB
KEGG_NON_SMALL_CELL_LUNG_CANCER	6.04E-01	7.85E-01	0.5530	0.9435	5511	25	CDK6 RASSF1 EGFR NRAS KRAS
KEGG_PROGESTERONE_MEDIATED_OOCYTE_MATURATION	6.25E-01	8.02E-01	0.5442	0.9250	5651	23	CPEB1 GNAI2 GNAI3 KRAS IGF1R RPS6KA3 AKT3 MAP2K1 PIK3CA
KEGG_ARGININE_AND_PROLINE_METABOLISM	6.48E-01	8.08E-01	-0.3453	-0.8487	966	15	ASS1 PRODH
KEGG_GNRH_SIGNALING_PATHWAY	6.41E-01	8.08E-01	0.5364	0.9211	5940	29	JUN MAP3K1 EGFR NRAS KRAS
KEGG_PURINE_METABOLISM	6.88E-01	8.46E-01	0.5118	0.8733	6278	25	NT5E NT5C2 APRT PKLR

Table S1.8 (Continued).

KEGG_BLADDER_CANCER	6.97E-01	8.46E-01	0.5049	0.8413	5998	16	RASSF1 EGFR NRAS MDM2 KRAS
KEGG_VALINE_LEUCINE_AND_ISOLEUCINE_DEGRADATION	7.45E-01	8.70E-01	0.4757	0.8027	6611	20	ACAT2 AUH
KEGG_PYRUVATE_METABOLISM	7.27E-01	8.70E-01	0.4870	0.8247	6490	21	ACAT2 LDHB PKLR
KEGG_VEGF_SIGNALING_PATHWAY	7.42E-01	8.70E-01	0.4792	0.8137	6667	22	NFAT5 NRAS KRAS MAPKAPK2 AKT3 MAP2K1 PPP3CB PIK3CA
KEGG_RIBOSOME	8.04E-01	9.06E-01	0.4515	0.7842	7674	39	RPL10A RPL22L1 RPS16 RPS9 RPL37A RPS18 RPL4 RPL38 RPL5 RPS28 RPL3 RPL39 RPS3A RPL35 RPS5 RPL21 RPS20 RPL18 RPL6 RPS19 RPL18A RPL8 RPL26 RPL13A RPS17 RPLP1 RPS24
KEGG_SPLICEOSOME	8.17E-01	9.06E-01	0.4388	0.7579	7677	33	THOC1 SRSF7 SRSF3 SF3B3 DDX39B TRA2B HNRNPA3 U2AF1 SNRPA DDX42 RBM25 U2AF2 CCDC12 THOC2
KEGG_LYSOSOME	7.94E-01	9.06E-01	0.4568	0.7919	7539	37	CD63 LGMN CLTC MANBA GALNS CTSB LAMP2 PSAP CTSA CTSD LAMP1 AP3S1 AP3D1
KEGG_LONG_TERM_DEPRESSION	8.15E-01	9.06E-01	0.4349	0.7421	7436	25	GRIA3 GNAI2 NRAS GNAI3 KRAS IGF1R GNA13 GNA12 LYN MAP2K1
KEGG_GLUTATHIONE_METABOLISM	8.57E-01	9.34E-01	-0.2829	-0.6953	1278	15	GGT1 GSTZ1 IDH2
KEGG_OOCYTE_MEIOSIS	8.63E-01	9.34E-01	0.4024	0.6894	7982	28	CPEB1 YWHAQ YWHAE IGF1R RPS6KA3 AR MAP2K1 PPP3CB
KEGG_VASCULAR_SMOOTH_MUSCLE_CONTRACTION	8.75E-01	9.34E-01	0.3962	0.6843	8224	33	ROCK2 RHOA CALD1 GNA13 PRKCD ARHGEF12 GNA12 PPP1R12A ROCK1 PPP1R12B MAP2K1
KEGG_FC_EPSILON_RI_SIGNALING_PATHWAY	9.13E-01	9.34E-01	0.3572	0.6094	8335	25	NRAS KRAS PRKCD GAB2 AKT3 LYN MAP2K1 PIK3CA
KEGG_INSULIN_SIGNALING_PATHWAY	9.10E-01	9.34E-01	0.3863	0.6765	8857	51	SOCS2 FLOT1 IKBKB PKLR NRAS FLOT2 KRAS RHOQ
KEGG_ALZHEIMERS_DISEASE	9.10E-01	9.34E-01	0.3954	0.6946	8945	59	APAF1 EIF2AK3 CAPN2 ADAM10 APOE APP CASP8
KEGG_ENDOMETRIAL_CANCER	8.90E-01	9.34E-01	-0.2513	-0.7283	625	30	EGF CTNNA2 PIK3R3

Table S1.8 (Continued).

KEGG_PARKINSONS_DISEASE	9.52E-01	9.62E-01	0.3368	0.5897	9228	48	APAF1 UBB
KEGG_MTOR_SIGNALING_PATHWAY	9.89E-01	9.89E-01	-0.1938	-0.5235	1006	22	VEGFA PIK3R3 MTOR TSC1 CAB39 CAB39L RPS6KB1 PRKAA2 MAPK1 PIK3R1 RPTOR RICTOR BRAF EIF4E RHEB STRADA STK11 PDPK1 PIK3CA AKT3 RPS6KA3 ULK2

Table S1.9. Gene set enrichment analysis on CTRL versus KDKD podocyte gene list.

pathway	pval	padj	ES	NES	nMoreExtreme	size	leadingEdge
KEGG_RIBOSOME	0.0001	0.0110	-0.6239	-1.9227	0	43	RPS19 RPS24 RPS28 RPS8 RPS5 RPL13A RPL4 RPL23 RPS17 RPL28 RPS11 RPL5 RPS23 RPL38 RPL18 RPS16 RPS9 RPS15A RPL6 RPL8 RPS3A RPLP1
KEGG_PATHOGENIC_ESCHERICHIA_COLI_INFECTION	0.0022	0.1028	-0.6509	-1.7544	16	21	ACTG1 ACTB ARHGEF2 TUBA1B TUBA1A YWHAQ NCK2 WASL ITGB1
KEGG_FATTY_ACID_METABOLISM	0.0170	0.2486	0.5415	1.6893	40	18	EHHADH ECI2 CYP4A11 ACADVL
KEGG_CARDIAC_MUSCLE_CONTRACTION	0.0219	0.2486	-0.5293	-1.5147	175	28	ATP1B1 ATP1B3 COX6A1 TPM1 COX7A2 CACNA2D1 UQCRC1 UQCR11 COX5A UQCRQ CACNB4
KEGG_ADHERENS_JUNCTION	0.0217	0.2486	-0.4994	-1.4930	179	36	ACTG1 IQGAP1 ACTB SORBS1 ACTN1 SMAD3 WASL CSNK2A2 EP300 MAPK1 VCL FGFR1 ACTN4
KEGG_LEUKOCYTE_TRANSENDOTHELIAL_MIGRATION	0.0188	0.2486	-0.4974	-1.5058	156	39	ACTG1 MSN GNAI1 ACTB F11R BCAR1 ACTN1 CXCL12 RAPGEF4 GNAI2 PTK2 ITGB1 VAV3 VCL MAPK12 ACTN4
KEGG_LONG_TERM_DEPRESSION	0.0252	0.2486	-0.5519	-1.5182	195	23	GNAI1 RAF1 GNA13 GNAI2 NRAS PPP2CA PLCB1 MAPK1 GRID2 BRAF
KEGG_REGULATION_OF_ACTIN_CYTOSKELETON	0.0182	0.2486	-0.4260	-1.4423	165	85	ACTG1 MSN IQGAP1 ABI2 PFN1 ACTB RAF1 PIP4K2A TMSB4Y BCAR1 ACTN1 GNA13 CYFIP2 SSH2 NRAS PTK2 WASL CRK ITGB1 DOCK1 VAV3 MAPK1 VCL PPP1R12A SSH1 FGFR1 ACTN4 BRAF
KEGG_HUNTINGTONS_DISEASE	0.0267	0.2486	-0.4277	-1.4229	239	73	VDAC2 DCTN4 RCOR1 COX6A1 BAX COX7A2 POLR2E CREB3L2 VDAC3 NDUFA2 UQCRC1 NDUFA7 UQCR11 COX5A NDUFA1 EP300 PLCB1 UQCRQ NDUFA9 NDUFA5 NDUFA4 NDUFB9 NDUFS7 NDUFB7 CLTA SLC25A5 PPARGC1A CYC1 AP2B1 SDHB NDUFS4
KEGG_ARRHYTHMOGENIC_RIGHT_VENTRICULAR_CARDIOMYOPATHY_ARVC	0.0267	0.2486	-0.5392	-1.5083	210	25	ACTG1 ACTB DMD ACTN1 CACNA2D1 PKP2 ITGB1 CACNB4 ACTN4
KEGG_PROTEASOME	0.0475	0.4018	-0.5859	-1.4610	352	15	PSMB6 PSMB2 PSMA7 PSMA3 PSMB1 PSMD7 PSMD11 PSMA1 PSMD2 PSMB5 PSMC6
KEGG_OXIDATIVE_PHOSPHORYLATION	0.0881	0.5122	-0.4035	-1.3068	773	60	COX6A1 COX7A2 ATP6V1H NDUFA2 UQCRC1 ATP6V0B NDUFA7 UQCR11 ATP6V1B2 COX5A NDUFA1 ATP6V0E1 UQCRQ NDUFA9 NDUFA5 ATP6AP1 NDUFA4 NDUFB9 ATP6V1A NDUFS7 NDUFB7 COX11 ATP6V1D ATP6V1G1 CYC1 ATP6V1E1 SDHB NDUFS4

Table S1.9 (Continued).

KEGG_TIGHT_JUNCTION	0.0679	0.5122	-0.4315	-1.3586	582	49	ACTG1 PPP2R2A GNAI1 VAPA ACTB F11R PRKCH ACTN1 SYMPK GNAI2 NRAS CSNK2A2 PPP2CA
KEGG_RIG_I_LIKE_RECEPTOR_SIGNALING_PATHWAY	0.0796	0.5122	-0.5313	-1.3876	603	18	NFKBIA TRAF3 OTUD5 AZI2 MAPK12 DDX3X CHUK
KEGG_ALZHEIMERS_DISEASE	0.0823	0.5122	-0.3975	-1.3092	732	68	APP COX6A1 COX7A2 NDUFA2 UQCRC1 NDUFA7 UQCR11 PPP3CA COX5A NDUFA1 MME CALM2 PLCB1 UQCRQ MAPK1 NDUFA9 ATF6 NDUFA5 NDUFA4 NDUFB9 NDUFS7
KEGG_PARKINSONS_DISEASE	0.0877	0.5122	-0.4048	-1.3064	769	58	VDAC2 UBB COX6A1 COX7A2 VDAC3 NDUFA2 UQCRC1 NDUFA7 UQCR11 COX5A NDUFA1 UQCRQ NDUFA9 NDUFA5 NDUFA4 NDUFB9 NDUFS7 NDUFB7 SLC25A5 CYC1 UBE2G1 SDHB NDUFS4 UQCRH PARK7 NDUFB4 UBE2L3
KEGG_PYRIMIDINE_METABOLISM	0.1468	0.5819	-0.5196	-1.2958	1089	15	POLR2E NME7 TXNRD1 POLR1D
KEGG_INOSITOL_PHOSPHATE_METABOLISM	0.1214	0.5819	0.4090	1.3164	285	20	PLCE1 ALDH6A1 INPP4B ITPKB PIK3C2A
KEGG_RNA_DEGRADATION	0.1162	0.5819	-0.5182	-1.3348	876	17	CNOT6 DCPS CNOT1 XRN2 PARN ENO1 HSPA9 CNOT10 CNOT6L CNOT4 EDC3
KEGG_HEDGEHOG_SIGNALING_PATHWAY	0.1502	0.5819	0.4268	1.2863	377	16	RAB23 CSNK1A1 LRP2 WNT5B
KEGG_LONG_TERM_POTENTIATION	0.1353	0.5819	-0.4417	-1.2872	1100	31	RAF1 PPP1R1A NRAS PPP3CA CALM2 EP300 PLCB1 MAPK1 PPP1R12A BRAF
KEGG_PANCREATIC_CANCER	0.1116	0.5819	0.3665	1.3090	207	31	VEGFA EGFR PIK3R3 BRCA2 E2F1 PIK3R1 RELA BCL2L1
KEGG_HYPERTROPHIC_CARDIOMYOPATHY_HCM	0.1327	0.5819	-0.4742	-1.3045	1032	23	ACTG1 TPM1 ACTB DMD CACNA2D1 ITGB1 CACNB4 PRKAA2 TPM3
KEGG_VIRAL_MYOCARDITIS	0.1377	0.5819	-0.4993	-1.3039	1044	18	ACTG1 ACTB DMD EIF4G2 EIF4G1
KEGG_ANTIGEN_PROCESSING_AND_PRESENTATION	0.1615	0.6009	-0.5051	-1.2800	1208	16	B2M HSPA4 HSP90AA1 HLAB HSPA5 PDIA3 TAPBP CTSB HLAF LGMN
KEGG_ALDOSTERONE_REGULATED_SODIUM_REABSORPTION	0.1841	0.6584	-0.5029	-1.2540	1366	15	ATP1B1 ATP1B3 SGK1 NR3C2 MAPK1
KEGG_MAPK_SIGNALING_PATHWAY	0.2092	0.7205	-0.3480	-1.1720	1898	81	DUSP1 DUSP16 RAF1 PPM1A MECOM FLNA PPM1B CACNA2D1 RPS6KA5 NRAS PPP3CA CRK JUND GADD45A MAPK8IP2 MAPK1 STK4 CACNB4 MAPK12 FGFR1 BRAF MAP4K3 MAP3K13 CHUK NF1 MAP2K3

Table S1.9 (Continued).

KEGG_NEUROTROPHIN_SIGNALING_PATHWAY	0.2444	0.7754	-0.3655	-1.1571	2109	51	BAX YWHAB RAF1 NFKBIA RPS6KA5 YWHAQ NRAS CRK ARHGDIA CALM2 MAPK1 MAPK12 BRAF BCL2 YWHAG
KEGG_MELANOGENESIS	0.2668	0.7754	-0.3986	-1.1553	2160	30	GNAI1 RAF1 CREB3L2 GNAI2 NRAS CALM2 EP300 PLCB1 MAPK1
KEGG_VASOPRESSIN_REGULATED_WATER_REABSORPTION	0.2468	0.7754	-0.4313	-1.1863	1920	23	DCTN4 DCTN6 CREB3L2 RAB5B RAB11A ARHGDIA DYNC1LI1 DYNC1I2 VAMP2
KEGG_AMYOTROPHIC_LATERAL_SCLEROSIS_ALS	0.2620	0.7754	-0.4647	-1.1776	1960	16	BAX CCS PPP3CA MAPK12 BCL2 CAT MAP2K3
KEGG_VIBRIO_CHOLERAE_INFECTION	0.2622	0.7754	-0.4220	-1.1709	2059	24	ACTG1 ACTB ATP6V1H ATP6V0B ATP6V1B2 ATP6V0E1 ATP6AP1 ATP6V1A GNAS ATP6V1D ATP6V1G1 ATP6V1E1 TJP1
KEGG_VALINE_LEUCINE_AND_ISOLEUCINE_DEGRADATION	0.3009	0.7773	0.3374	1.0993	695	21	EHHADH ALDH6A1 AUH PCCA IVD OXCT1 ALDH2 DBT ACADM
KEGG_SPLICEOSOME	0.2900	0.7773	-0.3659	-1.1235	2442	42	SRSF3 HNRNPA3 AQR CTNNBL1 SRSF2 TRA2B SF3B2 SRSF10 SRSF4 DDX42 RBM25 SRSF1 TRA2A THOC1 SRSF7 DDX39B SF3B3 RBM8A EFTUD2 SNRNP70 SNRPB
KEGG_TGF_BETA_SIGNALING_PATHWAY	0.2994	0.7773	-0.3978	-1.1307	2396	27	ID3 BMP7 SMAD6 SMAD3 PPP2CA EP300 MAPK1
KEGG_DILATED_CARDIOMYOPATHY	0.2966	0.7773	-0.4063	-1.1365	2340	25	ACTG1 TPM1 ACTB DMD CACNA2D1 ITGB1 CACNB4
KEGG_PROPANOATE_METABOLISM	0.3534	0.8017	0.3359	1.0656	837	19	EHHADH ALDH6A1 PCCA ALDH2 ACADM SUCLA2
KEGG_PPAR_SIGNALING_PATHWAY	0.3347	0.8017	0.3188	1.0719	717	24	EHHADH RXRG CYP4A11 LPL
KEGG_LYSOSOME	0.3303	0.8017	-0.3492	-1.0919	2820	47	PSAP AP4S1 CD164 IGF2R NPC2 ATP6V1H PPT1 ATP6V0B CTSD ATP6AP1 M6PR CD63 CTSZ CLTA AGA CTSB CTSA AP3B1 CTSH
KEGG_ECM_RECEPTOR_INTERACTION	0.3504	0.8017	-0.4279	-1.1022	2643	17	COL4A4 SPP1 ITGB1 SDC2
KEGG_SMALL_CELL_LUNG_CANCER	0.3513	0.8017	0.2933	1.0616	657	32	BIRC2 RXRG PIK3R3 E2F1 LAMA1 LAMA5 PIK3R1 RELA BCL2L1 RARB
KEGG_CYTOKINE_CYTOKINE_RECEPTOR_INTERACTION	0.3758	0.8320	0.3103	1.0434	805	24	VEGFA BMPR1B EGFR PDGFC ACVR2A GHR
KEGG_CHEMOKINE_SIGNALING_PATHWAY	0.3979	0.8605	-0.3283	-1.0489	3455	54	GNAI1 RAF1 NFKBIA BCAR1 CXCL12 GNAI2 NRAS PTK2 WASL CRK PLCB1 VAV3 MAPK1
KEGG_GAP_JUNCTION	0.4208	0.8756	-0.3521	-1.0367	3445	33	GNAI1 RAF1 TUBA1B TUBA1A CSNK1D GNAI2 NRAS PLCB1 MAPK1

Table S1.9 (Continued).

KEGG_B_CELL_RECEPTOR_SIGNALING_PATHWAY	0.4331	0.8756	-0.3525	-1.0273	3524	31	RAF1 NFKBIA NRAS PPP3CA VAV3 MAPK1 CD81 CHUK IFITM1 GSK3B SOS1 GRB2
KEGG_EPITHELIAL_CELL_SIGNALING_IN_HELICOBACTER_PYLORI_INFECTION	0.4307	0.8756	-0.3510	-1.0274	3500	32	F11R NFKBIA ATP6V1H ATP6V0B ATP6V1B2 ATP6V0E1 ATP6AP1 MAPK12 ATP6V1A NOD1 CHUK ATP6V1D ATP6V1G1 ATP6V1E1 TJP1
KEGG_BLADDER_CANCER	0.4432	0.8770	-0.3935	-1.0276	3363	18	RAF1 RPS6KA5 NRAS DAPK1 RASSF1 MAPK1 MDM2 BRAF
KEGG_PHOSPHATIDYLINOSITOL_SIGNALING_SYSTEM	0.4841	0.8833	0.2766	0.9731	940	29	PLCE1 PIK3R3 PIK3R1 INPP4B ITPKB
KEGG_MTOR_SIGNALING_PATHWAY	0.4621	0.8833	0.2954	0.9863	1024	23	VEGFA PIK3R3 MTOR PIK3R1
KEGG_INSULIN_SIGNALING_PATHWAY	0.4939	0.8833	-0.3032	-0.9913	4383	64	SORBS1 RAF1 LIPE ACACB PDE3B NRAS CRK RPTOR CALM2 MAPK1 PRKAA2 EIF4E2 BRAF CBL PRKAG2 PPARGC1A SOCS2 GSK3B SOS1 RHOQ GRB2 PRKCI
KEGG_MELANOMA	0.4789	0.8833	0.2852	0.9795	986	26	EGFR PDGFC PIK3R3 E2F1 PIK3R1
KEGG_CHRONIC_MYELOID_LEUKEMIA	0.4848	0.8833	-0.3281	-0.9971	4051	40	RAF1 MECOM NFKBIA NRAS SMAD3 CRK MAPK1 MDM2 BRAF CBL BCR CHUK
KEGG_FC_GAMMA_R_MEDIATED_PHAGOCYTOSIS	0.5258	0.9015	-0.3250	-0.9673	4337	35	RAF1 ASAP1 ASAP2 MYO10 WASL CRK VAV3 MAPK1
KEGG_COLORECTAL_CANCER	0.5152	0.9015	-0.3449	-0.9725	4090	26	BAX RAF1 SMAD3 MAPK1 BRAF BCL2 AXIN1
KEGG_NON_SMALL_CELL_LUNG_CANCER	0.5332	0.9015	0.2702	0.9453	1044	28	RXRG EGFR PIK3R3 E2F1 PIK3R1 RARB
KEGG_LYSINE_DEGRADATION	0.5472	0.9087	0.2830	0.9338	1222	22	EHHADH ASH1L SETD1B
KEGG_VEGF_SIGNALING_PATHWAY	0.5621	0.9171	-0.3463	-0.9443	4365	22	RAF1 NRAS PTK2 PPP3CA MAPK1 MAPK12
KEGG_CELL_CYCLE	0.5887	0.9237	-0.3036	-0.9321	4959	42	MAD1L1 YWHAB YWHAQ SMAD3 CDKN1C EP300 GADD45A MDM2 ORC4 YWHAG ORC5 ATR GSK3B RAD21 CDC27 GADD45G SMAD4 CDK7 ANAPC5 YWHAH CDC26 HDAC1
KEGG_P53_SIGNALING_PATHWAY	0.5959	0.9237	-0.3688	-0.9196	4425	15	BAX GADD45A CCNG1 RCHY1 MDM2
KEGG_PATHWAYS_IN_CANCER	0.5900	0.9237	-0.2725	-0.9469	5524	109	COL4A4 BAX RAF1 MECOM NFKBIA TRAF3 HSP90B1 NRAS DAPK1 PTK2 SMAD3 CRK ITGB1 TRAF5 RASSF1 EP300 MAPK1 ARNT HSP90AA1 STK4 FGFR1 MDM2 BRAF CBL BCL2 PML TPM3 ZBTB16 RALBP1 AXIN1 EGLN2 BCR CHUK

Table S1.9 (Continued).

KEGG_FOCAL_ADHESION	0.6201	0.9454	-0.2767	-0.9222	5586	74	ACTG1 COL4A4 ACTB RAF1 SPP1 FLNA BCAR1 ACTN1 PTK2 CRK ITGB1 DOCK1 VAV3 MAPK1 VCL PPP1R12A ACTN4 BRAF
KEGG_CITRATE_CYCLE_TCA_CYCLE	0.6693	0.9460	-0.3332	-0.8582	5049	17	IDH3B ACO2 CS SDHB SUCLG2 ACO1 MDH1 SDHC OGDH
KEGG_ARGININE_AND_PROLINE_METABOLISM	0.6917	0.9460	0.2787	0.8399	1740	16	PRODH2 ASS1 ALDH2 PRODH GLUD1 SAT1 GLUL DAO GLS ALDH7A1 LAP3 P4HA1 GOT2 GATM ODC1 AMD1
KEGG_NEUROACTIVE_LIGAND_RECEPTOR_INTERACTION	0.6645	0.9460	-0.3345	-0.8615	5013	17	GCGR PTGER3 GRID2 NR3C1 GABRA4
KEGG_AXON_GUIDANCE	0.6494	0.9460	-0.2812	-0.9033	5680	56	EPHA6 SRGAP3 GNAI1 CXCL12 GNAI2 SLIT2 NRAS NCK2 PTK2 PPP3CA ITGB1 MAPK1 EFNA5
KEGG_CELL_ADHESION_MOLECULES_CAMS	0.6354	0.9460	-0.3238	-0.8906	4945	23	F11R NLGN1 GLG1 ITGB1 SDC2 HLAB
KEGG_NATURAL_KILLER_CELL_MEDIATED_CYTOTOXICITY	0.6864	0.9460	-0.3021	-0.8587	5494	27	RAF1 NRAS PPP3CA VAV3 MAPK1 HLAB BRAF
KEGG_GLIOMA	0.6781	0.9460	0.2473	0.8654	1328	28	EGFR PIK3R3 E2F1 MTOR PIK3R1 CAMK2G
KEGG_GLYCEROPHOSPHOLIPID_METABOLISM	0.8160	0.9714	-0.2874	-0.7403	6156	17	CHKB GPD2 CHKA DGKA LPGAT1
KEGG_ERBB_SIGNALING_PATHWAY	0.7647	0.9714	-0.2655	-0.8153	6442	42	RAF1 NRG1 NRAS NCK2 PTK2 CRK MAPK1 ERBB4 BRAF CBL
KEGG_CALCIUM_SIGNALING_PATHWAY	0.8657	0.9714	0.2051	0.7715	1443	38	PLCE1 EGFR ADCY9 GNA11 CAMK2G PHKB ADCY1 ITPKB MYLK TRPC1 PRKACB
KEGG_PEROXISOME	0.7929	0.9714	0.2205	0.8076	1427	34	EHHADH ECI2 PHYH PEX13 CROT
KEGG_APOPTOSIS	0.8025	0.9714	0.2332	0.7785	1779	23	BIRC2 PIK3R3 PIK3R1 RELA BCL2L1 DFFA
KEGG_VASCULAR_SMOOTH_MUSCLE_CONTRACTION	0.8580	0.9714	-0.2465	-0.7463	7166	39	RAF1 PRKCH CALD1 GNA13 CALM2 PLCB1 MAPK1 PPP1R12A BRAF
KEGG_TOLL_LIKE_RECEPTOR_SIGNALING_PATHWAY	0.7453	0.9714	-0.2903	-0.8122	5881	25	SPP1 NFKBIA TRAF3 MAPK1 MAPK12 CHUK MAP2K3
KEGG_NOD_LIKE_RECEPTOR_SIGNALING_PATHWAY	0.7792	0.9714	-0.2981	-0.7784	5913	18	NFKBIA HSP90B1 MAPK1 HSP90AA1 MAPK12 NOD1 CHUK
KEGG_T_CELL_RECEPTOR_SIGNALING_PATHWAY	0.8494	0.9714	-0.2454	-0.7535	7155	42	RAF1 NFKBIA NRAS NCK2 PPP3CA VAV3 MAPK1 MAPK12 CBL CHUK
KEGG_FC_EPSILON_RI_SIGNALING_PATHWAY	0.8097	0.9714	-0.2687	-0.7640	6481	27	RAF1 NRAS VAV3 MAPK1 MAPK12 MAP2K3 SOS1 GRB2

Table S1.9 (Continued).

KEGG_PROGESTERONE_MEDIATED_OOCYTE_MATURATION	0.8448	0.9714	-0.2550	-0.7545	6927	34	GNAI1 RAF1 PDE3B GNAI2 MAPK1 HSP90AA1 MAPK12 BRAF
KEGG_ADIPOCYTOKINE_SIGNALING_PATHWAY	0.8227	0.9714	0.2241	0.7751	1642	27	RXRG JAK2 MTOR RELA AGRP CPT1A PCK1
KEGG_ENDOMETRIAL_CANCER	0.8588	0.9714	-0.2520	-0.7304	6955	30	RAF1 NRAS MAPK1 BRAF AXIN1 GSK3B SOS1 GRB2 EGF APC PDPK1
KEGG_PROSTATE_CANCER	0.8670	0.9714	-0.2363	-0.7457	7456	50	RAF1 NFKBIA HSP90B1 CREB3L2 NRAS EP300 MAPK1 HSP90AA1 FGFR1 MDM2 BRAF BCL2 CHUK
KEGG_ACUTE_MYELOID_LEUKEMIA	0.7417	0.9714	-0.2838	-0.8226	6007	30	RAF1 NRAS MAPK1 BRAF PML ZBTB16 CHUK PPARD SOS1 GRB2
KEGG_PYRUVATE_METABOLISM	0.8905	0.9859	-0.2571	-0.6714	6758	18	ACACB ME3 ACAT1 ACSS2
KEGG_PURINE_METABOLISM	0.9550	0.9984	-0.2128	-0.6130	7694	29	POLR2E NME7 PDE3B POLR1D AK5 PDE7A ADK AK4 PDE1A FHIT NT5C2 NPR1 POLR3C
KEGG_OOCYTE_MEIOSIS	0.9863	0.9984	-0.1836	-0.5697	8379	45	YWHAB YWHAQ PPP3CA PPP2CA CALM2 MAPK1 MAPK12
KEGG_UBIQUITIN_MEDIATED_PROTEOLYSIS	0.9267	0.9984	-0.2156	-0.6941	8117	57	UBE2H HERC1 UBE2I UBE3A STUB1 UBE2E2 RCHY1 MDM2 CBL UBE2D3 PML HERC2
KEGG_SNARE_INTERACTIONS_IN_VESICULAR_TRANSPORT	0.9869	0.9984	-0.1922	-0.4950	7445	17	BNIP1 VAMP2 VAMP7 STX6 USE1
KEGG_ENDOCYTOSIS	0.9657	0.9984	0.1679	0.7243	957	74	AP2A2 EGFR SMAP1 SH3GL2 VPS37A IQSEC1 CBLC GRK4 ARRB1 PRKCZ HLAC DAB2
KEGG_JAK_STAT_SIGNALING_PATHWAY	0.9877	0.9984	-0.1862	-0.5426	8038	31	LIFR EP300 IL6R IL15RA CBL IL6ST SOCS2 PIAS1 IL13RA1 SOS1 GRB2
KEGG_GNRH_SIGNALING_PATHWAY	0.9460	0.9984	-0.2188	-0.6444	7746	33	RAF1 NRAS CALM2 PLCB1 MAPK1 MAPK12 MAP2K3 GNAS SOS1 GRB2
KEGG_RENAL_CELL_CARCINOMA	0.9410	0.9984	-0.2221	-0.6473	7658	31	RAF1 NRAS CRK EP300 MAPK1 ARNT BRAF EGLN2
KEGG_WNT_SIGNALING_PATHWAY	0.9988	0.9988	-0.1530	-0.4764	8517	46	PPP3CA SMAD3 CSNK2A2 PPP2CA EP300 PLCB1 AXIN1 PPARD GSK3B APC ROCK1 PPP2R5C SMAD4 PPP3CB CTBP1 TBL1XR1 CHD8 PPP2R5E

Appendix 2:

Material Related to Chapter 3

A

Line	Age	Gender	Tissue Origin	iPS vectors
AS	NA	Male	Bone marrow CD34+ mononuclear cells	Episomal
N1	12	Female	Erythroblasts	Sendai virus
N2	46	Female	Erythroblasts	Sendai virus
ThF	NA	Female	CD34+ cord blood	Episomal

B

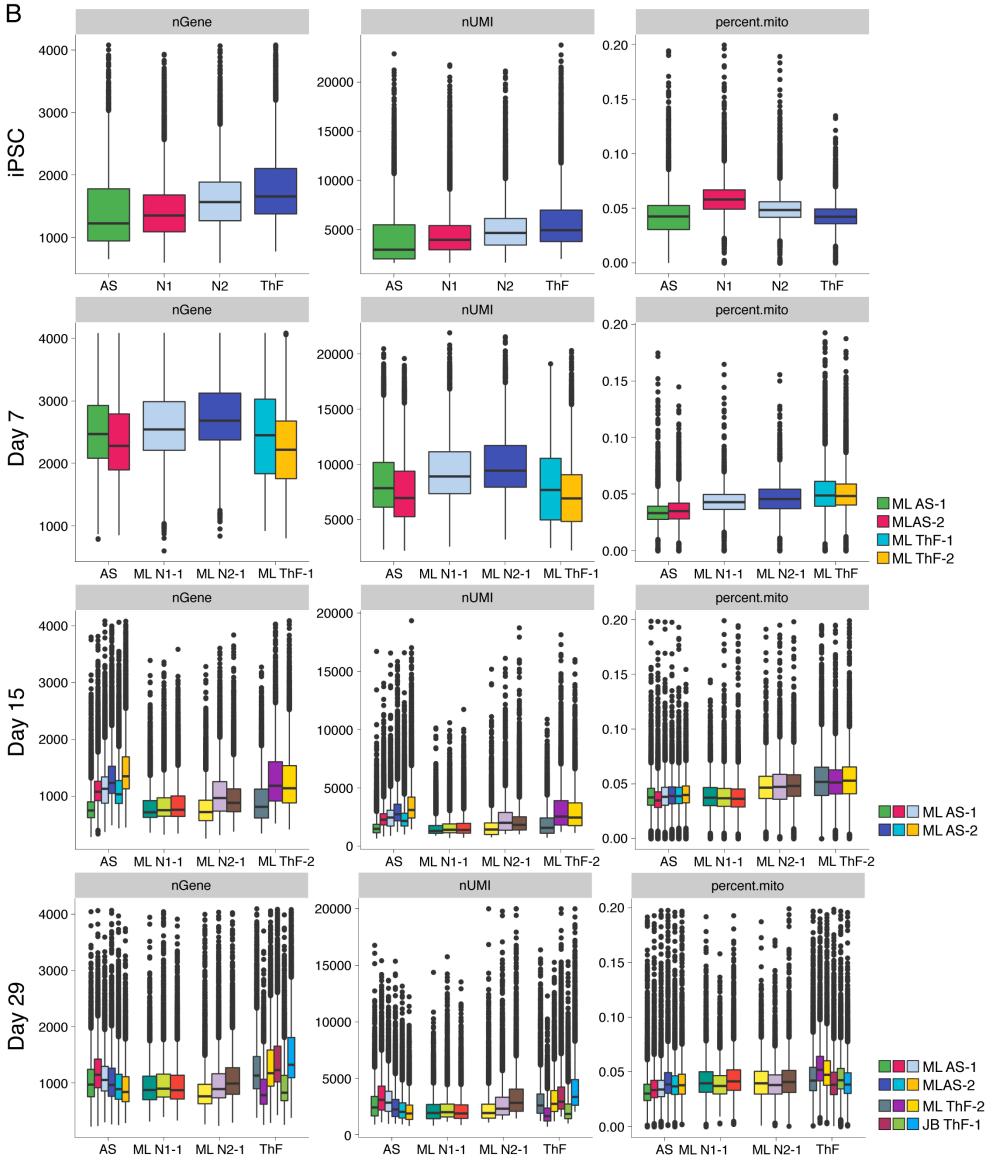

Figure S2.1. Data quality metrics for single cell analysis of kidney organoids across four iPSC lines. A. Table of reference for 4 different iPSC lines. **B.** Quality control metrics (nGene: number of genes with a normalized expression value above 0 per cell, lower QC cutoff 200; nUMI: the total number of Unique Molecule Identifiers (UMIs) detected per cell, lower QC cutoff 1000; percent.mito: The proportion of reads mapping to mitochondrial genes, upper QC cutoff of 20%) across cell lines and time points.

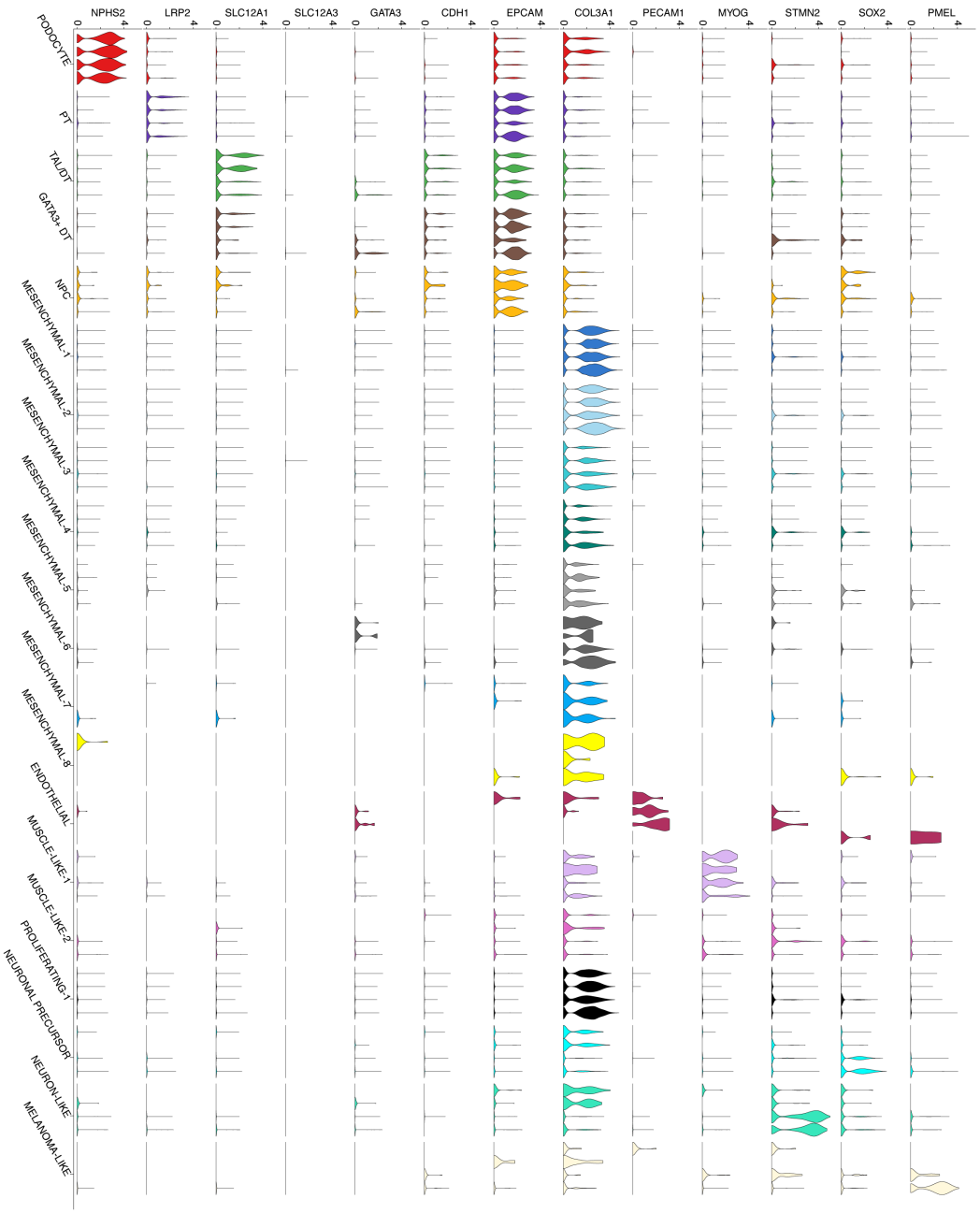

Figure S2.2. Day 29 kidney organoids express canonical markers of major nephron, mesenchymal and off-target cell types. Violin plots of single cell gene expression from day 29 kidney organoids for canonical markers. X-axis annotations represent clusters. Each violin per cluster represents a line, AS, N1, N2 and ThF in order from left to right.

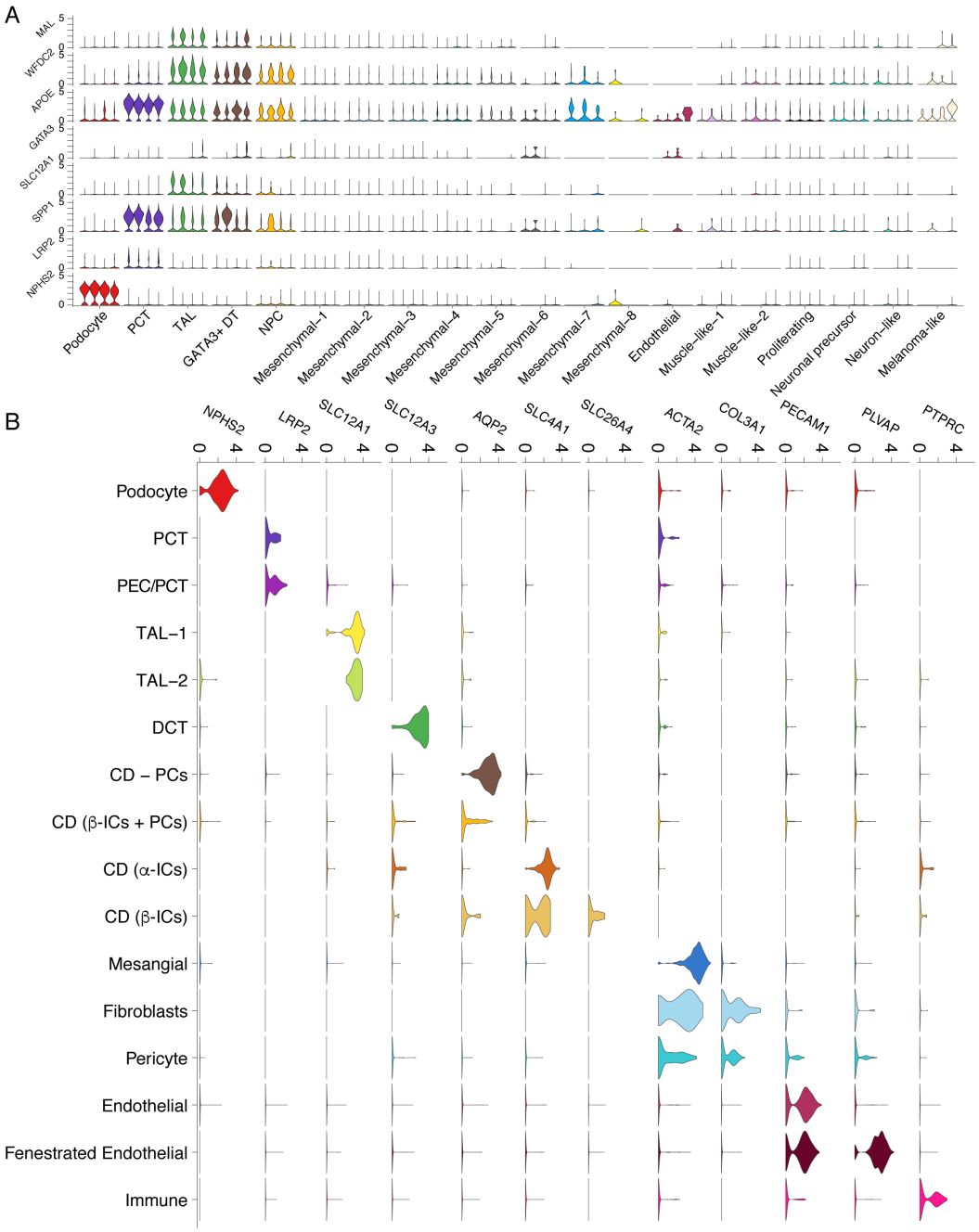

Figure S2.3. D29 data-derived markers and canonical markers of major human nephron and kidney cell types. A. Organoids from all lines at D29 express data-derived markers in a cluster specific manner as seen in Violin plots of single cell gene expression from day 29 kidney organoids. **B.** Violin plot of single cell gene expression from human adult nephrectomy for canonical markers. X-axis annotations represent clusters.

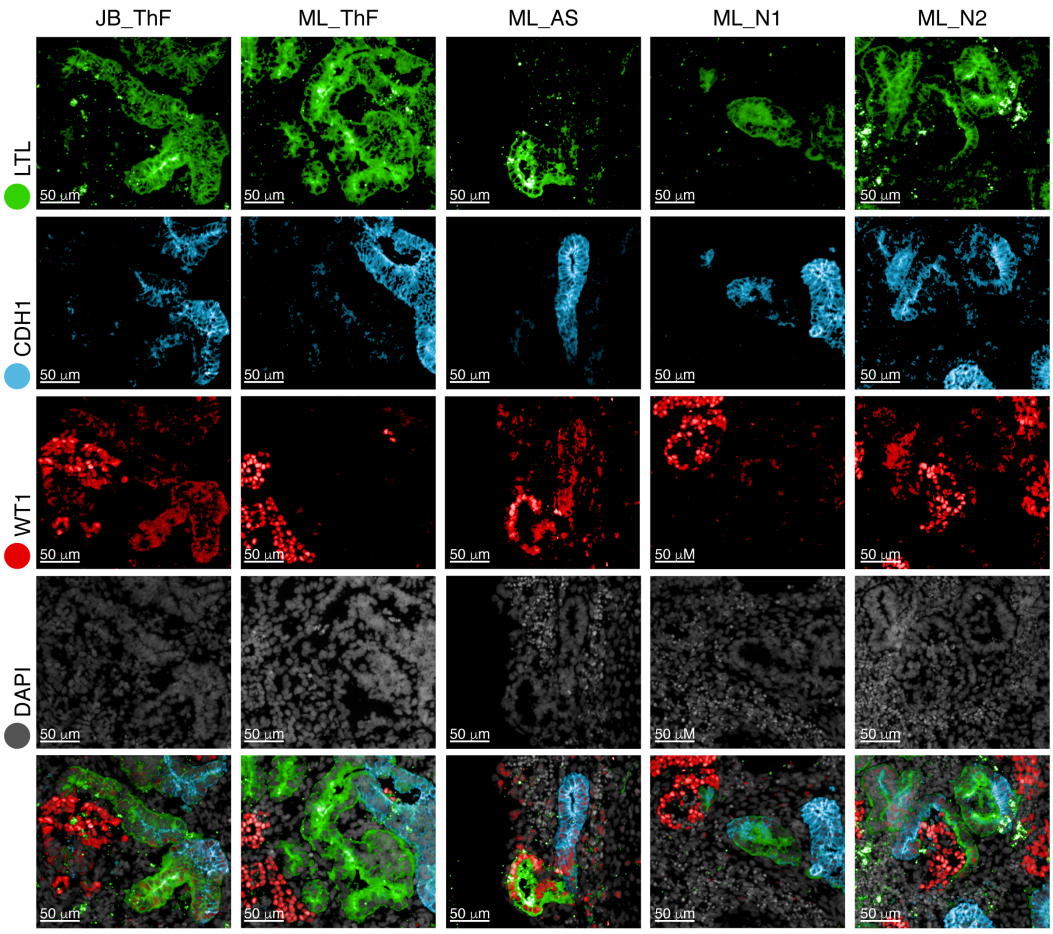

Figure S2.4. Immunofluorescence analysis of day 29 kidney organoids demonstrates presence of major nephron cell types from glomerulus to distal tubule. Immunofluorescence staining of day 29 kidney organoids for podocytes (WT1), proximal tubular cells (LTL), and the distal tubular compartment (ECAD) across two protocols (JB, ML) and four cell lines (ThF, AS, N1, N2).

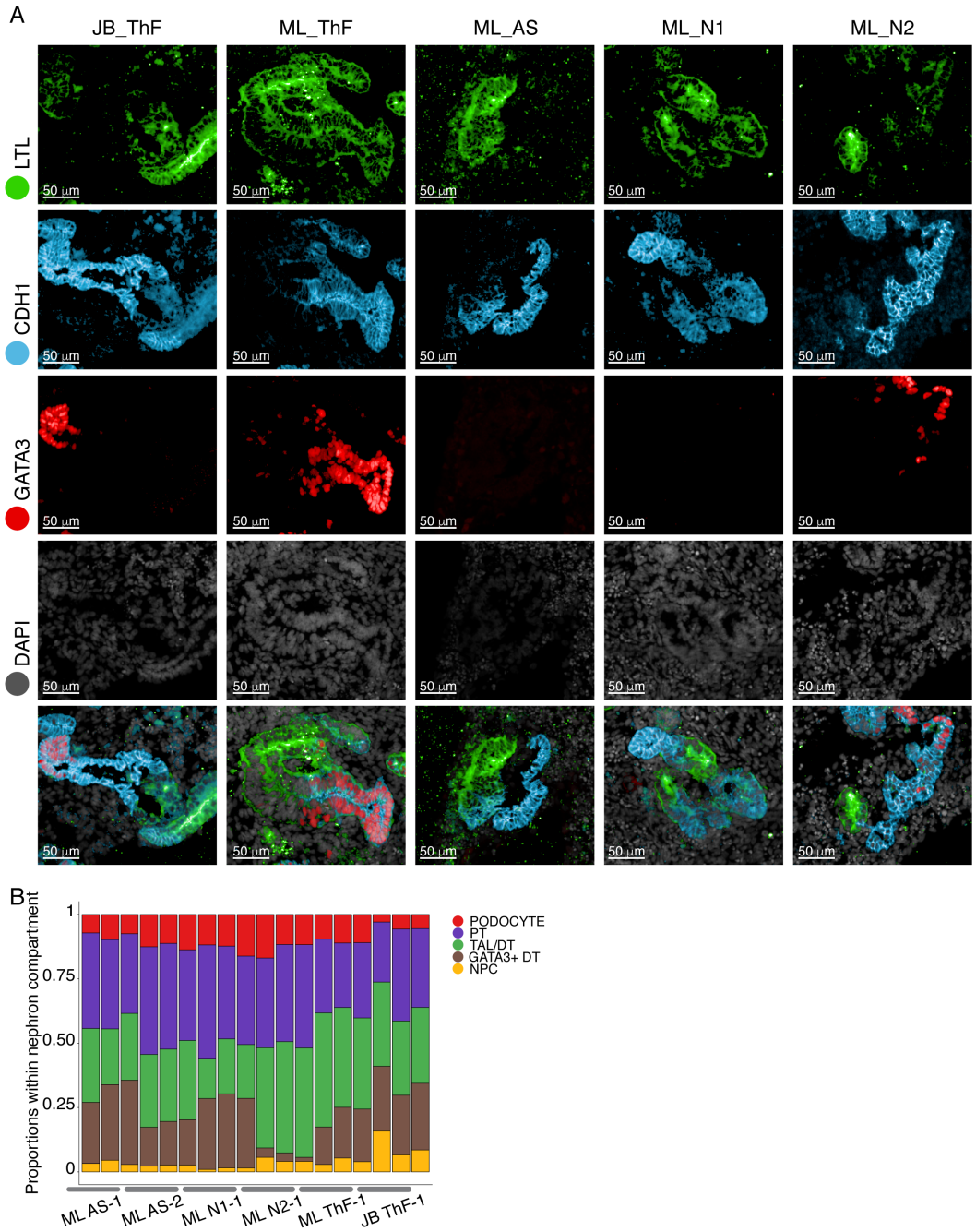

Figure S2.5. Immunofluorescence analysis of day 29 kidney organoids demonstrates presence of major kidney epithelial cell types from proximal to distal tubule. A. Immunofluorescence staining of day 29 kidney organoids for proximal tubule (LTL), and distal nephron compartment (ECAD, GATA3) across two protocols (JB, ML) and four cell lines (ThF, AS, N1, N2). **B.** Proportions of cell classes within the nephron compartment across all lines and replicates at D29.

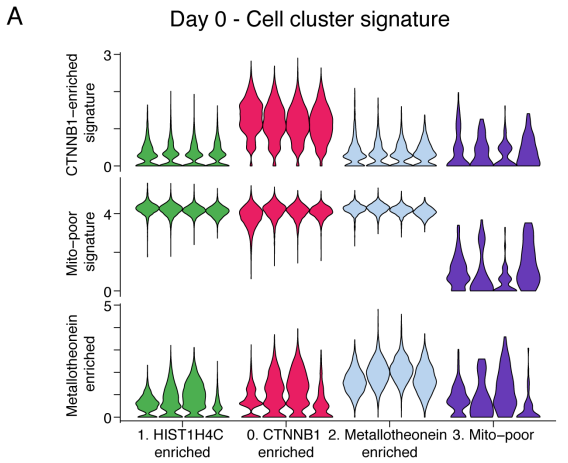

Cluster	Genes	
CTNNB1-enriched	CTNNB1, SOX11, CDC42, PTPRS	↑
Metallotheonein-enriched	MT1H,MT1G,MT1X	↑
Mito-poor	MT-CO3, MT-CYB, MT-ND4	↓

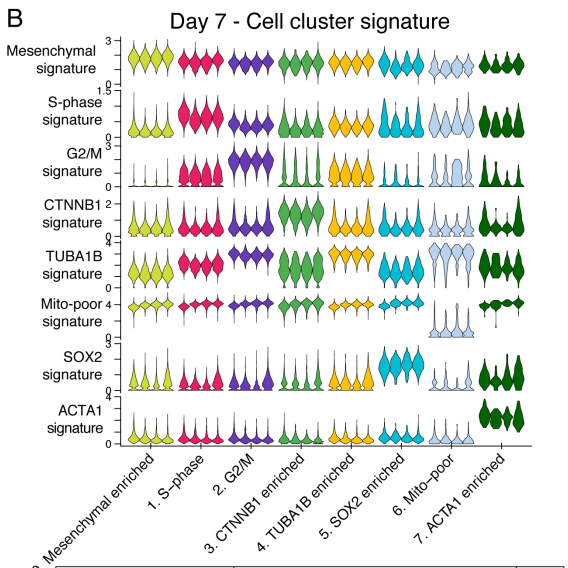

Cluster	Genes	
Mesenchymal enriched	ACTG1, DLK1, BST2,WT1	↑
S-phase enriched	RPA2,MCM4,RFC4,MCM6,PCNA,MCM5, LIG1,RNASEH2A,MCM7,RFC2,RPA3, MCM3,FEN1	↑
G2/M enriched	TOP2A, CENPF	↑
CTNNB1 enriched	CTNNB1, SOX11, CDC42, PTPRS	↑
TUBA1B enriched	TUBA1B,PTTG1	↑
SOX2 enriched	SOX2,HOXD1,TGFBI	↑
Mito-poor	MT-CO3, MT-CYB, MT-ND4	↓
ACTA1 enriched	ACTA2,MYL9,TAGLN,CTGF,ACTC1, TPM1,ANXA2, SPARC	↑

Figure S2.6. Cluster specific gene signatures for iPSC D0 and D7 stages. A. Violin plot of average expression of cluster specific gene signatures in cells in each line at the iPSC stage. Signatures are provided in the table. **B.** Violin plot of average expression of cluster specific gene signatures in cells in each line at D7. Signatures are provided in the accompanying table. In each cluster, violins for AS, N1, N2 and ThF are in order from left to right.

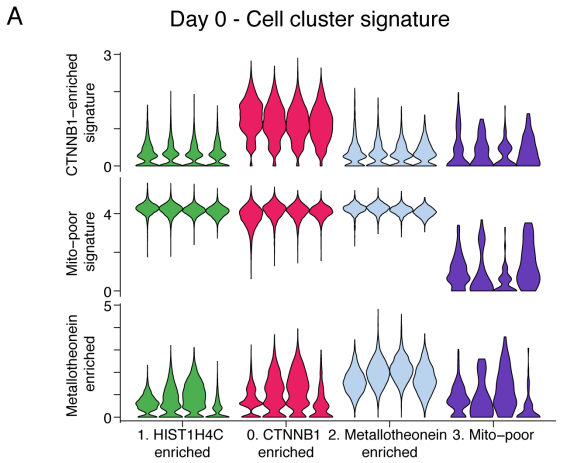

Cluster	Genes	
CTNNB1-enriched	CTNNB1, SOX11, CDC42, PTPRS	↑
Metallotheonein-enriched	MT1H,MT1G,MT1X	↑
Mito-poor	MT-CO3, MT-CYB, MT-ND4	↓

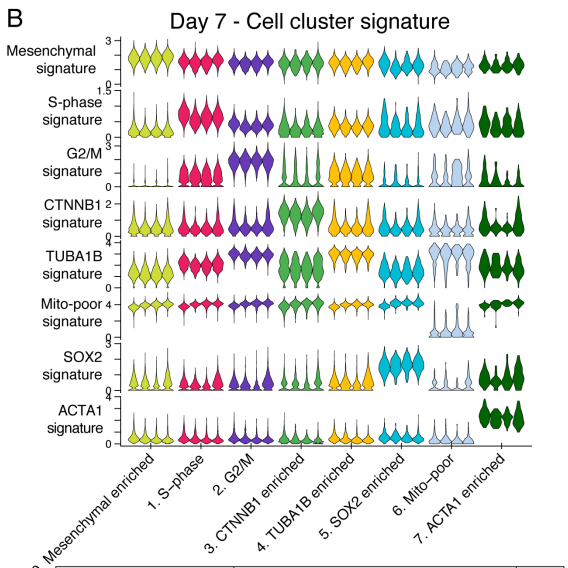

Cluster	Genes	
Mesenchymal enriched	ACTG1, DLK1, BST2,WT1	↑
S-phase enriched	RPA2,MCM4,RFC4,MCM6,PCNA,MCM5, LIG1,RNASEH2A,MCM7,RFC2,RPA3, MCM3,FEN1	↑
G2/M enriched	TOP2A, CENPF	↑
CTNNB1 enriched	CTNNB1, SOX11, CDC42, PTPRS	↑
TUBA1B enriched	TUBA1B,PTTG1	↑
SOX2 enriched	SOX2,HOXD1,TGFBI	↑
Mito-poor	MT-CO3, MT-CYB, MT-ND4	↓
ACTA1 enriched	ACTA2,MYL9,TAGLN,CTGF,ACTC1, TPM1,ANXA2, SPARC	↑

Figure S2.7. Single cell analysis of 4 iPSC lines reveals no priming for any specific germ layer and expression of cell-cycle markers. Violin plot of cluster-specific average expression of germ-layer signatures in single cells from the 4 iPSC lines at **A.** D0 and **B.** D7. In each cluster, violins for AS, N1, N2 and ThF are in order from left to right.

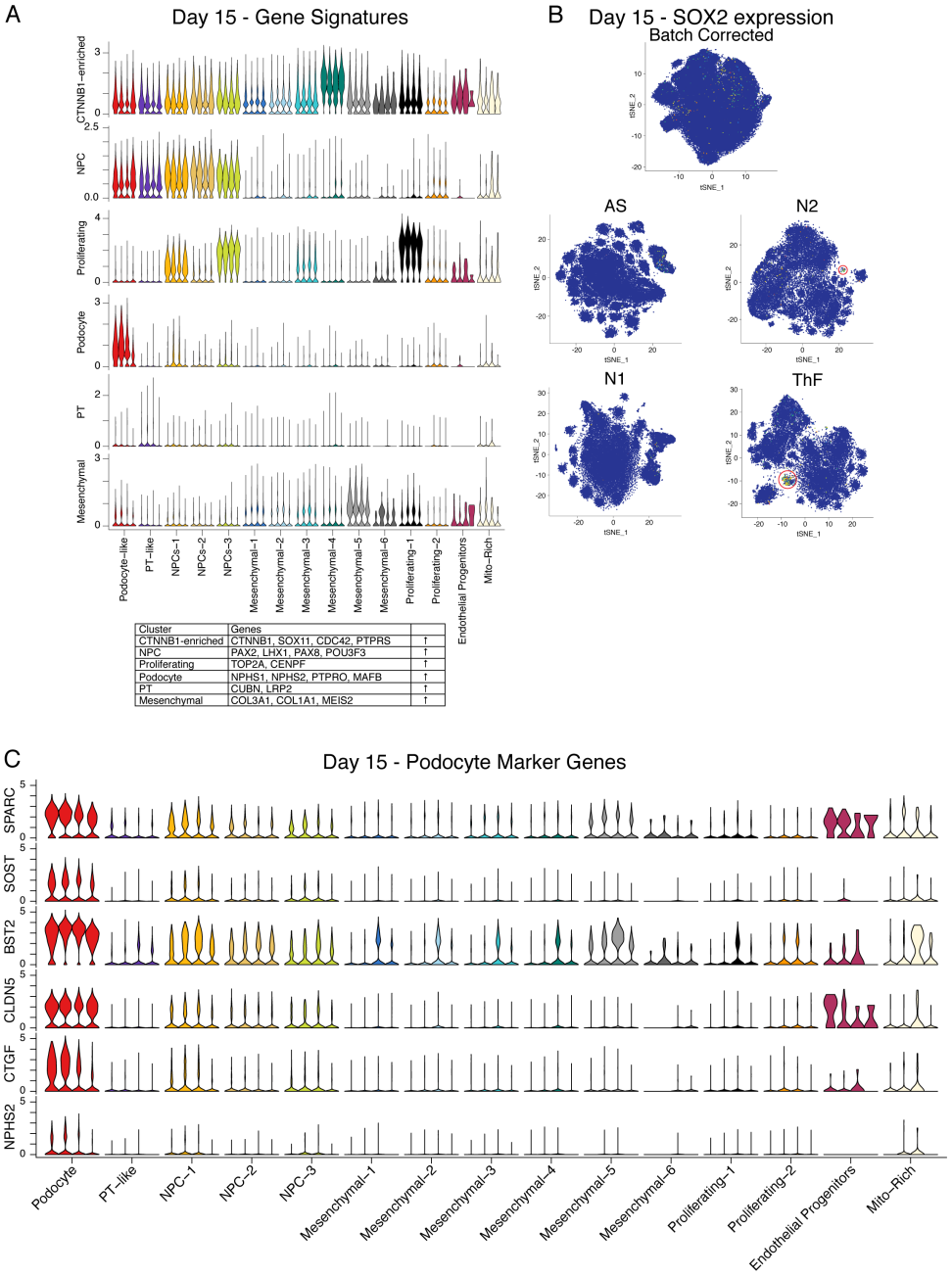

Figure S2.8. Expression of cluster specific gene signatures, line-specific SOX2+ progenitor pools and early markers of podocyte differentiation at D15. A. Violin plot of average expression of cluster specific gene signatures in cells in each line at D15 **B.** tSNE plot showing variability across the lines in presence of SOX2-positive progenitor cells at D15. Subpopulation of cells (in red circle) expressing SOX2 emerge as early as D15 in ThF and N2. **C.** Violin plots from D15 organoids for expression of canonical (NPHS2) and data-driven (CLDN5, SOST, BST2, SPARC, CTGF) podocyte marker genes. In each cluster, violins for AS, N1, N2 and ThF are in order from left to right.

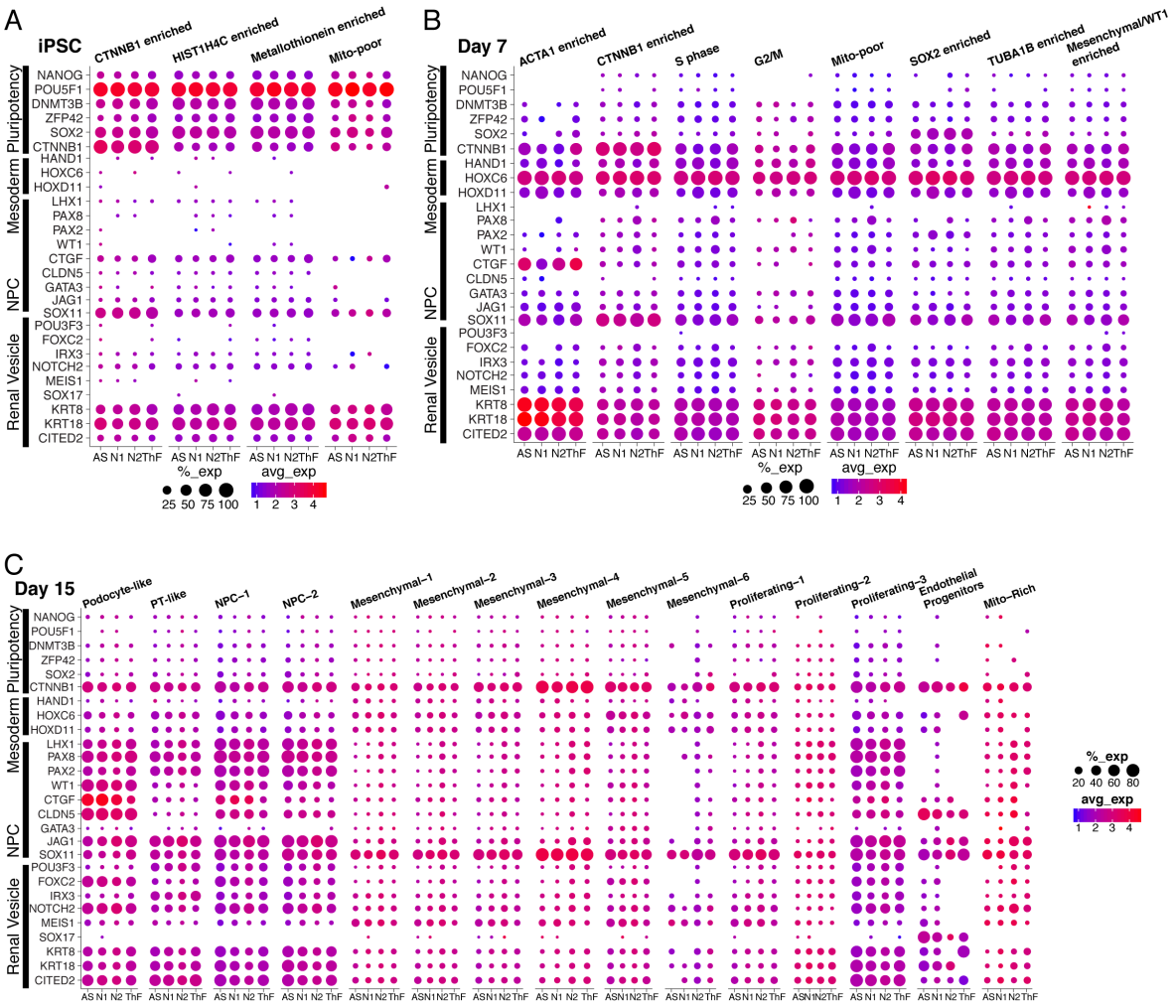

Figure S2.9. Kidney organoid differentiation follows kidney nephrogenesis as determined by expression of transcriptional programs across organoid development time. Dot plot comparison of expression of major transcription factors and other canonical markers of nephrogenesis across organoid differentiation (iPSC **A.**, Day 7 **B.**, Day 15 **C.**) across the 4 iPSC lines.

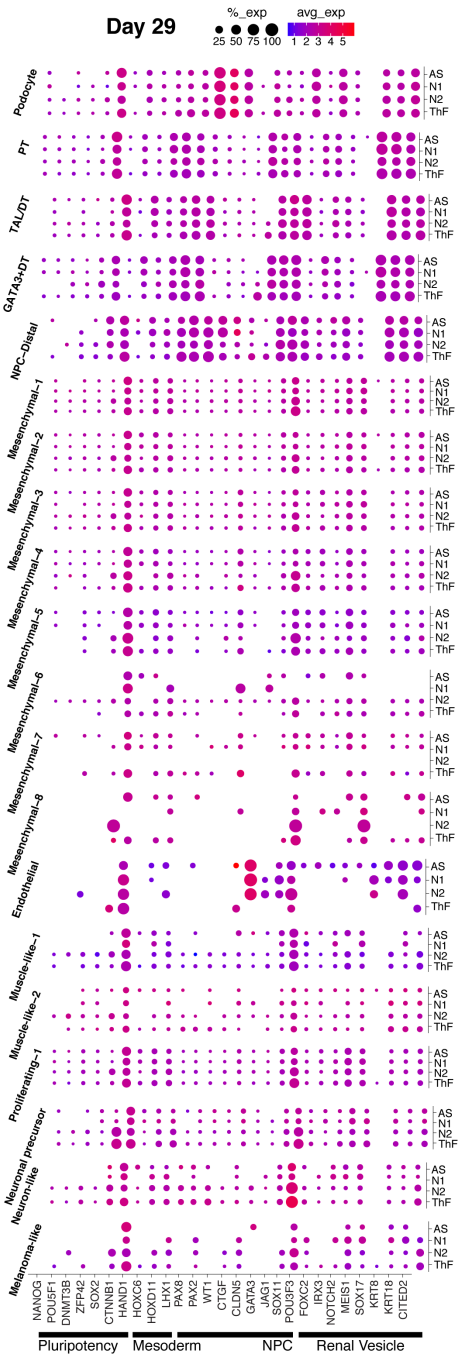

Figure S2.10. Kidney organoid differentiation follows kidney nephrogenesis as determined by expression of transcriptional programs across organoid development time. Dot plot comparison of expression of major transcription factors and other canonical markers of nephrogenesis in D29 organoids across 4 iPSC lines.

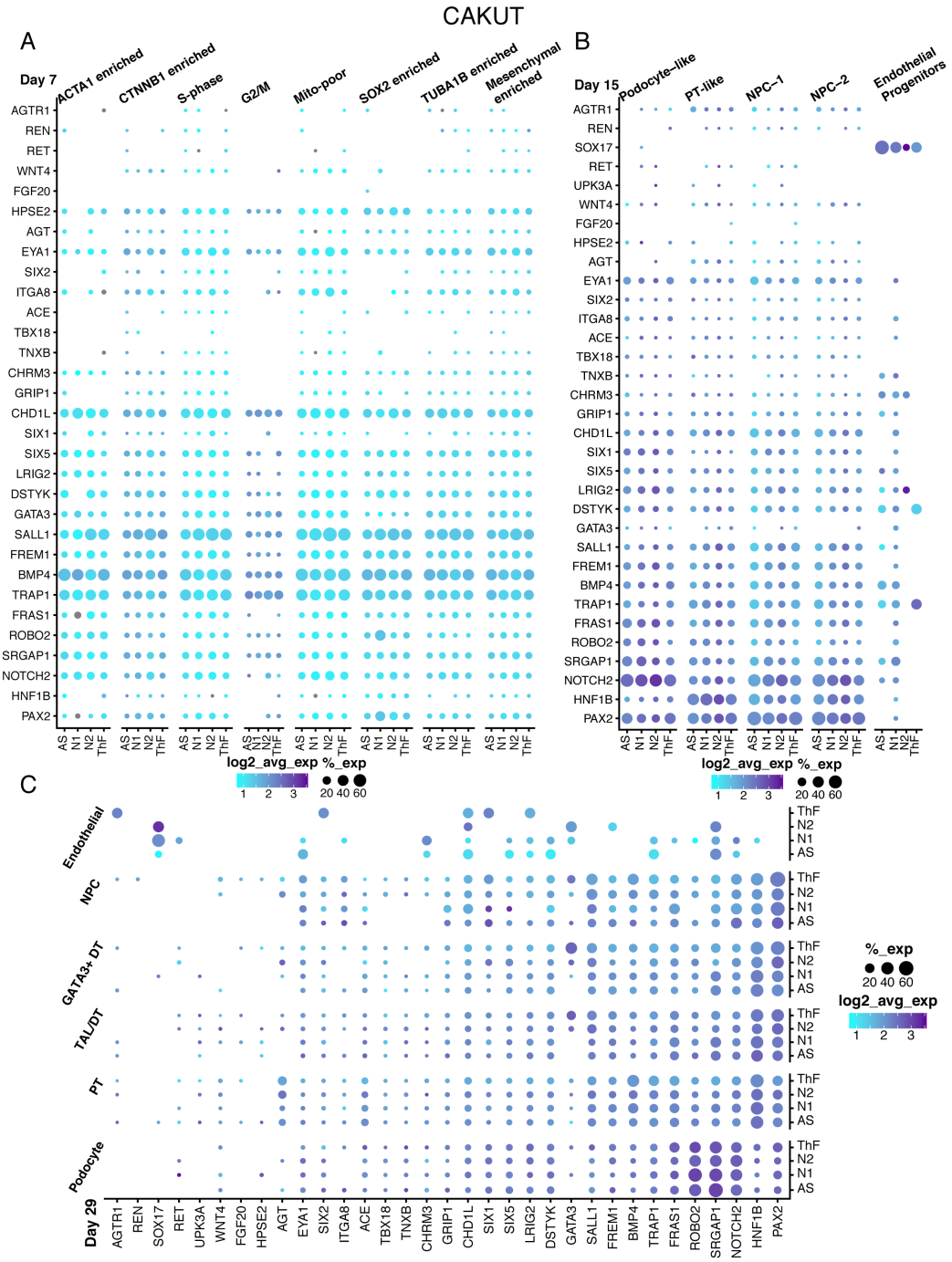

Figure S2.11. Expression of monogenic causes of congenital abnormalities of the kidney and urinary tract (CAKUT) in appropriate nephron epithelial cell types suggests utility of kidney organoids for understanding genetic kidney diseases. Dot plot comparison of gene expression in organoids across differentiation **A.** Day 7, **B.** Day 15, and **C.** Day 29 of CAKUT-causing genes in kidney epithelial cell clusters (Day 15, Day 29) across 4 iPSC lines.

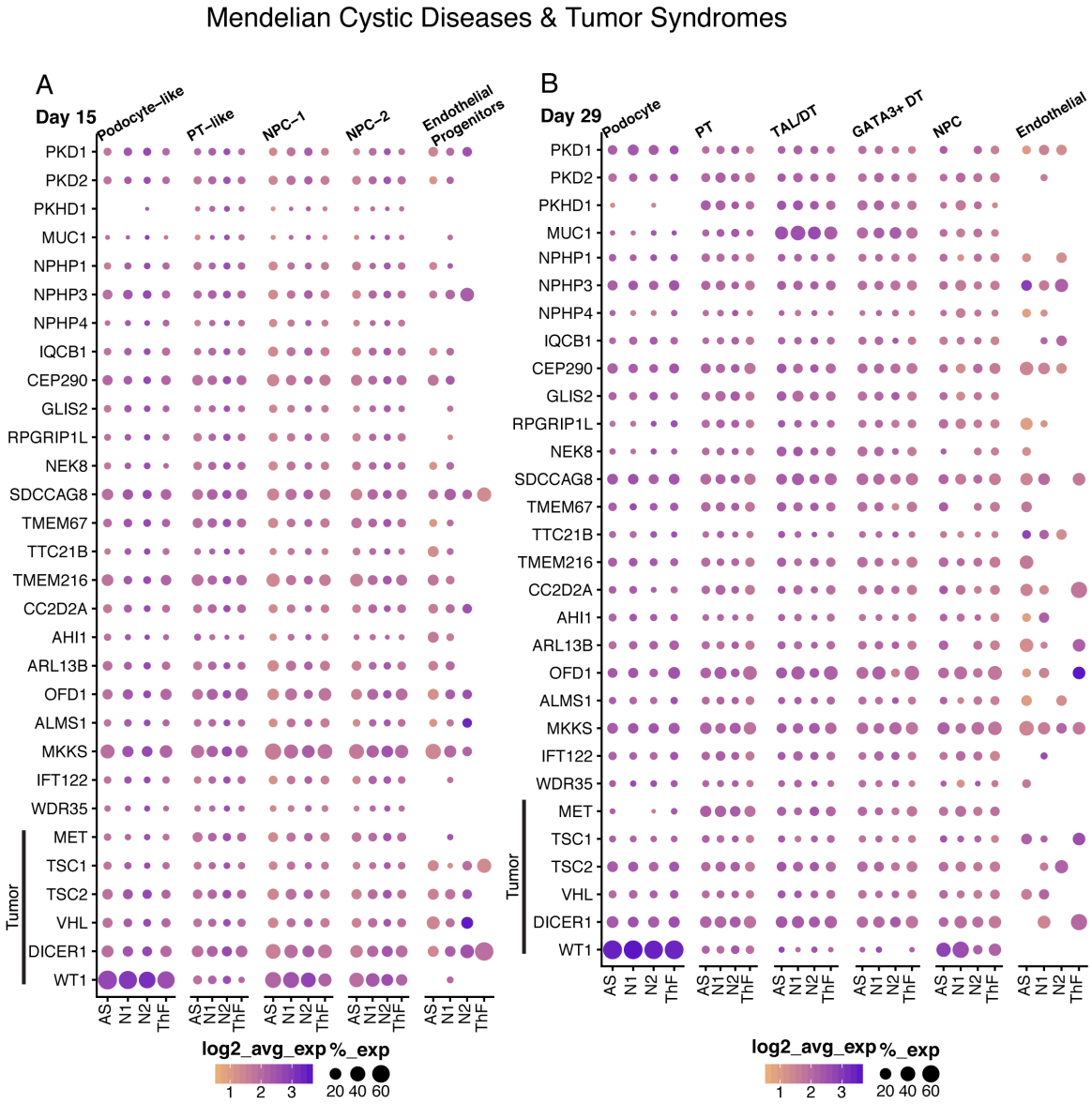

Figure S2.12. Expression of monogenic causes of hereditary renal cystic (HRC) diseases and tumor syndromes in appropriate nephron epithelial cell types suggests utility of kidney organoids for understanding genetic kidney diseases. Dot plot comparison of gene expression in organoids **A.** Day 15, **B.** Day 29 of HRC and tumor syndrome diseases-causing genes in kidney epithelial cell clusters across 4 iPSC lines.

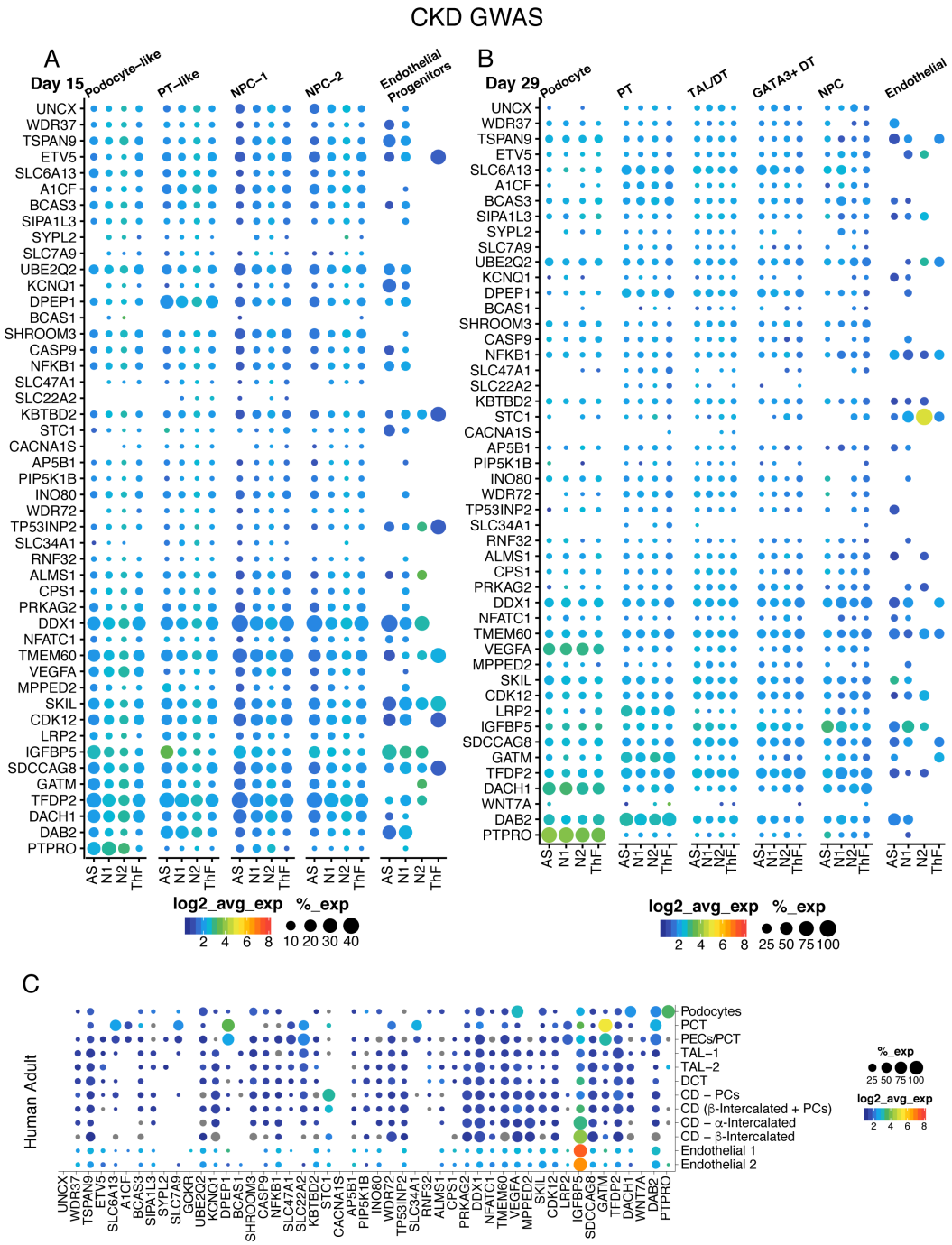

Figure S2.13. Expression of genes associated with chronic kidney diseases in appropriate nephron epithelial cell types suggests utility of kidney organoids for understanding genetic kidney diseases. Dot plot comparison of gene expression in organoids **A.** Day 15, **B.** Day 29) and **C.** human adult of genes associated with chronic kidney disease in kidney epithelial cell clusters across 4 iPSC lines.

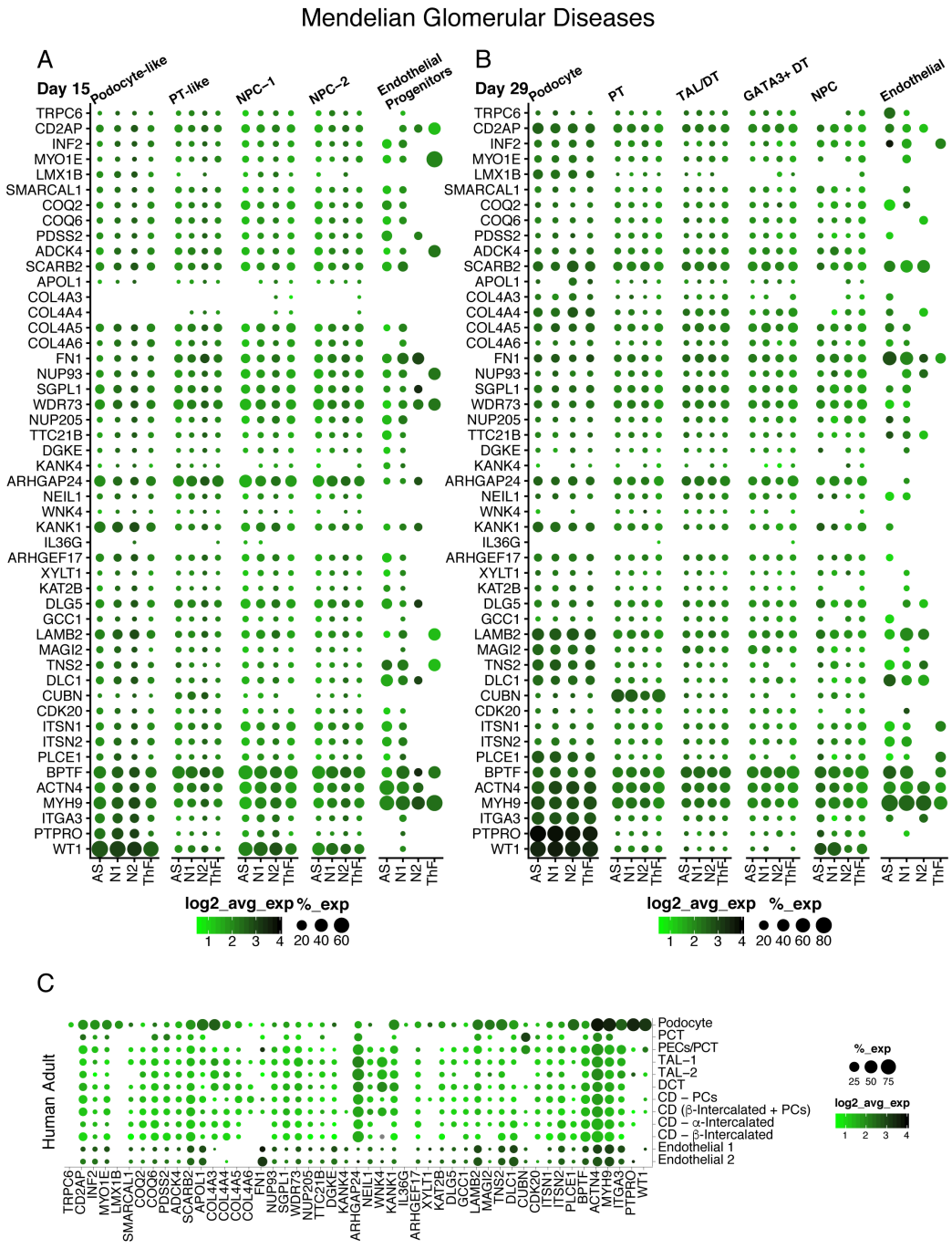

Figure S2.14. Expression of monogenic causes of hereditary glomerular diseases in appropriate nephron epithelial cell types suggests utility of kidney organoids for understanding genetic kidney diseases. Dot plot comparison of gene expression in organoids (Day 15 **A.**, Day 29 **B.**) and **C.** human adult of hereditary glomerular disease-causing genes in kidney epithelial cell clusters across 4 iPSC lines.

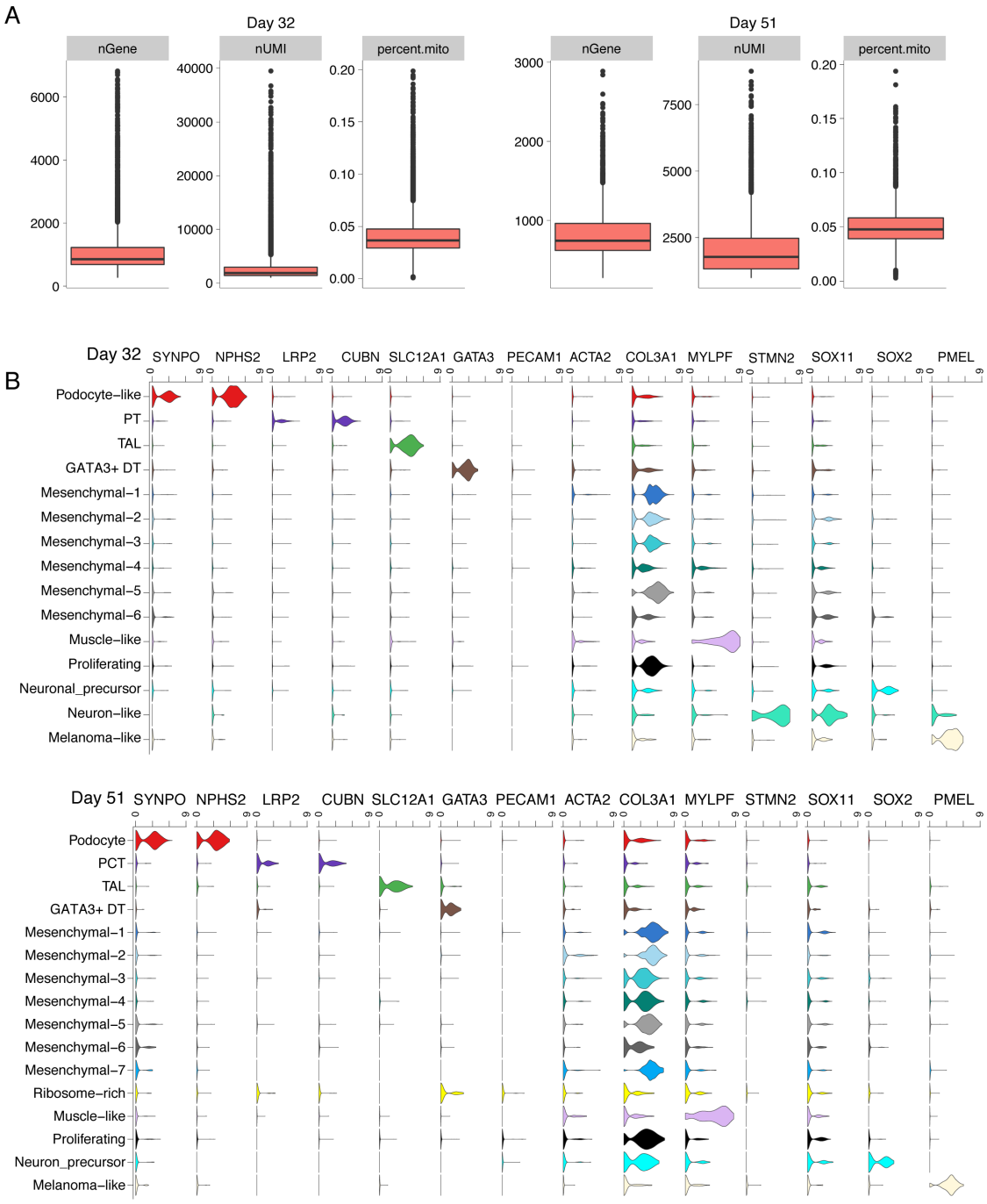

Figure S2.15. Expression of differentially enriched genes in organoids in prolonged culture found by clustering. A. Quality control metrics of D32 and D51 control organoids. **B.** Violin plot of single cells from D32 (top row) and D51 (bottom row) control organoids with gene expression of selected genes superimposed.

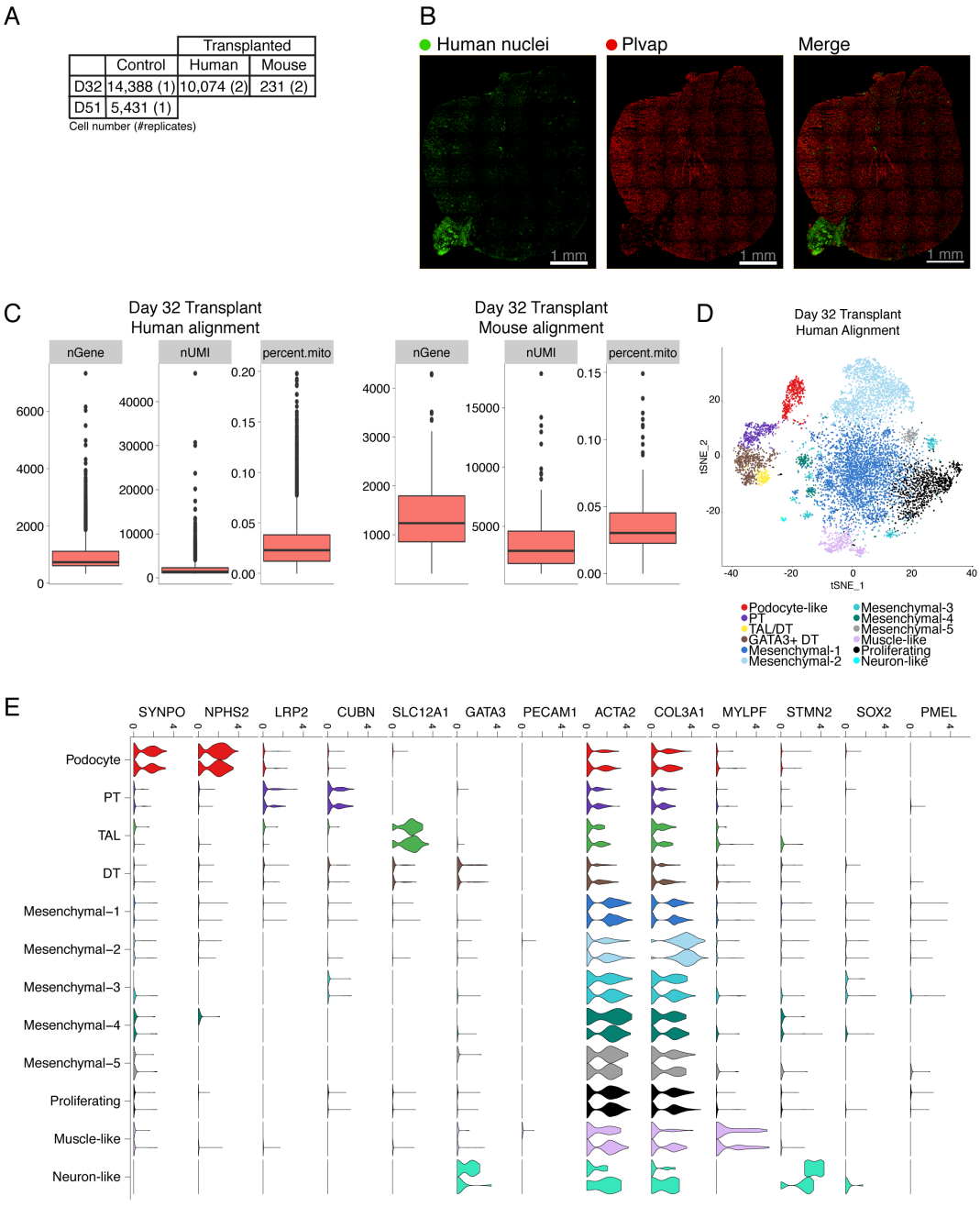

Figure S2.16. Single cell analysis of kidney subcapsular transplantation of organoids. A. Table of cell numbers from D32 cultured and transplanted organoids. **B.** Immunofluorescence staining of transplanted kidney organoids for human nuclei and endothelial cells (Plvap). **C.** Quality metrics of D32 transplanted kidney organoids from alignment to the combined human and mouse transcriptomes for (left) human and (right) mouse cells. **D.** t-SNE plot of human cells from D32 transplanted kidney organoids. **E.** Violin plot of gene expression of canonical cluster markers in single cells from D32 transplanted organoids (human).

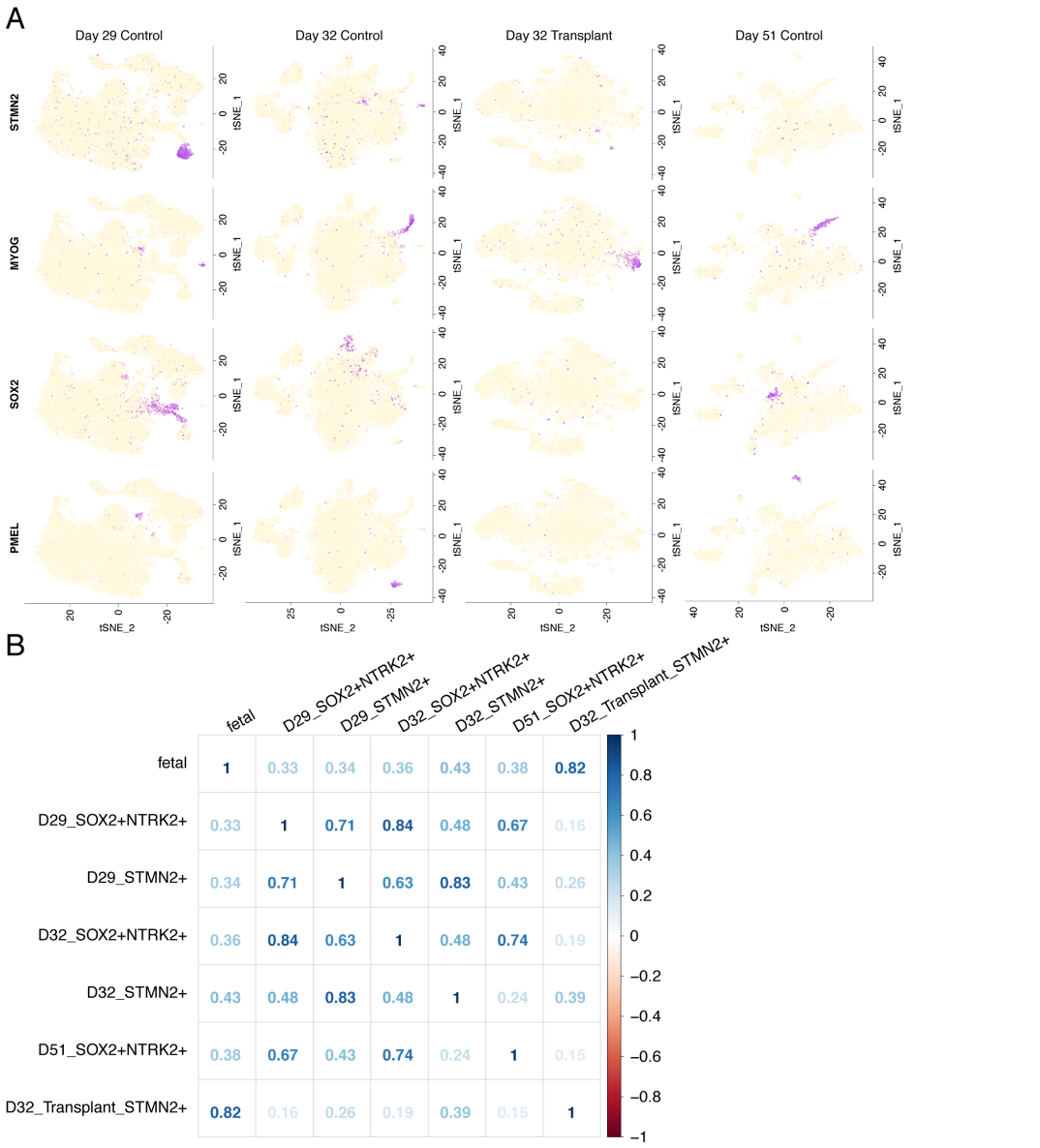

Figure S2.17. Off-target SOX2+ neuronal and PMEL+ melanoma off-target cells reduced in transplanted organoids. A. t-SNE plot of single cells from in vitro (D29 and D32, and prolonged culture D51) and transplanted organoids with expression of off-target gene markers (PMEL [myeloma], SOX2 [neuronal], MYOG [muscle], STMN2 [neuronal]). The colors indicate the range of expression from low (off-white) to high (purple). **B.** Spearman correlation plot indicates that STMN2+ cells in transplanted organoids correspond uniquely (= 0.82) to fetal kidney, in contrast to organoids grown in vitro.

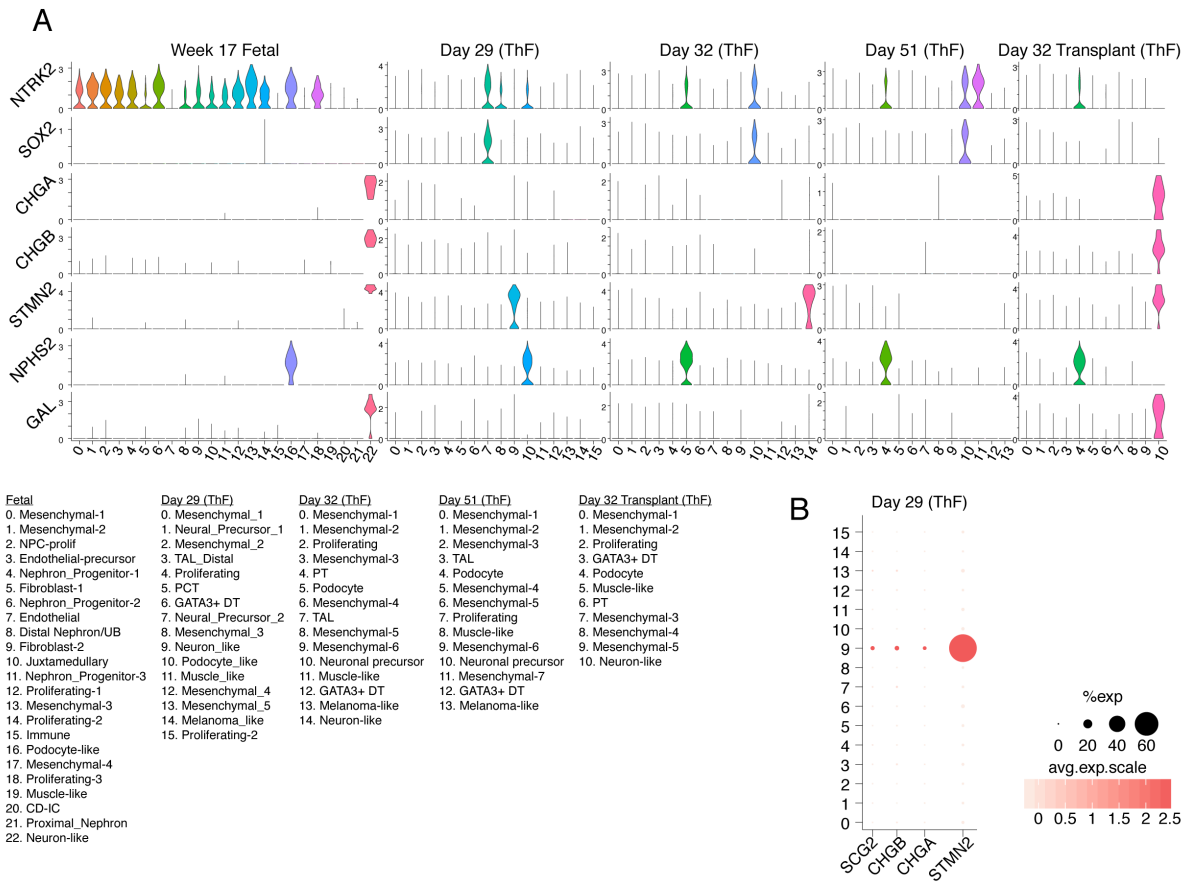

Figure S2.18. Transplanted organoids neuronal clusters are most similar to second trimester fetal kidneys. A. Violin plots of clusters from Day 29 and D32 controls, D51 prolonged culture and D32 transplanted showing expression of specific genes of interest. NRTK2 is abundantly co-expressed with NPHS2 (podocyte) in fetal kidney and across all organoids. The STMN2+ neuronal cluster in fetal kidney in enriched in CHGA, CHGB and GAL, and this pattern of gene expression is uniquely recapitulated in D32 transplant organoids, but not in organoids grown in vitro. **B.** Dot plot indicates expression of CHGA and CHGB was detectable in a small number of cells in D29 STMN2+ cells.

Table S2.1. Canonical gene marker list.

Kidney compartment	Canonical Markers used for identification		
	Organoid	**Human**	**Mouse**
Podocyte	NPHS2, SYNPO, WT1	NPHS2, SYNPO, WT1	
Proximal Tubule	CUBN, LRP2, AQP1	CUBN, LRP2, AQP1	
Thick Ascending Limb	SLC12A1	SLC12A1	
Distal Convoluted Tubule	GATA3, CDH1, MUC1	SLC12A3, MUC1, CDH1	
Distal Nephron		-	
Ureteric Bud		-	
Collecting Duct – Principal Cells	-	AQP2	
Collecting Duct – alpha Intercalated Cells	-	SLC4A1	
Collecting Duct – beta Intercalated Cells	-	SLC26A4	
Mesenchymal/vascular smooth muscle	COL3A1, MEIS2, MEIS1	ACTA2	
Mesenchymal/fibroblast		COL3A1	
Endothelial Cell	PECAM1	PECAM1, KDR	Pecam1, Kdr
Fenestrated Endothelial Cell	-	PECAM1, PLVAP	Pecam1, Plvap
Immune Cells	-	PTPRC	
Other			
Epithelial	EPCAM		
Neuronal	STMN2, SOX11		
Neuronal (progenitor)	SOX2		
Muscle	MYOG, MYLPF		
Melanoma-like	PMEL		
Nephron Progenitor Cells (Distal)	POU3F3, PAX8		
Nephron Progenitor Cells (Proximal)	STMN2, SOX11		

Table S2.2. Data driven gene marker list.

Organoid Stage	Kidney Cell	Data-driven Marker
D15	Podocyte	CLDN5
		SOST
		SPARC
		BST2
	Proximal Tubule (Proximal-distal gradient)	APOE
D29	Distal Nephron	WFDC2
		MAL
		DEFB1

Table S2.3. Classification of cell types into compartments.

putative_cell_types	Compartment
Endothelial Progenitors	Endothelial
Nephron Progenitor Cells-1	Nephron
Nephron Progenitor Cells-2	Nephron
Nephron Progenitor Cells-3	Nephron
Podocyte-like cells	Nephron
Proximal Tubule-like Cells	Nephron
Mesenchymal Cells-1	Mesenchymal
Mesenchymal Cells-2	Mesenchymal
Mesenchymal Cells-3	Mesenchymal
Mesenchymal Cells-4	Mesenchymal
Mesenchymal Cells-5	Mesenchymal
Mesenchymal Cells-6	Mesenchymal
Proliferating Cells-1	Mesenchymal
Proliferating Cells-2	Mesenchymal
Mito-Rich cells	Mesenchymal